

A Thesis Submitted for the Degree of PhD at the University of Warwick

Permanent WRAP URL:

<http://wrap.warwick.ac.uk/148311>

Copyright and reuse:

This thesis is made available online and is protected by original copyright.

Please scroll down to view the document itself.

Please refer to the repository record for this item for information to help you to cite it.

Our policy information is available from the repository home page.

For more information, please contact the WRAP Team at: wrap@warwick.ac.uk

Numerical analysis for active control of drag over flat plate using sinusoidal travelling wave method

By

Mohamed Ahmed Mohamed Elghorab

A thesis submitted in partial fulfilment of the requirements for the

degree of

Doctor of Philosophy in Mechanical Engineering

University of Warwick, School of Engineering

June 2020

I have learned to use the word “impossible” with the
greatest caution.

Wernher von Braun (1912–1977)

Table of Contents

Table of Contents	III
List of Figures	VI
List of Tables	XI
Acknowledgement	XII
Declaration	XIII
Abstract	XIV
List of Abbreviations	XV
Nomenclature	XVI
Chapter (1) Introduction	1
1.1 Motivation	1
1.2 Drag reduction control	2
1.3 Transition to turbulence	4
1.4 Transition scenarios	6
1.4.1 Transition due to Tollmien–Schlichting waves	8
1.4.2 Transition due to non-modal disturbance growth (Bypass transition)	9
Chapter (2) Literature Review on Turbulence and Bypass Transition	
Control	11
2.1 Introduction	11
2.2 Types of turbulence control	12
2.2.1 Opposition control	14
2.2.2 Travelling wave	16
2.2.3 Blowing and suction control	23
2.3 Transition control	30
2.4 Scope of the study	33
2.5 Thesis outlines	34
Chapter (3) Monotonically Integrated Large Eddy Simulation Solver (MILES)	35
3.1 Introduction	35

3.2	Governing Equations	41
3.2.1	Conventional LES	41
3.2.2	Monotonically Integrated large eddy simulation MILES	43
3.3	Flux Limiters	45
3.4	MILES Solver Validation	53
3.4.1	Mesh independence study	53
3.4.2	Fully developed channel with $Re\tau = 180$	56
3.4.3	Fully developed channel with $Re\tau = 395$	65
3.5	Summery	70
Chapter (4)	Isotropic Homogeneous Turbulence Inlet Boundary Condition	72
4.1	Introduction	72
4.2	Governing Equations	76
4.3	Synthetic turbulence modifications	82
4.4	Results	84
4.4.1	Computational Domain	84
4.4.2	Boundary condition results	85
4.5	Summery	94
Chapter (5)	Active Control for Drag Reduction in Transitional Boundary Layer	95
5.1	Introduction	95
5.2	Generation of bypass transition	96
5.2.1	Free stream turbulence decay	98
5.2.2	Skin friction study of $Tu = 7\%$	100
5.2.3	Effect of inlet turbulent Intensity on the bypass transition	101
5.2.4	Grid resolution study for $Tu = 3\%$	102
5.3	Active control via sinusoidal spanwise travelling wave	103
5.4	Results	107
5.4.1	Sinusoidal wave and mesh symmetry	108
5.4.2	Effect of wave amplitude	110
5.4.3	Inclined spanwise travelling wave	112
5.4.4	Effect of wave frequency	120
5.4.5	Effect of wavelength $\lambda z + \text{or } \phi i, i + 1$	121

5.4.6 Effect of mean velocity coming out from the slit <i>U_{Meanslit}</i>	123
5.4.7 Effect of streamwise location of slits on <i>\delta\tau_w</i>	128
5.4.8 Effect of streamwise length of slits	129
5.5 Summery	130
Chapter (6) Conclusion and Future Work	132
6.1 Conclusion Remarks	132
6.2 Suggestions for Future Work	134
Bibliography	136
Appendix	149

List of Figures

Figure (1.1) Change in CO ₂ emissions, 2016/2017 (estimated) (Eurostat, 2018).....	2
Figure (1.2) The paths from receptivity to transition (Saric et al., 2002).	7
Figure (1.3) Effect of the FST on the boundary layer over a flat plate (Ghasemi et al., 2013).....	10
Figure (2.1) Opposition control mechanism (Chung and Talha, 2011).	14
Figure (2.2) Spanwise travelling wave.....	18
Figure (2.3) Streamwise travelling wave.	20
Figure (2.4) Schematic of the test rig to generate the turbulent boundary layer (Bai et al., 2014).....	22
Figure (2.5) Distributions of $u(y,z)$ in (a-c) and $\omega x(y,z)$ in (b-d) near one wall of turbulent channel flow at $Re=1800$, without (a,b) and with (c,d) an imposed large-scale control flow (Schoppa and Hussain, 1998).....	23
Figure (2.6) Travelling wave-like wall deformation in the streamwise direction.....	26
Figure (2.7) Travelling wave-like wall deformation in the spanwise direction.	27
Figure (2.8) Schematic of drag reduction mechanism due to travelling wave-like wall deformation in the spanwise direction (Tomiyama and Fukagata, 2013).	27
Figure (2.9) Effect of the travelling wave on the near-wall QSVs. (a) without the wave; (b) with the wave (Tomiyama and Fukagata, 2013).....	28
Figure (3.1) Forced homogeneous isotropic turbulence: (a) iso-surface of Q ; (b) energy spectrum (Grinstein and Fureby 2005).	38
Figure (3.2) Fully developed channel flow: (a) instantaneous visualization in term of contours of vx , vortex lines and iso-surfaces of Q ; (b) vertical profiles of mean streamwise velocity from Grinstein (2005).	39
Figure (3.3) Grid schematic. P and N denote typical computational cell centres and f an interface; and A cell face area; d is the topological vector connecting neighbouring cells.....	42
Figure (3.4) Applied TVD regions for the first and second-order accuracy schemes.	48
Figure (3.5) TVD regions for the TVD schemes.	48
Figure (3.6) Square initial condition: numerical solutions for VanLeer flux limiter at $t = 40$ with 100 mesh-cells.....	50

Figure (3.7) Square initial condition: numerical solutions for superBee flux limiter at $t = 40$ with 100 mesh-cells.....	51
Figure (3.8) Square initial condition: numerical solutions for VanAlbada flux limiter at $t = 40$ with 100 mesh-cells.....	52
Figure (3.9) TVD regions for the first and second-order accurate TVD schemes together for the selected limiters.	52
Figure (3.10) Computational domain dimensions of the fully developed channel.	54
Figure (3.11) Grid-refinement study for MILES performance; (a) mean velocity profile, (b) streamwise fluctuation, (c) normal to the wall fluctuations, (d) spanwise fluctuations.	56
Figure (3.12) Spectrum of the total resolved turbulent energy of different used flux limiters at $Re\tau = 180$	57
Figure (3.13) Total shear stress behaviour through the fully developed channel.	58
Figure (3.14) (a) mean velocity profiles; (b) near-wall behaviour of the mean velocity.	59
Figure (3.15) Reynolds shear stress for fully developed channel normalized by the wall shear velocity: (a) in global coordinates (b) in-wall coordinates.	61
Figure (3.16) RMS velocity fluctuations in streamwise dir. normalized by the wall shear velocity: (a) in global coordinates; (b) in-wall coordinate.....	62
Figure (3.17) RMS velocity fluctuations in y-dir. normalized by the wall shear velocity: (a) in global co-ordinates; (b) in-wall coordinates.	63
Figure (3.18) RMS velocity fluctuations in z-dir. normalized by the wall shear velocity: (a) in global co-ordinates; (b) in-wall coordinate.....	64
Figure (3.19) Total shear stress, Reynolds stresses and wall shear stress for $Re\tau = 395$. Normalized by the wall shear velocity: (a) in-wall coordinates; (b) in the global coordinate.	67
Figure (3.20) Mean velocity profile of a fully developed channel flow of $Re\tau = 395$	67
Figure (3.21) RMS velocity fluctuations in streamwise dir. normalized by the wall shear velocity, (a) in-wall coordinates, (b) in the global coordinate ..	68
Figure (3.22) RMS velocity fluctuations in normal to the wall dir. normalized by the wall shear velocity, (a) in the wall coordinates, (b) in the global coordinate.	69
Figure (3.23) RMS velocity fluctuations in spanwise dir. normalized by the wall shear velocity, (a) in the wall coordinates, (b) in the global coordinate.	70

Figure (4.1) Geometry for the n^{th} mode.	77
Figure (4.2) The probability of a randomly selected direction of a wave in wave-space is the same for all dA on the shell of a sphere (Davidson 2007).	77
Figure (4.3) Model energy spectrum (Davidson 2007).	80
Figure (4.4) RMS pressure fluctuations along the channel, using the (uncorrected) generated B.C and the modified B.C with velocity scaled to ensure a constant bulk flow rate.	84
Figure (4.5) Mean velocity profiles at streamwise stations for the isotropic turbulence inlet boundary condition.	86
Figure (4.6) $u'v'$ Profiles at selected streamwise locations: (a) $x\delta=1$, (b) $x\delta=10$, (c) $x\delta=24$, (d) total behaviour between Davidson DNS and the generated B.C.	87
Figure (4.7) $u'v'$ profiles at selected streamwise locations for the modified inlet boundary conditions.	88
Figure (4.8) u' profiles at selected streamwise locations: (a) generated inlet boundary condition, (b) modified inlet boundary condition.	89
Figure (4.9) v' profiles at selected streamwise locations: (a) generated inlet boundary condition, (b) modified inlet boundary condition.	89
Figure (4.10) Streak identification shown for a typical flow field: streaks at $y+=20$ identified as regions of $u' < 0$ (blue-shading).	90
Figure (4.11) Fully developed channel flow: instantaneous visualization in term of contours of iso-surfaces of Q-criterion and coloured by the streamwise velocity fluctuations.	90
Figure (4.12) Sensitivity of the inlet boundary condition to different inlet time scales: (a) T_{in} , (b) T_{in4} , (c) T_{in12} , (d) all of them.	91
Figure (4.13) Sensitivity of the inlet boundary condition to different inlet length scales: (a) $0.5Lt$, (b) Lt , (c) $1.5Lt$, (d) all of them.	92
Figure (4.14) Controlling the required friction Reynolds number at the inlet plane.	94
Figure (5.1) Schematic of channel set-up for the generation of bypass transition (not to scale).	97
Figure (5.2) Turbulence intensity decay through the channel at $Tu = 7\%$	99
Figure (5.3) Skin friction coefficient relative to the previous DNS study (Ovchinnikov, 2006).	100
Figure (5.4) Tu effect on bypass transition onset.	102

Figure (5.5) Mesh independence study for $Tu = 3\%$	103
Figure (5.6) Sinusoidal wave travelling in the spanwise direction.	105
Figure (5.7) Sinusoidal wave in the normal to the wall axis.....	105
Figure (5.8) Inclination angle θ	105
Figure (5.9) Validation of skin friction coefficient behaviour with $Tu = 3\%$	108
Figure (5.10) Skin friction coefficient behaviour with applying the sinusoidal travelling wave and comparing with the symmetry case.....	109
Figure (5.11) Streamwise location for the maximum drag reduction and distance required for the drag recover its original values.....	109
Figure (5.12) Streamwise velocity fluctuations of the symmetry mesh and the complete channel mesh at different streamwise locations.....	110
Figure (5.13) Wave penetration inside the main flow and velocity contours out from slits: (a) case 2 α and (b) case 3.	111
Figure (5.14) Skin friction coefficient dependence on wave amplitude.	112
Figure (5.15) Streamwise location for the maximum drag reduction depending on wave amplitude.....	112
Figure (5.16) Skin friction coefficient dependence on inclination angles (a) $\theta = 3^\circ$, (b) $\theta = 10^\circ$, (c) $\theta = 45^\circ$, (d) $\theta = 135^\circ$, (e) $\theta = 160^\circ$	115
Figure (5.17) Skin friction coefficient dependence on the inclination angle.	115
Figure (5.18) Streamwise location for the maximum drag reduction depending on the angle of inclination.	116
Figure (5.19) Maximum drag reduction, $\delta\tau_w$ vs the inclination angle θ	116
Figure (5.20) Effect of inclination angle on the streamwise vortices, case 2 α , $\theta = 90^\circ$: (a) $\Delta x = -82$, (b) $\Delta x = 0$, (c) $\Delta x = 82$, (d) $\Delta x = 136$. ..	117
Figure (5.21) Effect of inclination angle on the streamwise vortices, case 5, $\theta = 10^\circ$: (a) $\Delta x = -82$, (b) $\Delta x = 0$, (c) $\Delta x = 82$, (d) $\Delta x = 136$. ..	118
Figure (5.22) Effect of inclination angle on the streamwise vortices, case 7, $\theta = 135^\circ$: (a) $\Delta x = -82$, (b) $\Delta x = 0$, (c) $\Delta x = 82$, (d) $\Delta x = 136$..	119
Figure (5.23) Skin friction coefficient dependence on wave frequency.	120
Figure (5.24) Streamwise location of maximum drag reduction achieved depending on different wave frequencies.....	121

Figure (5.25) Relation between the wave frequency and the maximum drag reduction	121
Figure (5.26) Skin friction coefficient dependence on $\lambda z +$ or $\varphi i, i + 1$: case 2 α : $\varphi = 12.41^\circ$, case 12: $\varphi = 37.24^\circ$, case 13: $\varphi = 49.65^\circ$, case 14: $\varphi = 62.06^\circ$	122
Figure (5.27) Streamwise location of maximum drag reduction achieved depending on different wavelengths.	123
Figure (5.28) Skin friction coefficient dependence on different $UMeanslit$	124
Figure (5.29) Streamwise location for the maximum drag reduction depending on $UMeanslit$	125
Figure (5.30) Relation between $\delta\tau_w$ and $UMeanslit$	125
Figure (5.31) Effect of mean velocity out from the slit on the streamwise vortices, case 15: (a) $\Delta x += -82$, (b) $\Delta x += 0$, (c) $\Delta x += 82$, (d) $\Delta x += 136$	126
Figure (5.32) Effect of mean velocity out from the slit on the streamwise vortices, case 17: (a) $\Delta x += -82$, (b) $\Delta x += 0$, (c) $\Delta x += 82$, (d) $\Delta x += 136$	127
Figure (5.33) Maximum drag reduction dependence on the streamwise location of slits.	128
Figure (5.34) Skin friction coefficient for longer slits.	129
Figure (5.35) Streamwise location for the maximum drag reduction depending on longer slits.....	129

List of Tables

Table (3.1) Mean flow properties obtained from MILES computations for mesh density investigation.....	54
Table (3.2) Mean flow properties obtained from MILES computations of the periodic channel flow at $Re\tau = 180$ and reference DNS of Kim et al. (1987).....	60
Table (3.3) Mean flow properties obtained from MILES computations of the periodic channel flow at $Re\tau = 395$ and the DNS reference of Abe et al. (2001).....	66
Table (4.1) Probability distributions of the random variables.	78
Table (4.2) Inlet length and time scales for the MILES simulations. The base flow used here with fixed constant RMS velocity fluctuations $u_{rms} = v_{rms} = w_{rms} = 1.5$ at the inlet of test cases for the MILES simulations.....	85
Table (4.3) Inlet and fully developed $Re\tau, ratio$	93
Table (5.1) Characteristics of the uncontrolled channels.	96
Table (5.2) Meshes used in the grid refinement study	102
Table (5.3) Set of wave parameters affecting the drag reduction $\delta\tau_w$ for $Tu = 3\%$	106
Table (5.4) Maximum drag reduction achieved by changing the inclination angle θ . (The values presented in this table are for indication only. For more information, see the Appendix)	114
Table (5.5) Applied frequencies and the resulted maximum drag reduction $\delta\tau_w$. (The values presented in this table are for indication only. For more information, see the Appendix)	120
Table (5.6) Maximum drag reduction according to $\lambda z +$ or $\phi i, i + 1$. (The values presented in this table are for indication only. For more information, see the Appendix)	122

Acknowledgement

I would like to express my sincere gratitude to my supervisors Professor Jennifer X. Wen and Dr Vendra C. Madhav Rao for their patients, invaluable guidance, encouragement and strong support in making this research possible. They have impressed me with their outstanding professional conduct, their strong conviction for science, and their belief that this research is only a step of a long-life of learning and experience. I appreciate their consistent support from the first day. Also, I would like to express very special thanks to my office mates for their scientific discussions.

I acknowledge my sincere indebtedness and gratitude to my mother, Nadia, my wife, Nourhan Alaa, and especially my children for their love, Adam and Lilly, dream and sacrifice throughout my life and finally special thanks to professor Ibrahim Saleh my great teacher who gave me the greatest support to reach this moment. I cannot find the appropriate words that could properly describe my appreciation for their devotion, support and faith in my ability to attain my goals. Special thanks should be given to my committee members. I would like to acknowledge their comments and suggestions, which were crucial for the successful completion of this study.

Mohamed Elghorab
University of Warwick

2020

Declaration

This thesis is submitted to the University of Warwick in support of my application for the degree of Doctor of Philosophy. I declare that the work in this thesis has been composed by myself and no portion of this work has been submitted in support of an application for another degree at any other university or institute. The work has been my own except where indicated

Abstract

The drag is present due to flow around bodies such as vehicles, aircraft, bullet trains or ships etc. It plays a significant role in vehicle performance, rate of fuel consumption and stability. This drag depends mainly on flow, fluid and surface properties. Different methods are used for drag reduction like controlling surface roughness and injecting long-chain polymers etc. In the current research, a method based on the generation of a spanwise mean velocity gradient in a flat plate boundary layer by applying a sinusoidal travelling wave in the spanwise direction before the transition to turbulence occurrence is used for the drag reduction purpose. A solver is developed using the open-source CFD software OpenFOAM libraries. It consists of routines for generating synthetic isotropic homogeneous turbulence at the inlet plane of the channel flow and solving the Navier Stokes equations using the Monotonically Integrated Large Eddy Simulation method (MILES).

The implemented inlet boundary condition showed improvements in the predictions of turbulence structures within a streamwise distance of approximately 5 times the half channel height (δ) from the inlet plane, a shorter distance than the other similar previous boundary conditions can predict. These improvements resulted in a considerable reduction in overall channel length required for numerical simulations and hence reduction in the associated computation costs. In addition, a prediction method for getting the required friction Reynolds number for setting up any simulation case is been developed and verified. The MILES solver and the inlet boundary condition are used together to generate the bypass transition through the channel flow.

A travelling sinusoidal wave in the spanwise direction is applied by the effect of blowing and suction from the bottom wall of the channel before the bypass transition occurrence. This travelling wave leads to a drop in the value of the skin friction coefficient which means a drop in the drag. This may be due to the increase of the mixing effect of the eddies and the induced streamwise travelling wave. The bypass transition onset also appears to be delayed when an inclined sinusoidal wave is applied in the streamwise direction. However, grid independence was not thoroughly tested in this study.

List of Abbreviations

CFD	Computational Fluid Dynamics
CFL	Courant-Friedrichs-Lewy (CFL) condition is the maximum allowable Courant number that a time-integrator can use
DFSEM	Divergence free synthetic eddy method
DNS	Direct numerical simulation
DTW	Downstream travelling waves
FCT	Flux-Corrected Transport
FIK	Identity namely after (Fukagata, Iwamoto, Kasagi)
FST	Free stream turbulence
ILES	Implicit Large Eddy Simulation
LES	Large Eddy Simulation
MILES	Monotonically Integrated Large Eddy Simulation
N.S.E	Navier Stokes Equations
NFV	Non-oscillatory finite volume algorithms
POD	Proper Orthogonal Decomposition
PPM	Piecewise Parabolic Method
QSVs	Quasi-streamwise vortices
RANS	Reynolds-Averaged Navier-Stokes simulation
RMS	Root mean square
RSS	Reynolds shear stress
RTPT	Required time per one trip
SEM	Synthetic eddy method
SGS	Sub-grid scale
TBL	Turbulent boundary layer
TV	Total Variation
TVD	Total Variation Diminishing
UB	Uniform blowing
US	uniform suction
UTW	Upstream travelling waves
WSS	Wall shear stress

Nomenclature

A	Amplitude
c	Wave speed
C_f	Skin friction coefficient
C_μ	Constant, $C_\mu = 0.09$
d	Mesh size
D	Mean strain rate
D_h	Hydraulic diameter
f	Wave frequency
f^+	Normalized wave frequency
f_L	Factor to enable controlling the length scale
$f_{rescale}$	Velocity rescaling coefficient
f_{wall}	Cut-off function factor
f_T	A factor used to control the value of the time scale
F_y	Wall-normal Lorentz force
F_z	Spanwise Lorentz force
I	Lorentz force amplitude
\bar{k}	Total turbulent kinetic energy
k_x	Streamwise wavenumber
κ_{max}	Maximum wavenumber
\mathcal{K}_1	Smallest wavenumber
\mathcal{K}_e	The most energetic length scale
\mathcal{K}_j^n	Fourier mode wave number
\mathcal{L}_t	Turbulence integral length scale
M	Mach number
N_w	Number of waves
Q	Second invariant of the velocity gradient
Re	Reynolds number
Re_B	Reynolds number based on the bulk velocity of the channel
Re_b	Bulk Reynolds number

Re_{cr}	Critical Reynolds number
Re_m	Reynolds number based on the mean velocity of the channel
Re_x	Reynolds number based on the streamwise distance
Re_θ	Reynolds number depends on inflow boundary layer thickness
$Re_{\tau,in}$	Friction Reynolds number at the inlet plane of the channel
Re_τ	Friction Reynolds number based on the friction velocity
S	Viscous-stress tensor
\mathcal{T}	Time scale
\mathcal{T}_{in}	Inlet time scale
T	Period of oscillation
Tu	Turbulence intensity
u'	Streamwise velocity fluctuations
$u_{laminar}$	The bulk mean velocity of the corresponding laminar flow
u_{rms}	Root mean square of the streamwise fluctuation
u_{slit}	Velocity gets out from the slits
$u_{\tau,inlet}$	Friction velocity as an input parameter for the inlet boundary condition
$u_{\tau,NoControl}$	Friction velocity of no control case
$u_{\tau,fullyDeveloped}$	Friction velocity for the fully developed turbulent channel
u_τ	Friction velocity
\hat{u}^n	Fourier mode amplitude
\bar{u}'	Streamwise RMS fluctuation
$\overline{u^+}$	Mean velocity profile
\bar{U}	Average velocity
U_b	Bulk velocity
U_c	Velocity at the channel centre line
U_{con}	Velocity component contains counter-rotating streamwise vortices in the streamwise direction
U_m	Mean velocity
U_∞	Free stream velocity
$UMean_{slit}$	The average velocity of the slits

v	Velocity component in normal to the wall direction
v'	Normal to the wall velocity fluctuations
v_w	Normal to the wall velocity on the channel wall
v_f	Flux function
$\overline{v'}$	Mean normal to the wall velocity fluctuations
V_{con}	Velocity component contains counter-rotating streamwise vortices in normal to the wall direction
V_{crt}	Critical velocity
w	Velocity component in the spanwise direction
w'	Spanwise velocity fluctuations
W_{con}	Velocity component contains counter-rotating streamwise vortices in the spanwise direction
x_0	Streamwise distance to get the required boundary layer thickness δ_{99}^0 at the inlet plane of the channel
X	Streamwise distance
y_d	Detection height of sensors in active control techniques
y_d^+	Detection height in wall units of sensors in active control techniques
Z_{slit}	Slit width in the spanwise direction
ψ^n	Fourier mode phase
δ	Half channel height
δ_{99}^0	Thickness of the boundary layer at a velocity equivalent to 99% of the free stream velocity at the inlet plane
$\delta_{\tau w}$	Drag reduction rate
ε	Flip-flop function
ε_d	Turbulent dissipation rate
ζ_i^n	Fourier mode direction
λ	Wavelength
λ^+	Wavelength in wall units
λ_z^+	Normalized wavelength
σ_i^n	Slop limiter
σ_n	Geometry length
Δ	Grid spacing

Δx^+	Streamwise distance in wall units
Δy^+	Wall-normal distance in wall units
Δz^+	Spanwise distance in wall units
Δt	Local time step
τ	Leading truncation error
$\overline{\tau_w}$	Average wall shear stress
ω	Specific dissipation
ω_y	Wall-normal vorticity
Ω	Vorticity
Γ	Flux limiter
β	Characteristic streak spacing
θ	Wave inclination angle
ρ	Density
ν	Kinematic viscosity
φ	Phase shift between slits

Chapter (1)

Introduction

1.1 Motivation

In the past, present and the future, people needs for travelling are increasing because of their desires to transport all life facilities and goods which come from across the globe and even travelling by themselves using different transportation means. These needs led to developing the industry of the transportations either in local or universal transportation means throughout the recent decades, which in turn led to achieving a very high rate of pollution all around the world especially in the industrial countries. For example, according to the total greenhouse emission breakdown in European Union, the percentage of gas emission due to the transportation facilities including the aviation facilities was increased from 14.9% in 1990 to around 22.2% in 2013 (commission, 2013). Recently, the Eurostat announced that the annual statistics of CO_2 emissions were increased in 2017 with 1.8% relative to the previous year 2016 as shown in Figure (1.1) (Eurostat, 2018).

From this study, it was found that the aviation transportation facilities achieved the highest growth between the other transportation facilities as it increased by 87% in the period between 1990 and 2006 (Commission). Therefore, a red alert has been given due to these statistics to start worrying about the environmental impact of this industry, transportation facilities and particularly the aviation industry.

At this point, a serious question enforces itself in this situation: *should we reduce our desires for the use of these facilities or search for more studies on how to reduce the emissions from them?*

There are many approaches that can be studied to solve or reduce the effect of this problem, one famous approach is to decrease the fuel consumption of the transportation facilities and consequently reducing their emission to the environment. There is a strong relationship between fuel consumption and the drag force which is produced by the flow around the transportation vehicles, such as air around aircraft,

bullet trains or around ships in the water. The total drag around vehicles is expressed by two parts, the first part comes from the pressure distribution around the body of the vehicles which participates with the highest percentage in the drag, while the second is due to the surrounding flow which is dominated by the skin friction drag. Many studies concerning the drag have been done before. For example, the skin friction drag contribution for a subsonic aircraft in the total amount of the drag is about 50% in cruise conditions (Joslin, 1998). Previously, Wood (2004) reported that about 16% of the energy consumption in the United States was due to the aerodynamic drag resulting from transportation systems. According to his estimation, if the available drag reduction techniques were applied to all those transportation means, at least 20 billion US dollars could be saved within the United States.

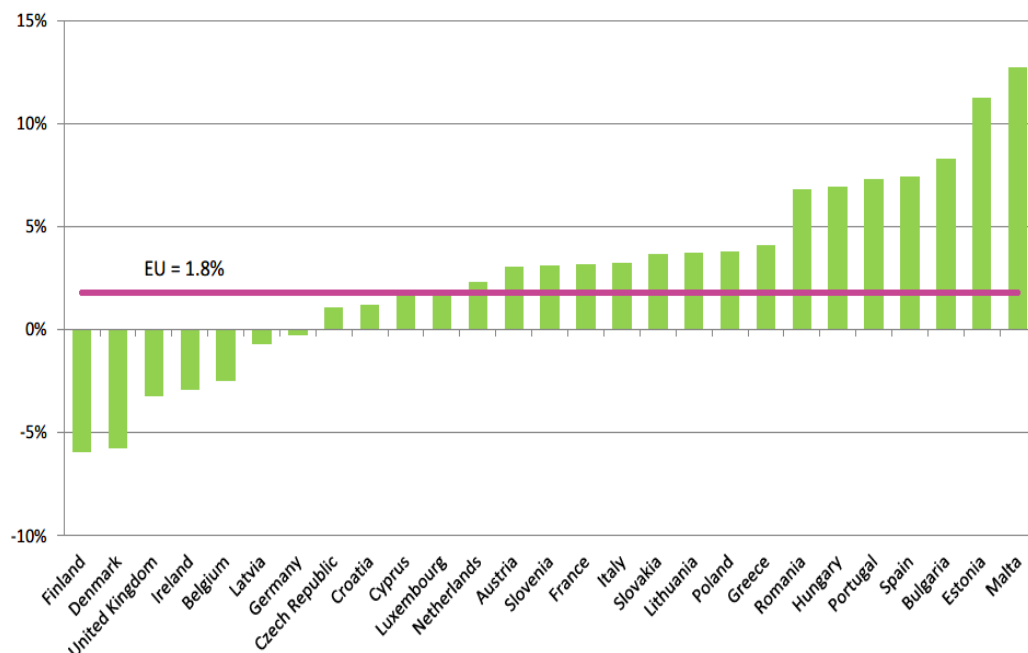


Figure (1.1) Change in CO₂ emissions, 2016/2017 (estimated) (Eurostat, 2018).

1.2 Drag reduction control

The skin-friction drag is generated into the boundary layer around the body surface, where the velocity profile of the fluid surrounding the body is going from free flow velocity to zero on the surface. The skin-friction drag differs according to the nature of the fluid around the body. If the flow is turbulent or in another description chaotic and irregular; then the drag value will be higher than that if it is laminar or smooth and regular. Scientifically speaking, the flow boundary layer in any application

is initially laminar and due to transition to turbulence occurrence near the surface, it turns into a turbulent boundary layer. In some applications which need less skin friction drag, the laminar boundary layer is preferred, while in other applications, the turbulent boundary layer is preferred due to the high mixing rate in the fluid

Generally, the turbulent flow boundary layer is being characterized by swirling eddies that increase the mixing and transport, in contrast to laminar flow which is stratified and smooth. In many cases, this feature of high mixing is an advantage for the flow as it leads to increasing the heat transfer, which could be useful in many situations such as the chemical reactions among multiple reagents. On the contrary, this feature of high mixing is not desired in many other cases like aerodynamics or hydrodynamics fields such as the design of plane wings, bullet trains, high-speed cars or military aircraft and submarines. Therefore, it can be concluded that each region of the laminar or the turbulent flow has its advantages, so it's very useful to be able to control the onset and the features of each region depending on which is more desirable relative to the required application. This field of research falls under the category of flow control, and it is based on the understanding of the primary mechanisms and physics leading to the transition from the laminar boundary layer to the turbulent boundary layer. From the economic side, controlling the transition from laminar to turbulent flow is very important. Many studies have been done to estimate the percentage of fuel-saving in plane wings if the laminar flow was kept without turning into turbulent or even reducing the required skin friction drag. For example, Reed et al. (1996) achieved 25% reduction in the fuel consumption due to the control of the transition boundary layer onset.

In the last few decades, many investigations have been applied on the friction drag reduction in even the laminar or turbulent boundary layer. Bewley et al. (2001) and Gad-el-Hak (2001) divided the drag reduction techniques into two groups: the first group is the passive control such as riblets (Walsh, 1983; Dean and Bhushan, 2010) and superhydrophobic surfaces (Rothstein, 2010), while the second is the active control, which needs an additional energy source from outside the system. Most of these studies have been applied on the application of turbulent boundary layers to get a friction drag reduction or on the transitional boundary layer for the laminar to turbulent transition delay. As the main part of losses through the fluid flow occurs in the transition region. These losses are divided into two parts: one is due to the

interaction between the molecules, friction losses, and the main part is due to change in the molecules status to adjust themselves from laminar motion to random motions. So, controlling this area is very important even to reduce the friction or rearrange the streaks motion to reduce the losses in this area.

This research focuses on the friction drag reduction approach in the transitional boundary layer over a flat plate and how to control the turbulence structures in that area to delay the bypass transition to turbulence. This approach is investigated numerically using the opensource software OpenFOAM via implementing the following steps:

1. Developing an opensource LES code which is able to simulate the turbulent structures accurately through a channel flow. This code is divided into two parts, the first is the monotonically integrated large eddy simulation (MILES) solver and the second is the isotropic homogeneous turbulence inlet boundary condition.
2. Generating a transitional boundary layer
3. Applying the active control technique of the drag over a flat plate by using a sinusoidal travelling wave in the spanwise direction
4. Parametric study for the sinusoidal travelling wave effect on the bypass transition onset and the rate of drag reduction over a flat plate.

As a result, the characteristics of this LES code can be identified for other applications and also specifying the key parameters to control the drag reduction rate and the transition to turbulence onset. Therefore, an introduction about the transition generation and its scenarios is produced in the next sections to investigate the suitable approach to generate the transition numerically through the current study.

1.3 Transition to turbulence

The understanding of why, where and when the transition from laminar to turbulent happens is related to the concept of the boundary layer stability. In which, the flow is defined as laminar or stable for small disturbances if it comes back to its original state after applying any small perturbations or disturbances to it. The boundary layer of laminar flow is defined as unstable when the disturbances generated by the

perturbations grow to higher amplitude and do not disappear which in turn convert the flow from laminar to turbulent flow.

Under which circumstances the laminar flow becomes turbulent or unstable?

The answer to this question is a field of study for many researchers from decades until now. A common feature is the dependence of the boundary layer properties on the Reynolds number (Re), which produces the importance of the relation between the convective and inertial flow mechanisms to the dissipation ones. From the previous experiments, it was shown that the flow becomes turbulent at high values of the Reynolds number. The first experimental work which demonstrated this dependence was by Reynolds in his famous experimental pipe flow (Reynolds, 1883). In his experiments, he noticed that the flow turns from laminar to turbulent or in other words the transition occurs at a critical value of a dimensionless number which is named critical Reynolds number, Re_{cr} , after the name of Reynolds, it's very important to note that the critical Reynolds number is the value at which the flow starts to show the developing of the instabilities, does not mean to be totally developed to turbulent flow as maybe some damping effects could be developed to reduce the instabilities. However, if the flow totally turned into fully turbulent, in this condition the Reynolds number will be called the transitional Reynolds number.

At this point, an answer for the following question is needed: *how are the flow instabilities in the boundary layer being excited?* In general, an exciting source is needed to excite the instability process, this source is accompanied by an exciting mechanism which will apply the external instabilities into the system. In his experiments, Reynolds was able to put a relationship of how these external disturbances effect on the spatial location for the transition occurrence. His experiment consisted of a tank filled with water connected to a pipe and he put a needle at the beginning of the pipe to supply a dye filament as a sort of visualization to the flow pattern. He found that the connection between the tank and the pipe has a great effect on delaying the transition, whereas if the pipefitting is too sharp or the internal surface of the pipe is not smooth, this will lead to anticipating the transition. These experiments showed how the transition is related to the external disturbances by which the excitation to the instabilities is produced (Reshotko, 1976).

Generally, the transition cannot occur without an external exciting disturbance and a mechanism to be produced into the flow. Nowadays, receptivity is the scientific word to define the ability to produce external perturbations into the flow boundary layer. To be noticed, receptivity with its definition does not mean the existed instabilities or the transition occurrence: if the base flow is laminar and the entered disturbances are weak or there are some factors affect to damp the instabilities so the flow will continue as a laminar flow. On the other hand, if the flow turns to unstable so it will complete being a turbulent flow. A great feature of the receptivity mechanism is making a strong relationship between the stability properties and the external disturbances. This relationship allows estimating the transition as a function of the environmental conditions. The stability of the flow can be described as a temporal in which the perturbations are applied at a certain initial time as a function of time or space in which the perturbations are applied at a specific location of the flow in all time steps.

So, there are many friction drag reduction techniques that aim to extend the laminar flow region, which are called laminar flow control techniques, or others control techniques which are trying to turn the turbulent flow into laminar again, this process is called laminarization, these techniques work on reducing the skin-friction drag on the surface. These control techniques have many types, one of them to re-shape the surface of the body to keep the flow laminar as far downstream as possible. Another one is to work on delaying the transition to turbulence or reducing the friction drag on the surface via modifying the receptivity mechanisms of the base flow such as blowing and suction from the surface, wall deformation and transverse travelling waves, these techniques are called sensor-less techniques. Other techniques are using sensors to feel the flow near the wall and applying the control to change the turbulence structures near the wall and this type of control is called ‘feedback control’.

1.4 Transition scenarios

As mentioned in the previous section, the instabilities inside the flow need external disturbances to be excited and consequently amplified to produce the transition to turbulence. However, there is a requirement for a physical mechanism that includes the excitation of the instabilities and lead to the transition, which is defined before as the receptivity and shown in Figure (1.2). This mechanism produces

the way of how the external disturbances enter the boundary layer and excite the internal instabilities, in other words, it describes how much sensitivity the boundary layer has to be to the surrounding environmental perturbations.

Initially, inside the boundary layer, these disturbances can't be measured in the initial stage, as they are very small until it reached to the second stage of linear amplification, Figure (1.2), path A. At this point, the disturbances grow linearly according to the linear stability process till the amplitude of the disturbances exceeds a certain threshold, at which nonlinear effects become important and lead to secondary instabilities. These secondary instabilities lead to breakdown to turbulence (Herbert, 1988; Reed et al., 1996; Saric et al., 2002). During the transition process, many instabilities can be excited such as the Görtler vortices, instabilities in jets and wakes, which related to the inviscid instabilities, Tollmien–Schlichting waves that effect on the viscous flow layer or algebraic instabilities which are responsible for the occurrence of the bypass transition. In all the previous kinds of instabilities, each case has its own feature like the external excitation and receptivity. Hence, the transition occurrence can be classified according to the kind of the disturbance's growth. Therefore, in the next two sub-sections, the most two famous kinds of transition will be discussed.

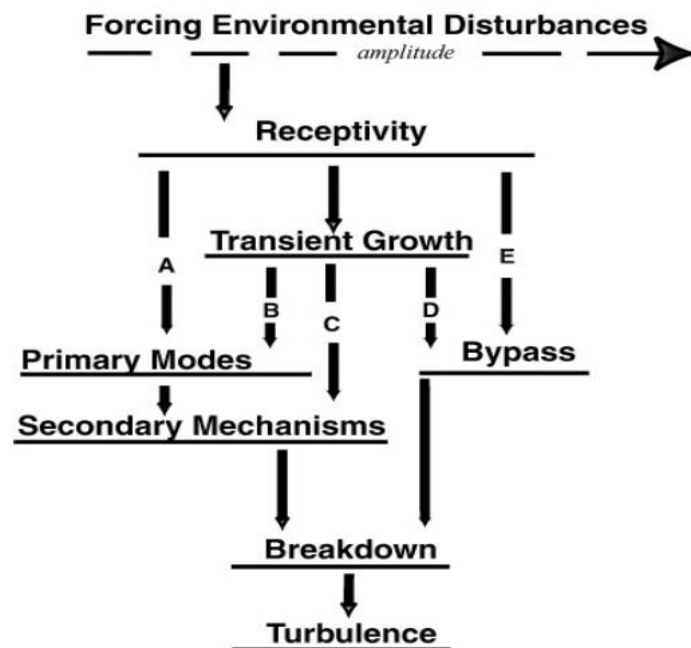


Figure (1.2) The paths from receptivity to transition (Saric et al., 2002).

1.4.1 Transition due to Tollmien–Schlichting waves

The external disturbances from the free stream like acoustic waves or vorticity penetrate the boundary layer as a steady and/or unsteady fluctuation. These disturbances and their amplitude, frequency and phase are the main sources for the laminar flow breakdown and transition to turbulent flow. As far as the two-dimensional boundary layer is concerned, the acoustic disturbances will be taken as an example, their existence in the free-stream turbulence (FST) may become resonant with the Tollmien–Schlichting waves, and produce transition, and this happens only when it is accompanied with another mechanism. This was described many times such as the studies by Murdock (1980), Goldstein (1983) and Fransson et al. (2005). In fact, there is a main feature of the acoustic wave that it does not have the typical wavelength of the Tollmien–Schlichting waves, therefore, wavelength conversion is needed to have the amplitude wave (Reshotko, 1976). This can be produced via the fast change in the boundary layer characteristics either from; the growth of the boundary layer close to the leading edge or the suction and/or blowing from the wall or wall roughness.

The essential mechanism that permits this “wave adaptation” is in a relationship with the nonlinear interaction between those disturbances generated by the wall roughness and that one generated by the acoustic wave. This mixing between the two disturbances produces a forcing term in the equation for the resonant wave from which the Tollmien–Schlichting waves can be excited. The generated wave from the previous can be excited or not based on the growth or decay specified by the linear theory. Many experiments have proved a good agreement with the linear theory when the generated Tollmien–Schlichting wave has a small amplitude relative to the free stream velocity of the flow, in order of a few tenths. On the other hand, if the unstable wave amplitude has a value in the order of 1% or more from the free stream velocity, these two-dimensional Tollmien–Schlichting waves turn to three dimensional and this is because of the increasing of the amplitude of the instability of the Tollmien–Schlichting waves, (Klebanoff et al., 1962), which can be called as secondary instabilities.

1.4.2 Transition due to non-modal disturbance growth (Bypass transition)

Laminar boundary layer can go faster to transition and not follow the normal traditional previous scenario based on the growing of the Tollmien–Schlichting waves. This mechanism of transition denoted as bypass transition. This scenario of transition presents an alternative amplification phenomenon and related to transient growth mechanisms and algebraic instabilities.

One of the most famous sources of the bypass transition is the free-stream turbulence (FST). The importance of this kind appears significantly and has a great interest in the engineering and practical fields, especially the studies which depend on the prediction of the transition and its properties such as flow over turbine blades or on aeroplane wings, and special concerns about it in the channel flow tests and their applications. Free stream turbulence (FST) needs to be reduced to specific levels in order to reproduce the real conditions of a flat plate, the plane wings or other applications, which in turn will produce bypass transition at a specific location on the body surface. Numerical and experimental studies have been carried out by many researchers to study the effect of the FST on the transition such as Brandt et al. (2004) and Rao et al. (2013) and especially (Alfredsson and Matsubara, 2000) who studied the effects of the FST on the boundary layer over a flat plate. The study of Alfredsson and Matsubara (2000) showed an initial growth for the perturbations proportional to the square root of the streamwise distance from the leading edge, in accordance to the theoretical study of Luchini (2000). Moreover, this study approved the agreement of the streamwise fluctuation growth, u_{rms} , with those obtained from this theoretical study. From the same study, by using flow visualization and hot-wire measurements, it was shown that the boundary layer, subjected to a specific range of free stream turbulence (FST), is able to produce regions with high and low streamwise velocity which denoted as high and low speed streamwise streaks, shown in Figure (1.3). The breakdown follows the growth of this streaky structure leads to the turbulence occurrence.

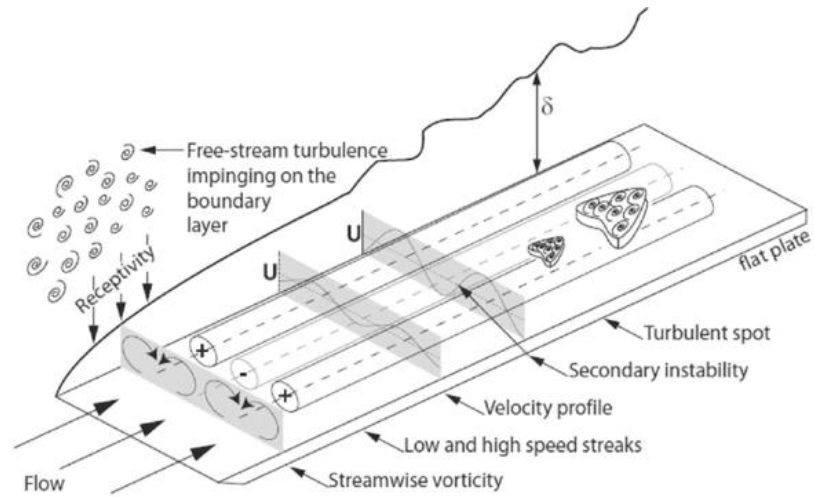


Figure (1.3) Effect of the FST on the boundary layer over a flat plate (Ghasemi et al., 2013).

But before that, a literature review about the types and previous studies of the control techniques for the friction drag reduction will be introduced in Chapter (2).

Chapter (2)

Literature Review on Turbulence and Bypass Transition Control

2.1 Introduction

Drag reduction through a transitional boundary layer and suppressing the turbulence structures in the turbulent boundary layer, perhaps with the aim of inducing relaminarization, or controlling the vortices and disturbances produced by a specific level of fluctuations are considered as a problem of great practical importance (Ioannou and Farrell, 1999). So, to discover the ways of delaying the transition or reducing the skin friction drag, past experiments and numerical studies have been done and have indicated a close association between quasi-streamwise vortices and large wall shear stresses which are considered as the main features of turbulence. The dynamics of streamwise vortices in the region near to the wall can be considered as the main source of the generation of mean Reynolds stresses, which lead to viscous drag increasing, (Bernard et al., 1993). These streamwise vortices are linked directly to the location of high skin friction regions as they are generally positioned directly above and displaced laterally from those regions (Kravchenko et al., 1993).

The well-known events, i.e. sweeps, ejections, bursts, and streak-like structures are all connected to the streamwise vortices in the flow near to the wall (Kim, 1983), as all of these events are motivated by the streamwise vortices. The ejection process consists of moving the low-speed fluid which is lifted up away from the wall to the upper side of the vortices and results in producing the low-speed streaks. This process of lifting up the slow-moving fluids produces inflexion in the mean velocity profile near the wall. When increased, this inflexion in the mean velocity profile causes a secondary instability and in turn grows in its amplitude to produce a burst of Reynolds stresses, this burst transfers the energy from large to small scales, leading to turbulent flow. The ejection mechanism is the main process responsible for transferring the energy, momentum and vorticity between the inner and the outer layers (Kline et al.,

1967). On the other hand, the high-speed streaks are produced by the sweep mechanism in the downdraught side of the vortices. These high-speed streaks are responsible for wall friction increasing (Kravchenko et al., 1993; Orlandi and Jiménez, 1994). Therefore, sweep acts particularly the main rule in the topic of drag reduction. Both sweep and ejection account for nearly 80% of the turbulent energy production (Lu and Willmarth, 1973).

Controlling the near to the wall streamwise vortices is the main key for the drag reduction techniques. Wallace et al. (1972) proved that ejections and sweeps are closely connected in the bursting process with about 15 wall units from the wall. Therefore, modifying the near to the wall region will effect on sweeps and ejections structure and certainly will produce changes in the drag skin friction values near the wall.

2.2 Types of turbulence control

Two different kinds of control have been investigated for a long time, active and passive control techniques. Various passive and active flow control techniques have been devised, in order to reduce the drag or delaying the transition to turbulence, also to control other flow properties such as heat transfer (Kim, 2003; Kasagi et al., 2009). Since the first direct numerical simulation (DNS) of turbulent channel flow was performed by Kim et al. (1987), control of skin friction drag in turbulent flows near to the wall has been started to be examined widely by using the numerical simulations. Spalart (1988) has been the pioneer in studying the spatially developing turbulent boundary layer numerically in the flow near to the wall.

Most of these control techniques have been studied both experimentally and numerically, i.e. riblets or compliant walls for the passive control are able to produce about 10% drag reduction in the flow (Walsh, 1983; Choi et al., 1993). Riblets have been extensively studied both numerically, (Fukagata et al., 2008; Peet and Sagaut, 2009) and experimentally, e.g. Bechert et al. (1997). From these studies, it has been confirmed that the drag reduction increases with increasing the riblet spacing when the spacing is in small scale while they are inversely proportional when the spacing reaches to a larger range than the typical diameter of the quasi-streamwise vortices (QSVs). The linear drag reduction of the riblets with small spacings (i.e. linear regime)

was theoretically examined by Luchini et al. (1991) who produced a solution to the Stokes flow on riblets and clarified with a demonstration that the effect of resistance for the cross-flow is higher than that for parallel flow due to the difference in the virtual regions. While for larger spacings, the linear regime breaks down and leads to an increase in the skin-friction drag value. The optimum performance of riblets is specified by this breakdown point, as illustrated by García-Mayoral and Jiménez (2011).

Although passive control has achieved good results for the drag reduction, it is expected from the active control techniques to produce better results. A famous typical example of the active control, which has been investigated numerically and experimentally, is the opposition control. It depends on sensing the flow and its structures near the wall within a small distance upstream to the position of applying the control effect (Choi et al., 1994). Aiming for larger drag reduction, optimal control can be performed by using blowing and suction (Kim and Bewley, 2007). Recently, control with constant predetermined input, i.e. without flow sensing, has been focused on the travelling wave-like blowing and suction from the wall (Min et al., 2006), wall oscillations (Kim and Bewley, 2007) (including intermittently oscillating walls (Mishra and Skote, 2015)), and wall deformations (Nakanishi et al., 2012; Zhang et al., 2016). Also, there are many other types of active control such as wall heating for delaying the transition, modifying fluid viscosity by injection of polymers or changing fluid temperature and using compliant walls (Karniadakis and Choi, 2003; Kim, 2003). From the point of view of the efficient energy utilization in industrial processes, the resulted drag reduction must accomplish with a suitable increase in the total system efficiency, otherwise, the active control will be useless as the energy saved from the control will be used in applying the control mechanism.

One of the most important obstacles in the numerical simulation for turbulence is that most of the investigations have been done at small Reynolds number due to the limited computation resources in their time and this differs from the actual applications which acting with high Reynolds numbers (Re). Therefore, developments in computational power have enabled numerical simulations to work at moderately high Reynolds numbers via RANS and LES methods (Schlatter et al., 2009; Schlatter and Örlü, 2010). Especially, the well-resolved large eddy simulation (LES) which have produced in the last decade as a real alternative to the direct numerical simulation

(DNS) in order to reach higher Reynolds numbers in the simulation with high accuracy and quality (Eitel-Amor et al., 2014).

In the next subsections, some of the well-known types of active control will be reviewed extensively especially the opposition control and the travelling waves.

2.2.1 Opposition control

Opposition control is known as a sensor dependence way of control, in which the sensors are located above the wall with a specific distance, y_d , in the normal to the wall direction and give feedback to the control system which in turn will apply the control with an opposite sign for the velocity measured by the sensors $v(x, 0, z; t) = -v(x, y_d, z; t)$, Figure (2.1), where x , y , and z express the coordinates in the streamwise, wall-normal, and spanwise, while t is the time. This type of control was examined by Choi et al. (1994) in a fully developed channel flow and recently was extended to work with the spatially developing turbulent boundary layer by means of large eddy simulations (LES) and (DNS), respectively, in Pamiès et al. (2007) and Xia et al. (2015). Interestingly, the opposition control system with blowing only produces higher drag reduction than that technique with both blowing and suction (Pamiès et al., 2007).

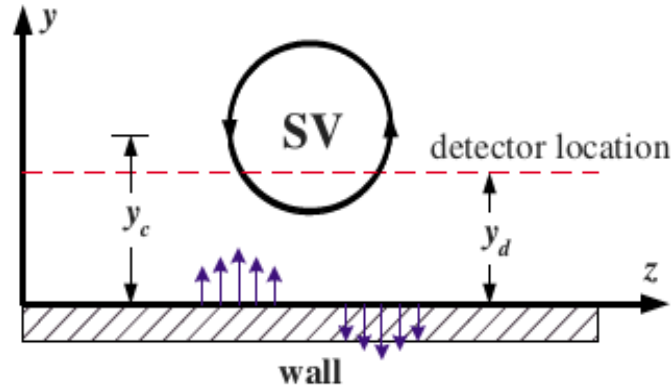


Figure (2.1) Opposition control mechanism (Chung and Talha, 2011).

Choi et al. (1994) applied a comparison between the different types of turbulence active control using sensors. They used the direct numerical simulations (DNS) at two different friction Reynolds numbers $Re_\tau = 110 - 180$ to explore the concepts of the active control leading to skin friction drag reductions. In their investigations, they used three different techniques to apply the control on the flow near the wall such as;

v-control in which the control is applied in the normal to the wall direction, w-control in which the control is applied in spanwise direction and the combined control which is a combination between both previous techniques. As a result of their studies, it was found that v-control achieved about 25% drag reduction while w-control and the combined control achieved 30% at the detection plane of $y_d^+ = 10$. In addition, they have briefed the difference between the v-control and w-control in concepts as the former alters the interaction between the primary vortex pair and the secondary vorticity by presenting the lifting of the secondary vorticity in the ejection process. While the latter creates stronger secondary vorticity at the wall and eventually resulted in primary vortex pair lifting farther away from the wall.

Direct numerical simulations (DNSs) of Hammond et al. (1998) for a turbulent channel flow at $Re_\tau = 180$ investigated the effect of the detection plane location on the drag reduction rate. The maximum drag reduction obtained during their study was 25% accompanying with evidently attenuated streamwise vortices at detection plane of $y_d^+ = 15$. Also, they concluded the formation of a virtual wall between the actual wall and the detection plane which could disturb and may prevent the vertical transport of the momentum. While Chung and Talha (2011) investigated the effect of the detection plane as well as the control amplitude via v-control at $Re_\tau = 180$. An amplitude parameter (A) to describe the strength of wall blowing and suction was produced, $v(x, 0, z; t) = -Av(x, y_d, z; t)$. This amplitude is equivalent to one in the other studies. Maximum drag reduction was obtained at $y_d^+ = 15$ as well. Also, they noticed that the drag was reduced again in the region of $20 < y_d^+ < 30$ if the amplitude $A < 1$. Iwamoto et al. (2002) conducted DNSs of turbulent channel flows at $Re_\tau = 110$ – 650 . They reported that the effectiveness of the opposition control at $y_d^+ = 10$ decreased with the increasing Reynolds numbers.

Chang et al. (2002) performed large eddy simulations (LES) of turbulent channel flows at $Re_\tau = 80$ – 720 . In these experiments, the flow was laminarized by the control at $Re_\tau = 80$, while, the flow remained turbulent at higher Reynolds number. They concluded that the effect of the control decreases with the increase of the friction Reynolds number, Re_τ , as they got a maximum drag reduction rate based on optimal detection plane of 26% at $Re_\tau = 100$ and dropped to 19% at $Re_\tau = 720$. Although it was mentioned that the effectiveness of this control strategy deteriorates with

increasing the friction Reynolds Number, it was found that most of the previous work was performed at friction Reynolds numbers lower than $Re_\tau = 200$ (Touber and Leschziner, 2012). Those authors observed that this deterioration was proposed to be related to the outer layer large-scale structures.

2.2.2 Travelling wave

2.2.2.1 Transverse travelling wave due to Lorentz force

In physics, the Lorentz force is defined as the combination between magnetic and electrical forces to generate electromagnetic field affecting on a moving particle with a specific charge. This force has been used many times in the study of the skin friction drag reduction especially in a fully developed channel flow in the form of embedding electrodes and permanent magnets in the flat surface over which the flow passes. Its effect has been used numerically as well.

Body forces are always considered as a famous method in the skin friction drag reduction application through a turbulent channel flow (Karniadakis and Choi, 2003). A fully developed channel flow was performed by Berger et al. (2000) to study the effect of the skin friction drag reduction. In which, they applied an open-loop controlled oscillating spanwise Lorentz force to a channel flow with a value such as that value in equation (2.1), i.e.,

$$F_z = I \exp\left(-\frac{y}{\Delta}\right) \sin\left(\frac{2\pi t}{T}\right) \quad (2.1)$$

The parameters I , Δ and T express the force amplitude, the penetration length, and the period of time of oscillation, respectively. From this investigation, it was found that 40% friction drag reduction was achieved, although this control mechanism was not practical because of the resulted efficiency for it was very low. Also, Pang and Choi (2004) investigated the drag reduction effect in a turbulent boundary layer experimentally. In which, water was used as a working fluid mixed with the electro-conductive solution. Lorentz force was generated through an array of permanent magnets interleaved with copper electrodes. They achieved 40% drag reduction as well. Other variants of spanwise forcing, such as the spanwise position of the wave, were studied by means of DNS with different formulas such as those used by Du and Karniadakis (2000) and Du et al. (2002), in equation (2.2).

$$F_z = I \exp\left(-\frac{y}{\Delta}\right) \cos\left(\frac{2\pi}{\lambda} z - \frac{2\pi}{T} t\right) \quad (2.2)$$

And in the streamwise direction by Huang et al. (2010) in equation (2.3)

$$F_z = I \exp\left(-\frac{y}{\Delta}\right) \cos\left(\frac{2\pi}{\lambda} x - \frac{2\pi}{T} t\right) \quad (2.3)$$

where λ is the wavelength. A DNS study was studied to investigate the effectiveness of a transverse travelling wave on the drag reduction by applying Lorentz force in the spanwise direction, which induced a near-wall spanwise force (Du and Karniadakis, 2000; Du et al., 2002). From this study, the authors achieved a drag reduction exceeding 50%, in addition to observing a significant change to near-wall streaks. Lorentz actuators and shape-memory alloys were used in their preliminary experiments and introduced results in a good agreement with the previous DNS data.

On the other hand, besides the use of spanwise body force, the friction drag was expected to be reduced by using a wall-normal body force. This wall-normal body force induces a wall-normal velocity, which is often applied to pacify and calm the near-wall coherent structure. Mamori and Fukagata (2011) run a DNS of a fully developed channel flow controlled by a travelling wave-like in the direction of wall-normal and streamwise or a stationary wall-normal body force in a fully developed channel flow. Their visualization of the vortical structure under the standing wave-like wall-normal Lorentz force revealed that the near-wall streamwise vortices, which increased the skin-friction drag, disappeared and spanwise roller-like vortices were generated instead. Three components decomposition of the Reynolds shear stress indicated that the spanwise roller-like vortices contributed to the negative Reynolds shear stress in the region near the wall, similarly to the case of laminar flows. Equation (2.4) expresses the streamwise Lorentz force as i.e.,

$$F_y = F_z = 0, \quad (2.4)$$

$$F_x = I \exp\left(-\frac{y^+}{\Delta^+}\right) \cos\left(\frac{2\pi}{\lambda} (x - ct)\right)$$

The work of Mamori and Fukagata (2014) is an extended version of the work of Mamori and Fukagata (2011) and differs from Berger et al. (2000) in which, they used a streamwise wave-like wall-normal body force to act as a predetermined control. Such control was more easily in practice than feedback control. In their work, the used body

force, which was travelling in the streamwise direction, had a sinusoidal variation in the streamwise direction and decayed in the normal to the wall direction, y , in the lower half of the channel. The travelling wave-like wall-normal Lorentz force was defined in equation (2.5) as:

$$F_x = F_z = 0,$$

$$F_y = I \exp\left(-\frac{y^+}{\Delta^+}\right) \cos\left(\frac{2\pi}{\lambda}(x - ct)\right) \quad (2.5)$$

It was expected by the use of this body force that it would induce the fluid motion like what happened in the case of using a travelling wave-like blowing and suction. The results showed that the skin friction was reduced when the wave travelled in a slower velocity than that value of the bulk-mean velocity, such as a minimum skin-friction drag of 40% was achieved in the case of stationary control input. As a disadvantage of this method, a 5% positive efficiency, an increase in efficiency, was hardly achieved as a maximum net energy saving rate.

2.2.2.2 Spanwise oscillating

In this type, the control is performed via periodic spanwise wall oscillation, Figure (2.2). This method depends on distorting the spatial relation streamwise vortices and low/high-speed streaks by formation a Stoke layer directly above the oscillated surface and disturbs the elongation of the streamwise vortices via generating negative spanwise vorticity in the Stokes layer.

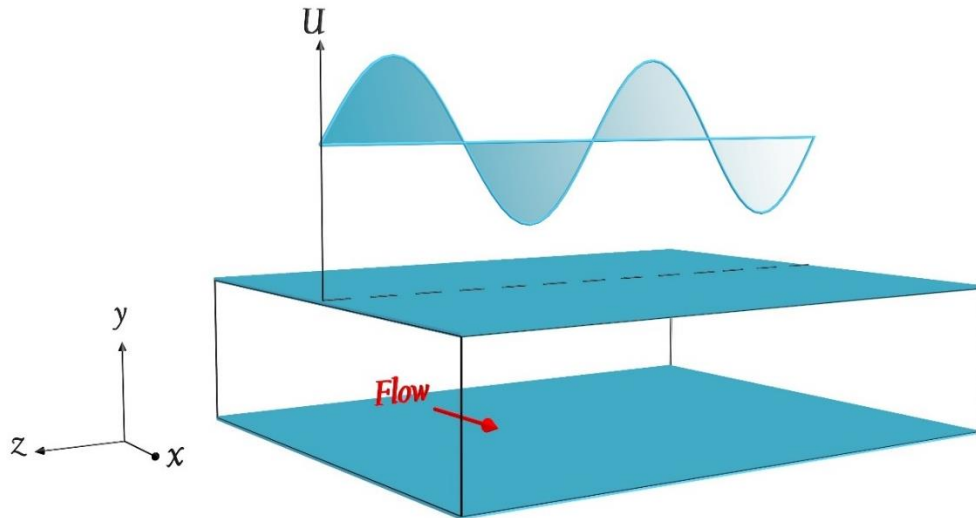


Figure (2.2) Spanwise travelling wave.

Jung et al. (1992) were the pioneers who performed DNS studies for controlling the turbulent flow by using a temporally periodic spanwise wall oscillation. The wall oscillated with sinusoidal velocity as shown in equation (2.6).

$$w = A \sin(\omega t) \quad (2.6)$$

where (w) is the velocity in the spanwise direction, (A) expresses the amplitude and (ω) refers to the wave angular frequency. They achieved a maximum drag rate of 40%. While in (Choi et al., 1998), a spanwise oscillating wall was applied and it was found that the skin friction drag was reduced up to 45 %, but due to the using of auxiliary mechanical movement for the oscillation motion, a maximum net energy saving of 7% was produced. Also, Quadrio and Ricco (2004) investigated 37 cases numerically for the turbulent drag reduction by using the wall oscillation, in these simulations many different control parameters were studied. A maximum drag reduction, compared with uncontrolled turbulent studies, was reported as 44.7%. However, analysis of the power spent by the movement of the wall showed that a maximum net power gain of only 7.3% was achieved. This way of control was used in many other control techniques, e.g. the stationary spanwise velocity with a streamwise variation which appears in equation (2.7) and illustrated in Figure (2.3). This type of action controls the wave properties in the streamwise direction (Touber and Leschziner, 2012).

$$w = A \sin(k_x x) \quad (2.7)$$

where k_x is the streamwise wavenumber. The authors showed that the unsteady cross-flow straining caused major spanwise distortions in the streaks near-wall structures, and the transverse wall oscillations led to the formation of a thin layer, highly sheared Stokes layer, which was observed to cause a significant reduction in streamwise wall friction. The performance of this mechanism mainly based on the created Stokes layer and its penetration depth, dictated by the oscillation frequency, and also on the spanwise shear magnitude in the viscous sublayer relative to the streamwise shear. On the other hand, a parametric study of the streamwise travelling wave-like wall oscillation by (Quadrio et al., 2009), equation (2.8), confirmed a maximum drag reduction rate of 48% but the authors didn't refer to the efficiency obtained during their calculations.

$$w = A \sin(k_x x - \omega t) \quad (2.8)$$

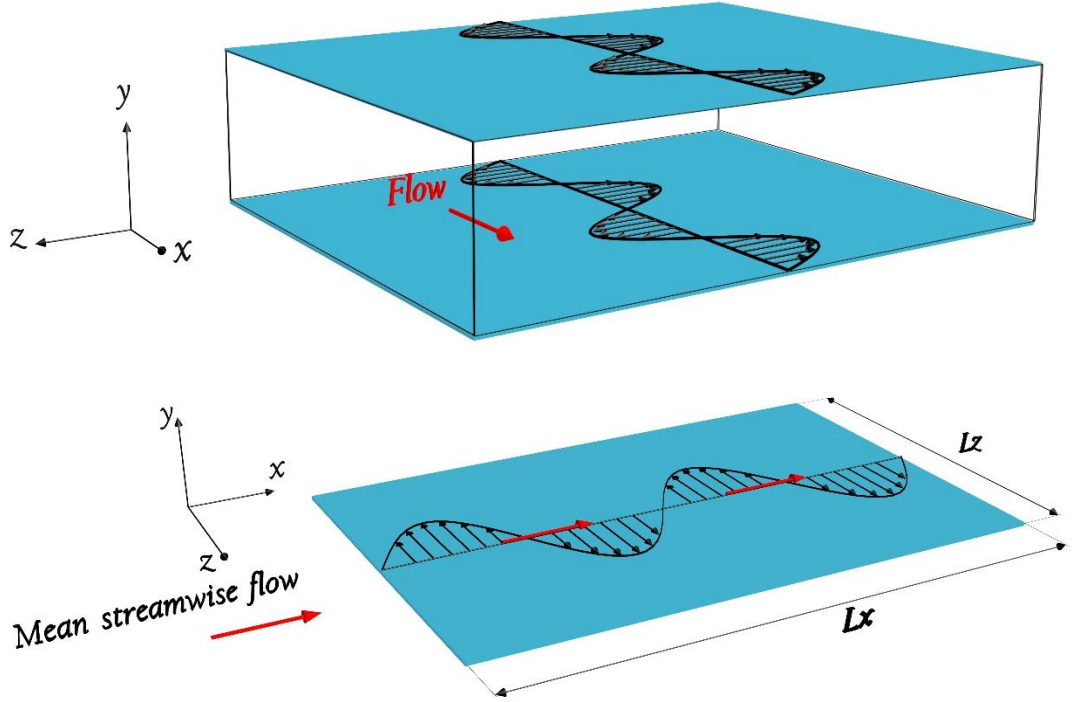


Figure (2.3) Streamwise travelling wave.

Recently, the DNSs of turbulent channel flows with wall undergoing spanwise oscillating and streamwise travelling wave motions were performed at $Re_\tau = 1000$ and 1600 , respectively, by Hurst et al. (2014). They reported a connection between the friction Reynolds number and the skin friction drag reductions rates as they declined when the friction Reynolds number, Re_τ , increases. The authors suggested a friction Reynolds number scaling of the drag reduction rate in the form of $Re_\tau^{-\epsilon}$, where ϵ is a factor in the range of $0 < \epsilon < 0.5$. The maximum drag reduction rates were obtained based on the optimal oscillation period also decreased as the friction Reynolds number increases, from 38% at $Re_\tau = 200$ to 29% at $Re_\tau = 1000$.

2.2.2.3 Wall deformation

Wall Deformation can be considered as one of the most effective actuators between other different kinds of actuators due to its robustness against the surrounding environments, in which the wall surface moves up and down to change the structure of the flow near the wall and hence effects on the development of the streamwise vortices.

Pneumatic wall-deformation actuators depended on micro-electromechanical system (MEMS) techniques proved its effectiveness as it survived during transonic flight tests with large temperature variations (Grosjean et al., 1998). While Wilkinson and Balasubramanian (1985) and Kang and Choi (2000) showed the ability of the wall deformation to alter the streaky structures in a turbulent boundary layer (TBL) by using a predetermined wall deformation. Also, Segawa et al. (2002) demonstrated that a spanwise array of actuators generating inclined wavy disturbances were able to interact with the low-speed streaks near the wall and the behaviour of the normal streaks instabilities tended to disappear. However, the drag reduction value was not reported. Endo et al. (2000) investigated the effect of the wall deformation via using an array of actuators with sensors to sense the behaviour of the flow near the wall and send feedback to the actuators to control the quasi-streamwise vortices. With this system of sensors and actuators, 10% skin friction drag was obtained via controlling the streak meandering. The authors reported a positive efficiency for the system as the power used in the control was smaller than the pumping power saved with about one order of magnitude.

As an example for the simulation of the wall deformation, Itoh et al. (2006) utilized a loudspeaker as a source of excitation to a flexible polythene sheet with the dimensions of (5000*5000) wall units, to act a transverse travelling wave. This kind of boundary layer control achieved 7.5% drag reduction which is not a big percentage relative to the used power for the control. Also, it was noticed that the log-law regions near the wall became narrower compared with the other cases with a rigid surface. Recently, Bai et al. (2014) investigated experimentally the reduction in the skin friction drag in a turbulent boundary layer. In their experiments, they used a spanwise-aligned piezo-ceramic (PZT) actuator array, as shown in Figure (2.4). By applying a phase shift between the adjacent actuators, the actuators were able to generate a transverse travelling wave along the wall. The main parameters to control the wave such as the wavelength, amplitude, frequency of the oscillation, and their influence on the skin-friction drag were studied. They reported a maximum drag reduction of 50% after 17 wall units downstream the actuators. Although they get high drag reduction, the resultant efficiency was very low, owing to the rapid recovery of the reduced wall shear stress. So, they suggested that the small efficiency could be increased by increasing the length of the actuators in the streamwise directions.

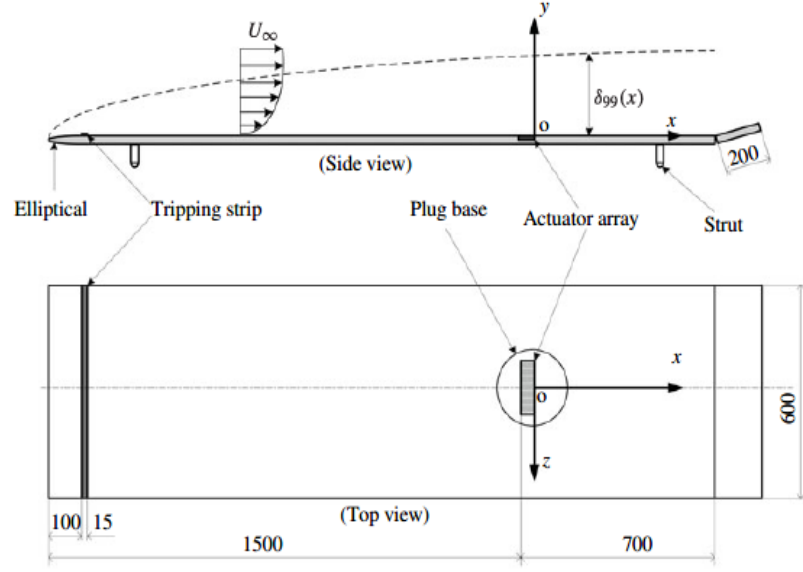


Figure (2.4) Schematic of the test rig to generate the turbulent boundary layer (Bai et al., 2014).

Following that, Li and Zhou (2016) verified the suggestion of Bai et al. (2014), experimentally, that an increase in the effective streamwise length of the actuators could prolong the downstream drag-reduced distance. They achieved a maximum local skin friction reduction of 70% at 33 wall unit downstream of the actuators. This meant that the drag recovery was slower than that of Bai et al. (2014) and also they proved that the drag reduction rate (δ_{τ_w}) depends on both jet frequency and amplitude of the flow from the slits.

By using direct numerical simulations DNSs for turbulent channel flow, Schoppa and Hussain (1998) achieved skin friction reduction by forcing the large-scale flow without requiring instantaneous flow information. With an amplitude of only 6% of the centreline velocity, they produced a significant sustained drag reduction of 20% for imposed counter-rotating streamwise vortices (V_{con}) and 50% for colliding, Z-directed wall jets (W_{con}), equation (2.9). The longitudinal vortices near to the wall were weakened due to the effect of the jets by suppressing the underlying streak instability mechanism and this led to the drag reduction. This effect weakened the wall-normal vorticity (ω_y) accompanied with the low-speed streaks, thereby arresting the streaks' sinuous instability which directly generated new streamwise vortices in uncontrolled flows. Figure (2.5) shows the instabilities and the vortices before and after the control.

$$U_{con} = 0,$$

$$V_{con}(y, z) = -A\beta \cos(\beta z)(1 + \cos \pi(y/\delta - 1)), \quad (2.9)$$

$$W_{con}(y, z) = -A\pi \sin(\beta z) \sin \pi(y/\delta - 1)$$

where (A) is the control amplitude and (β) is the characteristic streak spacing of approximately 100 wall units.

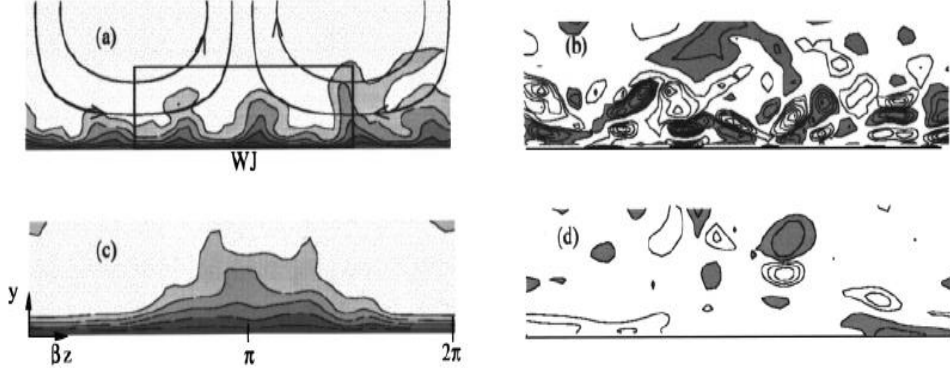


Figure (2.5) Distributions of $u(y, z)$ in (a-c) and $\omega_x(y, z)$ in (b-d) near one wall of turbulent channel flow at $Re=1800$, without (a,b) and with (c,d) an imposed large-scale control flow (Schoppa and Hussain, 1998).

A streamwise travelling wave-like wall deformation was performed by a direct numerical simulation (DNS) of a turbulent channel flow at $Re_\tau = 180$ (Nakanishi et al., 2012). They found that relaminarization for the flow was achieved and with a specific set of parameters, it led to a 69% drag reduction and 65% net energy saving. Also, they reported that at a higher amplitude of actuation the relaminarized flow was unstable and exhibited a periodic cycle between high and low drag.

2.2.3 Blowing and suction control

Fukagata et al. (2002) produced a relation between the skin friction coefficient, C_f , and the Reynolds shear stress (RSS), it is called (FIK) identity, namely after their names (Fukagata, Iwamoto, Kasagi). The FIK identity divided the skin friction coefficient in any fully developed turbulent flow into a laminar, first term in the right-hand side (RHS) in equation (2.10), and a turbulent part, the second term in the RHS, i.e.

$$C_f = \frac{12}{Re_b} + 12 \int_0^1 2(1-y)(-\overline{u'v'})dy \quad (2.10)$$

where Re_b refers to the bulk Reynolds number and y is the distance in the normal to the wall direction. From the RHS of the equation, it can be concluded that the turbulent part is a y -weighted integration of the RSS, which related to the activity of quasi-streamwise vortices (QSVs). They reported as a result of this equation that to reduce the friction drag, the flow should be designed to suppress the near-wall turbulence or to generate a negative RSS. FIK identity was applied to many different applications such as studying the dynamical effects on the frictional drag in the turbulent channel, pipe and plane boundary layer flows.

The FIK identity in a turbulent boundary layer with uniform blowing (UB) or uniform suction (US) from the wall was used to perform analysis which aimed to explore the skin friction drag reduction (Kametani and Fukagata, 2011). Constant wall-normal velocity was applied from the control region in the range of $-0.01U_\infty \leq V_{crt} \leq 0.01U_\infty$. They concluded that blowing achieved skin friction drag reduction, while suction stabilizes the turbulence in the boundary layer. From the point of view of turbulent fluctuations, upstream blowing enhanced the turbulence, while upstream suction suppressed it, and they quantitatively discussed different mechanisms of those effects.

While Kametani et al. (2015) extended their work from Kametani and Fukagata (2011) to ensure the capability of FIK identity with higher Reynolds numbers by means of well-resolved Large Eddy Simulation (LES). In this study, both the Reynolds number dependence as well as the influence of the control position and its length were investigated. The studies of Kametani and Fukagata (2011) and Kametani et al. (2015) indicated, in particular, that the more increasing in the blowing amplitude, the larger drag reduction occurs. In addition, using a longer streamwise length of a uniform blowing region results in a larger drag reduction effect. This also was ensured recently by the experimental work of Li and Zhou (2016) as mentioned before.

Min et al. (2006) applied a linear analysis to a laminar channel flow by using blowing and suction from the wall generating streamwise travelling wave, as shown in equation (2.11):

$$v_w = A \sin\left(\frac{2\pi}{\lambda}(x - ct)\right) \quad (2.11)$$

where (v_w) is the velocity in the normal to the wall direction at channel wall; (A , λ , and c) refer to the wave amplitude, wavelength, and the wave speed; x and t denote the streamwise coordinate and the time, respectively. In the upstream travelling wave, the wave travels in the opposite direction to the flow, a negative RSS was produced in the region near the wall, which resulted in a friction drag sustained below that of the laminar level (i.e., a sub-laminar drag). The greatest drawback from this method is the high cost required to apply the control relative to the existed feedback schemes. Therefore, Mamori et al. (2010) extended the linear analysis of Min et al. (2006) to get a unified explanation for the resulted drag reduction effect. A non-zero Reynolds Shear Stress RSS took place because of a non-quadrature between the velocity disturbances resulted from the travelling wave. This non-quadrature was a consequence of a viscous phase shift from the base phase relationship (i.e., the solution of the inviscid disturbance equation). A negative RSS was produced due to the induced phase shift by the upstream travelling wave. while the downstream travelling wave created a positive RSS.

In contrast to the upstream travelling wave-like blowing and suction, which produces a sub-laminar drag in exchange for flow destabilization, Moarref and Jovanović (2010) reported that fast downstream travelling waves, Figure (2.6), were able to not only reduce the drag but also stabilize the flow. They investigated experimentally how to control the turbulence onset through a channel flow by applying streamwise travelling waves generated by zero net-mass flux surface blowing and suction changing with the streamwise distance and time, equation (2.12). They used a nonlinear analysis to evaluates the base flow modifications and to assess the resulting net power balance. Then they implemented it numerically in Lieu et al. (2010).

$$V(\bar{y} = \pm 1) = \mp 2A \cos(w_x(x - ct)) \quad (2.12)$$

where c , x , A and w_x are the wave speed, streamwise distance, wave amplitude and the angular frequency of the wave.

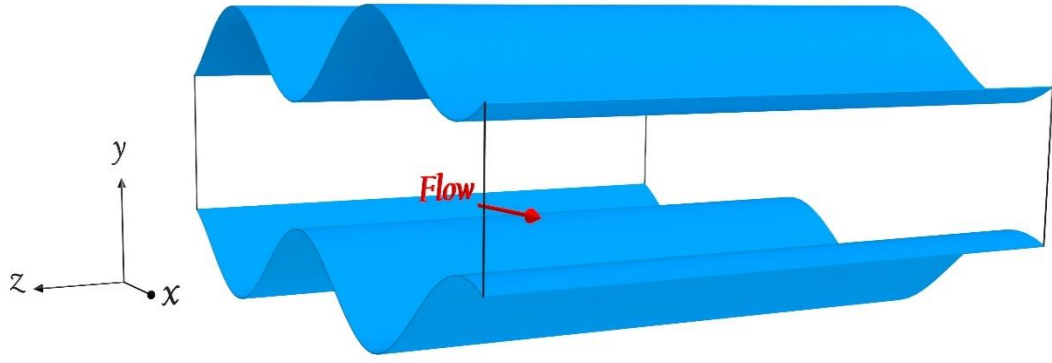


Figure (2.6) Travelling wave-like wall deformation in the streamwise direction.

They deduced that the downstream travelling waves (DTW) (positive wave speed), in equation (2.12), with properly designed speed and frequency significantly reduced the turbulence receptivity which made them well-suited for controlling the turbulence onset. In contrast, the velocity fluctuations around the upstream travelling waves (UTW) (negative wave speed) exhibited larger receptivity to disturbances, (UTW) were poor candidates for prevention of transition. They verified the observations of Lee et al. (2008) that the UTWs are able to destabilize the laminar flow when using small control amplitudes in the range of 1-5% of the centreline velocity. On the other hand, the DTWs with phase speeds higher than the centreline velocity stay stable even for large wave amplitudes. Moreover, the UTWs (DTWs) exhibit larger (smaller) transient growth relative to the uncontrolled flow.

On the other hand, Mamori et al. (2014) investigated the range of the wave speed, c , the wavelength, λ , and the amplitude of the wave, a , at which the travelling wave-like using blowing and suction through a fully developed turbulent channel flow achieved a flow relaminarization. They specified a range for the wave parameters in which the relaminarization has to be achieved, this range is as follow $c/u_{laminar} > 1.5$, $200 < \lambda^+ < 500$, and $A/u_{laminar} > 0.1$, where $u_{laminar}$ denotes the bulk mean velocity of the corresponding laminar flow and the superscript of (+) denotes the wall units.

Tomiyama and Fukagata (2013) studied by using DNS the effect of a spanwise travelling wave-like wall deformation, as shown in Figure (2.7), in a turbulent channel flow on the rate of the drag reduction at $Re_B = 5600$ based on the bulk velocity of the channel. They examined the effect of the wave parameters with the spanwise

wavelength of the order of 100 wall units on the drag reduction, as a wave having such a wavelength is expected to better interact with QSVs. Analysis by FIK identity revealed that the reduction in the random Reynolds shear stress played the dominant role in the drag reduction. The maximum drag reduction achieved was 13.4% and the maximum net energy saving was 12.2%.

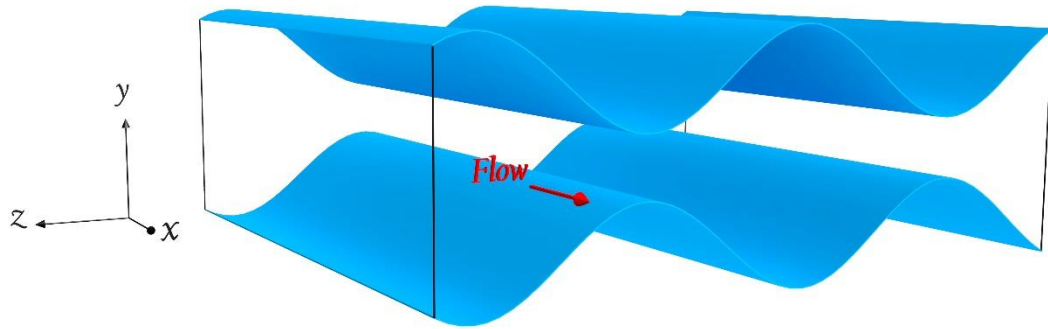


Figure (2.7) Travelling wave-like wall deformation in the spanwise direction.

They also explained the spanwise travelling wave influence on the flow near to the wall and on the quasi-streamwise vortices, as shown in Figure (2.8) and Figure (2.9).

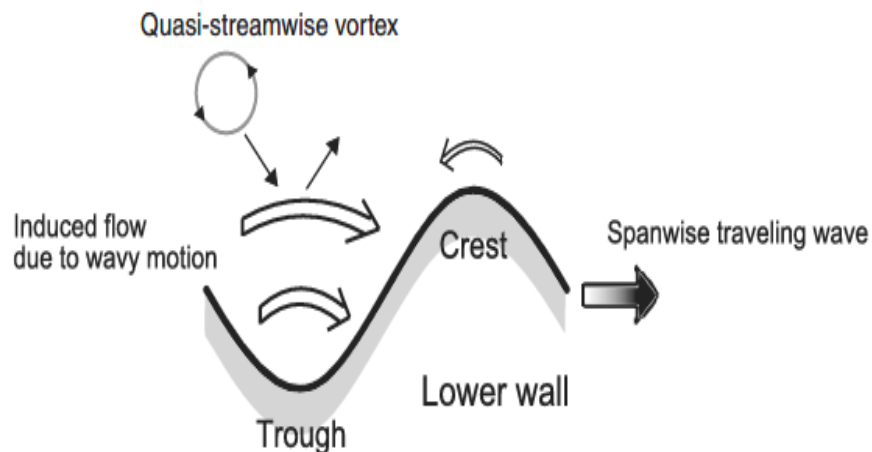


Figure (2.8) Schematic of drag reduction mechanism due to travelling wave-like wall deformation in the spanwise direction (Tomiyama and Fukagata, 2013).

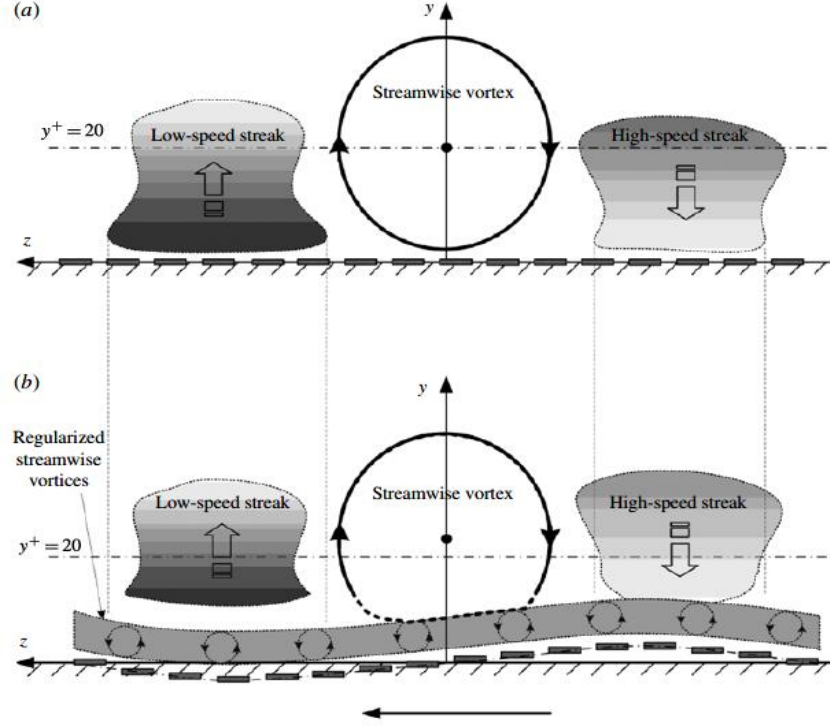


Figure (2.9) Effect of the travelling wave on the near-wall QSVs. (a) without the wave; (b) with the wave (Tomiyama and Fukagata, 2013).

Streamwise intermittent uniform blowing sections with identical total mass flux within spatially developing turbulent boundary layers using LES were used to investigate the dependence of the drag control on the number of blowing sections (Kametani et al., 2016). The blowing region was separated into N sections, $N = 3, 6, 20$, and 30 with constant mass flux. The FIK identity from Fukagata et al. (2002) was exploited to assess the blowing influence on the physically decomposed components of the skin friction drag. It was concluded that, by separating the blowing regions, the skin-friction drag oscillated with immediate recovery on the non-blowing wall. With $N=1$, a net-energy-saving rate of around 18% was achieved, which initially decreased at most 2% points for $N = 3$ but recovered with increasing N . This indicated that the practically desirable (from maintenance and feasibility point of view) spatially intermittent blowing regions still achieve large net-energy saving rates.

Considering the drag reduction control in spatially developing flows, Stroh et al. (2015) performed a DNS simulation of opposition control in a spatially developing turbulent boundary layer. They found that the skin-friction drag was increased downstream of the control region where the control was not applied anymore compared to the uncontrolled turbulent boundary layer. In contrary, a uniform blowing

control was found to sustain the drag reduction effect downstream the control region. They concluded that this difference came from the mechanisms involved to reduce the skin-friction drag. This led to that drag reduction was achieved through the mean flux from the wall for uniform blowing, while it was turbulence reduction near the wall for opposition control.

A combination of uniform suction and blowing regions was used to investigate the friction drag reduction effect by Noguchi et al. (2016). In which, the Reynolds-Averaged Navier-Stokes simulation (RANS) was used to deal with a spatially developing boundary layer on a flat plate at a practically high Reynolds number. As a result, the combined control was found to reduce the global skin friction coefficient by 44.1%, whereof the contribution of transition delay by the uniform suction was about 90%, and that of turbulent drag reduction by the uniform blowing was about 10%. It was also found that the position of the blowing region should better be located in the upstream side of the turbulent region because the drag reduction effect was sustained for a while even after the blowing was terminated.

According to the practical application on rough walls, uniform blowing is considered as an effective method to reduce the drag. Mori et al. (2017) applied DNS in a fully developed turbulent flow in a channel with a two dimensional irregularly rough wall, the drag reduction effect was investigated due to two different cases of uniform blowing (UB) on rough surfaces at $Re_B = 5600$ and 14000 . The drag reduction was caused by two different mechanisms depending on decomposing it into friction and pressure contribution. One mechanism was expressed by the vertical shift of the mean velocity profile and the turbulence structures which is similar to that one in smooth wall cases. This mechanism produces less friction drag. The second mechanism is due to the reduced flow rate around the roughness elements of the surface which can be considered as a distinctive feature on the rough wall. Such a mechanism reduces the pressure drag. Owing to the small pressure drag reduction, the total drag reduction rate was considered to be slightly less than that one in the smooth wall cases. In contrast, the absolute amount of drag reduction was found to be larger on the rough surface due to the presence of pressure drag.

Uniform blowing can effectively be used also for supersonic turbulent boundary layers as well. Compressible turbulent channel flows with uniform blowing and

suction DNS series were performed in order to investigate the Mach-number effect on the drag reduction (Kametani et al., 2017). A comparison between two different values of Mach number of values 0.8 and 1.5 was applied. It was revealed that similar to the incompressible turbulent channel flow, the drag was reduced on the blowing side while it was increased on the suction side. Also, the drag reduction rate was primarily affected by the control amplitude rather than the bulk Mach number. While the Mach number had a clear effect on the control gain as it increased with increasing the Mach number and this was explained by the decrease of wall-normal velocity due to the increased density near the wall. Finally, The decomposition of the skin friction drag using the FIK identity (Fukagata et al., 2002) also confirmed the absence of the Mach number dependence except for the viscosity term, which came from the viscosity variation due to temperature.

2.3 Transition control

As the main aim from the current research is to study the control of the transition to turbulence and drag reduction in this region, so, an additional literature review is produced in the current section with the recent studies for this application.

In an open circuit wind tunnel, Grundmann and Tropea (2007) used three arrays of plasma actuators in a flat plate boundary layer with an adverse pressure gradient to effect on the transition to turbulence onset of the flow boundary layer. The first array of the actuators downstream of the leading edge was applied in pulsed mode to excite the instabilities inside the boundary layer to generate the transition. While the other 2 arrays of actuators in the streamwise direction were used to reduce the amplitude of the instabilities which in turn produced transition delay. As a result, the velocity fluctuations in the case of using the actuators were reduced to 50% compared with that value without using the actuators.

Recently, Lohse et al. (2016), in the open test section of the wind tunnel at the Institute of Aerodynamics and Flow Technology, DLR, in Göttingen, investigated the effect of a pneumatic actuator system for shifting the bypass transition in the downstream direction and controlling the crossflow vortex-induced laminar breakdown. In this study, the authors used steady blowing or suction through a spanwise row of periodically arranged orifices to initiate a system of longitudinal

vortices which reduces the amplitude of the most amplified stationary crossflow vortices. By using the optimal parameters for the control, both suction and blowing were able to produce significant shifts in the position of the bypass transition up to 15% in the chordwise direction. On the other hand, Xiao and Papadakis (2017) used the blowing and suction technique to control and suppress the perturbations leading to bypass transition in a zero-pressure gradient boundary layer. The blowing and suction slot was applied in the region of the transition. Two different approaches were used, the first one is blowing and suction with zero-mass flow rate and the second is with non-zero-mass flow rate. The authors concluded that applying a zero-mass flow rate blowing and suction was able to reduce the amplitude of the boundary layer instabilities but with less efficiency than that one with the non-zero mass flow. The spanwise averaged velocity was distorted by the control action, resulting in a significant reduction of the skin friction coefficient which meant delaying in the bypass transition occurrence.

Another way to control the transition onset in channel flow is to generate disturbances in the spanwise direction. For example, Hack and Zaki (2014) applied time-harmonic spanwise wall motion to control the bypass breakdown to turbulence and produced an optimal oscillation amplitude and frequency to be used through their DNS trials. As a result from their simulations, it was found that the amplitude of the secondary instabilities was weakened and the amplitude of the boundary layer streaks was reduced with percentage up to 50% while, the most energetic streaks were eliminated which resulted in a shift in the streamwise direction to the bypass transition to turbulence onset. Also, Sattarzadeh and Fransson (2017) used the Minimum Turbulence Level (MTL) wind tunnel at KTH-Royal Institute of Technology to create experimentally a spanwise mean velocity gradient (SVG) to delay the transition to turbulence onset via applying a discrete uniform suction in a flat plate boundary layer. The point of view of this method was to attenuate the rate of growth of (T-S) waves which in turn led to delay the transition occurrence. From their work, the authors were able to elongate the laminar flow by at least 120% for a suction amplitude of 0.8% of the free stream velocity. Also, a 30% transition delay achieved when applying the same technique for a natural transition.

Surface roughness was experimentally used to control the flat plate boundary layer bypass transition induced by an upstream convected two-dimensional (2D)

circular cylinder wake. In the study of Chong et al. (2012), they used the surface roughness to control the hairpin vortices, which are the dominant coherent structures to promote the transition process. As a result, the regularisation process of the hairpin vortices was observed under the influence of roughness elements. Significant scale reduction and localisation of these hairpins were achieved, which enhanced the possibility of the hairpin self-annihilation process. In this sense, roughness elements impeded the cascade of the large-scale structures during the transition process.

A viscosity stratification can be considered as a possible mean to postpone the onset of transition to turbulence in a channel flow. As a numerical prototype problem, Nouar et al. (2007) focused on the linear stability of shear-thinning fluids modelled by the Carreau rheological law. The authors reported that to assess whether there is stabilization for the transition process and by how much, it is important to account for the viscosity disturbance in the perturbation equations and to employ an appropriate viscosity scale in the definition of the Reynolds number. Failure to achieve that can yield qualitatively and quantitatively incorrect conclusions. Results were obtained for both exponentially and algebraically growing disturbances. A transition to turbulence delay was achieved when a viscosity contrast was produced in the critical layer. These results demonstrated that a viscous stratification is a viable approach to maintain laminarity. While the properties of the main flow near the wall and the effect of the flow viscosity were investigated to produce its effect on the bypass transition location. In the work of Jung and Zaki (2015), DNS was used to examine the bypass transition in a two-fluid boundary layer. The main idea of that research was using a low viscosity flow film near the wall and evaluating its impact on the bypass transition onset. Two different viscosity ratios, between the wall film and the main flow, and free-stream turbulence intensities were used. In the case of using less viscous wall film, it absorbed the mean shear from the outside stream which in turn weakened the lift-up mechanism and resulted in a shift of the onset of turbulence.

Also, many algebraic models have been applied recently for the bypass transition over a flat plate or turbomachinery boundary layer such as that one of Kubacki and Dick (2016), in which the authors produced a simple algebraic model, using $k-\omega$ RANS turbulence model, for laminar to turbulent transition via applying a specific range of medium freestream turbulence. This model was applied over a flat plate, T3C cases of ERCOFTAC, and tested for cascades of N3-60 ($Re=6 \cdot 10^5$) steam turbine

stator vanes, V103 ($Re=1.385 \times 10^5$) compressor blades and T106A ($Re=1.6 \times 10^5$) gas turbine rotor blades. This model produced acceptable results for the attached and separated boundary layer for 2D and 3D RANS simulations.

2.4 Scope of the study

Chang et al. (2002), Pamiès et al. (2007) and Kametani et al. (2016) used the large eddy simulations in their studies for the turbulence control, and many other researchers used the DNS. LES and DNS proved their ability to mimic the turbulence structures with high accuracy through the flow. Therefore, in this study and according to the literature review, the large eddy simulation will be used to study the point of the research using the opensource CFD OpenFOAM libraries. As the scope of this study is to investigate the effect of the sensorless active control on the bypass transition onset and the drag reduction rate through the channel, an isotropic homogeneous turbulence at the inlet plane of the channel with a medium turbulence intensity of 3-7% will be implemented to be able to produce the bypass transition through the channel.

LES and DNS offer valuable insight into sensorless strategies for turbulence control in fully developed turbulent flow, so their utilities can be significantly enhanced to be used for delaying the transition to turbulent or reducing the skin friction drag. According to Bewley (2001) and Bewley and Aamo (2004) who proposed the following conjecture ('Bewley's conjecture'):

“The lowest sustainable drag of an incompressible constant mass-flux channel flow, when controlled via distribution of zero-net mass-flux blowing/suction over the no-slip channel walls, is exactly that of the laminar flow.”

From that, a question that emerges from the above review in Section 2.2 is that:

“Is the combination between the techniques of the travelling wave and that one of uniform blowing and suction to give an inclined travelling wave will be a suitable and effective technique for the skin friction drag reduction and delaying the transition?”

Schoppa and Hussain (1998) studied the normal to the wall control to generate vortices and the collided jets with the low-speed streaks in the spanwise direction separately. Bai et al. (2014) and Li and Zhou (2016) investigated the spanwise

travelling wave in the normal to the wall direction only. So, a combination between them may lead to a new method to control the transition onset and the amount of total drag reduction, with inclined jets in the streamwise direction. So, a model-based framework for generating the bypass transition with the features of sensorless flow control design will be developed. This model will consist of a spanwise array of streamwise slits with a phase shift between each slit to generate the travelling wave. The travelling wave itself will have two components in wall-normal and streamwise direction to generate the inclined travelling wave.

2.5 Thesis outlines

In Chapter Three, the Monotonically Integrated Large Eddy Simulation (MILES) solver will be developed by modifying the Navier Stokes equations used in the conventional LES. The open-source CFD software OpenFOAM libraries will be used.

In the fourth chapter, an inlet boundary condition which is able to produce isotropic homogeneous turbulence at the inlet plane of the channel will be implemented. Through this boundary condition, most of the inlet turbulence parameters such as friction Reynolds number, length scale, time scale and root mean square (RMS) of the fluctuation velocity for the required turbulent intensity at the inlet can be controlled and specified before the start of the simulation.

While in the first part of the fifth chapter, a combination between the two parts from the third and fourth chapters will be produced using a medium turbulence intensity to get the bypass transition through the channel flow. In the second part, a sensorless inclined travelling wave in the spanwise direction will be generated. This wave will be formed from wall slits in the spanwise direction, each slit has a phase shift relative to the adjacent one to be able to produce sinusoidal inclined travelling wave. The velocity of each slit is uniform with two components in the streamwise and normal to the wall directions. This method will be evaluated via the behaviour of the skin friction coefficient, total drag reduction, its effect on transition onset, and the turbulence statistics near the wall.

Finally, conclusion and future work will be discussed in the sixth chapter.

Chapter (3)

Monotonically Integrated Large Eddy Simulation Solver (MILES)

3.1 Introduction

In most of the fluid mechanics areas, the understanding of any phenomena is strongly connected to the presence of turbulence. Despite many turbulence cases have been studied numerically, experimentally and even theoretically and their significant contribution in increasing the physical understanding of turbulence, but still, till now there is no predictive and accurate theory for the turbulent flow, and it is unlikely to emerge in the foreseeable future. Turbulence modelling is still in the developing stage. Nowadays, there are many researches and efforts are going on to improve the numerical methods to get an effective simulation for the real turbulence structures and their resulted energy dissipation, by using the empirical and experimental information. Moreover, even with the large computation facilities, it is impossible to simulate high friction Reynolds numbers (Re_τ) turbulent flows cases directly by totally resolving all ranges of scales of motions in space and time. As an alternative, at least small scales with specific ranges have to be approximated or modelled to make these calculations feasible and give accurate results close to those results of the experimental studies. The real challenge is to develop such a simulation algorithm that, although they may not be explicitly incorporating all dynamic scales, they will still be able to give accurate and reliable results for at least the large and medium energy-containing scales and even for a limited range of the small scales during the flow motion. The simulation of those small scales is responsible for presenting the energy dissipation through the energy cascade process.

Hence, any process done on the fluid flow is dissipative, so, the amount and the form of the dissipated energy are very important in all issues of any numerical algorithm design (Margolin and Rider, 2005). The importance of energy dissipation appears clearly in the cases with high Reynolds numbers and high-speed compressible

flows with shock, in which, the energy dissipation occurs at length scale too small to be resolved by the used numerical algorithms. The turbulence is usually forced at large scales of motion, at which the energy cascade process starts to transfer the energy from larger scales of motion to the smaller scales till the turbulence eddies reach to a specific small scales, microscales, at which the molecular viscosity is larger than the kinetic energy of the eddies. At this point, the molecular viscosity converts the kinetic energy into heat. In the cases where these small scales cannot be resolved, absence of dissipation, the energy will build up at the smallest resolved scales and lead to the deviation of the flow solution (Margolin and Rider, 2005).

The turbulence community has realized this conundrum and its effect on their studies, therefore, they started to add explicit terms to their governing equations (i.e. subgrid-scale models) to model the effect of the turbulence and compensate the absence of the energy dissipation at small scales such as the conventional Large Eddy Simulation (LES). With the increase in computations power, LES started to gain industrial relevance due to its ability to provide more accurate information about the instantaneous fluctuations rather than the Reynolds Average Navier Stokes Equations (RANS). Conventional or classical LES has been evolved from using the limited sub-grid viscosity models to more accurate and specialized dynamic mixed models. Eddy-viscosity models are able to simulate sub-grid scale (SGS) dissipation with acceptable accuracy but on the other hand, they are not good with the SGS stresses which participate in the momentum equation and suffer from primary error source due to the numerical discretization schemes. That's why this approach is less suited for complex high friction Reynolds number (Re_τ) flows which by necessity are usually poorly resolved (Adedoyin et al., 2015). More recent efforts have been focused on developing the mixed models to provide more accuracy, by adding the dissipative models to those of higher accuracy. These mixed models produce better predictions, but their applications and usage are limited because of their implementation complexity and high computational cost relative to performing a coarse DNS case and thus become very expensive for the practical flows of interest at moderate-to-high Re .

Recognizing the disadvantages mentioned in the previous paragraph, a number of researchers have tried to get rid of the classical formulations and they have started using unfiltered flow equations instead of the filtered ones and putting non-oscillatory constraints via non-linear limiters infinite volume formulations, to work as an implicit

filter instead of the explicit one in the conventional LES. They have developed the Implicit Large Eddy Simulation (ILES) approach in which the energy dissipation of the algorithm itself is used to provide the required energy dissipation resulted from the energy cascade process instead of adding extra explicit terms (Sagaut, 2006). The point of view of ILES is to apply the sub-grid scale models to simulate the small scales under a specific range of filter via using specific features of the non-linear numerical algorithms on which the simulation model is based. To capture the inherent small-scale anisotropy of high-Re turbulent flows (e.g. worm vortices, shocks), the ILES uses an adaptive (dynamic, non-oscillatory) numeric. The energy dissipation in ILES is resulted from imposing of monotonicity constraints to the momentum equation through the solution (Margolin and Rider, 2005).

A special class of ILES depends on using monotonicity-preserving methods called Monotonically Integrated Large Eddy Simulation approach (MILES), named by Boris et al. (1992). MILES is an attractive approach for modelling turbulence in high Re number flows, which depends in its theory on finding a solution for the filtered Navier Stokes Equations without using any explicit sub-grid scale (SGS) model (Grinstein and Fureby, 2006). In which, the action of the SGS model is included implicitly by intrinsic nonlinear high-frequency filters built into the convection discretization schemes. The most important feature of MILES is that it generates implicitly a nonlinear tensor-valued eddy-viscosity during the convection term discretization, which acts predominantly on stabilizing the flow and suppresses the unphysical oscillations near sharp velocity gradients. This class uses special methods such as Flux-Corrected Transport (FCT), Piecewise Parabolic Method (PPM), and Total Variation Diminishing (TVD) algorithms, which has been used in the current research. Major properties of any implicit SGS model, especially in MILES, are specified as following (Grinstein and Fureby, 2006):

1. Selection of the high and low order schemes which are responsible for the model behaviour in the smooth and near sharp flow gradient regions respectively.
2. Selection of the flux limiter which controls the blending percentage of the above schemes depending on the flow region.

3. Achieve the balance between the dissipation and dispersion contributions to the solution, which relies on the design specifications for each numerical method.

MILES performance has been evaluated previously in many case studies, using FCT and Gamma as flux limiters for canonical flows (homogeneous isotropic turbulence). In which, Grinstein and Fureby (2005) investigated a forced homogeneous isotropic turbulence for a Taylor Re-number of $Re_\tau = 96$ at 32^3 and 64^3 mesh resolution. As a result, MILES produced a slightly larger fractions of small-scales vorticity than that one from the normal eddy-viscosity models. From those results, Figure (3.1)-(a) presents typical visualizations at 64^3 mesh resolution of the second invariant of the velocity gradient, i.e., $Q = 1/2 (\|\bar{\Omega}\|^2 - \|\bar{D}\|^2)$, where Ω is the vorticity and D is the mean shear strain rate. While Figure (3.1)-(b) compares the time-averaged energy spectrum for the same resolution at different schemes and $Re_\tau = 305$ compared with the DNS study of Jiménez et al. (1993) and the theoretical model of Driscoll and Kennedy (1983).

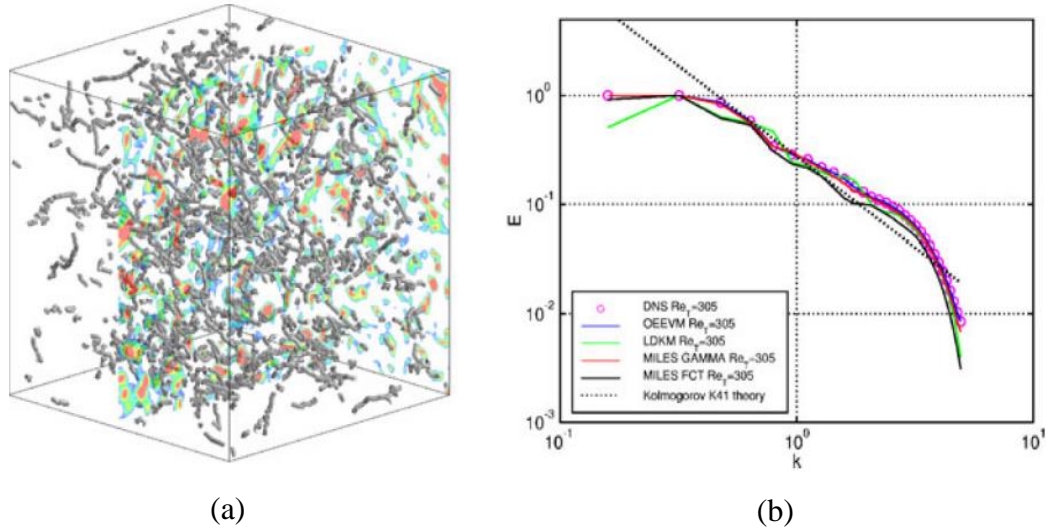
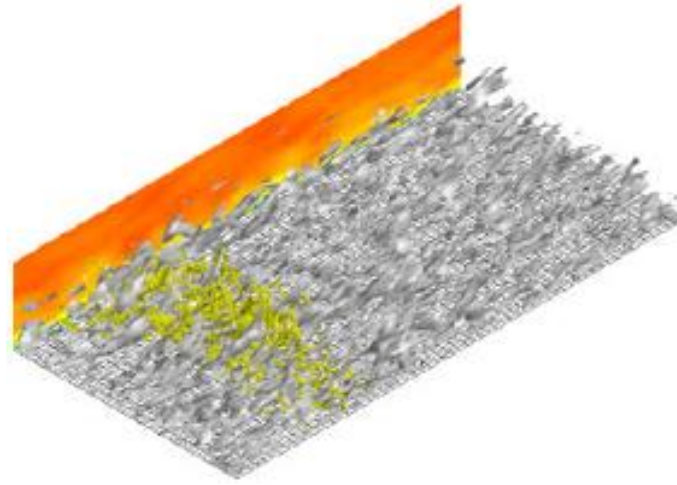


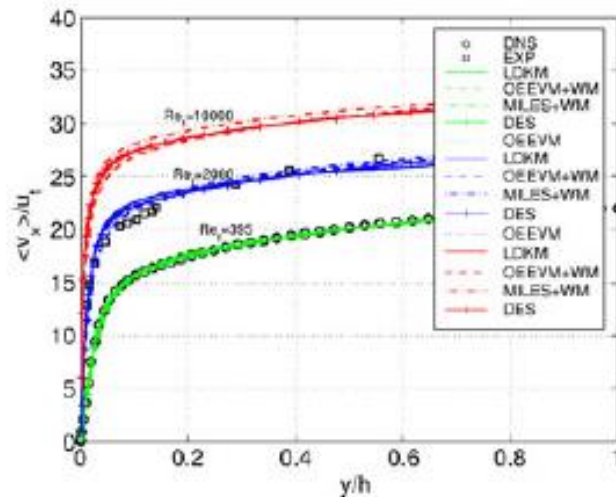
Figure (3.1) Forced homogeneous isotropic turbulence: (a) iso-surface of Q ; (b) energy spectrum (Grinstein and Fureby 2005).

On the other hand, MILES has been evaluated at different values of friction Reynolds number for the application of fully developed flow such as $Re_\tau = 395, 2000$ and $10,000$ in Fureby and Grinstein (2002) and also has been compared with the DNS data from Colella and Woodward (1984) and the experimental one from Wei and Willmarth (1989). Figure (3.2)-(b) shows the resulted streamwise mean velocity profile averaged in time and space while Figure (3.2)-(a) visualizes in terms of

contours the mean velocity, vortex lines and the iso-surfaces of the second invariant of the velocity gradient, Q , which represents the local balance between shear strain rate and vorticity magnitude and defining vortices as areas where the vorticity magnitude is greater than the magnitude of rate-of-strain. It is clear that MILES has shown good agreement with the DNS and experimental results because its capability to mimic the resolved flow anisotropies. In addition, MILES has been able to produce an equally decaying rate of isotropic turbulence with that one of the DNS via a comparison with the energy spectra for both cases. The MILES technique has been successfully applied on free jets by investigating the development of space and time of the vortex rings in low aspect-ratio (AR) rectangular jets (Grinstein, 1995).



(a)



(b)

Figure (3.2) Fully developed channel flow: (a) instantaneous visualization in term of contours of $\overline{v_x}$, vortex lines and iso-surfaces of Q ; (b) vertical profiles of mean streamwise velocity from Grinstein (2005).

The numerical dissipation of the MILES approach has been assessed by an approach to computing the effective numerical eddy viscosity in numerical simulations of decaying isotropic turbulence using a non-oscillatory algorithm MPDATA which has been produced by Domaradzki et al. (2003). They have concluded that the wavenumber dependent numerical viscosity reproduces qualitative features of the theoretical and intrinsic eddy viscosities but there are several quantitative differences.

MILES method with the high-resolution space-time conservation element/solution element (CE/SE) scheme was used in the study of REN et al. (2018). The authors simulated the two-dimensional free jet flows and their penetration length inside the flow, laminar and turbulent, without any effect on the surrounding flow. The flow structures averaged and instant velocity, turbulence intensity, velocity profiles at different cross-sections were examined through this study and all these properties produced good results in comparison with the previous experimental studies. Zhu et al. (2018) investigated the laminar separation phenomenon on the SD7003 airfoil under the low Reynolds numbers condition by using the MILES. They utilized the AUSM, Advection Upstream Splitting Method, scheme for spatial discretization. The numerical simulations were able to capture the instantaneous and averaged flow structures clearly such as temporal and spatial evolution process of the flow vortex structure. The results in this study approved that MILES is able to simulate the complex flow phenomena of separation, transition and reattachment accurately.

Also, MILES has been used for the prediction of adiabatic and isothermal supersonic flat plate boundary layers in Yan et al. (2002) at different Mach numbers $M = 2.88$ and 4. The adiabatic and isothermal supersonic flat plate boundary layer has been studied at $Re_\theta = 2 * 10^4$ based on the inflow boundary layer thickness. The results gave good agreement with the experimental work. They showed that the relation between the computed heat transfer coefficient and the skin friction coefficient is following the Reynolds analogy which refers to the ability of the MILES to produce the right dissipation comparing with the experimental work. Recently, Adedoyin et al. (2015) evaluated the combination of SGS model and discretization schemes for the LES in a complex turbulent flow and they compared their results with those results from MILES under same conditions. To achieve this target, a quantification of

combination between the modelling and discretization errors presented in finite-volume/finite-difference simulations was conducted for isotropic decaying turbulence. In Adedoyin et al. (2015), a comparison between the behaviour of the MILES using upwind and QUICK schemes and BCD, Bounded Central Difference scheme was produced. In this comparison, the performance of MILES with second-order upwind or QUICK schemes was better than MILES with BCD for the prediction of large-scale turbulent structures in axisymmetric jet flow at $Re \sim 10^5$. The upwind and QUICK schemes were approved to be dissipative and appear to provide an appropriate level of dissipation when combined with the MILES approach. As the upwind scheme is a type of the TVD schemes, so in this chapter, MILES solver is developed by applying schemes use upwind as the first-order scheme in their flux limiters. The open-source CFD software OpenFOAM libraries are used to modify the Navier Stokes equations and develop this solver. The results show good agreement with the previous DNS results at friction Reynolds numbers of $Re_\tau = 180$ and 395.

3.2 Governing Equations

3.2.1 Conventional LES

Navier-Stokes equations are applied for an incompressible flow as shown in equation (3.1).

$$\partial_t(V) + \nabla \cdot (V \otimes V) = -\nabla p + \nabla \cdot S \quad (3.1)$$

In conjunction with the incompressible continuity equation $\nabla \cdot V = 0$, where \otimes refers to the tensorial product, $S = 2\nu D$, and $D = 1/2 (\nabla V + \nabla V^T)$ are the viscous-stress and strain-rate tensors. The classical LES simulations have been divided into three components:

1. low-pass filtering by the convolution equation (3.2)

$$\bar{f}(x, t) = G * f(x, t) = \int_D G(x - x', \Delta) f(x', t) d^3 x' \quad (3.2)$$

with a prescribed kernel $G = G(x, \Delta)$ of width or filter size, Δ

2. Finite volume, element or difference discretization,
3. Explicit SGS modelling to close the low-pass filtered equations.

Applying (1) and (2) to equation (3.1) by using a second-order finite volume algorithm and reformulating the resulted terms of the Navier Stokes equations, they will produce equation (3.3):

$$\partial_t(\bar{V}) + \nabla \cdot (\bar{V} \otimes \bar{V}) = -\nabla \bar{p} + \nabla \cdot \bar{S} - \nabla \cdot B + m^v + \tau \quad (3.3)$$

where

$$B = \overline{V \otimes V} - \bar{V} \otimes \bar{V},$$

$$m^v = [G *, \nabla](V \otimes V + pI - S),$$

$$\tau = \nabla \cdot \left[\left[\frac{1}{6} \nu \nabla^3 V - \frac{1}{8} \nabla^2 V \right] (d \otimes d) + \dots \right]$$

and

- B ... SGS stress tensor,
- m^v ... commutation error term,
- τ ... total (convective, temporal and viscous) truncation error,
- I ... unit tensor,
- d ... topological vector connecting neighbouring control volumes
(see Figure (3.3)),

m^v is often merged with the SGS force $\nabla \cdot B$, prior to modelling, and resulted from a generalized SGS stress tensor B which has to be prescribed in terms of discretized filtered fields for the closure of the new equations which constituted above.

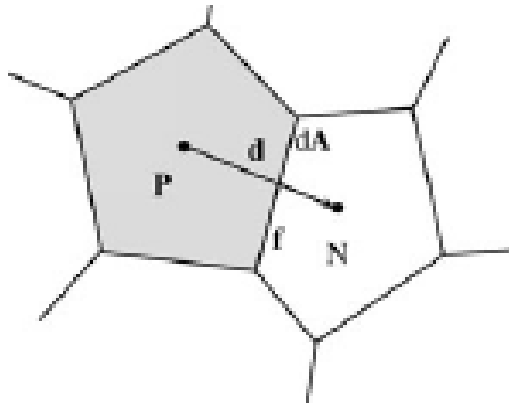


Figure (3.3) Grid schematic. P and N denote typical computational cell centres and f an interface; and A cell face area; d is the topological vector connecting neighbouring cells.

3.2.2 Monotonically Integrated large eddy simulation MILES

MILES approach has been analysed theoretically in many studies, for example, Fureby et al., 1997, Fureby and Grinstein, 1999 and Grinstein and Fureby, 2002, in the framework of flux-limiting finite volume discretization. These studies have produced a relationship between the leading numerical error terms and tensorial sub-grid viscosities in the form of implicit SGS models. In which, the implicit SGS models are created by controlling the leading truncation error. This process is limited to high-resolution methods for the convection flux to be able to keep second-order accuracy in the flow smooth regions. Also, the leading truncation error has to vanish at $d \rightarrow 0$ (where d is the mesh size) so, it remains consistent with the Navier Stokes equations and the conventional LES model (Grinstein and Fureby, 2006). In the current work, the incompressible Navier stokes equations are modified in the developed CFD solver based on the work of Grinstein and Fureby (2005), as shown in equations (3.4), (3.5), and (3.6) in which the turbulent viscosity (v_t) is set to zero:

Continuity equation:

$$\nabla \cdot V = 0 \quad (3.4)$$

Momentum equation:

$$\begin{aligned} \partial_t(V) + \nabla \cdot (V \otimes V) \\ = -\nabla p + \nabla \cdot S \\ + \nabla \cdot \left[C(\nabla V)^T + (\nabla V)C^T \right. \\ + \chi^2(\nabla V)d \otimes (\nabla V)d \\ \left. + \left[\frac{1}{6}v\nabla^3 V - \frac{1}{8}\nabla^2 V \right] (d \otimes d) \right] \end{aligned} \quad (3.5)$$

where

$$\begin{aligned} C &= \chi(V \otimes d), \\ \chi &= (1/2)(1 - \Gamma)(\beta^- - \beta^+), \\ \beta^\pm &= \frac{(1/2)(v_f \cdot dA \pm |v_f \cdot dA|)}{|v_f \cdot dA|} \end{aligned} \quad (3.6)$$

From equation (3.5) and (3.6), v_f is the flux function and Γ is the flux limiter. Equation (3.7) shows the value of the leading truncation error term if equation (3.5) is compared with the unsteady N.S.E.

$$\nabla \cdot \left[C(\nabla V)^T + (\nabla V)C^T + \chi^2(\nabla V)d \otimes (\nabla V)d + \left[\frac{1}{6}v\nabla^3 V - \frac{1}{8}\nabla^2 V \right] (d \otimes d) \right] \quad (3.7)$$

It can be noticed that in smooth regions, where $\Gamma = 1$, this led to $\chi = 0$ and $C = 0$, and then the leading truncation error becomes as in equation (3.8):

$$\tau = \left[\left[\frac{1}{6}v\nabla^3 V - \frac{1}{8}\nabla^2 V \right] (d \otimes d) \right] \quad (3.8)$$

Comparing the momentum equation in MILES, equation (3.5), approach with that one from the classical LES approach, equation (3.3), it is found that MILES adds additional dissipative and dispersive terms, which define the implicit SGS stress term as in equation (3.9).

$$B = C(\nabla V)^T + (\nabla V)C^T + \chi^2(\nabla V)d \otimes (\nabla V)d \quad (3.9)$$

The implicit SGS tensor can be divided, according to equation (3.9), into two parts, the first is $B(1) = C(\nabla V)^T + (\nabla V)C^T$ which expresses a tensor valued eddy-viscosity model, while the second is $B(2) = \chi^2(\nabla V)d \otimes (\nabla V)d$ which has a form similar to the scale similarity model. On the other side, this division of equation (3.9) can be interpreted as breaking B into its slow and rapid varying parts according to the time scale of its response to variations in the mean flow (Shao et al., 1999). In MILES approach, the rapid part that cannot be captured by the isotropic models relates to $B(2)$, while the slow part relates to $B(1)$ (Grinstein and Fureby, 2005). Borue and Orszag (1998) have shown improvement between the exact and the modelled SGS stress tensor because of the use of $B(2)$ term. A further review by Margolin and Rider (2002) showed that the effectiveness of ILES formulation depends upon local monotonicity (or sign) preservation concepts; they explained that the value of the leading order truncation error produced by NFV algorithms supplies a physical flow regularization term which provides the required modifications to the governing equations that arise when the flow motion is observed over finite intervals of time.

It can be concluded that the behaviour of the implicit SGS model is significantly dependent on the value of the flux limiter Γ . Also, Γ controls the percentage of the choice between the high and low order schemes and other properties such as the monotonicity and griding. Therefore, a study about the flux limiter types and their accuracy relative to its usage with the MILES is investigated in the next section.

3.3 Flux Limiters

The study of Godunov's, order barrier theorem, proved that linear methods are not able to provide non-oscillatory solutions higher than first order (Van Leer, 1974). They lead to discontinuous solutions at a finite time even when the initial conditions are smooth (Zeng, 2016). This limitation has encouraged most of the researchers to develop new techniques to overcome this limitation, especially those techniques which are able to avoid the spurious or non-physical oscillations at which the sharp velocity gradients exist. These non-physical oscillations during the solution have a big effect on the solution accuracy, to measure these oscillations in a solution, the Total Variation (TV) of the discrete representation of V has to be defined as in equation (3.10) (Gottlieb and Shu, 1998):

$$TV(V) = \sum_{i=1}^N |V_i - V_{i-1}| \quad (3.10)$$

where $i = 1$ and $i = N$ are the left and right boundaries of the numerical domain grid respectively. For a monotonically increasing function V , the $TV(V)$ is equal to $|V_1 - V_N|$. The function maintains its monotonicity as long as V_1 and V_N are constants which means that $TV(V)$ is considered as a constant. However, if the values of V_i develop and vary between the minimum and maximum values, this leads to increasing the TV . The increase in TV is considered as a measure of the development of oscillation in any solution (Gottlieb and Shu, 1998). A numerical scheme is called Total Variation Diminishing (TVD) if and only if the equation (3.11) is applied:

$$TV(V_i) \leq TV(V_{i-1}) \quad (3.11)$$

Such a scheme is able to avoid any oscillation development near a jump; a jump is characterized as a monotonically in/decreasing function. So, from equation (3.11) TVD scheme will not increase the TV and hence keeping TV as a constant and this is

a required property for stable numerical schemes. While in the case of starting with values that have minimum and maximum TV , then the local maximum and minimum will be gradually smoothed out by the TVD schemes. It was found that at first-order accuracy schemes, most of the interpolation schemes methods are able to satisfy the positive property, while they are not able to satisfy it at second-order accuracy. Therefore, first-order upwind is considered as one of those methods to have the merit of keeping the solution monotonically varying in regions where the solution has to be monotone, even though the accuracy is not very good. While second-order accuracy methods give much better accuracy on smooth solutions than the first-order upwind method but fail near discontinuities, where oscillations may appear due to their dispersive nature (Grinstein and Fureby, 2005). Hence, searching for a method to combine both first and second-order accuracy led to the use of the flux limiter. The idea of the flux limiter is to combine the best features of both methods. Flux limiter's values are computed by evaluating a limiter function with a smoothness monitor as an input, which measures the local solution regularity (Zeng, 2016).

At this point, it is better to take a look at the time-averaged flux through a cell interface, equation (3.12). For the arbitrary sign of (u) , the time-averaged flux through a cell interface becomes:

$$f_{i-1/2}^{n+1/2} = \begin{cases} uV_{i-1}^n + \frac{1}{2}u_{i-1/2}\sigma_{i-1}^n(\Delta x - u_{i-1/2}\Delta t) & \text{if } u_{i-1/2} \geq 0 \\ uV_i^n - \frac{1}{2}u_{i-1/2}\sigma_i^n(\Delta x + u_{i-1/2}\Delta t) & \text{if } u_{i-1/2} \leq 0 \end{cases} \quad (3.12)$$

where n denotes the time step, velocity u , in this formulation, is defined at the cell interfaces, σ_i^n is the slop limiter, varies according to different types of flux limiter, while the value of V is always defined at the cell centre (LeVeque, 2002). A flip-flop function is introduced; as in equation (3.13):

$$\varepsilon_{i-1/2} \equiv \varepsilon(u_{i-1/2}) = \begin{cases} +1 & \text{for } u_{i-1/2} \geq 0 \\ -1 & \text{for } u_{i-1/2} \leq 0 \end{cases} \quad (3.13)$$

Then equation (3.12) can be written as in equation (3.14):

$$\begin{aligned} f_{i-1/2}^{n+1/2} = & \frac{1}{2}u_{i-1/2}[(1 + \varepsilon_{i-1/2})V_{i-1}^n + (1 + \varepsilon_{i-1/2})V_i^n] \\ & + \frac{1}{4}|u_{i-1/2}|\left(1 - \left|\frac{u_{i-1/2}\Delta t}{\Delta x}\right|\right)\Delta x[(1 + \varepsilon_{i-1/2})\sigma_{i-1}^n \\ & + (1 - \varepsilon_{i-1/2})\sigma_i^n] \end{aligned} \quad (3.14)$$

The form in equation (3.14) is identical with equation (3.12). it is just written by using the flip-flop function $\varepsilon_{i-1/2}$ which has a value of (+1) with positive advection velocity and (-1) for negative advection velocity. This form is suitable for all types of grids, regular and non-regular (LeVeque, 2002). It is the form required for the main goal of the research in which the grid size will vary through the channel streamwise and normal to the wall directions.

Now, it is possible to enhance equation (3.14) by replacing the flux limiter, as in equation (3.15):

$$\begin{aligned} \frac{1}{2}\Delta x[(1 + \varepsilon_{i-1/2})\sigma_{i-1}^n + (1 - \varepsilon_{i-1/2})\sigma_i^n] \\ \rightarrow \Gamma(r_{i-1/2}^n)(V_i^n - V_{i-1}^n) \end{aligned} \quad (3.15)$$

where $\Gamma(r_{i-1/2}^n)$ is the flux limiter and $r_{i-1/2}^n$ is the ratio of consecutive gradients and is defined as in equation (3.16) (LeVeque, 2002):

$$r_{i-1/2}^n = \begin{cases} \frac{(V_{i-1}^n - V_{i-2}^n)}{(V_i^n - V_{i-1}^n)} & \text{for } u_{i-1/2} \geq 0 \\ \frac{(V_{i+1}^n - V_i^n)}{(V_i^n - V_{i-1}^n)} & \text{for } u_{i-1/2} \leq 0 \end{cases} \quad (3.16)$$

Equation (3.17) produces equation (3.14) after the modification as a function of the flux limiter $\Gamma(r_{i-1/2}^n)$ (LeVeque, 2002):

$$\begin{aligned} f_{i-1/2}^{n+1/2} = \frac{1}{2}u_{i-1/2}[(1 + \varepsilon_{i-1/2})V_{i-1}^n + (1 - \varepsilon_{i-1/2})V_i^n] \\ + \frac{1}{2}|u_{i-1/2}|\left(1 - \left|\frac{u_{i-1/2}\Delta t}{\Delta x}\right|\right) \Gamma(r_{i-1/2}^n)(V_i^n - V_{i-1}^n) \end{aligned} \quad (3.17)$$

It can be seen that this expression of the flux is still the donor-cell flux (first line) plus some correction term (second line). To determine the regions of first and second-order accurate TVD numerical scheme according to the value of the flux limiter, equation (3.18) is used and is drawn in Figure (3.4). (clearly, none of the following linear limiters generates a TVD scheme)

$$\begin{aligned}
\text{Donor-cell:} \quad & \Gamma(r) = 0 \\
\text{Lax-Wendroff:} \quad & \Gamma(r) = 1 \\
\text{Beab-Warming:} \quad & \Gamma(r) = r \\
\text{Fromm:} \quad & \Gamma(r) = \frac{1}{2}(1 + r)
\end{aligned} \tag{3.18}$$

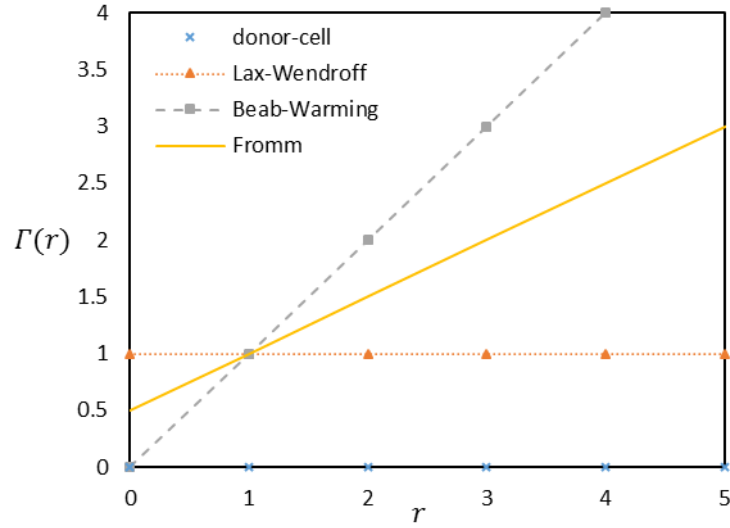


Figure (3.4) Applied TVD regions for the first and second-order accuracy schemes.

To guarantee the second-order accuracy in the smooth regions and avoid excessive compression of solutions, Sweby suggested the following reduced portion, in Figure (3.5), concluded from Figure (3.4) for the TVD region as a suitable range for the flux limiting functions (Sweby, 2007). All the flux limiters used in this research exist in the mentioned TVD region:

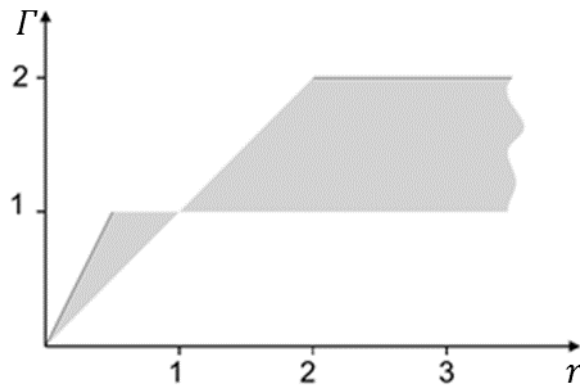


Figure (3.5) TVD regions for the TVD schemes.

Generally and to simplify the previous equations, a flux-limiter method can be obtained by combining any low-order flux formula $F_f^L(\bar{v})$, which well-behaves near the sharp gradients, (such as the upwind flux) and any higher-order formula $F_f^H(v)$, which acts well in the smooth flow regions (such as the Lax-Wendroff). It can be expressed as in equation (3.19) to obtain a total flux-limiter effect (Sagaut, 2006):

$$F_f^C(\bar{u}) = F_f^H(\bar{v}) - (1 - \Gamma)[F_f^H(\bar{v}) - F_f^L(\bar{v})] \quad (3.19)$$

If $\Gamma = 0$, then this reduces to the low-order method, while when $\Gamma = 1$, it produces the higher-order one. Hence, equation (3.20) produces the total flux-function for the velocity (V_f) as:

$$V_f = V_f^H - (1 - \Gamma(r))(V_f^H - V_f^L) \quad (3.20)$$

Choosing the suitable flux limiting scheme gives the appropriate interpolation between the selections of V_f^H and V_f^L and allows the possible correction to $(V_f^H - V_f^L)$ in the governing equation without increasing the variation of the solution (i.e. to comply with the physical principles of causality, monotonicity and positivity, and thus to preserve the properties of the Navier Stokes Equations (N.S.Es) (Grinstein and Fureby, 2005)). The flux limiter Γ has the main effect on the properties of the implicit SGS model such as the monotonicity and grid spacing. Also, methods implemented using flux limiters, which are used in order to suppress spurious oscillations, perform much better than other methods without flux limiters. Therefore, flux limiters play a major role in turbulence structure capturing in any CFD code.

As a brief, flux limiter role at any region in the flow can be produced as follow:

1. When working on a solution for the smooth parts, the flux limiter will act as a second-order accurate flux-conserved advection.
2. When working on regions near a jump or very sharp and sudden velocity gradient, the flux limiter will be switched to a first-order donor-cell (i.e. upwind) flux-conserved advection.

Using flux limiters along with an appropriate high-resolution scheme makes the solutions TVD. The main advantage of the TVD schemes is that it ensures capturing of discontinuities or the sharp change in the velocity gradients in the solution. Therefore, a second-order centred scheme is used as it is very simple and produces fast computational speed, but it may smoothen the sharp velocity gradients over many

computational cells, so the first-order upwind scheme is blended to it in the TVD scheme. Second-order TVD limiter must satisfy the following criteria in equation (3.21) (Grinstein and Fureby, 2005):

$$\begin{aligned}
 r \leq \Gamma(r) \leq 2r, (0 \leq r \leq 1), \\
 1 \leq \Gamma(r) \leq r, (1 \leq r \leq 2), \\
 1 \leq \Gamma(r) \leq 2, (r > 2), \\
 \Gamma(r) = 1
 \end{aligned}
 \tag{3.21}$$

Well-known TVD flux-limiters are used in the current research. MATLAB code is used to show the performance of those flux limiters relative to general instability function within 100 mesh cells and a time of 40 seconds:

1. VanLeer flux-limiter, (Van Leer, 1974), shown in equation (3.22):

$$\Gamma(r) = \frac{r + |r|}{1 + |r|}
 \tag{3.22}$$

VanLeer limiter charts a careful compromise path through the Sweby TVD region. Its behaviour deviates slightly at the peak of the wave as compared with a general instability function in Figure (3.6).

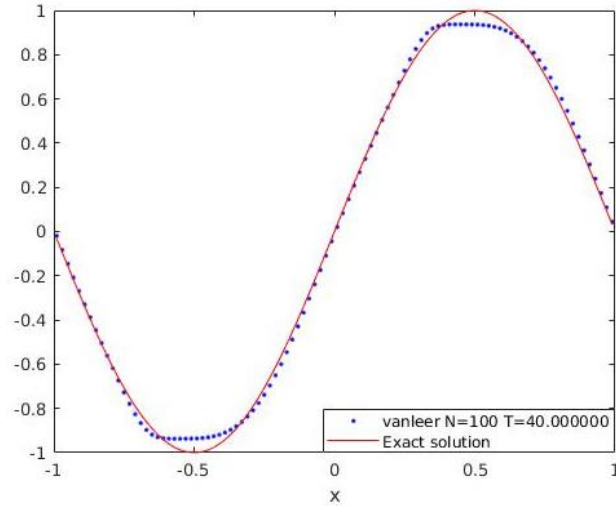


Figure (3.6) Square initial condition: numerical solutions for VanLeer flux limiter at $t = 40$ with 100 mesh-cells.

2. SuperBee flux-limiter, (Roe, 1986), shown in equation (3.23):

$$\Gamma(r) = \max\left(0, \max(\min(2r, 1), \min(r, 2))\right) \quad (3.23)$$

SuperBee limiter tries to apply the minimum limiting and maximum steepening allowable to maintain as a TVD scheme. This limiter is known to suffer from the excessive sharpening of slopes as a result. Notice the flattening of the peaks and the steepening of the slopes as shown in Figure (3.7).

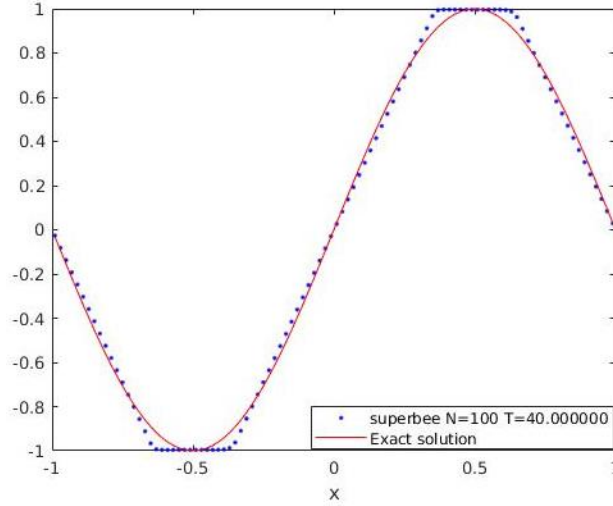


Figure (3.7) Square initial condition: numerical solutions for superBee flux limiter at $t = 40$ with 100 mesh-cells.

3. VanAlbada flux-limiter, (Grinstein and Fureby, 2005), is presented in equation (3.24). Its behaviour has the same effect as VanLeer limiter as shown in Figure (3.8):

$$\Gamma(r) = \frac{r + r^2}{1 + r^2} \quad (3.24)$$

4. Gamma flux-limiter, (Grinstein and Fureby, 2005), shown in equation (3.25):

$$\Gamma(r) = \frac{1-k}{k} r \left[H(r) - H\left(r - \frac{k}{1-k}\right) \right] + H\left(r - \frac{k}{1-k}\right) \quad (3.25)$$

where k is a parameter of the scheme such that $k \in [0, 1]$, and H is the Heaviside step function (unit step function). Note that when $k = 0.5$, this scheme becomes TVD

which is used in the current study. Each limiter has its switching characteristics, these characteristics differ according to the type of the problem and the solution scheme. No specific limiter has been found to work well for all problems, and a separate choice is usually made on a trial and error basis. Therefore, the next subsection will evaluate the second-order TVD flux-limiter schemes in capturing turbulence structures through a fully developed channel flow. Figure (3.9) shows the behaviour of each flux limiter and proves their existence in the TVD region mentioned before.

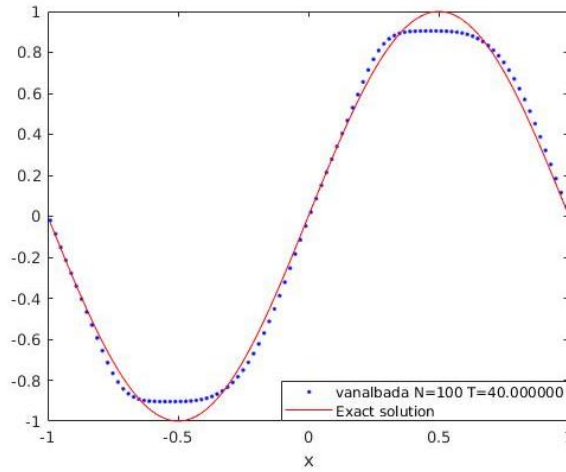


Figure (3.8) Square initial condition: numerical solutions for VanAlbada flux limiter at $t = 40$ with 100 mesh-cells.

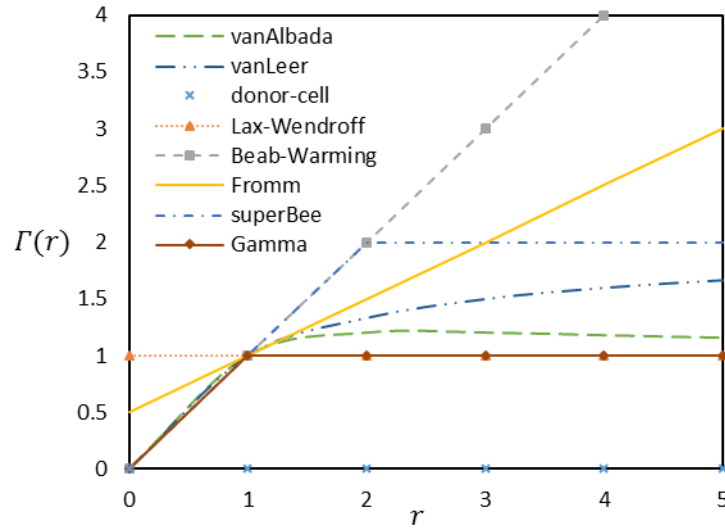


Figure (3.9) TVD regions for the first and second-order accurate TVD schemes together for the selected limiters.

The numerical predictions for the mentioned flux limiters are presented in the ‘results’ sections. Turbulent statistical quantities obtained using different flux limiters

are compared with the available previous DNS data (Kim et al., 1987) and (Abe et al., 2001). The open-source CFD software OpenFOAM libraries are used in the present study to develop the MILES solver. This solver will be combined with the synthesized turbulence boundary condition in Chapter (4) to study the transition control.

3.4 MILES Solver Validation

The primary objective of this part of the work is to assess the prediction of each flux limiter mentioned above for capturing the turbulent structures in a fully developed channel flow. Flux limiters, namely Gamma, superBee, VanLeer, and VanAlbada are compared in terms of the predicted turbulence statistics of fully developed steady-state channel flow at a friction Reynolds number $Re_\tau = 180 - 395$ (Kim et al., 1987; Abe et al., 2001). N.S.E of incompressible flow is solved by using this particular class of flux-limiting schemes and their associated built-in (or implicit) SGS models. MILES solver is developed by using OpenFOAM libraries in which the Crank-Nicholson scheme is used for time discretization of all equations with a factor of 0.6. A mesh independence study is investigated to ensure the effect of mesh density on the behaviour of the MILES solver. Also, the effect of increasing the friction Reynolds number is studied.

3.4.1 Mesh independence study

In MILES, the smallest mesh size is considered as the cut-off filter size like in the conventional LES because of no explicit SGS model is used to specify the required filter size, therefore, mesh refinement has a significant effect on the performance of MILES solver. An investigation for the computational cost of MILES solver should be taken into consideration compared with the previous DNS studies to be able to evaluate the dependence of the results on the mesh resolution. Therefore, to gain confidence in the MILES solver results, a mesh refinement study is performed for capturing the turbulence structures using superBee as a flux limiter. Mesh refinement near to the wall is expressed in wall units. This gives an indication of the number of points near the wall used to discretize the smallest structure of the flow. The grid distribution is uniform in the streamwise and spanwise directions, while a refinement for the grid in the wall-normal direction at both walls is pre-calculated to get the required mesh-size at the walls.

Table (3.1) summarizes the mean flow properties computed from the three MILES runs relative to the reference DNS data of (Abe et al., 2001) at $Re_\tau = 395$. The computational box for this section, shown in Figure (3.10), has the dimensions of $(L_x, L_y, L_z) = (4\pi\delta*2\delta*2\pi\delta)$ which is chosen to match that one from (Kim et al., 1987). The coarse mesh in case A uses $(100 \times 80 \times 80)$ cells in the streamwise, wall-normal and spanwise directions, respectively, whereas mesh of case B uses $(192 \times 139 \times 160)$ cells and the mesh of case C uses $(220 \times 180 \times 180)$. All values in Table (3.1) are normalized using the friction velocity, u_τ , and the half channel height, δ .

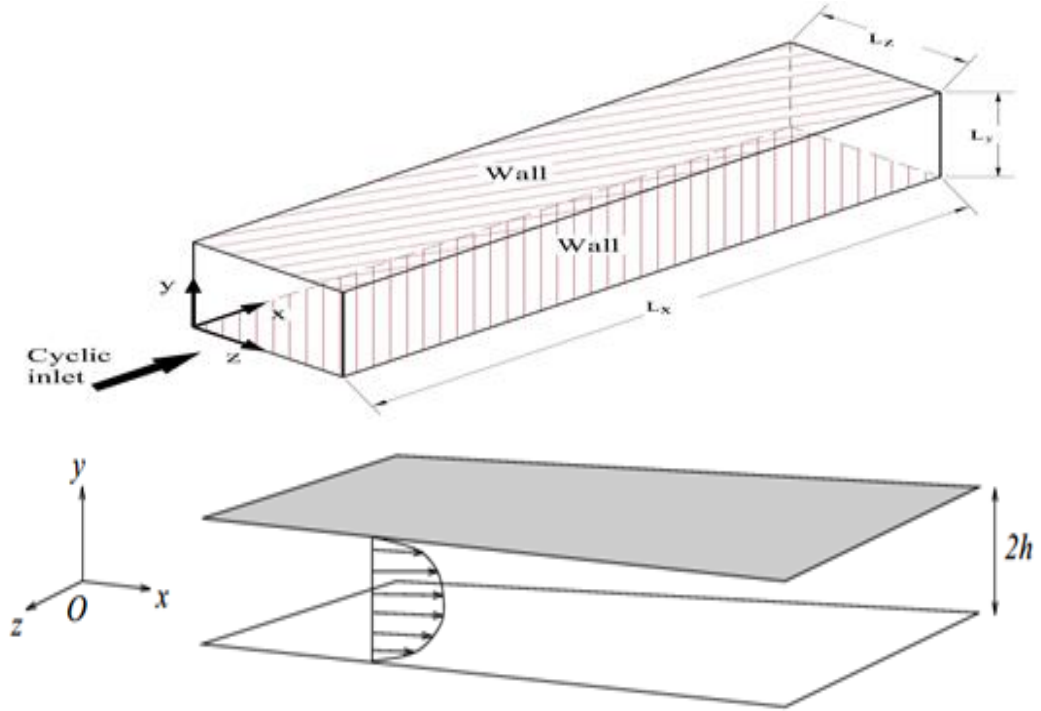
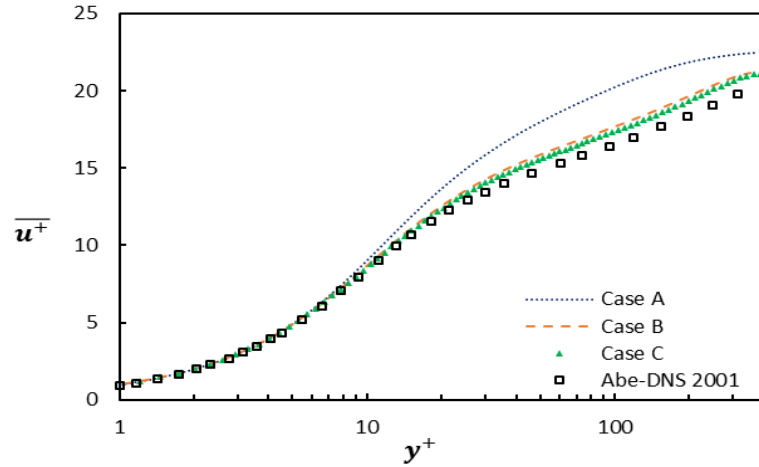


Figure (3.10) Computational domain dimensions of the fully developed channel.

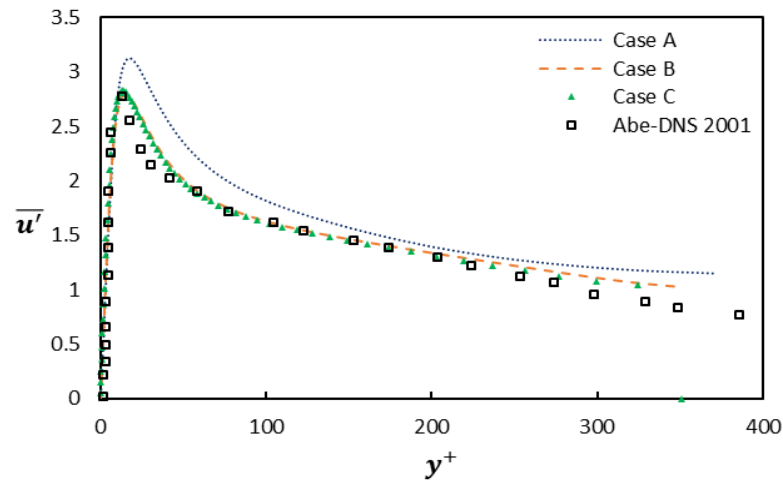
Table (3.1) Mean flow properties obtained from MILES computations for mesh density investigation.

Case	Total number of cells	Δx^+	Δy_{min}^+	Δz^+	Re_τ $= \frac{(u_\tau * \delta)}{\nu}$	Re_m $= \frac{(U_m * 2\delta)}{\nu}$
A	6.4×10^5	24	0.434	16	396	16130
B	4.27×10^6	16	0.25	8	395	14600
C	7.128×10^6	11	0.2	7	397	14500
DNS	12.582×10^6	9.88	0.2	4.94	395	13981

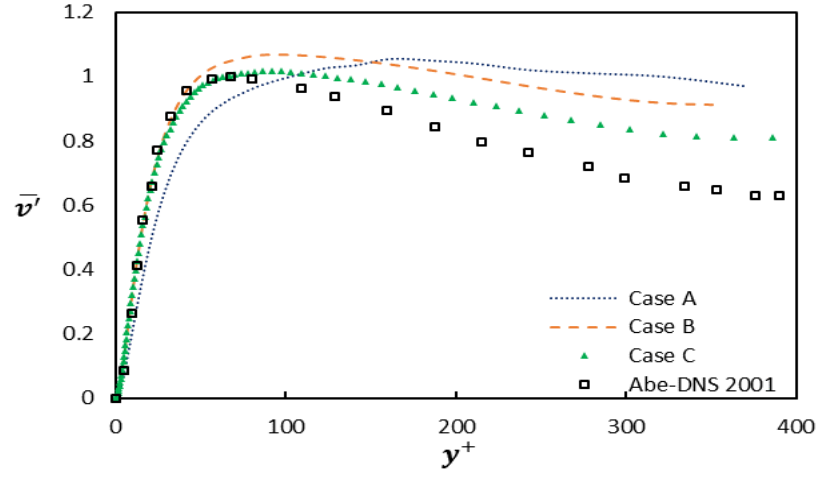
Figure (3.11) produces the turbulence structures of a fully developed channel flow after reaching the turbulence steady-state and averaging the results in time and space. All meshes show close behaviour to the DNS results. Figure (3.11)-(a) shows the mean velocity profile near the wall, it can be seen that the coarse mesh, case A, has a thicker logarithmic region and this is due to the high bulk velocity which is used to get the required friction Reynolds number, $Re_\tau = 395$. While for case B and C the difference is not too big, and their behaviour is nearly identical, also, Re_m produces good agreement with the previous DNS study in the range of 13%. While, Figure (3.11)- (b, c, and d) produce the streamwise, wall-normal and spanwise fluctuations respectively. As shown, case B gives the appropriate performance and very close to that one of the DNS results at reasonable computation cost although there is a small deviation in the wall-normal and spanwise fluctuations.



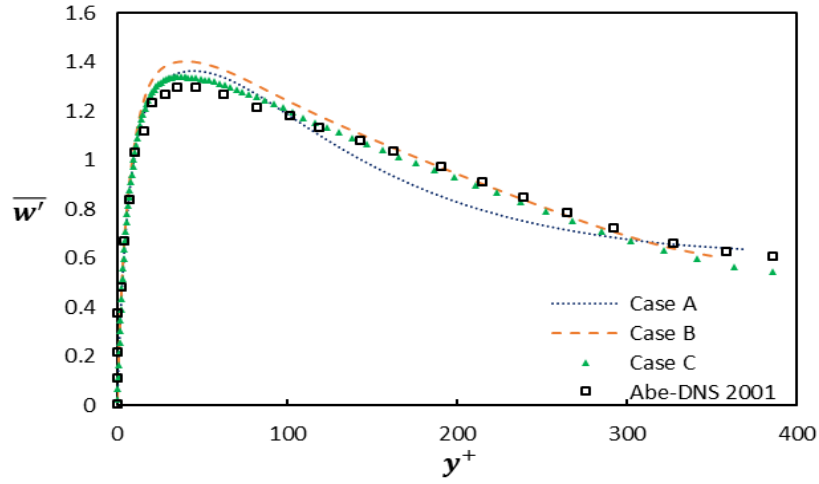
(a)



(b)



(c)



(d)

Figure (3.11) Grid-refinement study for MILES performance; (a) mean velocity profile, (b) streamwise fluctuation, (c) normal to the wall fluctuations, (d) spanwise fluctuations.

Finally, it is obvious that case C is the most accurate mesh compared with DNS results but with high computation cost and much time to run. Therefore, the mesh of case B is chosen to investigate the performance of the MILES solver in the following sections

3.4.2 Fully developed channel with $Re_\tau = 180$

3.4.2.1 Computational domain

The computational domain considered here has dimensions of $4\pi\delta$ and $2\pi\delta$ in streamwise and spanwise direction respectively, with channel height of 2δ in wall-normal direction, all of them are normalized by the channel half-height, δ . Periodic

boundary conditions are applied in both streamwise and spanwise directions, while the top and bottom walls of the channel are applied as a no-slip boundary condition, as shown in Figure (3.10). The mesh distribution applied is uniform spacing in the streamwise and spanwise directions, while in wall-normal direction, an expanding mesh towards the channel centre is used such that the first mesh point next to the wall boundary is with wall units $y^+ = 0.05$, with this computational domain, the grid spacing in the streamwise and spanwise directions are respectively $\Delta x^+ = 12$ and $\Delta z^+ = 7$ in wall units. Flow bulk velocity, U_b , is adjusted during the runtime to maintain a friction Reynolds number value of $Re_\tau = 180$. The friction Reynolds number ' Re_τ ' is evaluated with the characteristic length scale and velocity scales as half channel height, δ , and wall shear velocity, $u_\tau = \sqrt{\tau_w/\rho}$, respectively.

3.4.2.2 Results

The performance of MILES solver as a function of flux limiter is discussed in the current section. The study of a fully developed turbulent channel flow at a friction velocity based on $Re_\tau = 180$ is compared with the DNS results of Kim et al. (1987) and Abe et al. (2001). Also, for this Reynolds number, the $(-5/3)$ slope for the energy spectrum is drawn in the one-dimensional power spectrum for the all mentioned flux limiters, as shown in Figure (3.12).

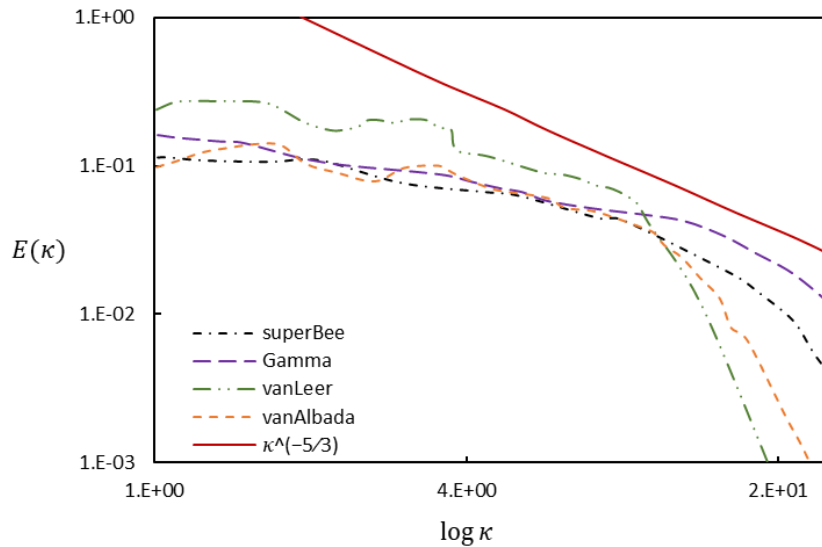


Figure (3.12) Spectrum of the total resolved turbulent energy of different used flux limiters at $Re_\tau = 180$.

The statistical steady state of a fully developed channel flow is identified by a linear profile of the total shear stress, $-\overline{u'v'} + (1/Re_\tau)(\partial\bar{u}/\partial y)$, where $\overline{u'v'}$ is the

Reynolds stress and $(1/Re_\tau)(\partial\bar{u}/\partial y)$ expresses the wall shear stress, as shown in the plots for different cases in Figure (3.13) to Figure (3.15). Once the flow through the channel reaches the statistically steady state, the values are averaged in time to obtain a running time average and in space to obtain the spatial average of the various statistical correlations. The behaviour of the total shear stress appears in Figure (3.13) to be a straight line which goes from the highest shear at the wall, where the viscous force is dominant, to the lowest value at the centre of the channel, where the inertia force is larger.

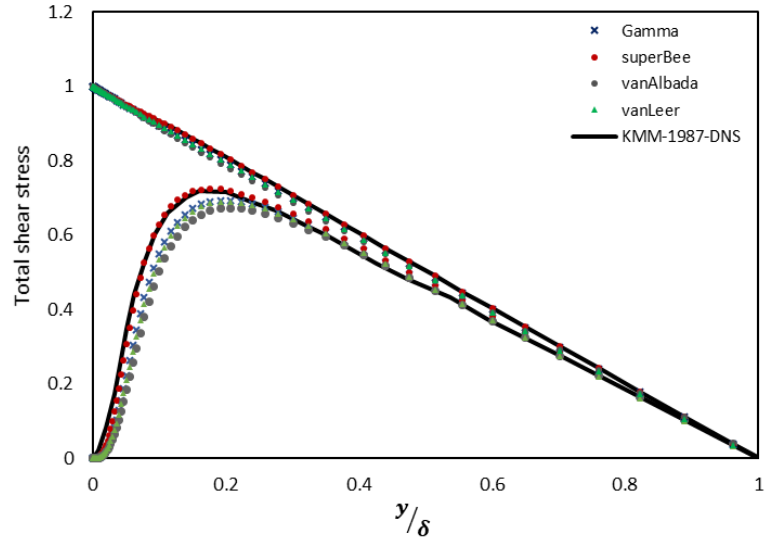
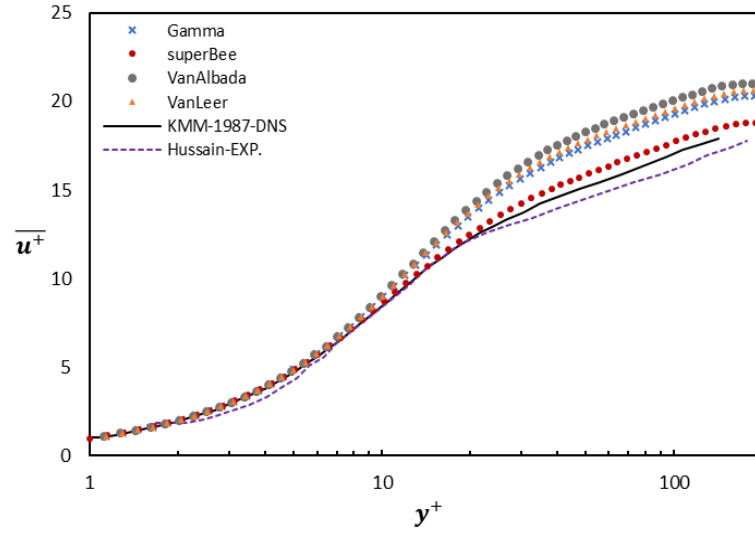


Figure (3.13) Total shear stress behaviour through the fully developed channel.

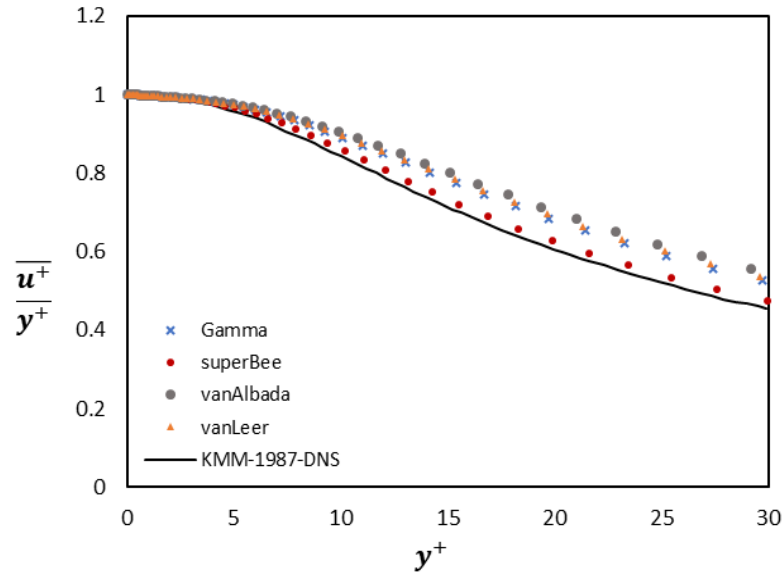
The mean velocity distribution is compared with the experiment from Hussain and Reynolds (1975) and the DNS results of fully developed turbulent channel flow from Kim et al. (1987) and Lee and Moser (2015) in Figure (3.14). Table (3.2) produces the mean flow properties obtained from MILES computations at $Re_\tau = 180$ compared with the reference DNS study of Kim et al. (1987). SuperBee flux limiter simulation results show good agreement with the DNS results for the same $Re_\tau = 180$ till wall units $y^+ = 35$. While, it has a slight deviation in the logarithmic region from the experimental result (Hussain and Reynolds, 1975), as shown in Figure (3.14)-(a), this may be due to the characteristic difference between the channel flows and the turbulent boundary layer flows. Also, this difference was observed by Abe et al. (2001) in their DNS study when they compared their results with the same experimental results. Gamma, VanAlbada and VanLeer limiters produce over-

prediction in the velocity profiles in the outer region of the boundary layer while they have the same performance in the inner region.

The near-wall behaviour of the mean velocity profile for all cases are drawn in Figure (3.14)-(b), all limiters predict the same behaviour in the sub-viscous region while Gamma, VanAlbada, and VanLeer flux limiters start to deviate around $y^+ = 8$ with increase in the values of the velocity as it goes towards the channel centre.



(a)



(b)

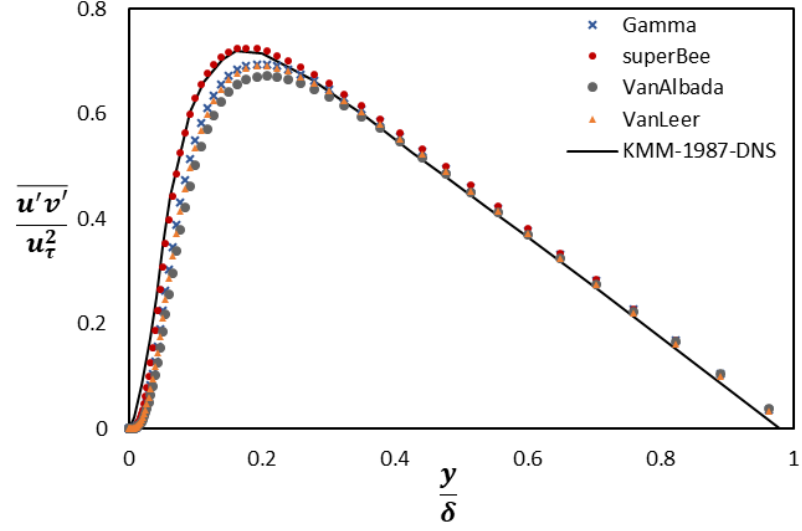
Figure (3.14) (a) mean velocity profiles; (b) near-wall behaviour of the mean velocity.

Table (3.2) Mean flow properties obtained from MILES computations of the periodic channel flow at $Re_\tau = 180$ and reference DNS of Kim et al. (1987).

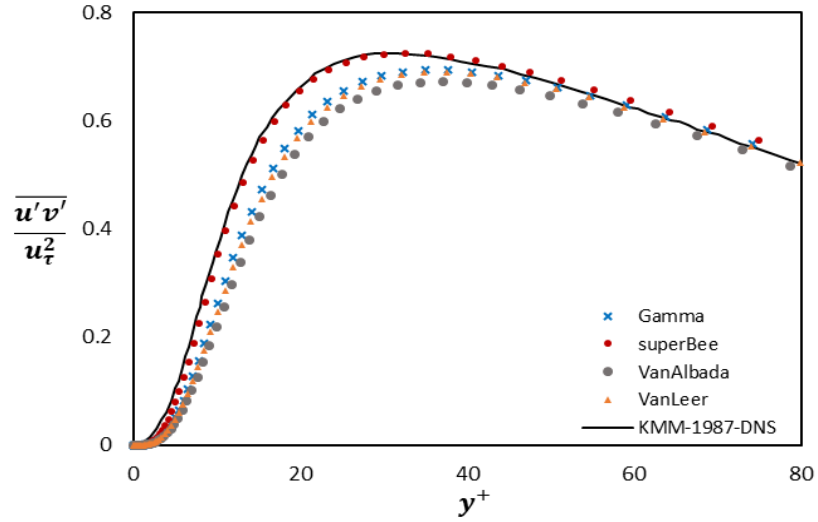
Flux limiter	U_m	U_c	$\frac{U_c}{U_m}$	$\frac{U_c}{U_m} = f(Re_m)$	$Re_\tau = \frac{(u_\tau * \delta)}{\nu}$	$Re_m = \frac{(U_m * 2\delta)}{\nu}$
Gamma	16.8	20.6	1.15	1.156	182	6400
superBee	15.8	19	1.175	1.17	183	5876
VanAlbada	18	21.1	1.157	1.156	179	6520
VanLeer	17.1	20.6	1.152	1.156	181	6480
DNS	15.72	18.38	1.17	1.157	180	5662

The behaviour of the Reynolds stresses is presented in Figure (3.15)-(a). It is clear that superBee flux limiter predictions are identical with those of (Kim et al., 1987). The predictions of Gamma, VanAlbada and VanLeer flux limiters are nearly identical with under-estimations for the values before $y^+ = 60$. The Reynolds stresses reach their peak value at $y^+ = 32$ for the DNS and superBee while at $y^+ = 37$ for VanLeer and VanAlbada with a percentage of 5% between both peak values and $y^+ = 34$ for Gamma with a percentage of 4%. The difference significantly appears in Figure (3.15)-(b) with the wall coordinates where superBee limiter reproduces values comparable with the DNS results. Also, as a comparison between the current results and the previous relevant studies, Dean (1978) produced a correlation for the relation between the mean centreline velocity to the mean bulk velocity as in equation (3.26). The present results also produce a good agreement with this correlation. U_c and U_m are normalized with the friction velocity u_τ .

$$\frac{U_c}{U_m} = 1.28Re_m^{-0.0116} = 1.16 \quad (3.26)$$



(a)

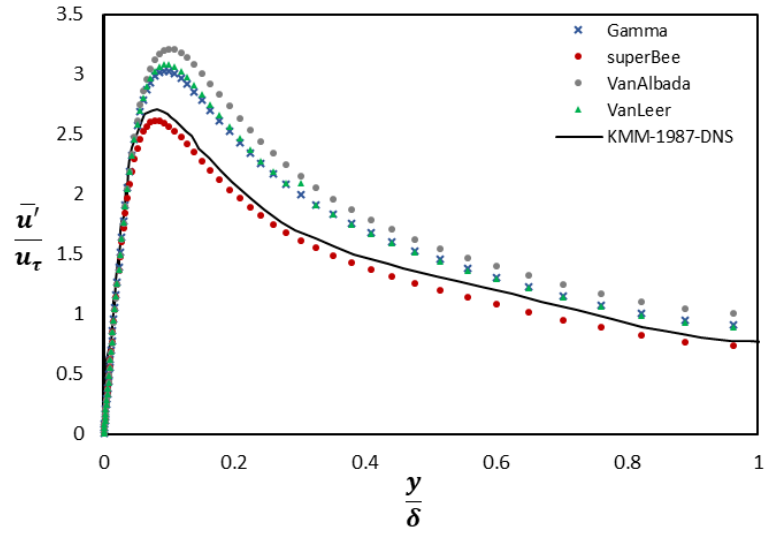


(b)

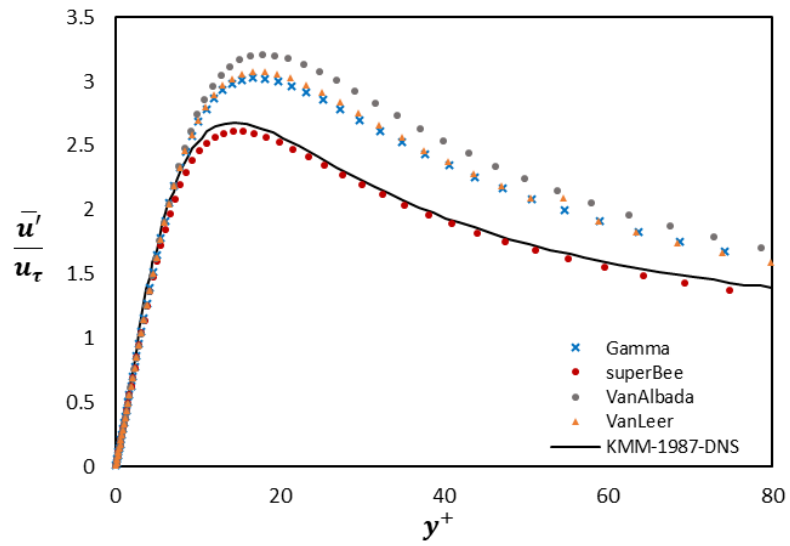
Figure (3.15) Reynolds shear stress for fully developed channel normalized by the wall shear velocity: (a) in global coordinates (b) in-wall coordinates.

Root mean square (RMS) velocities of the fluctuations, normalized by the wall shear velocity, u_τ , from each case, are compared with those of the DNS study. In Figure (3.16)-(a), the streamwise RMS velocity fluctuations of superBee limiter show very close matching with the results from the DNS. On the other hand, overestimated values are predicted by Gamma, VanLeer and VanAlbada limiters even in the near-wall region with ratios of 11%, 12%, and 16%, respectively (as a ratio of the DNS maximum value to their values) at $y^+ = 17$. Also, there is a shift in the position of the maximum value of each limiter, as shown in Figure (3.16)-(b), in-wall coordinates. This shift means enlarging of the sub-viscous layer with about $\Delta y^+ = 5$ in wall units.

Also, it can be noticed from Figure (3.16) that the behaviour of Gamma and VanLeer are always identical.

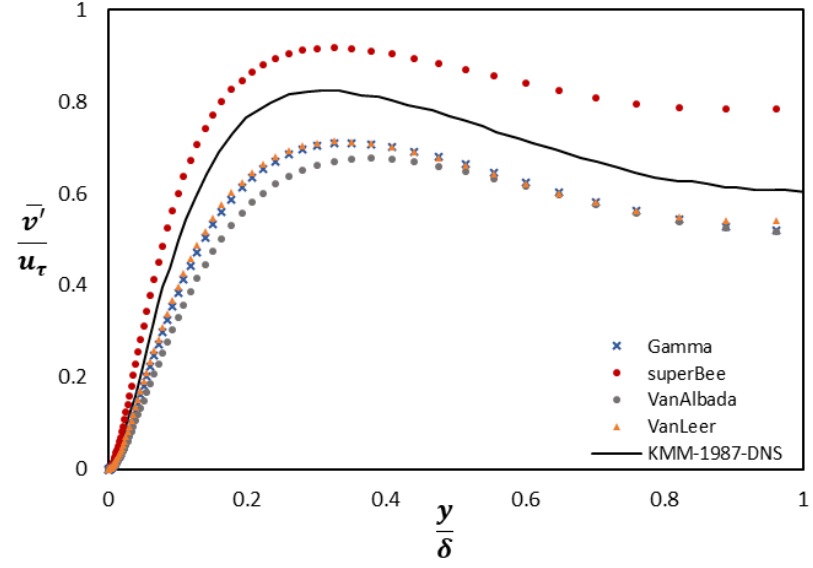


(a)

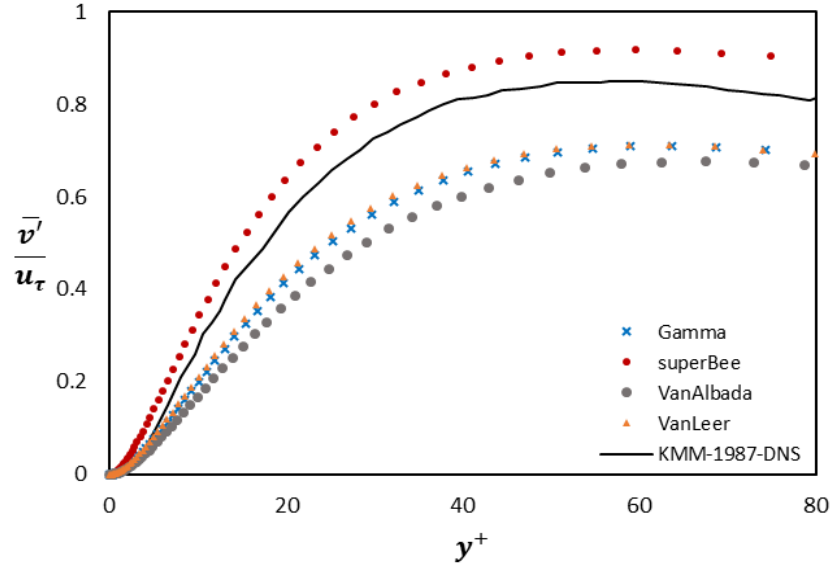


(b)

Figure (3.16) RMS velocity fluctuations in streamwise dir. normalized by the wall shear velocity: (a) in global coordinates; (b) in-wall coordinate.



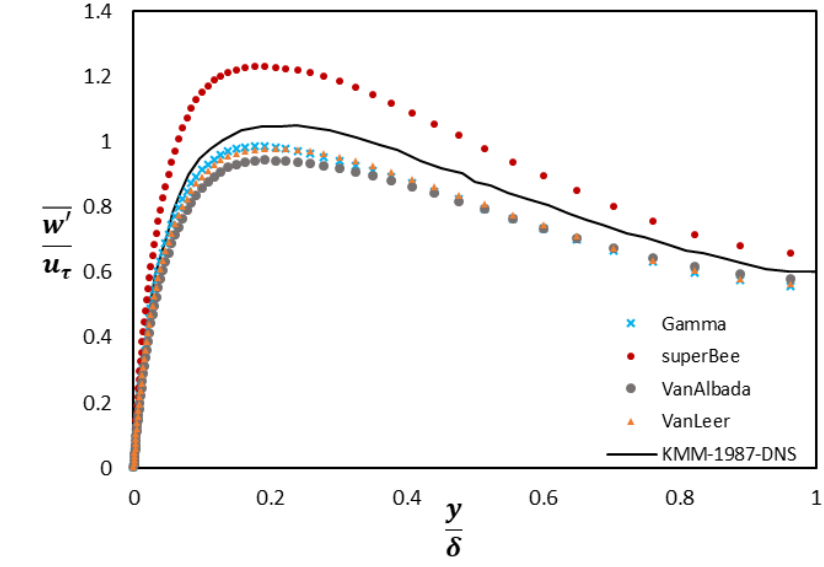
(a)



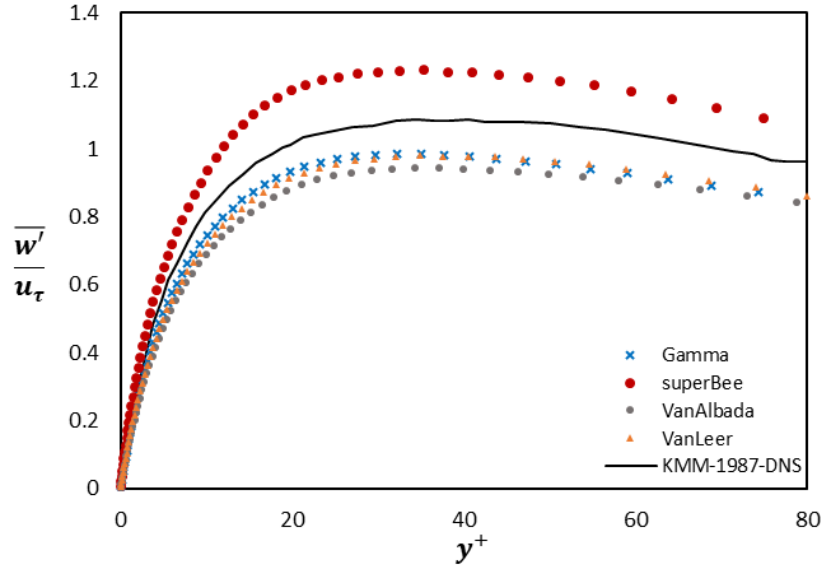
(b)

Figure (3.17) RMS velocity fluctuations in y-dir. normalized by the wall shear velocity: (a) in global co-ordinates; (b) in-wall coordinates.

Similar behaviour for the spanwise velocity fluctuations is observed as shown in Figure (3.18). Gamma, VanAlbada, and VanLeer flux limiters produce under predictions for the spanwise fluctuations relative to the reference DNS data with a maximum value ratio of 10% for VanLeer and Gamma, while VanAlbada gives under-estimation with a ratio of 14% relative to the maximum value of the fluctuation of the DNS results. On the other hand, superBee produces consistent over-estimation for the fluctuation with a maximum value ratio of nearly 10% at $y^+ = 40$.



(a)



(b)

Figure (3.18) RMS velocity fluctuations in z-dir. normalized by the wall shear velocity: (a) in global co-ordinates; (b) in-wall coordinate.

From the results shown in Figure (3.13) to Figure (3.18), it is clear that superBee flux limiter predictions match well to the DNS studies in the streamwise direction, while having a little over predictions in capturing the turbulence structures quantities in the other two directions for the fully developed channel. It can be concluded that superBee limiter is the most diffusive limiter between all simulated limiters. Physically speaking, this act may be due to it allows the linear discontinuities, change in the velocity gradient, to propagate for an indefinitely long time without numerical

diffusion (Roe, 1986), while it gives the least non-physical oscillations of the values compared with other flux limiters (Harimi and Pishevar, 2013). On the other hand, it is obvious that Gamma, VanAlbada and VanLeer limiters are less diffusive than superBee limiter.

3.4.3 Fully developed channel with $Re_\tau = 395$

3.4.3.1 Computational Domain

Another simulation with $Re_\tau = 395$ is applied to confirm the ability of superBee flux limiter as an interpolation scheme for the main part of the current research. The computational domain of the previous case of $Re_\tau = 180$ is used here after adjusting the flow velocity through the channel to get the required Re_τ . With this computational domain, the grid spacing in the streamwise and spanwise directions are $\Delta x^+ = 16$ and $\Delta z^+ = 8$ in wall units, respectively.

3.4.3.2 Results

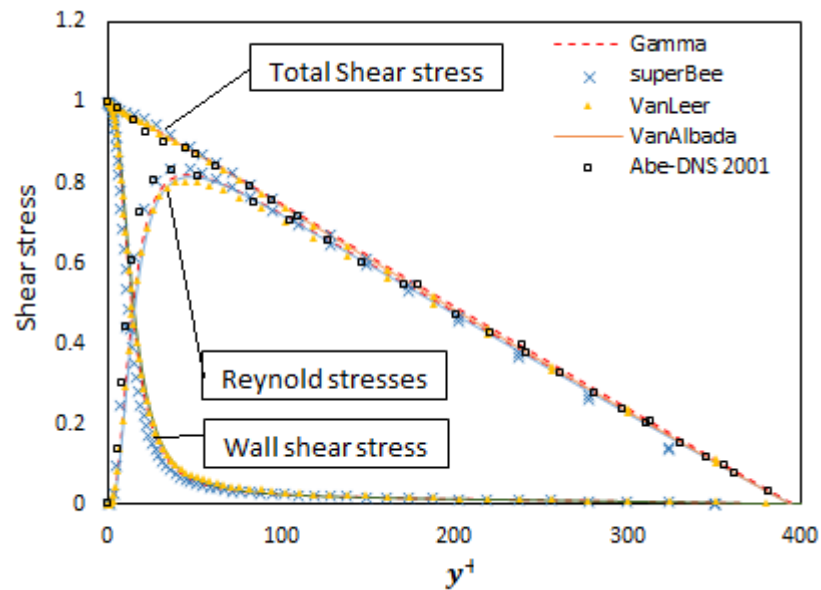
As it was mentioned before, all the results are averaged in time and space after reaching the steady-state. Figure (3.19) presents the combination of the wall shear stress in addition to the flow Reynolds stresses to give the total shear stress for different flux limiters used in a periodic channel flow. Figure (3.19)-(a) illustrates the stresses in wall coordinates, while Figure (3.19)-(b) produces them in global coordinates. Gamma, superBee, VanAlbada and VanLeer flux limiters results are compared with previous DNS results of Abe et al. (2001). Table (3.3) produces the mean flow properties obtained from MILES computations of the periodic channel flow at $Re_\tau = 395$.

The near-wall behaviour of the mean velocity profile, \overline{u}^+ , for all cases are drawn in Figure (3.20), all limiters produce the same behaviour as that one of $Re_\tau = 180$. In this figure all limiters predict the same behaviour in the sub-viscous region. Gamma, VanAlbada, and VanLeer start to deviate significantly at $y^+ = 10$ with an increase in the values of the velocity as it goes towards the channel centre relative to the DNS mean velocity profile.

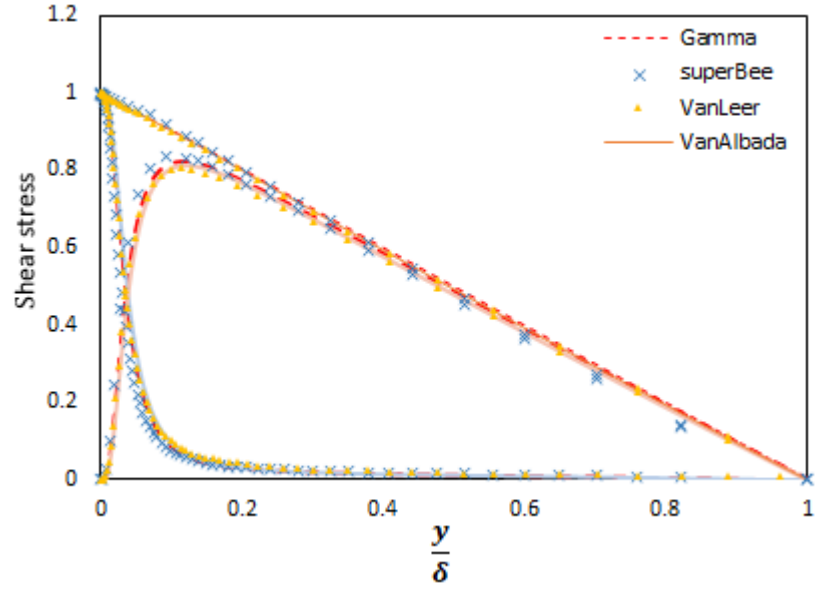
Table (3.3) Mean flow properties obtained from MILES computations of the periodic channel flow at $Re_\tau = 395$ and the DNS reference of Abe et al. (2001)

Flux limiter	U_m	U_c	$\frac{U_c}{U_m}$	$\frac{U_c}{U_m} = f(Re_m)$	$Re_\tau = \frac{(u_\tau * \delta)}{\nu}$	$Re_m = \frac{(U_m * 2\delta)}{\nu}$
Gamma	19.647	22.16	1.128	1.14	395	15530
superBee	18.55	21.2	1.143	1.145	395	14600
VanAlbada	20.67	23.07	1.115	1.14	395	16300
VanLeer	19.893	22.8	1.146	1.144	395	15600
DNS	17.7	20.48	1.16	1.145	395	13981

Comparing with those results from $Re_\tau = 180$ all flux limiters behave with the same manner for the streamwise RMS fluctuation, $\overline{u'}$, although there is an improvement for Gamma and VanLeer limiters to produce more accuracy than that one at $Re_\tau = 180$. In Figure (3.21), Gamma and VanLeer overestimate the values of peak fluctuation for superBee and the DNS results with a percentage of 9%, while VanAlbada produces the highest over-estimation percentage of 16% at $y^+ = 15$ compared with that one from $Re_\tau = 180$ with a percentage of 8% at $y^+ = 17$. Also, it can be noticed that there is a shift in the position of the maximum streamwise fluctuation between the limiters such as for DNS and superBee it is at $y^+ = 15$ while Gamma and VanLeer at $y^+ = 18$ and vanAlbada at $y^+ = 19$.



(a)



(b)

Figure (3.19) Total shear stress, Reynolds stresses and wall shear stress for $Re_\tau = 395$. Normalized by the wall shear velocity: (a) in-wall coordinates; (b) in the global coordinate.

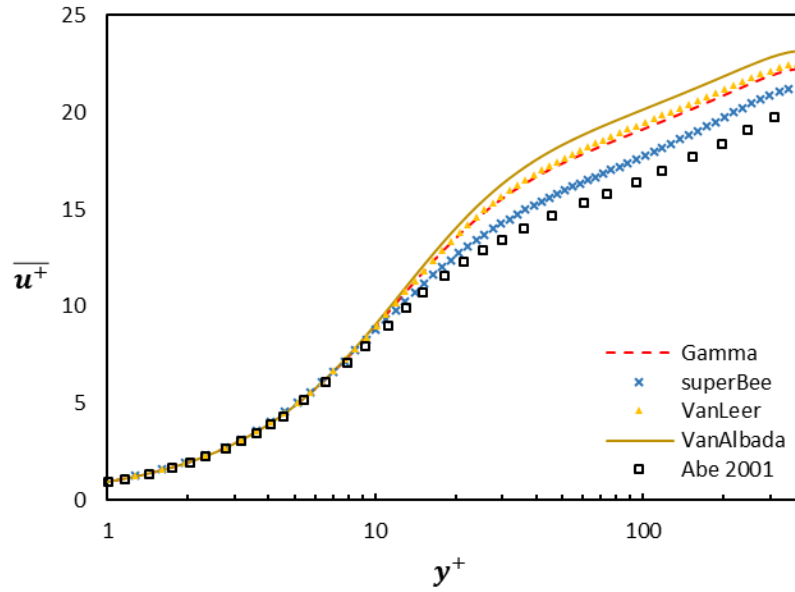
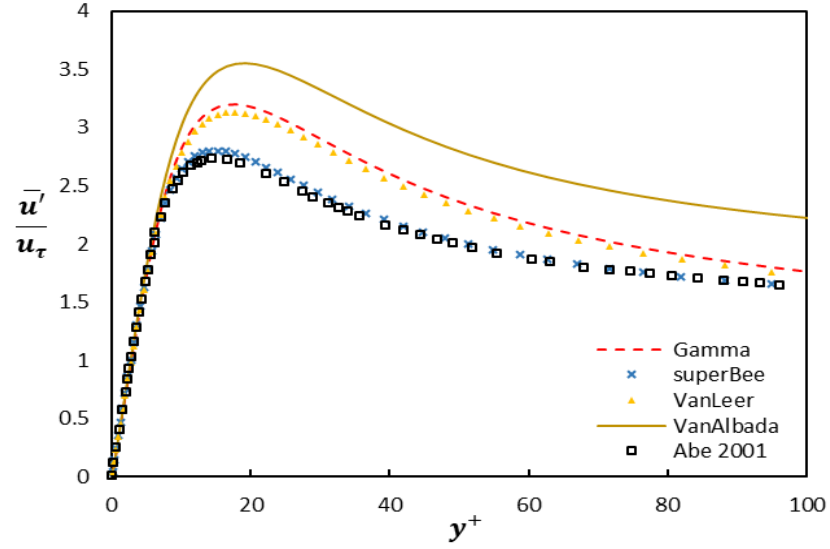


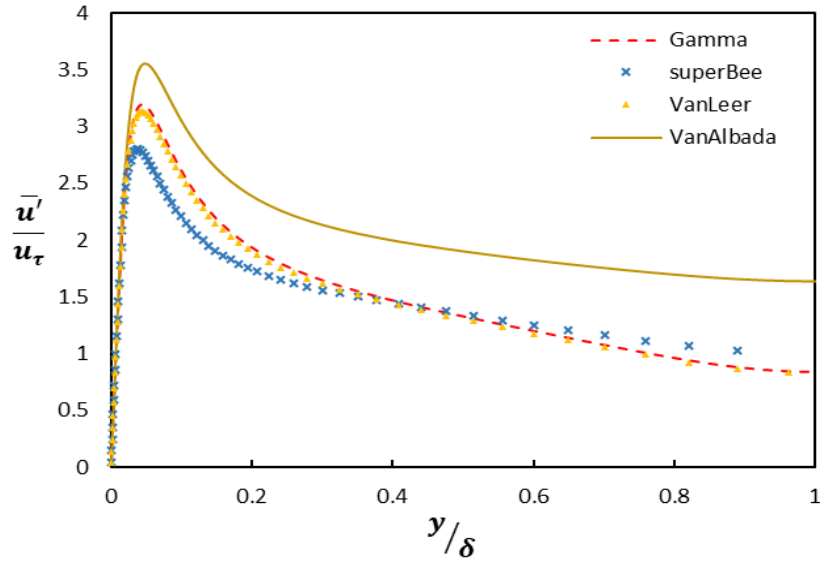
Figure (3.20) Mean velocity profile of a fully developed channel flow of $Re_\tau = 395$.

Figure (3.22) shows the behaviour of normal to the wall fluctuations, \bar{v}' . Increasing Re_τ relative to the previous case of $Re_\tau=180$ achieves some improvement in the accuracy of superBee flux limiter till $y^+ = 50$. It is clear that superBee has a good agreement with DNS results till $y^+ = 50$ at which it starts to deviate towards the channel centre. Almost Gamma, VanLeer, and VanAlbada flux limiters have the same behaviour as for $Re_\tau = 180$. A similar improvement in the spanwise fluctuations

exists like that one of wall-normal fluctuations. At $Re_\tau = 180$, superBee flux limiter achieves over-estimation for the maximum value of 10% compared with the DNS, shown in Figure (3.23), while for $Re_\tau = 395$ it is about 8%. Also, Gamma, VanLeer, and VanAlbada improved their accuracy compared to the DNS results. The under-estimation of their performance becomes 7% and 9% instead of 10% and 14% at $Re_\tau = 180$ and $y^+ = 40$.

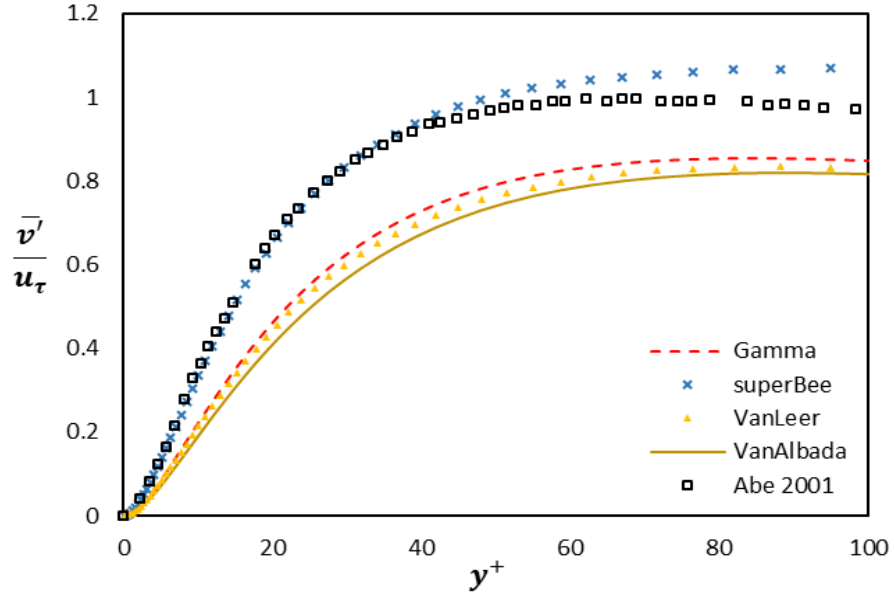


(a)

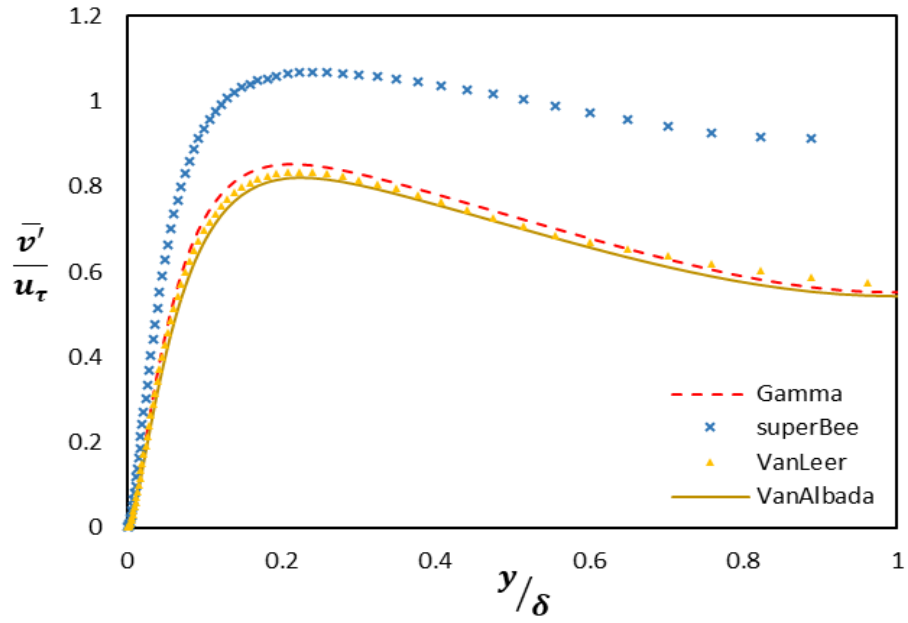


(b)

Figure (3.21) RMS velocity fluctuations in streamwise dir. normalized by the wall shear velocity, (a) in-wall coordinates, (b) in the global coordinate

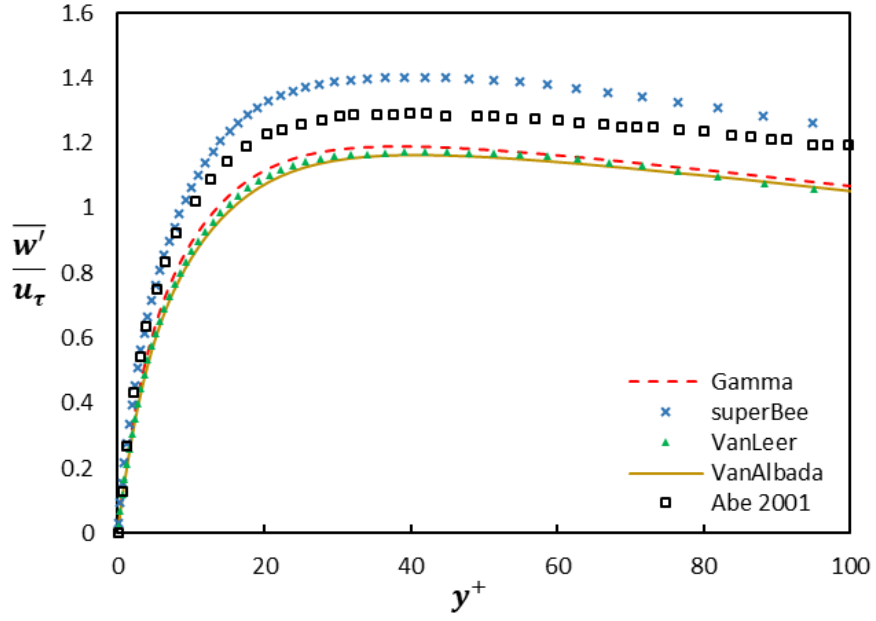


(a)

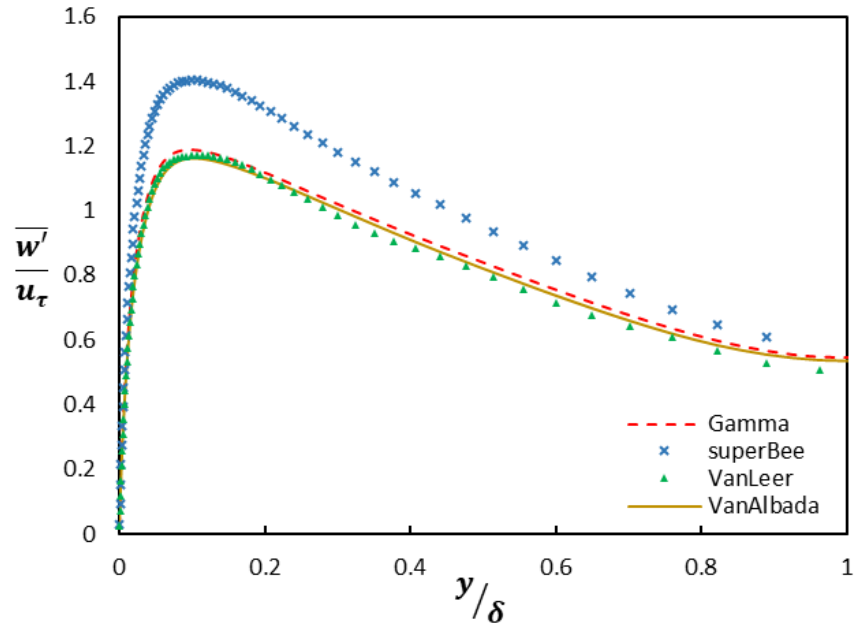


(b)

Figure (3.22) RMS velocity fluctuations in normal to the wall dir. normalized by the wall shear velocity, (a) in the wall coordinates, (b) in the global coordinate.



(a)



(b)

Figure (3.23) RMS velocity fluctuations in spanwise dir. normalized by the wall shear velocity, (a) in the wall coordinates, (b) in the global coordinate.

3.5 Summery

MILES solver is developed by using the open-source CFD OpenFOAM libraries. Numerical simulations are performed to investigate its ability to capture the turbulence

structures through a fully developed channel flow at friction Reynolds numbers of $Re_\tau = 180$ and 395. Its ability is studied by using different flux limiters schemes namely, Gamma, superBee, VanAlbada, VanLeer via evaluating the statistical turbulent quantities for the channel flow. On the other hand, an investigation of the effect of grid-refinement on the performance and the accuracy of the MILES solver is performed. The results show that Gamma and VanLeer are identical in their behaviour and along with VanAlbada limiter can be considered as the less diffusive limiters. While superBee limiter produces acceptable behaviour, which is very close to the previous DNS data in the streamwise direction while deviates slightly in the spanwise and normal to the wall directions for the case of coarse mesh, case A. This deviation is enhanced after refining the mesh, cases B and C. Also, MILES solver presents enhancement in the performance with increasing Re_τ especially with superBee as a flux limiter, which makes it a good alternative to the DNS in those cases with high Re_τ . This enhancement will lead to reducing the computation costs and time. Finally, it can be concluded from this chapter that MILES solver is able to predict the turbulence structures in a fully developed channel with moderate mesh resolution combined with superBee flux limiter which is looking promising for the developed MILES solver in OpenFOAM context. Therefore, this combination will be used as the main solver in all the upcoming numerical studies which include generation of an isotropic homogeneous turbulence boundary condition in Chapter (4) and studying the effect of spanwise travelling wave on the skin friction drag reduction of a flow over a flat plate in Chapter (5).

Chapter (4)

Isotropic Homogeneous Turbulence Inlet Boundary Condition

4.1 Introduction

Despite all the modern technology and development in the computation resources, the simulation of turbulence in a turbulent flow remains a big challenge. Therefore, choosing the proper turbulent inlet boundary condition is very important when studying the turbulence through a channel flow to prevent the turbulence from decaying and turning it into a laminar flow. Also, selecting the proper mesh resolution and its distribution has a big effect on the accuracy of the results. Usually, in high Reynolds number flow, a high percentage of the total number of cells is concentrated near the wall in order to capture most of the turbulence structures inside the boundary layer, wakes and recirculating regions, while, the number of cells near the inlet boundary condition is low to be able to resolve all the existing large portions of the turbulent spectrum. For most of the conventional LES and MILES simulations, the turbulence integral length scale may be smaller than the grid size at the inlet, therefore the turbulence during the simulation may decay faster than the normal rate and lead to disappearing of turbulence structures at a small streamwise distance from the inlet plane. Therefore, the appropriate aim of any turbulent inlet boundary condition for a channel to feed the channel not only with the required time and length scale but also with a length scale relative to the grid size, Δy and Δz assuming that the flow in the x-direction, at the channel inlet plane and also both scales have to be related to the computational time step Δt . In addition, such a synthetic turbulence boundary condition should require a minimum spatial development distance downstream the channel inlet plane, so that the channel dimensions can be decreased and then the computation cost can be minimized.

Generating a velocity inlet boundary condition for a channel flow which comprises a spatial and temporal variation has been the goal of many researchers in recent decades. Many of them have been developed their own boundary conditions for specific applications and solution techniques. Therefore, in this section, a small review related to the current boundary condition is provided. Tabor and Baba-Ahmadi (2010) have split the approaches of the inlet boundary condition into two main categories: the first one is the most popular one in which a DNS precursor simulation with specific characteristics is used to generate the database required at the inlet of the channel. An important drawback of this approach is that the DNS simulations run at low friction Reynolds numbers (Re_τ), and till now it is not clear how to re-scale the DNS fluctuations to higher Reynolds numbers. This is because it is difficult to re-scale the turbulent length and time scales, while it is easy to re-scale the amplitude of the fluctuations in addition to the computational cost for the DNS precursor case. The second category is those boundary conditions which use various algorithms to synthetically reproduce ‘turbulence-like’ behaviour. According to Tabor and Baba-Ahmadi (2010), this category can be further divided into four sub-categories:

1. Techniques applying Fourier techniques, such as Batten et al. (2004) and (Davidson and Billson, 2006);
2. Techniques applying data obtained from experimental measurements to reconstruct turbulence via Proper Orthogonal Decomposition POD, such as (Druault et al., 2004);
3. Techniques involve digital filters such as Di Mare et al. (2006).
4. Techniques base on the Lagrangian treatment of vortices, which are transported within a virtual box such as Jarrin et al. (2009) and Poletto et al. (2013).

In this chapter, the second category is reviewed exclusively and developed to be used in the rest of this research. Generating velocity inlet boundary condition via imposing a random fluctuation to a mean velocity profile field is well known to be insufficient, as it requires a long development streamwise distance inside the channel and space and time correlations before the flow reaches the realistic turbulent state. Therefore, many trials have been done to get rid of this problem. Lund et al. (1998) imposed a spatial correlation between fluctuations and this led to some improvement to the synthetic turbulence development. Although improvement was achieved,

shortfalls still existed as shown in Glaze and Frankel (2003). Some enhancements were proposed by Sergent (2002), who used randomly generated concentrations of vorticity in the streamwise direction to generate spanwise and wall-normal fluctuations. This method was a two-dimensional approach and it had a drawback that the streamwise fluctuation was generated using separate equations, therefore, there was no correlation with the other components of the fluctuations.

Another form of the synthesized fluctuations called the vortex method and it was introduced by Jarrin et al. (2005). The main idea of this method based on the superposition of coherent eddies in which each eddy is determined by a shape function which is localized in the space. The generated eddies are randomly distributed in the inlet plane and then transferred through it. One of the advantages of this method is that it can reproduce first and second-order statistics in addition to two-point correlations. After few years, Jarrin et al. (2009) produced a different approach in which the fluctuations were produced by eddies transferred through a virtual volume, this method was called as synthetic eddy method (SEM). This approach based on a three-dimensional correlation of fluctuations with a predefined shape function. This method achieved some improved development compared with the previous methods; although it needed a long distance, in the order of 10 half-channel heights, to be recovered to the required values. Subsequent work by Pamiès et al. (2009), in which a more detailed definition of the shape-function was used, showed some improvement over the original SEM. For more explanation, this method defines multiple zones near the wall in which the structure was adjusted to match well-documented observations of vorticity in the turbulent boundary layer. Although, this method achieved some improvements in the recovery distance but still has an important drawback that the generated fluctuating velocity fields are not divergence-free. Despite the generated velocity in this method is always imposed in 2D inlet plane, there is a three-dimensionality associated with it, as the generated eddies are entered to the channel through the inlet plane. Recently, Poletto and Craft developed the original SEM to be able to produce a fluctuating velocity field that is divergence-free, while it is still able to return any given Reynolds stress statistics (Poletto et al., 2013). This developed approach is called a divergence-free synthetic eddy method (DFSEM). The most important drawback of this approach is that it still needs a precursor RANS or DNS simulation to provide it with the mean velocity profile, inlet length scale and Reynolds

stresses as an input database for this method. In addition, results demonstrated that the stresses still need a recovery streamwise distance in the order of 10 half-channel heights to become like that one produced from a periodic LES simulation with the same required turbulence structures.

Isotropic synthesized fluctuations depending on the study of (Kraichnan, 1970) were used in many different kinds of research to generate turbulent fluctuation, see e.g. (Karweit et al., 1991; Bailly and Juve, 1999). In this method, the amplitude of the fluctuations is prescribed via an energy spectrum which in turn is a function of the wavenumber. Le et al. (1997), Smirnov et al. (2001) and Billson (2004) generated non-isotropic fluctuations in which the time-averaged synthesized fluctuations match a prescribed Reynolds stress tensor by determination of the fluctuations. But unfortunately, this method had an important drawback due to this scaling which is that if the Reynolds stress tensor is non-homogeneous, the required spectrum and hence the two-point correlation will be modified. Most of the referred work above used a Fourier series to achieve correlation in time and space. A three-dimensional box with generated fluctuation was investigated by Lee et al. (1992) in which the fluctuations correlation in the streamwise directions were transformed into correlations in time. In the work of Batten et al. (2004) and Davidson and Billson (2006), a spectral distribution for the required fluctuation was imposed by super-positioning of goniometric functions. A modified Von Kármán spectrum was used in this method to approximate the spectral signature of the turbulence. In the work of Billson et al. (2003), they updated the correlation in time to be applied by using an asymmetric infinite time filter. This method offered the use of separate definitions and prescriptions for the turbulent length and time scales. This method has been adopted in the current work.

Channel flow is a popular test case for studying turbulence development through the boundary layer. Since this flow is entirely dependent on the near-wall turbulence, it is a challenging test case. It is also a useful test case for evaluating the applied inlet boundary conditions. In the present study, MILES solver from the previous chapter is used to solve the incompressible unsteady Navier Stokes equation while a mean velocity profile at the channel inlet is applied using the equations of the law of the wall. The generated instantaneous turbulent fluctuations are superimposed on the mean velocity profile at the inlet plane. This boundary condition and fluctuations

depend on many turbulence parameters at the inlet of the channel such as the length and time scales, required friction Reynolds number for the resulted channel, and the computational time step as well. A digital time filter, same as that one in Billson et al. (2003), is applied to make a time correlation for the generated fluctuation. The influences of different integral length and time scales and friction Reynolds number of the turbulent inlet boundary conditions are investigated.

4.2 Governing Equations

An unsteady turbulent velocity field is generated by superimposing of isotropic synthetic fluctuations into the mean velocity profile, generated from the law of wall for a fully developed profile or taken from a precursor DNS case, at the inlet plane of a channel. This velocity field is based on the methodology used in Kraichnan (1970), Karweit et al. (1991) and Davidson (2007). But in the current work, the definition of some inlet parameters has been changed to improve the development of the generated isotropic synthetic fluctuations performance near the inlet of the channel in the streamwise direction.

A time-space homogeneous turbulent velocity field can be mimicked using random Fourier modes such as in the above mentioned references and furthermore in LES studies such as Billson et al. (2003), Davidson and Billson (2006) and Lardeau et al. (2012). Equation (4.1) illustrates the generated fluctuations as a function of Fourier modes parameters.

$$u'_i(x_j) = 2 \sum_{n=1}^N \hat{u}^n \cos(\mathcal{K}_j^n x_j + \Psi^n) \zeta_i^n \quad (4.1)$$

where

- u'_i Velocity fluctuation
- n Number of modes $0 \leq n \leq N$
- \hat{u}^n Fourier mode amplitude
- \mathcal{K}_j^n Fourier mode wave number
- x_j Coordinates
- Ψ^n Fourier mode phase
- ζ_i^n Fourier mode direction

The n^{th} Fourier mode amplitude, \hat{u}^n , always has geometry length of $|\sigma_n| = 1$ as shown in Figure (4.1). To ensure the isotropy of the generated field, the orientation of the wavenumber vector is distributed randomly on the surface of a sphere with a radius of \mathcal{K}_n , Figure (4.2). Therefore, from the continuity equation of incompressible flow, equation (4.2) can be deduced to show that both \mathcal{K}_n and σ_n are perpendicular for all n . Figure (4.2) ensures that they are perpendicular.

$$\mathcal{K}_n \cdot \sigma_n = 0 \quad (4.2)$$

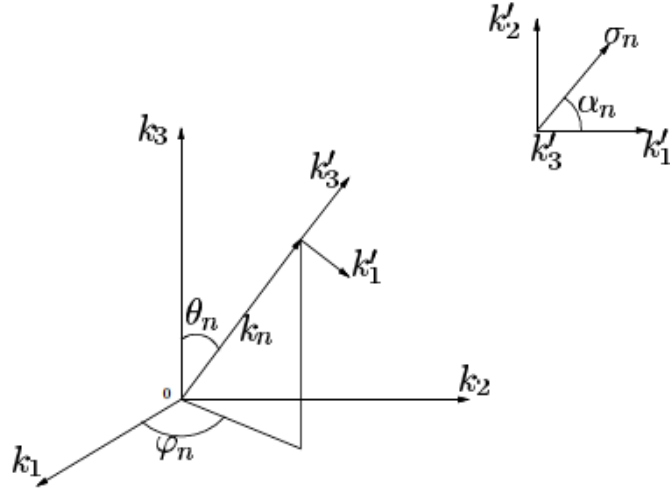


Figure (4.1) Geometry for the n^{th} mode.

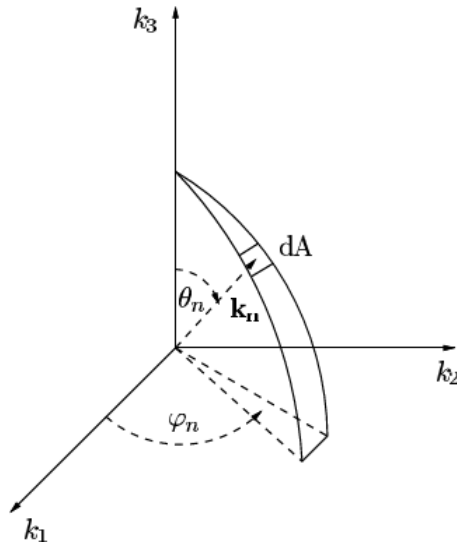


Figure (4.2) The probability of a randomly selected direction of a wave in wave-space is the same for all dA on the shell of a sphere (Davidson 2007).

Each random function, such as $\varphi_n, \psi_n, \theta_n$ and α_n , has its probability according to Table (4.1).

Table (4.1) Probability distributions of the random variables.

$p(\varphi^n) = 1/(2\pi)$	$0 \leq \varphi^n \leq 2\pi$
$p(\Psi^n) = 1/(2\pi)$	$0 \leq \Psi^n \leq 2\pi$
$p(\theta^n) = 1/2 \sin(\theta)$	$0 \leq \theta^n \leq \pi$
$p(\alpha^n) = 1/(2\pi)$	$0 \leq \alpha^n \leq 2\pi$

Therefore, to generate isotropic synthetic turbulence and its value can be produced as a function of the inlet length scale and time scale, the following procedures are applied:

1. The number of Fourier modes, N , is assumed as an input and for each mode, n^{th} , random functions are used to create the angles φ^n, α^n and θ^n , the probability function for θ^n are chosen as $p(\theta^n) = 1/2 \sin(\theta)$ to ensure uniform distribution for the \mathcal{K}_n direction over a hemisphere surface, (see Figure (4.1) and Figure (4.2)).
2. Calculating the value of the maximum wavenumber as a function of the inlet plane grid size, $\kappa_{max} = 2\pi/(2\Delta)$, where Δ is the grid spacing, $\Delta = \sqrt{\Delta y_{max} * \Delta z}$ assuming that the streamwise direction of the flow is in the x-direction and the grid is with uniform distribution in the spanwise z-direction. No-slip condition is applied for the fluctuations at the top and bottom walls.
3. u_{rms} is the root mean square of the velocity fluctuations, u' , which is needed to be assigned as an input for the validation purpose and then in the next chapter it will be deducted from the required turbulence intensity Tu .
4. Turbulence integral length scale, \mathcal{L}_t , is defined in equation (4.3) from the Reynolds Averaged Navier Stokes equations (RANS) solution as:

$$\mathcal{L}_t = f_L \frac{\bar{k}^{3/2}}{\varepsilon_d} \quad (4.3)$$

where f_L is a factor to enable controlling the length scale of the synthesized turbulence at the inlet of the channel. \bar{k} is the total turbulent kinetic energy,

$\bar{k} = (3/2) u_{rms}^2$. ε_d is the turbulent dissipation rate, $\varepsilon_d = C_\mu * \bar{k} * \omega$ and ω is the specific dissipation while C_μ is a constant, $C_\mu = 0.09$.

5. Before generating the wavenumber vector for each n^{th} mode, it is important to know the smallest wavenumber, \mathcal{K}_1 , as a bound for wavenumber which is defined in equation (4.4) and (4.5) as

$$\mathcal{K}_1 = \frac{\mathcal{K}_e}{p} \quad (4.4)$$

$$\mathcal{K}_e = \frac{9\pi\alpha}{55\mathcal{L}_t} \quad (4.5)$$

\mathcal{K}_e is defined as the most energetic length scale and $\alpha = 1.4526$ is a constant, determined from the RANS solution (Billson, 2004). p is a factor which has to be always larger than one to ensure that the largest length scales are larger than those corresponding to \mathcal{K}_e . In the present work $p = 2$.

6. The wavenumber space is divided into equations (4.6) and (4.7) with linear distribution into N modes:

$$\Delta\mathcal{K} = \frac{\mathcal{K}_{max.} - \mathcal{K}_1}{N - 1} \quad (4.6)$$

$$\mathcal{K}_n = \mathcal{K}_1 + \Delta\mathcal{K}^{n-1} \quad (4.7)$$

After generating the random angles, required for Fourier series, and the distribution of the wavenumber values, then the randomized components of \mathcal{K}_j^n are now ready according to Figure (4.2).

7. A modified Von-Karman spectrum is applied to mimic the energy spectrum for the isotropic homogeneous synthetic turbulence, as in equation (4.8):

$$E(\mathcal{K}) = \alpha \frac{u_{rms}^2}{\mathcal{K}_e} \frac{(\mathcal{K}/\mathcal{K}_e)^4}{[1 + (\mathcal{K}/\mathcal{K}_e)^2]^{17/6}} e^{\left[-2\left(\frac{\mathcal{K}}{\mathcal{K}_e}\right)^2\right]} \quad (4.8)$$

where

$$\mathcal{K} = (\mathcal{K}_i \mathcal{K}_i)^{1/2}, \quad \mathcal{K}_\eta = \varepsilon_d^{1/4} \nu^{-3/4}$$

ν is the kinematic viscosity of the fluid. Such a spectrum is suitable for large scales asymptotically proportional to \mathcal{K}^4 , whereas it matches the Kolmogorov-(5/3)-law for small scales as illustrated in Figure (4.3).

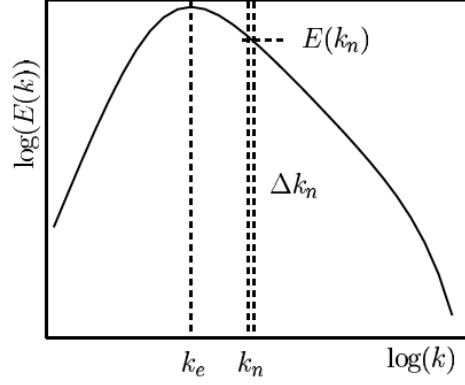


Figure (4.3) Model energy spectrum (Davidson 2007).

8. After determining equations (4.6) and (4.8), the amplitude \hat{u}^n of each mode in equation (4.1) is then obtained from equation (4.9):

$$\hat{u}^n = (E(|\mathcal{K}_j^n|)\Delta\mathcal{K})^{1/2} \quad (4.9)$$

Till here, it can be deduced that the sum of \hat{u}^n squares for all n^{th} modes is equal to the total turbulent kinetic energy as in equation (4.10):

$$\bar{k} = \sum_{n=1}^N \hat{u}^{n^2} \quad (4.10)$$

9. After calculating the amplitude \hat{u}^n , wavenumber vector \mathcal{K}_j^n and the random angles of each mode in equation (4.1) then the isotropic fluctuations (u', v', w') can be generated at each time step at the inlet (Y-Z) plane.

The generated fluctuations at this point are not related to each other at each time step and hence their time correlation is equal to zero, which means that they will not be able to develop and decay like the normal channel turbulence. This is an unphysical approach. One of the most effective ways to enhance the behaviour of the generated turbulence and keep an acceptable level of computation costs is applying a time correlation for the generated fluctuation by using a time filter. This time filter has to be applied after generating the fluctuations directly (Billson et al., 2003). By this way,

the newly developed velocity field is time-dependent, equation (4.11) introduces the new fluctuations (U', V', W') after the time filter.

$$\begin{aligned}(\mathcal{U}')^m &= a(\mathcal{U}')^{m-1} + b(u')^m, \\(\mathcal{V}')^m &= a(\mathcal{V}')^{m-1} + b(v')^m, \\(\mathcal{W}')^m &= a(\mathcal{W}')^{m-1} + b(w')^m\end{aligned}\tag{4.11}$$

where the superscript m denotes to the time step number, $a = \exp(-\Delta t/\mathcal{T})$ and $b = (1 - a^2)^{1/2}$ which is used to ensure that $\langle \mathcal{U}_i'^2 \rangle = \langle u_i'^2 \rangle$. This time filter is the asymmetric digital filter produced in Klein et al. (2003). \mathcal{T} is the time scale which expresses the time separation for which the autocorrelation function is reduced to $\exp(-1)$ and Δt is the local time step. Equation (4.12) uses the RANS solution to calculate the time scale \mathcal{T} .

$$\mathcal{T} = f_{\mathcal{T}} \frac{\bar{k}}{\varepsilon_d}\tag{4.12}$$

where $f_{\mathcal{T}}$ is a factor used to control the value of the time scale at the inlet plane. Also, it was advised by Billson et al. (2003) to use a small number of modes with that kind of time filter to ensure accurate statistics. After applying this time filter, the resulted fluctuations field is a weighted value for all the previous generated fluctuations, and this is how they are correlated in time.

At this point, the isotropic synthetic fluctuations (U', V', W') expressed in equation (4.11) are ready to be added to the mean velocity field and also are able to express the required length and time scales required at the inlet of the channel. In Davidson (2007), the mean velocity profile was taken from a precursor DNS study of a fully developed flow or else can be calculated from using the law of the wall. Finally, the velocity field at the inlet can be expressed as shown in equation (4.13) in which $V_{in} = W_{in} = 0$.

$$\begin{aligned}\bar{u}(0, y, z, t) &= U_{in}(y) + u'_{in}(y, z, t), \\ \bar{v}(0, y, z, t) &= V_{in}(y) + v'_{in}(y, z, t), \\ \bar{w}(0, y, z, t) &= W_{in}(y) + w'_{in}(y, z, t)\end{aligned}\tag{4.13}$$

4.3 Synthetic turbulence modifications

Davidson (2007) concluded from his work at friction Reynolds number $Re_\tau = 500$, that the generated isotropic fluctuations need at least 10δ streamwise distance, where δ is the half height of the channel, after the inlet plane of the channel to improve itself and produce the required fully developed behaviour from the isotropic turbulence. While at $Re_\tau = 395$, Poletto et al. (2013) showed that this method required a streamwise distance in the range of 30δ to be fully developed.

Hence, in the current section, this method is modified to improve its performance and reduce the required distance to the flow to be fully developed after the inlet of the channel which in turn will save the computational costs and the run time. On the other hand, it works as an effective way to get rid of the requirement of a precursor DNS simulation to get the required fluctuations. Therefore, the following modifications are applied to get the current method:

1. The integral length scale was calculated based on an assumption for the input total turbulent kinetic energy, \bar{k} . While here, the integral length scale is calculated as a function of the mesh resolution in equation (4.14), following the work of Tennekes et al. (1972), to ensure that the integral length scale at the inlet is suitable for the mesh resolution used and all the eddies can be captured during the simulation.

$$\mathcal{L}_t = \frac{1.8}{\mathcal{K}_{max}} \quad (4.14)$$

2. The fully developed mean velocity profile at the inlet is generated using the law of wall according to equation (4.15):

$$U_{in}^+ = \begin{cases} y^+ & y^+ \leq 5 \\ -3.05 + 5 \ln(y^+) & 5 < y^+ < 30 \\ \frac{1}{\kappa} \ln(y^+) + B & y^+ \geq 30, \end{cases} \quad (4.15)$$

where y^+ is calculated as a function of the friction velocity, $u_{\tau,in}$, which is produced by the calculated friction Reynolds number, $Re_{\tau,in} = (\delta * u_{\tau,in})/\nu$, at the inlet.

3. The generated noise is forced to go to zero at the wall, following the no-slip condition, by multiplying it with a hyperbolic tangent cut-off function. This function is expressed by a factor f_{wall} in equation (4.16) in the case of a Blasius velocity profile at the inlet while this function becomes linear in the case of the fully developed inlet.

$$f_{wall} = \begin{cases} 1 & \frac{y}{\delta} > 0.05\delta \\ \tanh\left(\frac{y_i}{\delta_{99}^0}\right) & \frac{y}{\delta} \leq 0.05\delta \quad \text{Blasius inlet} \\ 250\left(\frac{y_i}{\delta}\right) & \frac{y}{\delta} \leq 0.05\delta \quad \text{Fully developed} \end{cases} \quad (4.16)$$

It is known that the generated velocity fluctuations due to most of the synthetic isotropic turbulence boundary condition have a net-zero mass flow at the inlet plane of the channel and therefore the flow goes smoothly from the inlet to the outlet with negative mean pressure gradient. But it is found that in the current generated boundary condition, some of the timesteps have positive mean pressure gradients which means that the pressure at the outlet is higher than that one at the inlet although the flow goes from inlet to outlet smoothly without any backflow. This phenomenon affects the behaviour of the turbulence structures through the channel and increases the pressure fluctuations through the channel especially after the inlet plane. To explore this phenomenon, the bulk velocity is measured at each time step, required to achieve the continuity, at the inlet and the outlet of the channel and it was found that small difference between the values for each time step which may cause this phenomenon. To solve this problem, a bulk correction is applied to the inlet velocity profile, such as that one used in Poletto et al. (2013), by simply rescaling the inlet velocity profile via a velocity rescaling coefficient, $f_{rescale}$, to ensure a constant mass flow rate at the inlet plane of the channel to achieve the continuity. Values of this rescaling coefficient range from 0.999 to 1.001 which mean no significant change in the velocity profile as these values change the velocity field with a percentage of $\pm 0.1\%$. As a result, for this rescaling process, the computation time required is reduced due to reducing the number of pressure iterations required to almost 65% and this helps to save more computation costs. The difference in the RMS of pressure fluctuation through the channel before the rescaling process and after is illustrated in Figure (4.4).

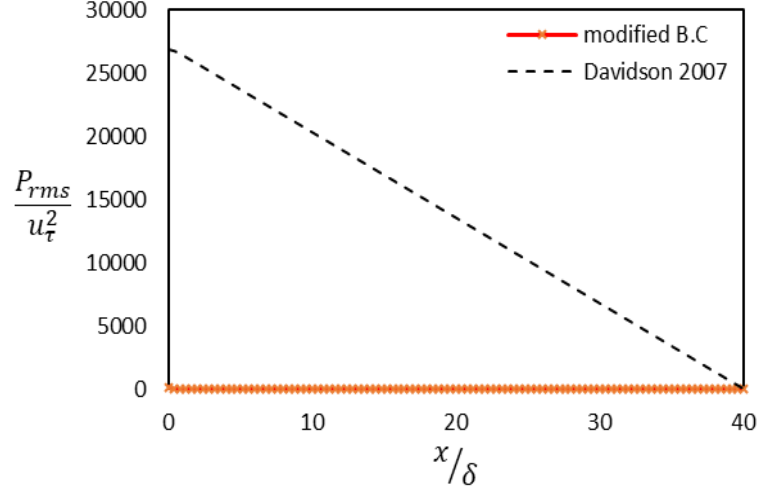


Figure (4.4) RMS pressure fluctuations along the channel, using the (uncorrected) generated B.C and the modified B.C with velocity scaled to ensure a constant bulk flow rate.

4.4 Results

In this section, the results of the modified method are discussed and compared with the original method from Davidson (2007). As shown in Davidson (2007), the best results are obtained when using the inlet length scale as $\mathcal{L}_t = 0.11\delta$ and the inlet time scale as \mathcal{T}_{in} . Therefore, for the validation purpose of the modified method these inlet length and time scale are used.

4.4.1 Computational Domain

The isotropic homogeneous turbulence inlet boundary condition for the MILES solver is validated using a channel flow test case. The size of the computational domain is used as $(L_x, L_y, L_z) = (12\pi \times 2 \times 0.5\pi)$. The mesh size is $(N_x, N_y, N_z) = 400 \times 120 \times 65$ in the streamwise (x), wall-normal (y) and spanwise (z) directions respectively. The mesh distribution is uniformly spaced in the streamwise and spanwise directions, while in wall-normal directions, an expanding mesh towards the channel centre is used such that the first mesh point next to the wall boundary is within $y^+ = 0.3$. With such a computational domain, the grid spacing in the streamwise and spanwise directions are $\Delta x^+ = 50$ and $\Delta z^+ = 12$ respectively in wall units. All parameters used in this section are normalized by the friction velocity, u_τ , and the channel half-height, δ . Table (4.2) presents the base flow parameters for the following simulations. They differ in the values of the inlet length and time scales and the

calculated a, b constants (in equation (4.11)) for each simulation. Time step is adjusted and normalized, to give a maximum CFL number of approximately 0.3 to 0.6, so that $\Delta t^+ = 0.004$ from the required time per one trip (RTPT), where RTPT is the time required for the fluid particle to start from the inlet and arrive at the channel outlet, $RTPT = L_x/U_b$. By adjusting the mean velocity profile at the inlet plane, a flow with a friction Reynolds number of $Re_\tau = 500$ is obtained. The boundary condition is executed in parallel and simulations are run using 168 processors on the cluster, for a computation total time in the order of 80 hours of wall time per processor.

Table (4.2) Inlet length and time scales for the MILES simulations. The base flow used here with fixed constant RMS velocity fluctuations $u_{rms} = v_{rms} = w_{rms} = 1.5$ at the inlet of test cases for the MILES simulations.

Case number	\mathcal{L}_t	\mathcal{T}_{in}	$u_{in,rms}$	a	b
Case (1)	\mathcal{L}	$\mathcal{T}_{in}/12$	1.5	0.966	0.2582
Case (2)	\mathcal{L}	$\mathcal{T}_{in}/4$	1.5	0.9885	0.1508
Case (3)	\mathcal{L}	\mathcal{T}_{in}	1.5	0.9971	0.0757
Case (4)	$0.5 \mathcal{L}$	$\mathcal{T}_{in}/12$	1.5	0.9676	0.2522
Case (5)	$1.5 \mathcal{L}$	$\mathcal{T}_{in}/12$	1.5	0.9676	0.2522

4.4.2 Boundary condition results

The results of the generated and modified boundary conditions are discussed and validated with the DNS results of Davidson (2007). Case (1) from Table (4.2) is used to show the results of the turbulence structures comparison while cases (2, 3, 4 and 5) are used in studying the sensitivity of the boundary condition performance relative to different inlet length and time scales. Figure (4.5) shows the behaviour of the mean velocity profile near the wall at different streamwise stations through the channel ($x/\delta = 1, 5, 10, 24, 30$). It is clear that all velocity profiles are in well match with the DNS simulation of Davidson (2007) except that one at $x/\delta = 1$ in which it gives over-estimation for the velocity in the logarithmic region. This may be due to the flow is still under developing.

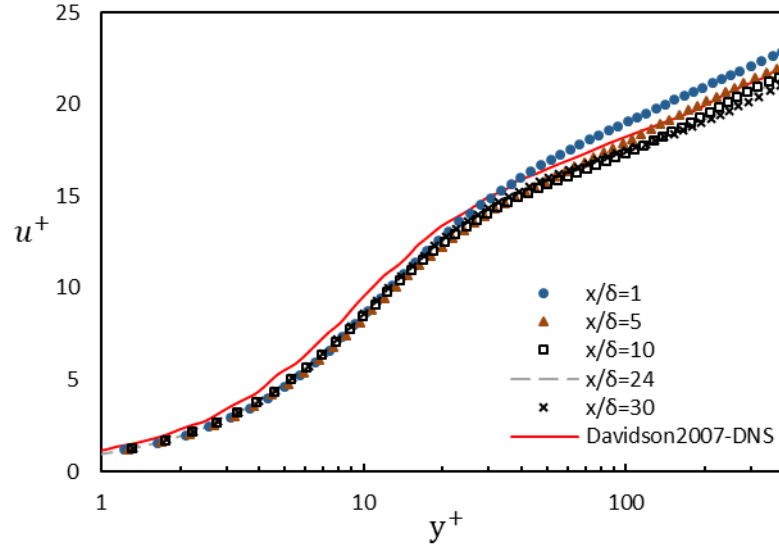


Figure (4.5) Mean velocity profiles at streamwise stations for the isotropic turbulence inlet boundary condition.

In order to investigate more validation results for the flow development through the channel, the resolved shear stresses, $\overline{u'v'}$, produced the isotropic turbulence generation in Figure (4.6). At $x/\delta = 1$ there is an over-estimation for the stresses far away from the wall with a max percentage difference of about 35 %, while it decreases again towards the channel centre, Figure (4.6)-(a). This may be due to a sudden drop in the correlation between u' and v' after the inlet which in turn leads to a discrepancy in the shear stresses development after the inlet and until streamwise distance about $x/\delta = 10$. Also, this discrepancy has been mentioned in the study of Poletto et al. (2013) when they compared their work, Divergence Free Synthetic Eddy Method (DFSEM), with the work of Davidson (2007) at friction Reynolds number of $Re_\tau = 395$. In their study, they have shown that this discrepancy can extend to $x/\delta = 30$. This effect will be further discussed later when studying the effect of the inlet length and time scales. The Reynolds stresses behave well relative to the previous DNS studies at $x/\delta = 10$ till 24, Figure (4.6)-(b and c). Figure (4.6)-(d) produces the homogeneity of the flow compared with previous DNS results, before the modifications.

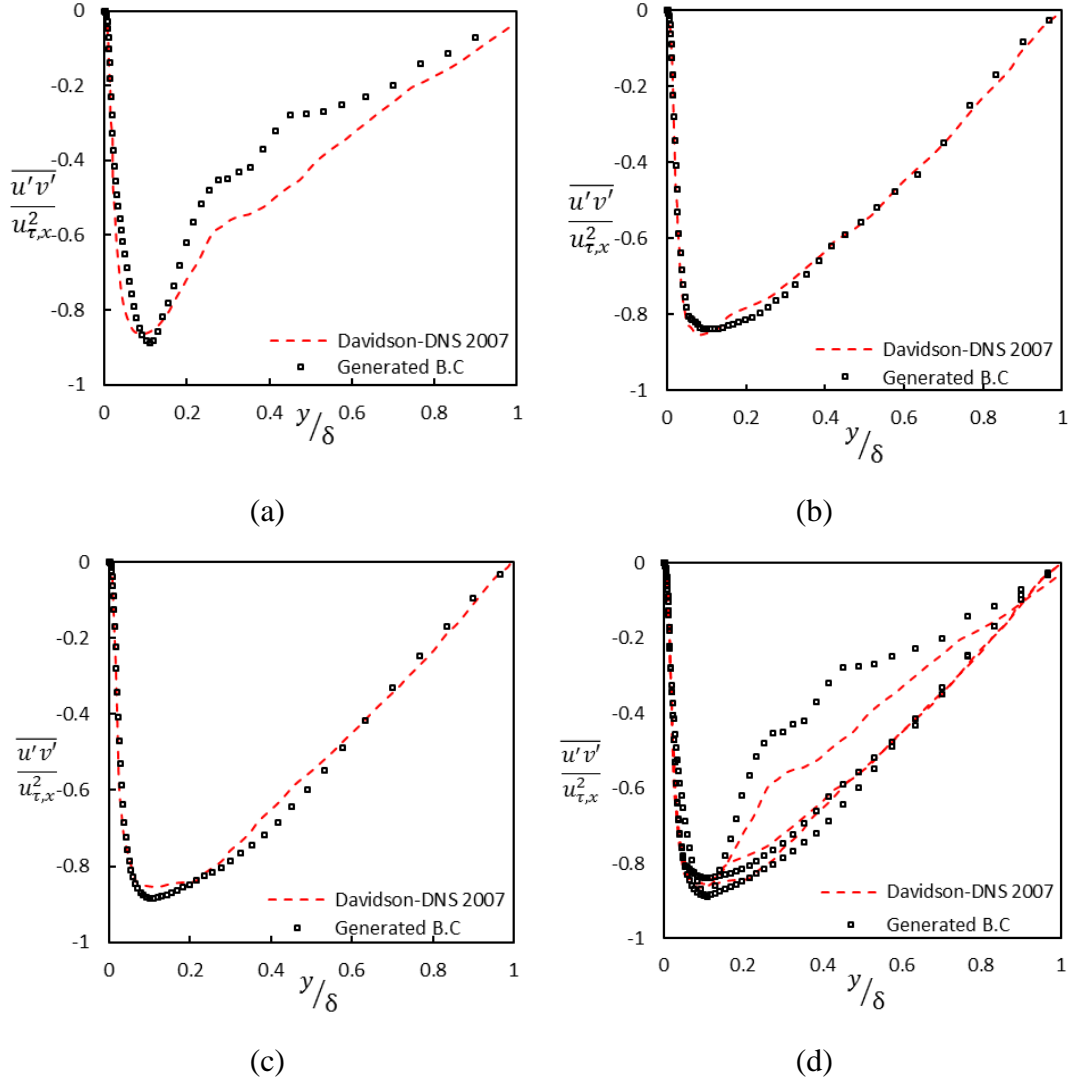


Figure (4.6) $\overline{u'v'}$ Profiles at selected streamwise locations: (a) $x/\delta=1$, (b) $x/\delta=10$, (c) $x/\delta=24$, (d) total behaviour between Davidson DNS and the generated B.C.

Improvements in the behaviour of the isotropic synthetic inlet boundary condition are obtained after the modifications have been done. Figure (4.7) shows the improvement of the behaviour of the Reynolds stresses near the wall which start to give almost completely isotropic homogeneous turbulence at $x/\delta = 5$ after the inlet plane. It can be noticed in Figure (4.7) that there is a deviation in the stresses between the two streamwise stations $x/\delta = 10$ and 24 which reached its maximum value of 5% at $y/\delta = 0.6$. The stresses start to decrease towards the channel centre. This enhanced behaviour may be due to the reduction in the development streamwise distance for the flow after the inlet plane to attain isotropic turbulence to a streamwise distance of $x/\delta = 5$ instead of $x/\delta = 10$ in the previous DNS work.

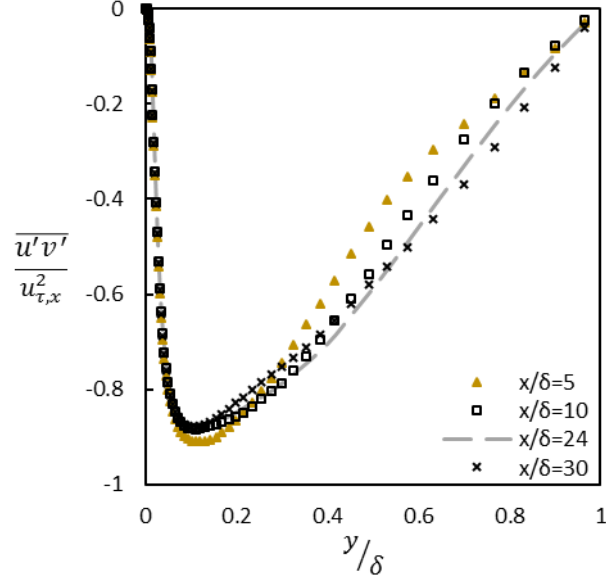


Figure (4.7) $\overline{u'v'}$ profiles at selected streamwise locations for the modified inlet boundary conditions.

A similar picture emerges for the streamwise and wall-normal fluctuations, $\overline{u'}$ and $\overline{v'}$, in Figure (4.8) and Figure (4.9). The streamwise fluctuations, $\overline{u'}$, is averaged in time and space for different streamwise locations along the channel and it shows some unsteady behaviour for the generated inlet turbulence till almost streamwise distance up to $x/\delta = 10$, Figure (4.8)-(a). While after the modification, $\overline{u'}$ is recovered smoothly to the isotropic behaviour in a shorter distance, almost at $x/\delta = 5$, and this may have happened because of the attainment of the homogeneity in the turbulence as evident in Figure (4.8)-(b). It can also be seen from Figure (4.9) that the averaged wall-normal fluctuations have significant improvement in their behaviour for the modified boundary condition. They become totally isotropic from almost $y/\delta = 0.2$ in Figure (4.9)-(b) and then slightly deviate comparing with these fluctuations from the generated boundary condition, Figure (4.9)-(a), until $y/\delta = 0.05$ and after that, they subjected to irregularities.

Figure (4.10) shows one of the streak statistics, individual streaks are extracted in a region with the dimensions of $\Delta x^+ = 1000$ and $\Delta z^+ = 700$ from the fully developed turbulent flow along the channel after the turbulence development streamwise distance of $x/\delta = 5$. The average spanwise spacing of 90 wall units between the streaks is obtained at $y^+ = 20$ which is in the same range of 100 wall units mentioned in other studies (Schoppa and Hussain, 2002; Bai et al., 2014). Also, the iso-surfaces contours of Q-criterion, the second invariant of the velocity gradient,

is shown in Figure (4.11) and rendered by the averaged streamwise velocity fluctuations. The flow features shown in Figure (4.10) and Figure (4.11) are typical to well-observed wall generated turbulence.

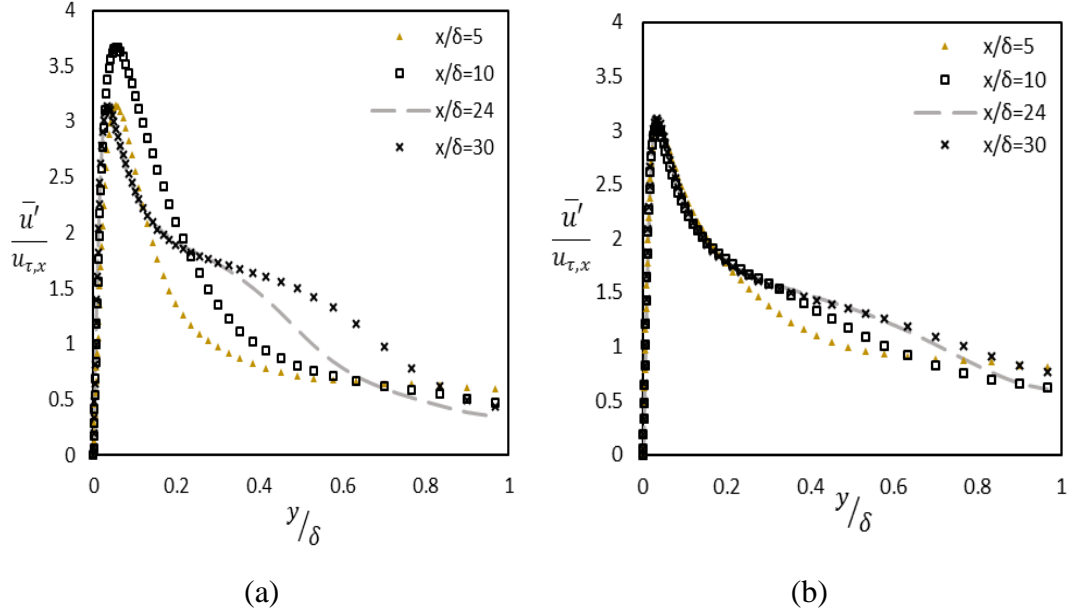


Figure (4.8) $\overline{u'}$ profiles at selected streamwise locations: (a) generated inlet boundary condition, (b) modified inlet boundary condition.

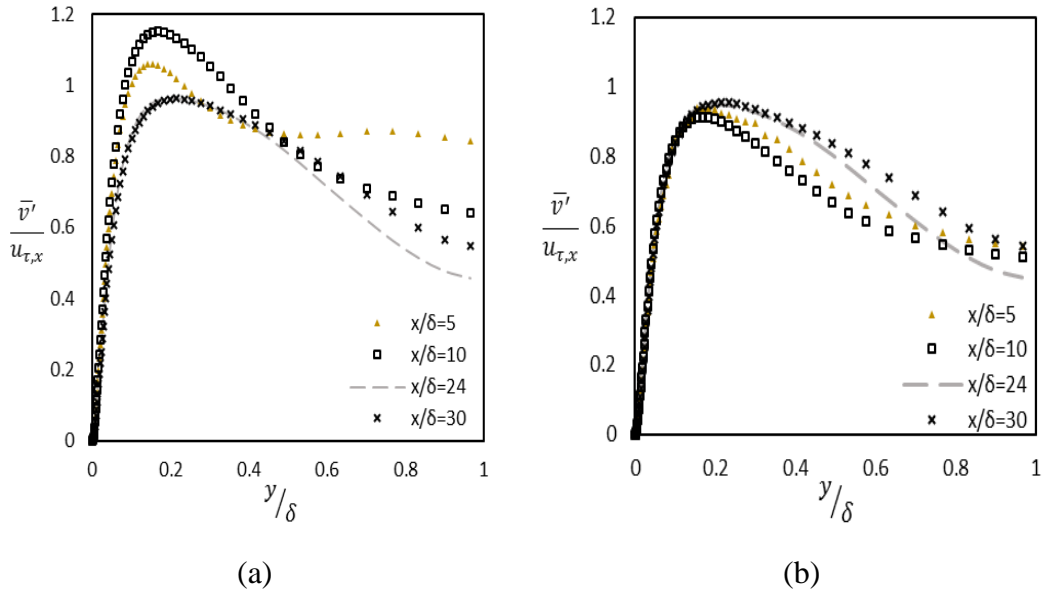


Figure (4.9) $\overline{v'}$ profiles at selected streamwise locations: (a) generated inlet boundary condition, (b) modified inlet boundary condition.

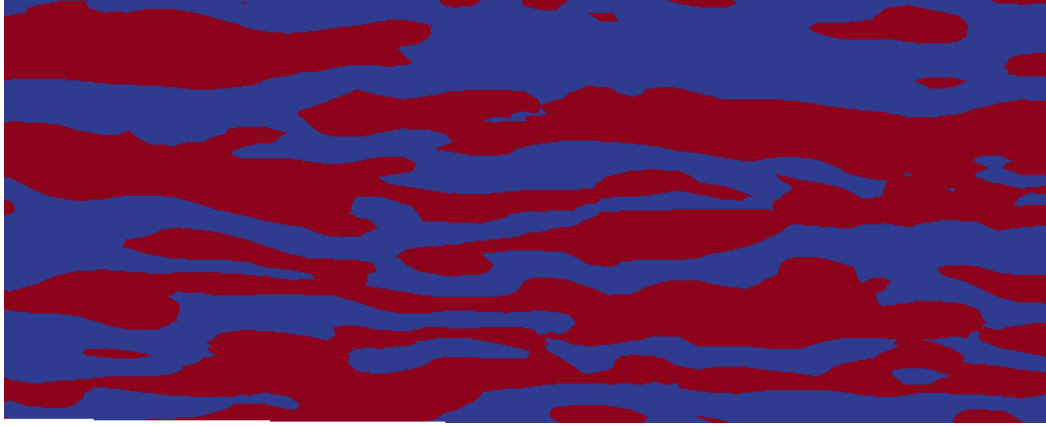


Figure (4.10) Streak identification shown for a typical flow field: streaks at $y^+ = 20$ identified as regions of $u' < 0$ (blue-shading).

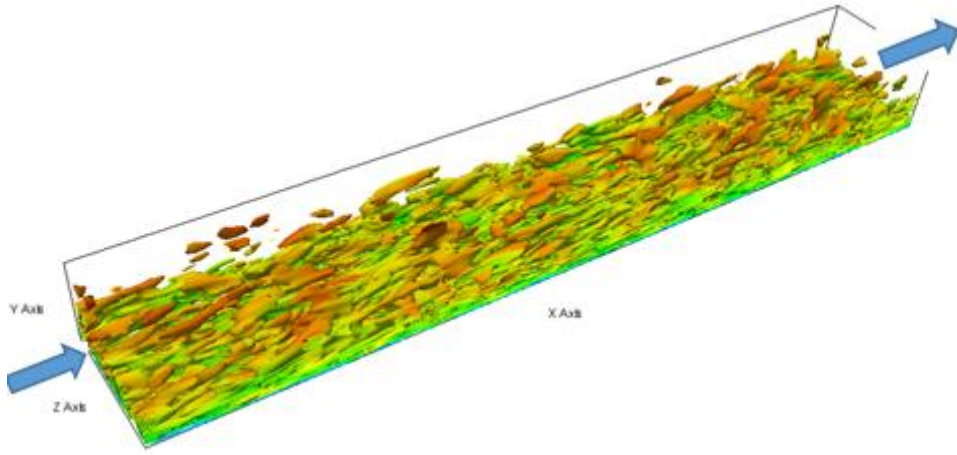


Figure (4.11) Fully developed channel flow: instantaneous visualization in term of contours of iso-surfaces of Q-criterion and coloured by the streamwise velocity fluctuations.

Investigation for the sensitivity to different inlet time scales is applied between the boundary conditions after the modifications and the previous DNS study using cases (1, 2, 3). it is presented in the form of the development of the friction velocity through the channel relative to the fully developed behaviour. In Figure (4.12), the effect of different inlet time scales is presented. Figure (4.12)-(a) shows the developing of the friction velocity through the channel for inlet time scale, \mathcal{T}_{in} , using the modified boundary condition, it is clear that it reaches a value within 1% from the normalized target value $u_\tau = 1$ after a streamwise distance of $x/\delta = 8$ compared with $x/\delta = 11$ in (Davidson, 2007) inlet boundary condition. Also, it produces a small drop in the value of the friction velocity during the developing streamwise distance. $\mathcal{T}_{in}/4$ and $\mathcal{T}_{in}/12$ in Figure (4.12)-(b, c) show small improvement between the modified and the previous DNS boundary conditions although both of them suffer from a higher drop

in the developing streamwise distance. In general, this improvement may relate to the enhanced behaviour of the RMS fluctuation velocities as seen in Figure (4.8) and Figure (4.9) and reaching the isotropic homogenous state after a short distance from the inlet plane, $x/\delta = 5$. The drop of the friction velocity values after the inlet plane increases with the decreasing of the inlet time scale as shown in Figure (4.12)-(d).

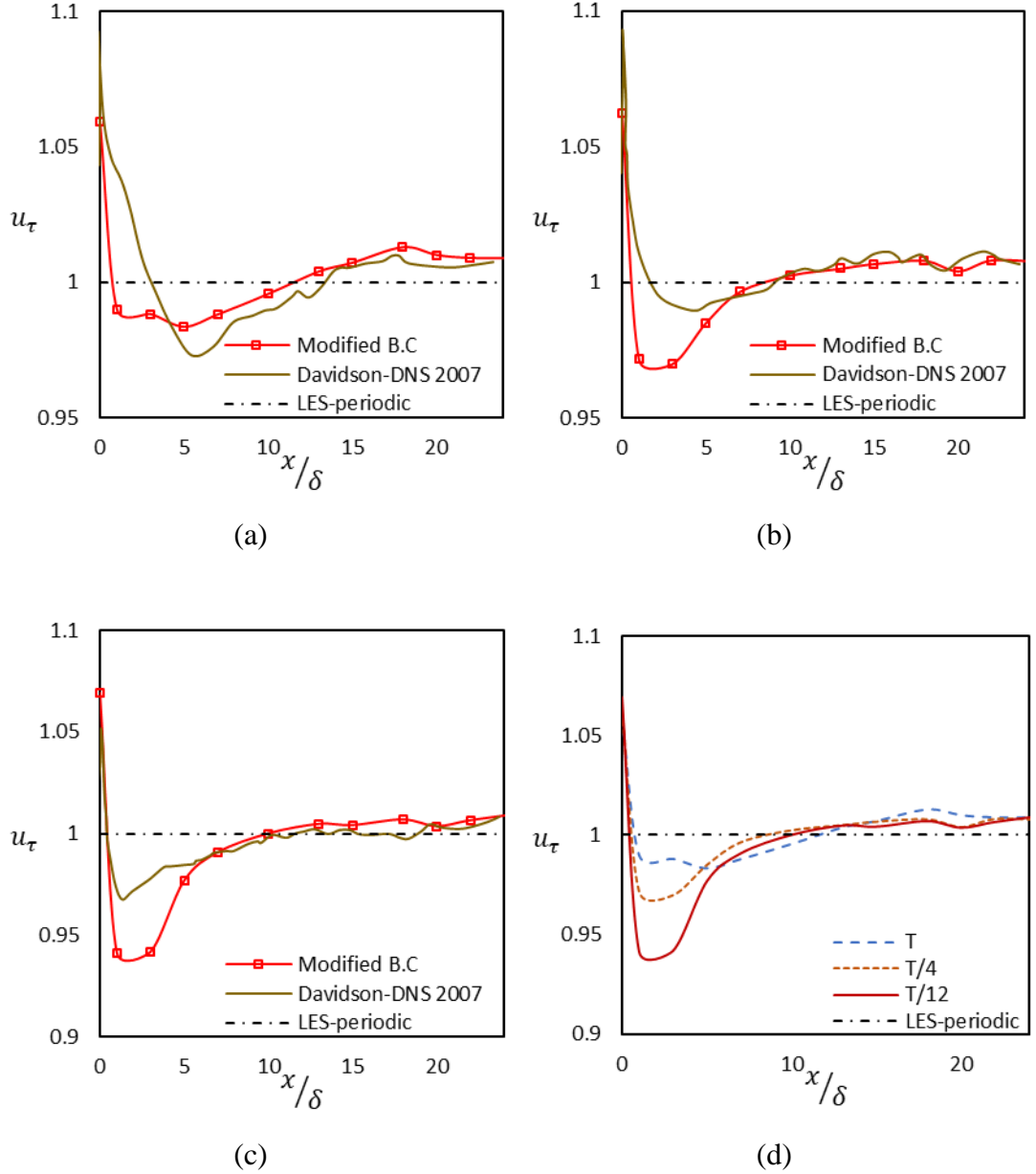


Figure (4.12) Sensitivity of the inlet boundary condition to different inlet time scales: (a) T_{in} , (b) $T_{in}/4$, (c) $T_{in}/12$, (d) all of them.

Cases (1, 4, 5) are used to study the sensitivity of the modified synthetic turbulence inlet boundary condition to different inlet length scales and presented in Figure (4.13). Friction velocity starts to be in a range of 1% from the target value of a

fully developed flow $u_\tau = 1$ at almost $x/\delta = 9$ for $0.5\mathcal{L}_t$ while $x/\delta = 8$ for \mathcal{L}_t and $x/\delta = 7.5$ for $1.5\mathcal{L}_t$, shown in Figure (4.13)-(a, b, c, and d). Small length scales produce better improvement with the modified boundary conditions and short developing distance until length scale \mathcal{L}_t , while for inlet length scale $1.5\mathcal{L}_t$ it starts to increase the developing length distance more than that one in the DNS boundary condition, Figure (4.13)-(a, b and c). Also, the big drop in the friction velocity values after the inlet plane has no significant effect on the performance of the modified boundary condition as it recovers itself quickly to match the required value.

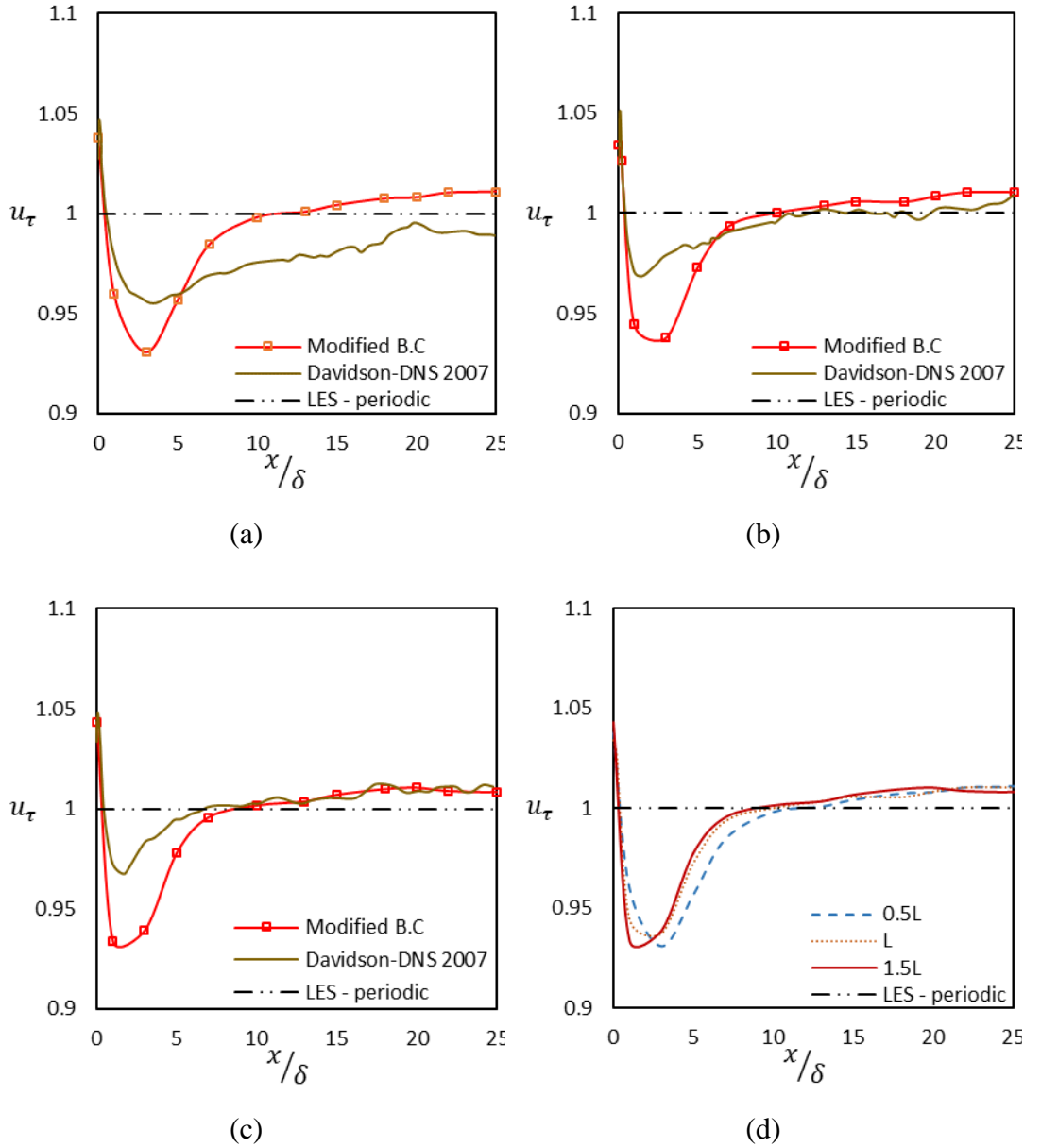


Figure (4.13) Sensitivity of the inlet boundary condition to different inlet length scales: (a) $0.5\mathcal{L}_t$, (b) \mathcal{L}_t , (c) $1.5\mathcal{L}_t$, (d) all of them.

Finally, as the inlet boundary condition depends on the friction velocity, as an input parameter to generate the mean velocity profile according to the law of wall, Therefore, a correlation is required to pre-estimate its values. Therefore, the inlet friction velocity is presented as a turbulence input parameter within the required inlet friction Reynolds number, $Re_{\tau,in}$. Different cases have been run to get a correlation between $Re_{\tau,inlet}$ and the required friction Reynolds number for the fully developed channel, $Re_{\tau,fullyDeveloped}$, according to Table (4.3), The final correlation obtained is as in equation (4.17) and (4.18), also drawn in Figure (4.14).

$$Re_{\tau,in} = 0.0003Re_{\tau,fully\ Developed}^2 + 0.8147Re_{\tau,fully\ Developed} + 54.869 \quad (4.17)$$

where

$$Re_{\tau,in} = \frac{u_{\tau,inlet}\delta}{\nu} \quad (4.18)$$

$$Re_{\tau,fullyDeveloped} = \frac{u_{\tau,fullyDeveloped}\delta}{\nu}$$

where, $u_{\tau,inlet}$ is an input parameter, while $u_{\tau,fullyDeveloped}$ is calculated from the required $Re_{\tau,fullyDeveloped}$, and ν is the kinematic viscosity.

Table (4.3) Inlet and fully developed $Re_{\tau,ratio}$.

$Re_{\tau,Inlet}$	$Re_{\tau,fullyDeveloped}$	$R(\frac{fullyDeveloped}{Inlet})$
180	168	0.9333
413	350	0.8474
500	480	0.96
525	500	0.9523
570	540	0.9473
600	563	0.9383
620	582	0.9387
788	700	0.8883
1000	869.085	0.8690

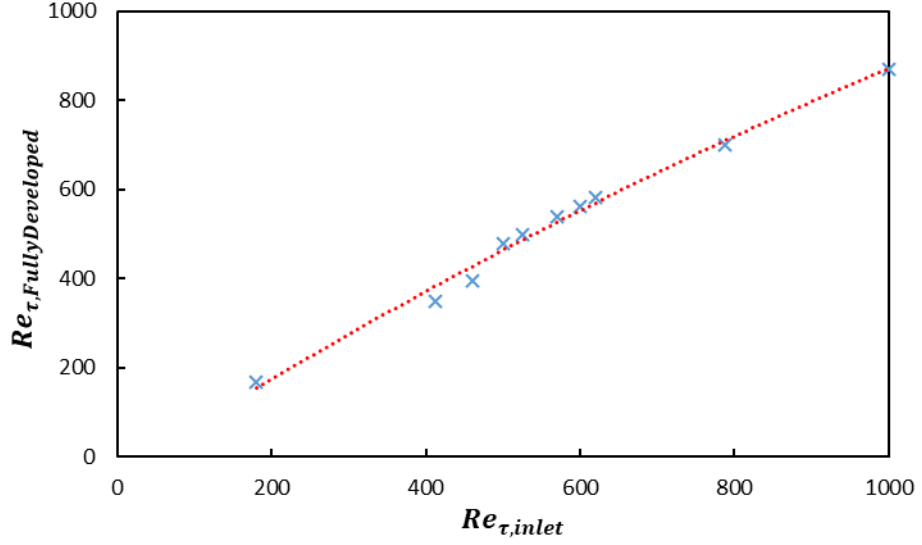


Figure (4.14) Controlling the required friction Reynolds number at the inlet plane.

4.5 Summery

A systematic synthetic isotropic turbulence inlet boundary condition for a transient Monotonically Integrated Large Eddy Simulation (MILES) is validated. This boundary condition is formulated to produce a synthetic isotropic turbulence field which is able to reproduce Reynolds stress anisotropy in a short developing streamwise distance from the inlet plane of the channel. The most important advantage for this boundary condition is that all the important turbulence parameters such as inlet length, time scales, and the required friction Reynolds number can be assigned precisely before the start of the simulation to generate the required turbulence flow field. Simulation results have shown improvement in the development of turbulence structures within a streamwise distance of 5 times the half channel height (δ) after the inlet plane which is shorter than the other streamwise distance from the similar boundary conditions. Also, the Reynolds shear stresses produce acceptable isotropic behaviour at the same streamwise distance. MILES solver is able to capture the turbulence structures in a turbulent channel flow at moderate friction Reynolds numbers. This improvement results in a considerable reduction in overall channel length and hence also a reduction in the associated computation cost.

Chapter (5)

Active Control for Drag Reduction in Transitional Boundary Layer

5.1 Introduction

Preventing the transition from laminar flow to turbulent state and reducing the skin friction drag maybe with the aims of relaminarization of the flow or controlling the turbulence structures produced by the eddies are in themselves problems of a high level of importance in practical applications (Ioannou and Farrell, 1999). Experimental and numerical investigations during the last decade on the drag reduction techniques have clearly shown that appreciable drag reduction of about 30-70% can be produced through either adaptive or non-adaptive schemes. Many different techniques have been used in that application as explained before in the literature review, Bewley (2001) and Tardu et al. (2008) can be reviewed for more ideas and developments. The main point of reducing the skin friction drag is by minimizing the wall shear in time and space. Blowing and suction method of fluid near the wall is one of the most common methods for minimizing the wall shear. Many studies applied this method numerically using (DNS) depending on detecting sensors through the flow for the drag active control purposes. The drawback of this method, when applied numerically, is the necessity of a dense mesh resolution near the wall to the range of the viscous sublayer thickness. As the streamwise and spanwise scales of the coherent eddies in the near-wall region have to be at least an order of magnitude larger than the required control space step. From the review, it can be said that the quasi-streamwise vortices generated in the buffer layer can extend to the range of about 300-500 streamwise wall units and about 100 spanwise wall units. The skin friction is developed by the ejections and sweeps of the vortices, while their regeneration and locations are random. Therefore,

the mesh resolution has to be dense enough to be able to catch all of these vortices and the blowing and suction effects on them.

In this chapter, skin friction drag reduction is investigated with a series of numerical experiments in a transitional boundary layer using an unsteady sinusoidal wave travelling in the spanwise direction generated by slits array on the bottom wall of the channel which acts as a flat plate. This slits array consists of 30 slits. By specifying a phase shift between the adjacent slits, the sinusoidal travelling wave can be produced. And as mentioned before that this kind of numerical simulations needs a dense mesh, so, the accuracy of the current simulations should be validated via a thorough grid independence study which will be considered as a future work for the current study. The main parameters that are investigated include the amplitude, frequency, phase shift between the slits, mean velocity gets out from the slits, inclination angle for the flow out from the slits. The maximum drag reduction and its location are measured by the maximum drop for the skin friction coefficient through the channel and a comparison between the results with and without control is applied.

5.2 Generation of bypass transition

The MILES solver and the isotropic homogeneous boundary condition, discussed in chapter 3 & 4, are applied to generate the bypass transition in the channel flow. The ability of that solver to produce the bypass transition and control the drag reduction in the transition region is investigated. The computational domain is expressed as a rectangular box, the dimensions and flow parameters, at the inlet plane, are illustrated in Table (5.1). $Re_x = 6000$ is applied as a constant property at the inlet boundary layer. All parameters are normalized by the average velocity \bar{U} and δ_{99}^0 which is the thickness of the boundary layer at a velocity equivalent to 99% of the free stream velocity at the inlet plane, (Ovchinnikov, 2006), as shown in Figure (5.1).

Table (5.1) Characteristics of the uncontrolled channels.

Mesh resolution $L_x \times L_y \times L_z$	U_∞ (m/s)	δ_{99}^0 (m)	Re_x	u_τ	$Tu\%$
$620\delta_{99}^0 \times 40\delta_{99}^0 \times 30\delta_{99}^0$	0.3	0.0012961	6000	0.01614	7
$1080\delta_{99}^0 \times 40\delta_{99}^0 \times 27\delta_{99}^0$	0.3	0.0012961	6000	0.01364	3

$Tu = 7\%$ is used as a part of the solver combination validation. In which, the computation experiments are discretized into 4.608×10^6 finite volume cells, to match that coarse mesh of Ovchinnikov (2006), with $(500 \times 96 \times 96)$ mesh divisions in streamwise, normal to the wall and spanwise direction respectively. The mesh distribution is adjusted in the streamwise direction to be fine in the expected region of the transition and uniform in the spanwise directions, while in wall-normal direction, an expanding mesh towards the channel centre is used such that the first mesh point next to the wall boundary is with wall units of $y^+ = 0.281$. The integral length scale equals to $L = 3\delta_{99}^0$ and the number of modes is $N = 150$. All parameters are normalized by the average velocity \bar{U} and δ_{99}^0 .

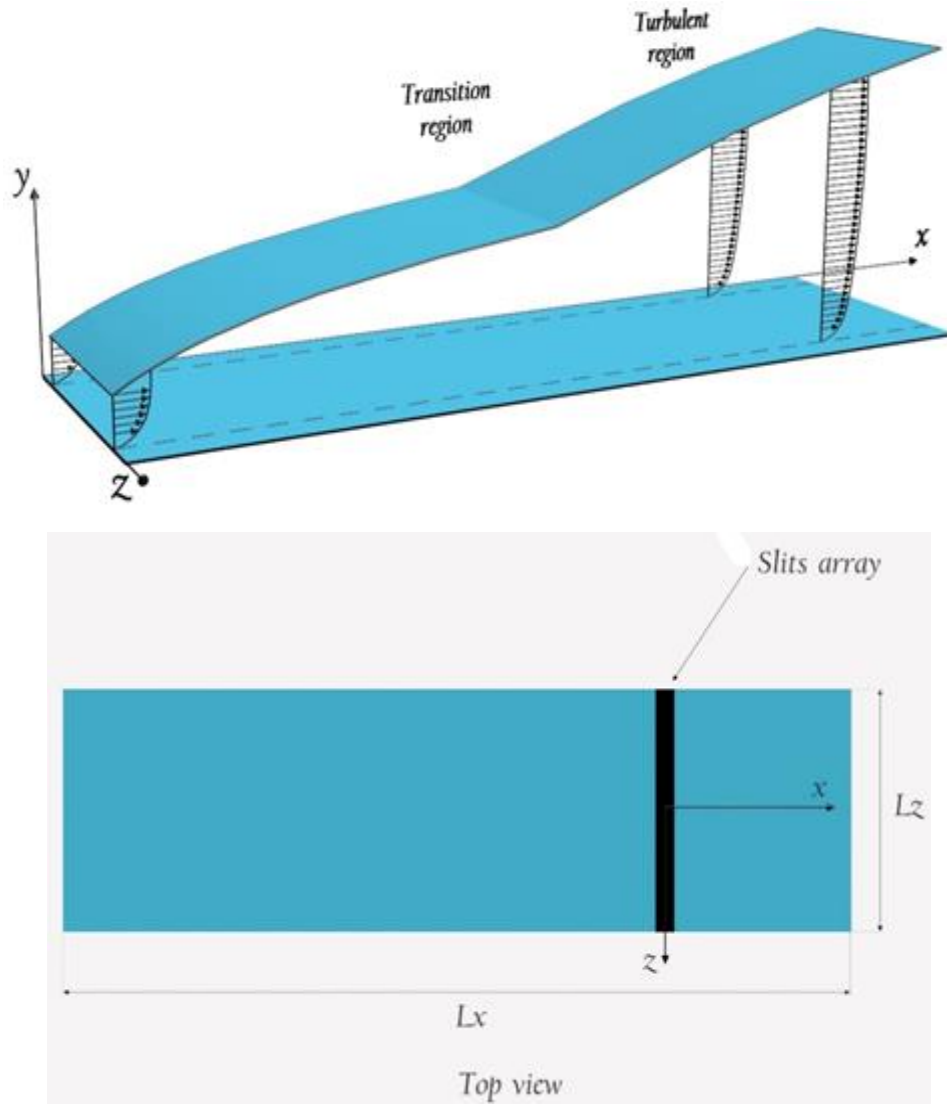


Figure (5.1) Schematic of channel set-up for the generation of bypass transition (not to scale).

The following boundary conditions are applied to the channel geometry:

1. In all numerical experiments, the velocities at the inlet plane are imposed by adding a specific amount of perturbations to a Blasius base flow. After generation the perturbations using the algorithm in Chapter (4), the perturbations are added to the mean velocity profile of a laminar flow. Then the resulted velocity profile is multiplied by the cut-off ratio which forces the final velocity field to go to zero at the wall, equation (5.1)

$$U_{in} = constant * \tanh\left(\frac{y}{\delta_{99}^0}\right) \quad (5.1)$$

Where ‘constant’ is the required inlet streamwise velocity.

2. The outlet boundary condition is applied as a non-reflecting boundary condition. This boundary condition prevents the backflow at the outlet of the channel. Also, to ensure the stability of the measured properties, the measurements from the last 5% of the channel length have been removed.
3. On the spanwise sides, a cyclic boundary condition is applied.
4. In the normal to the wall direction, both sides are applied as a wall.
5. In the free stream region, the mean velocities are applied as:

$$V_{in} = W_{in} = 0.$$

5.2.1 Free stream turbulence decay

After running the case for a suitable time and reaching the stable state, the turbulence intensity, Tu , equation (5.2), is found to decay in the streamwise direction starting from its value 7% at the inlet plane. For the validation purpose, it was compared with the experimental results of Roach and Brierlay (1989) with $Tu = 6\%$ and the DNS results of Ovchinnikov (2006), $Tu = 7\%$. From Figure (5.2), the free-stream turbulence decay is drawn against the streamwise Reynolds number, equation (5.3). It is clear that the current results are in good agreement with that one from Ovchinnikov (2006) with a higher rate of decay further than the experimental work.

$$Tu = \frac{\sqrt{\frac{(u_{rms}^2 + v_{rms}^2 + w_{rms}^2)}{3}}}{U_{\infty}} \quad (5.2)$$

$$Re_x = \frac{(x_0 + x)U_\infty}{\nu} \quad (5.3)$$

where x_0 is the streamwise distance to get the required boundary layer thickness δ_{99}^0 at the inlet plane of the channel.

From Roach and Brierlay (1989), the authors investigated the effect of the FST intensity in the streamwise direction and didn't investigate the effect of the integral length scale. While in Ovchinnikov et al. (2008), the authors referred to the definition of the energy dissipation length scale as in equation (5.4):

$$L_k = -\frac{k^{3/2}}{U_\infty \frac{dk}{dx}} \quad (5.4)$$

Where k denotes the turbulent kinetic energy, which can be related directly to the turbulence intensity. And as seen from the previous equation that the larger the length scale at the inlet plane, the smaller the turbulence intensity decay rate, also suggested by Jacobs and Durbin (2001) and Brandt et al. (2004). In the current research and for the validation purpose, a specific length scale at the inlet plane is used which is equivalent to that one used in Ovchinnikov (2006), $L = 3\delta_{99}^0$. While, in the previous experimental study of Roach and Brierlay (1989), the length scale was equivalent to $L = 18.2\delta_{99}^0$ and this explains the difference in the turbulence intensity decay rate between the curves in Figure (5.2).

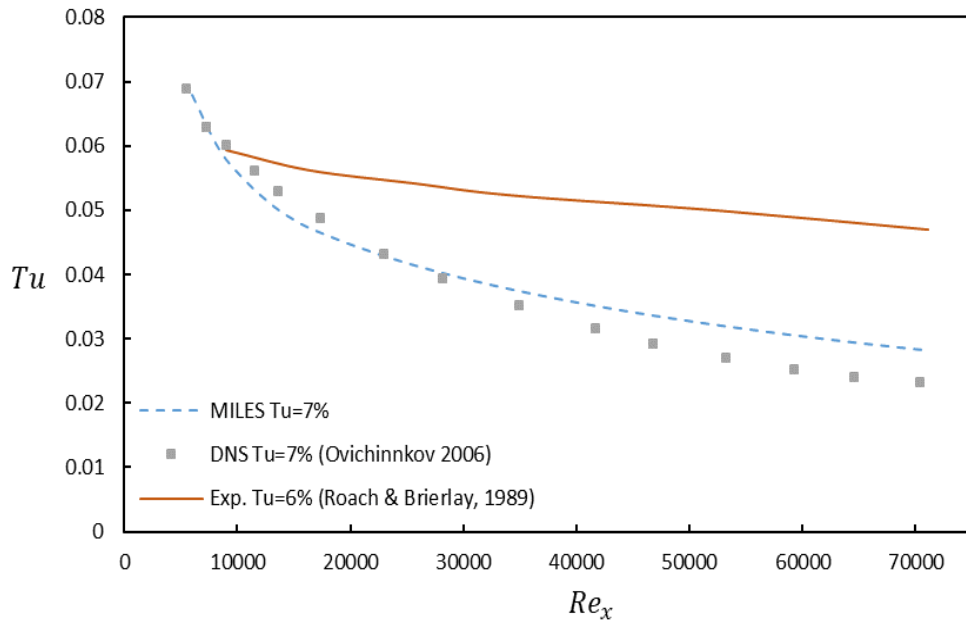


Figure (5.2) Turbulence intensity decay through the channel at $Tu = 7\%$.

5.2.2 Skin friction study of $Tu = 7\%$

The best effective parameter to visualize the transition to turbulence is the skin friction coefficient which originated mainly from the fluid viscosity on the surfaces. Due to the transition from laminar to turbulence within the boundary layer, the skin friction coefficient, C_f , equation (5.5), increases dramatically relative to its laminar values. To reduce C_f and consequently the skin friction drag and control other parameters such as heat transfer due to mixing, various active and passive flow control techniques have been designed (Kametani et al., 2016).

$$C_f = \frac{\overline{\tau_w}}{\frac{1}{2}\rho U_\infty^2} \quad (5.5)$$

where $\overline{\tau_w}$ is the averaged shear wall stress and U_∞ is the free stream velocity.

$$\overline{\tau_w} = \nu \frac{\partial \overline{U_{Mean}}}{\partial y}$$

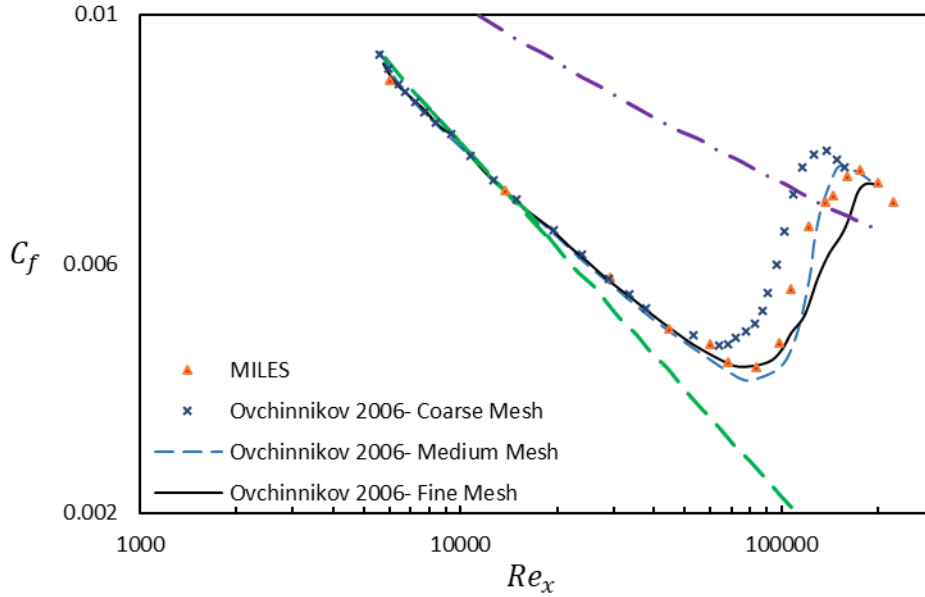


Figure (5.3) Skin friction coefficient relative to the previous DNS study (Ovchinnikov, 2006).

Ovchinnikov (2006) used in his study three different meshes to show the mesh resolution effect on the behaviour of the skin friction coefficient, coarse mesh of $(N_x \times N_y \times N_z) = (500 \times 96 \times 96)$, medium mesh of $(N_x \times N_y \times N_z) = (900 \times 180 \times 150)$, and fine mesh of $(N_x \times N_y \times N_z) = (1200 \times 256 \times 180)$. In the current part and for

validation purpose only, his course mesh was used to validate the performance of the solver. Figure (5.3) shows the development of the skin friction coefficient in the streamwise direction. It is clear that the resulted skin friction coefficient from the generated solver combined with the inlet boundary condition gives an acceptable behaviour with the medium mesh of the DNS study, (Ovchinnikov, 2006). The two curves give identical behaviour from the inlet plane till the start of the transition onset at $Re_x = 68000$ after that little deviation between them leads to early rising for the generated solver behaviour and then come together again near the turbulent curve. This deviation may be due to the difference in the streamwise mesh resolution. As a conclusion, the current solver is able to reproduce the transition clearly with acceptable accuracy relative to the DNS simulations. In the next section, a drag reduction study will be investigated via applying a sinusoidal travelling wave in the spanwise direction, applied at a specific streamwise distance from the inlet plane of the channel.

5.2.3 Effect of inlet turbulent Intensity on the bypass transition

Transitional flow study depends on many parameters especially the turbulence intensity value at the inlet plane of the channel. Here, an investigation to show the Tu effect on the location of the bypass transition onset is produced. As shown in Figure (5.4), the higher the turbulence intensity at the inlet, the faster the transition occurs. This phenomenon is logic as increasing Tu means increasing the capability of the flow to turn into turbulent flow, $Tu \geq 10\%$. And this can be illustrated from the start of each curve, as Tu increases, it goes near to the behaviour of turbulent flow curve. It can be also seen from Figure (5.4) that $Tu = 3\%$ has the longest streamwise distance to get the transition which is available to apply the active control before the transition occurrence. This effect was confirmed by the study of Ge et al. (2014) during his study for applying a model to produce the bypass transition and the inlet effective parameters on its onset. In addition to that, the scope of this research is to study the flow behaviour in the instabilities region before the transition onset, so, a $Tu = 3\%$, which is widely used in the bypass transition studies such as in Hack and Zaki (2014), at the inlet plane of the channel is used in the rest of the numerical simulations through this chapter.

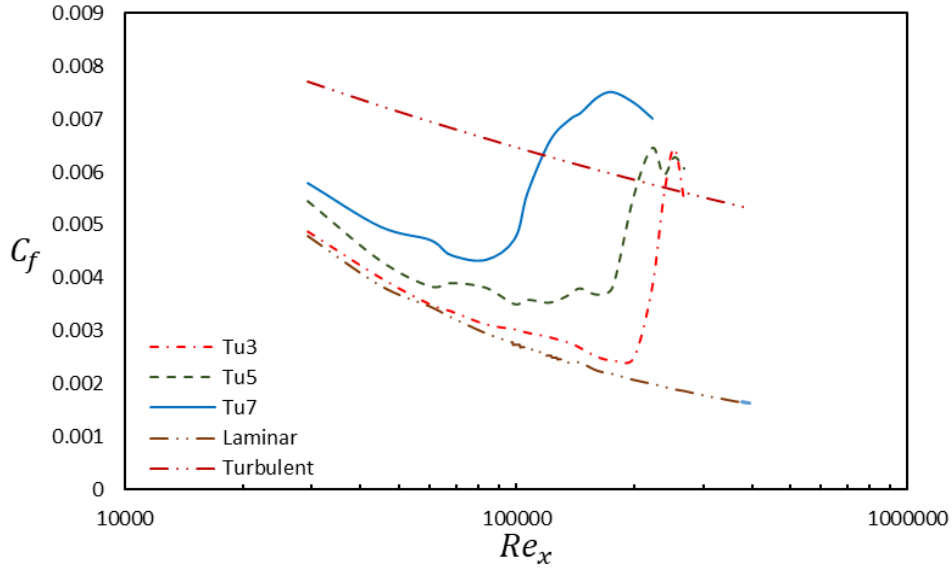


Figure (5.4) Tu effect on bypass transition onset.

5.2.4 Grid resolution study for $Tu = 3\%$

A grid refinement investigation has to be run to get some confidence in the accuracy of the numerical predictions of the MILES solver at the required turbulence intensity. Therefore, $Tu = 3\%$ at the inlet plane of the channel is chosen and verified by a comparison with the previous DNS study of Jacobs and Durbin (2001) with $Tu = 3.5\%$. The dimensions of the current computational box are addressed in Table (5.1). These dimensions are chosen to match those of Ovchinnikov (2006) with some difference, in which the channel length in the streamwise direction is elongated to avoid the disturbances due to the outlet boundary condition. A reasonable approximation is obtained when all cases are compared together. Table (5.2) shows the different mesh resolution used here.

Table (5.2) Meshes used in the grid refinement study

Meshes	$N_x \times N_y \times N_z$
Coarse	265x200x123
Medium (case 1)	400x250x123
Fine	485x300x123
Jacobs and Durbin 2001	2048x180x192

Figure (5.5) reports the effect of the mesh resolution study. It's clear that the fine mesh gives the nearest behaviour to the DNS study but with high computation cost

and long time. While the coarse mesh gives very early transition. As the accurate location of the bypass transition is not the main goal of this study, while, the main target is how to control the skin friction drag reduction in the transitional boundary layer and to delay the transition from its location. Therefore, the medium mesh is selected to be used in the next numerical experiments as it has medium size leading to medium cost and less time for simulations.

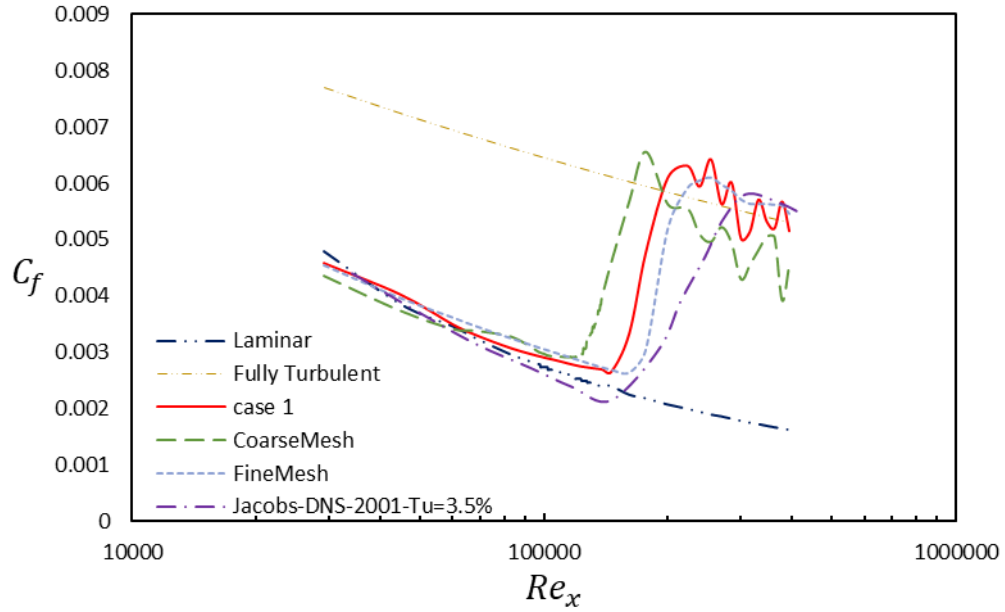


Figure (5.5) Mesh independence study for $Tu = 3\%$.

5.3 Active control via sinusoidal spanwise travelling wave

The streamwise vortices and the resulting low-speed streaks are the closest turbulence structures to the wall accompanied by high wall shear stress causing the skin friction drag. Therefore, trials to reduce or to disturb them with the blowing and suction effects of a sinusoidal wave are investigated. A well-behaved spanwise control of the drag has been introduced by Bai et al. (2014). Based on their experimental work, they found that when applying a sinusoidal travelling wave in the spanwise direction near to the wall, it is capable of achieving drag reduction of about 50% at 17 wall units downstream the actuators used to generate the spanwise wave in a turbulent boundary layer. This study was followed by the research of Li and Zhou (2016), which has ensured the effect of length of the slits, source of the sinusoidal wave. They showed that the increase in the slit length in the streamwise direction leads to increasing in the drag reduction achieved and produced 70% drag reduction.

In the current study, to investigate the effect of the external disturbances on the bypass transition and the skin friction drag, a sinusoidal travelling wave in the spanwise direction is applied using 30 slits with rectangular shapes in a transitional boundary layer. Each slit has the dimensions of $x^+ = 142$ and $z^+ = 3.3$ in wall units. As the average spacing between the low-speed streak and high-speed streak is evaluated to be in the range of 100 wall units, (Kline et al., 1967), the entire control array occupies 406 wall units in the spanwise. Also, this range of control dimensions was suggested by Jacobson and Reynolds (1998) in their experimental work to control the near-wall streaks in the region between the laminar and turbulent flow. The gap between each slit is around 9.9 wall units. And as mentioned before that this kind of numerical simulations needs a dense mesh, so, the accuracy of the simulations in the rest of the chapter should be validated via a thorough grid independence study which will be considered as a future work for the current study. The flow is uniformly distributed across each slit. While the peak and valley of the wave are generated by applying a phase shift between each slit. Also, the number of waves can be controlled via the value of the phase shift between slits.

The wave behaviour in Figure (5.6) is adjusted through its parameters such as the mean velocity, wave amplitude, frequency of the wave, number of slits and phase shift between slits. Equations (5.6) and (5.7) produce the formula of the slit output velocity. All values are normalized relative to the friction velocity of no control case, $u_{\tau, NoControl}$, in which $u_{slit} = 0$.

$$\begin{aligned} u_{slit,x} &= [UMean_{slit} + Asin(2\pi ft + N_w\varphi)] * \cos \theta \\ u_{slit,y} &= [UMean_{slit} + Asin(2\pi ft + N_w\varphi)] * \sin \theta \end{aligned} \quad (5.6)$$

$$u_{slit,z} = 0$$

$$\varphi = (slitOrder - 1) * \left(\frac{360}{slitsNumber - 1} \right) \quad (5.7)$$

where

$u_{slit,x}$... streamwise (x) component of the slit velocity vector at the wall
 $u_{slit,y}$... normal to the wall (y) component of the slit velocity vector at the wall

$u_{slit,z}$... spanwise (z) component of the slit velocity vector at the wall
$UMean_{slit}$... mean velocity out from the slit
A	... wave amplitude
φ	... phase shift between slits, Figure (5.7)
N_w	... number of waves
f	... wave frequency
θ	... wave inclination angle measured from the (+ve) streamwise direction, illustrated in Figure (5.8)

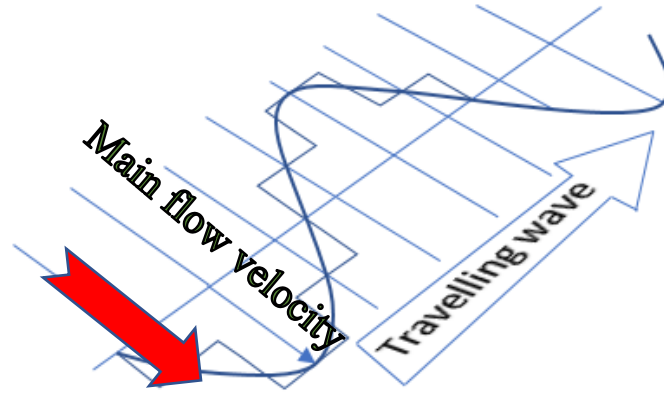


Figure (5.6) Sinusoidal wave travelling in the spanwise direction.

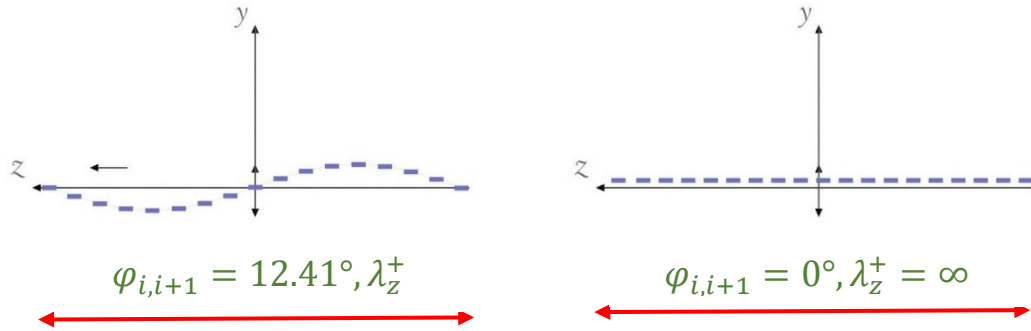


Figure (5.7) Sinusoidal wave in the normal to the wall axis.

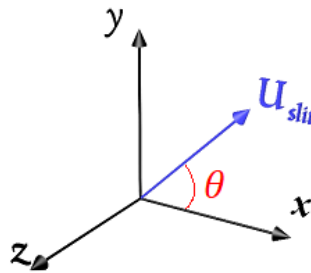


Figure (5.8) Inclination angle θ .

In all the following simulations, illustrated in Table (5.3), the output flow from each slit is uniform with a specific amplitude and phase shift. During all cases through the current study, the amplitude and the frequency of each wave are introduced as in equations (5.8) and (5.9). Turbulence intensity of 3% is selected for all cases.

Table (5.3) Set of wave parameters affecting the drag reduction δ_{τ_w} for $Tu = 3\%$.

case	$\frac{A}{u_{\tau, NoControl}}$	f^+	θ	N_w	$\frac{UMean_{slit}}{u_{\tau, NoControl}}$	Slit location Δx^+	Slit length Δx^+
Case 1	-	-	-	-	-	-	-
Case 2	0.198	0.42	90	1	0.66	4075	163
Case 3	0.396	0.42	90	1	0.66	4075	163
Case 4	0.198	0.42	3	1	0.66	4075	163
Case 5	0.198	0.42	10	1	0.66	4075	163
Case 6	0.198	0.42	45	1	0.66	4075	163
Case 7	0.198	0.42	135	1	0.66	4075	163
Case 8	0.198	0.42	160	1	0.66	4075	163
Case 9	0.198	0.1	90	1	0.66	4075	163
Case 10	0.198	0.2	90	1	0.66	4075	163
Case 11	0.198	0.6	90	1	0.66	4075	163
Case 12	0.198	0.42	90	3	0.66	4075	163
Case 13	0.198	0.42	90	4	0.66	4075	163
Case 14	0.198	0.42	90	5	0.66	4075	163
Case 15	0.198	0.42	90	1	0.2	4075	163
Case 16	0.198	0.42	90	1	1.5	4075	163
Case 17	0.198	0.42	90	1	3	4075	163
Case 18	0.198	0.42	90	1	0	4075	163
Case 19	0.198	0.42	90	1	0.66	3740	163
Case 20	0.198	0.42	90	1	0.66	5435	163
Case 21	0.198	0.42	90	1	0.66	4075	245

$$A^+ = \frac{\bar{U}}{u_{\tau, NoControl}} \quad (5.8)$$

$$f^+ = \frac{fv}{u_{\tau, NoControl}^2} \quad (5.9)$$

The results report the effect of different wave parameters by expressing the drag reduction percentage $\delta_{\tau_w} \%$ as in equation **Error! Reference source not found.** Drag reduction, $\delta_{\tau_w} \%$, is defined as the ratio between the reduced pumping power when the waves are applied and that one before applying the waves.

$$\delta_{\tau_w} = \frac{\overline{\tau_{w,control}} - \overline{\tau_{w,NoControl}}}{\overline{\tau_{w,NoControl}}} * 100\% \quad (5.10)$$

δ_{τ_w} is measured at first cell near to the wall according to $\overline{\tau_w}$ at $y^+ = 0.6714$

All those test cases are executed in parallel using 224 processors on the HPC cluster. The computation total time is in the order of 100 hours of wall time per processor.

5.4 Results

The goal of these numerical simulations is to gain insight into the active control of the bypass transition process and its effect on the skin friction drag reduction. The sinusoidal wave is generated through an array of 30 slits at a distance of $\Delta x^+ = 4075$ in wall units from the inlet plane of the channel to give suitable distance for the flow to be stable as explained before in Chapter (3) and Chapter (4). The sinusoidal wave parameters are studied according to the cases in Table (5.3) and give the following results. But first, a base case without applying the active control, case 1, is run to prepare the computational domain for generating the sinusoidal wave into the flow and get the behaviour of the bypass transition and its location through the channel. As shown in Figure (5.9), the behaviour of skin friction coefficient, C_f , of $Tu = 3\%$ is validated relative to the previous DNS study of Jacobs and Durbin (2001) with a mesh size of (2048*182*190) and $Tu = 3.5\%$, studied before in Section 5.2.4. Their behaviour is almost identical in the laminar region till the transition start at which case 1 behaviour rises sharply to reach the turbulent state before the DNS results. This is because of the difference in the mesh resolution between the two cases in the streamwise direction, this effect appears obviously in Ovchinnikov (2006) when he runs a mesh resolution test for $Tu = 7\%$.

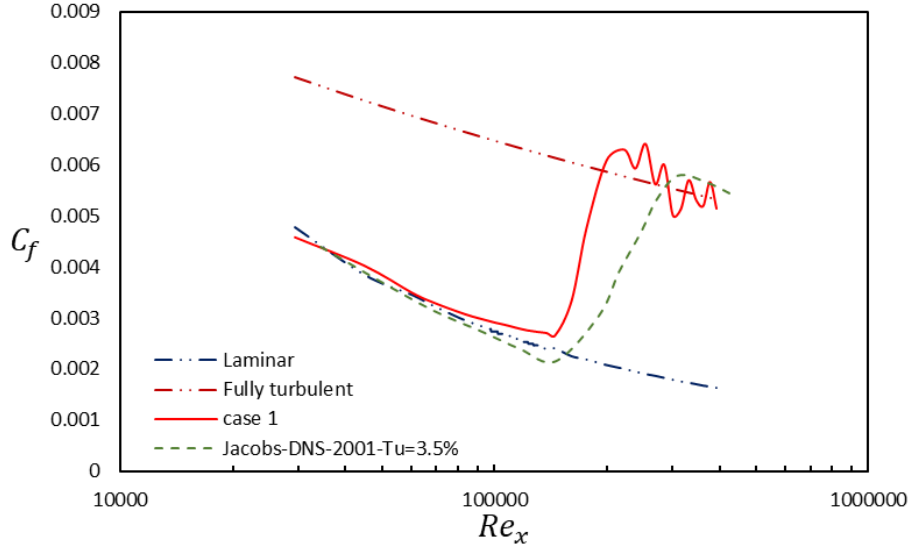


Figure (5.9) Validation of skin friction coefficient behaviour with $Tu = 3\%$.

5.4.1 Sinusoidal wave and mesh symmetry

Streamwise vortices are always above and slightly further than the regions of high skin friction drag (Kravchenko et al., 1993), therefore, any disturbances applied on the wall will affect the ejection and sweep processes of the vortices which in turn change the skin friction drag on the wall. By applying the sinusoidal travelling wave in the spanwise direction via the slits, case 2, with $A = 0.3U_{Mean_{slit}}$ and $f^+ = 0.42$, it starts to change the flow near to the wall and its behaviour. According to Figure (5.10), the skin friction coefficient starts at the inlet of the channel with the same way as the curve of the laminar flow. While it suffers from a drop before the start of the slits and recovered its values again at the bypass transition onset. This may be due to that the wave weakens the streamwise vortices and reduces the wall shear stresses as it is injected normal to the streamwise vortices direction. Figure (5.11) shows that the decreasing in the skin friction coefficient reaches its maximum value and starts to regain its original values very slowly. The distance required for the skin friction coefficient to regain its original values is much larger than that one when applying the control in a turbulent boundary layer, $Tu \geq 10\%$, such as in (Bai et al., 2014) in which they got $\Delta x^+ = 160$ with maximum drag reduction of 50%, and that one from Li and Zhou (2016) of $\Delta x^+ = 460$ with a maximum drag reduction of 70%, illustrated in Figure (5.11). This extension in the streamwise distance to recover the original values of the skin friction may be due to the effect of the additional term of

$U_{Mean_{slit}}$ in the equation of the slit velocity, equation (5.6), so, it cannot be considered as a zero net mass flux, while this amount of added mass flux is very small relative to the mass flux through the channel.

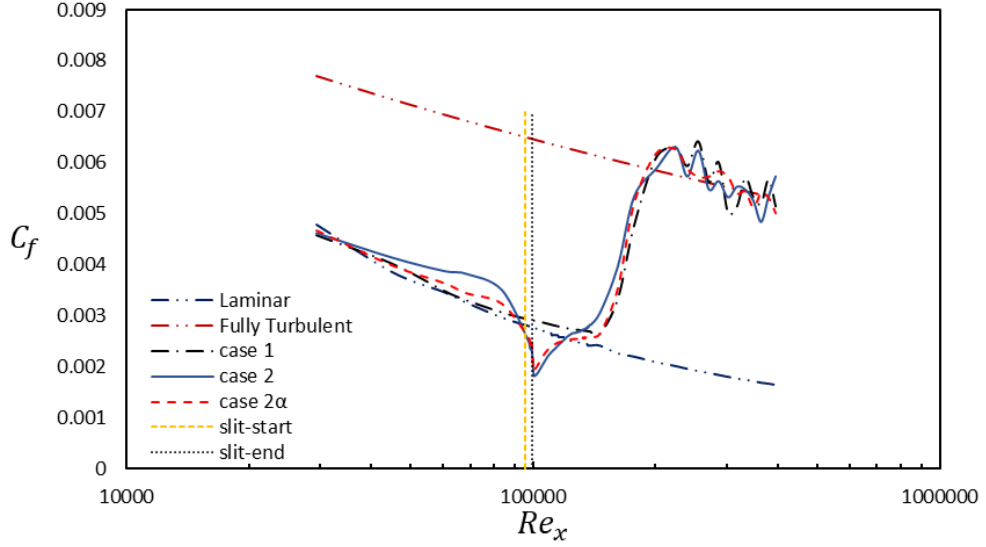


Figure (5.10) Skin friction coefficient behaviour with applying the sinusoidal travelling wave and comparing with the symmetry case.

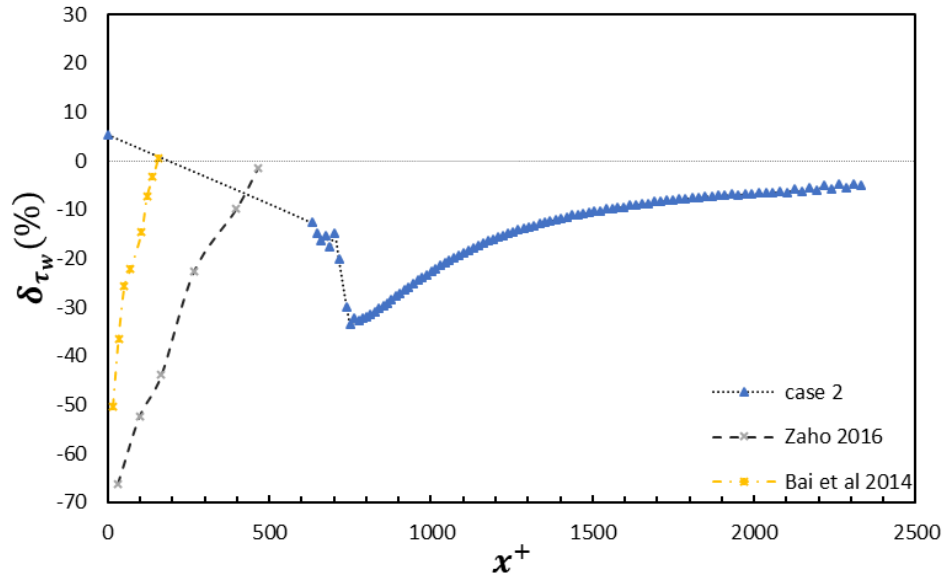


Figure (5.11) Streamwise location for the maximum drag reduction and distance required for the drag recover its original values.

To save the time and the computation resources, the channel is divided into two halves in the wall-normal direction. Therefore, case 2 will be called as case 2α in which the top boundary condition, at the channel centre, is applied as a symmetry plane with a modified mesh resolution of the channel with (400x125x123) cells and

dimensions of $(1080\delta_{99}^0 \times 20\delta_{99}^0 \times 27\delta_{99}^0)$ in the streamwise, normal to the wall and spanwise directions respectively. It can be noticed from Figure (5.10) that the onset of the bypass transition was slightly delayed in the streamwise direction when using the symmetry boundary condition for the top surface at the channel centre relative to the case of the complete channel. This delay of the bypass transition onset was mentioned in the study of Ovchinnikov et al. (2008), in which the bypass transition onset was delayed by $\Delta x^+ = 50$. Same behaviour was produced in the study of Ge (2015), in which an intermittency model was proposed for representing the bypass transition in unsteady (RANS) computations through a channel flow. Also, the streamwise velocity fluctuations at different streamwise locations, $x/\delta_{99}^0 = (1, 3, 20, 30)$, were compared in the case of symmetry mesh to that one of a complete channel and the results produced a good agreement between the two cases, as shown in Figure (5.12).

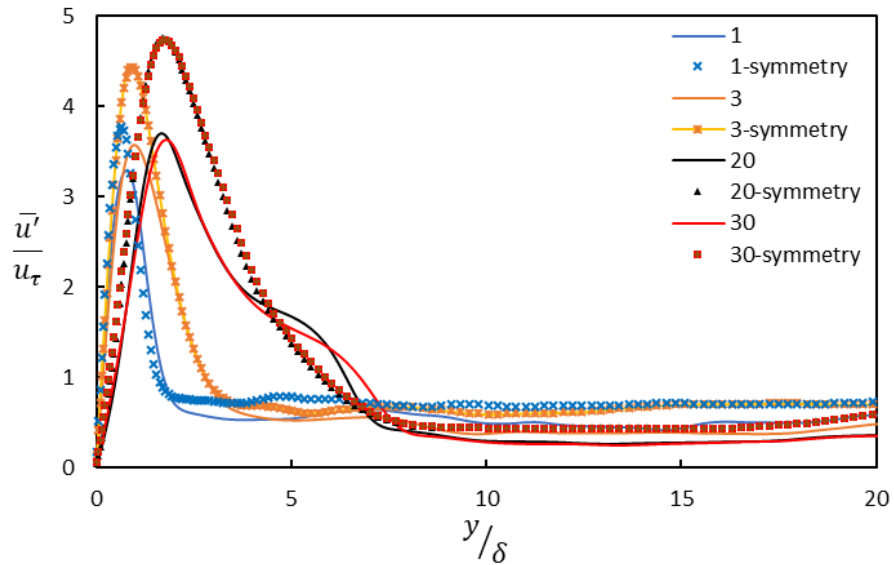
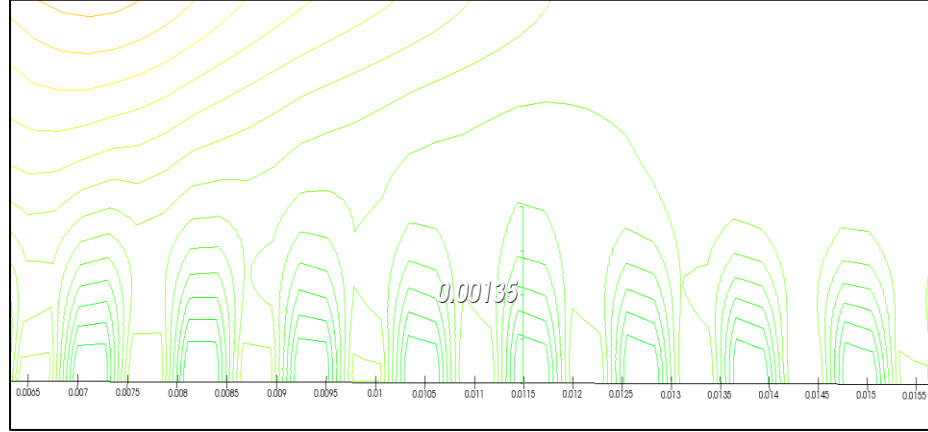


Figure (5.12) Streamwise velocity fluctuations of the symmetry mesh and the complete channel mesh at different streamwise locations

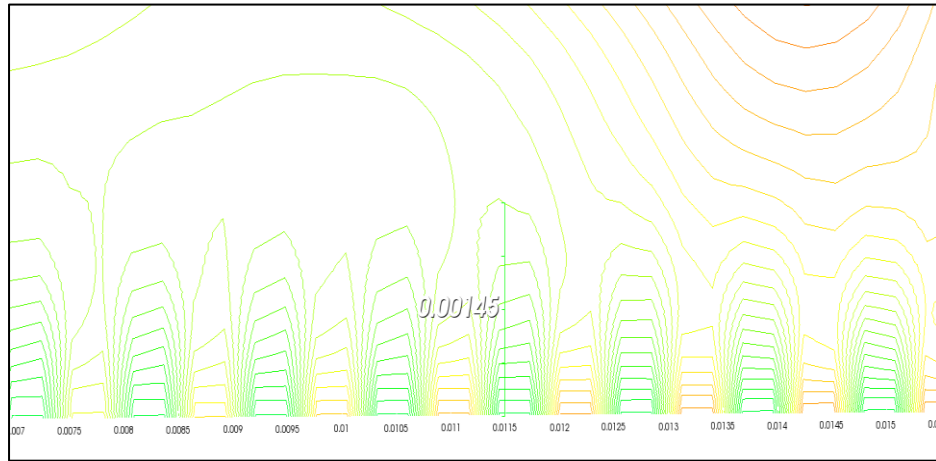
5.4.2 Effect of wave amplitude

Wave amplitude refers to the penetration depth of the wave inside the main flow and respectively how far the wave is able to affect the turbulence structures of the flow in that region near to the wall. In case 3, the amplitude of the sinusoidal wave is doubled relative to that of case 2α . Figure (5.13) shows the penetration depth of the wave inside the main flow and how it can change the velocity field structure around it and redistribute its profile again relative to the parameters of the wave and its

amplitude. This range of wave amplitude has no great effect on the maximum drag reduction even in value or location relative to the centre of the slit as shown in Figure (5.14). It gives almost the same $\delta\tau_w$ as that one in case 2 α . Figure (5.15) presents the streamwise distance that skin drag reduction value takes to regain its original value after its reduction due to increasing the wave amplitude.



(a)



(b)

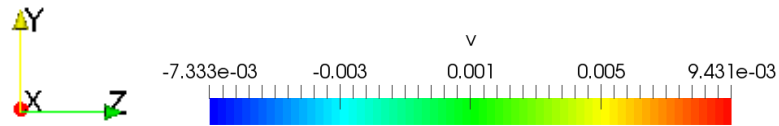


Figure (5.13) Wave penetration inside the main flow and velocity contours out from slits: (a) case 2 α and (b) case 3.

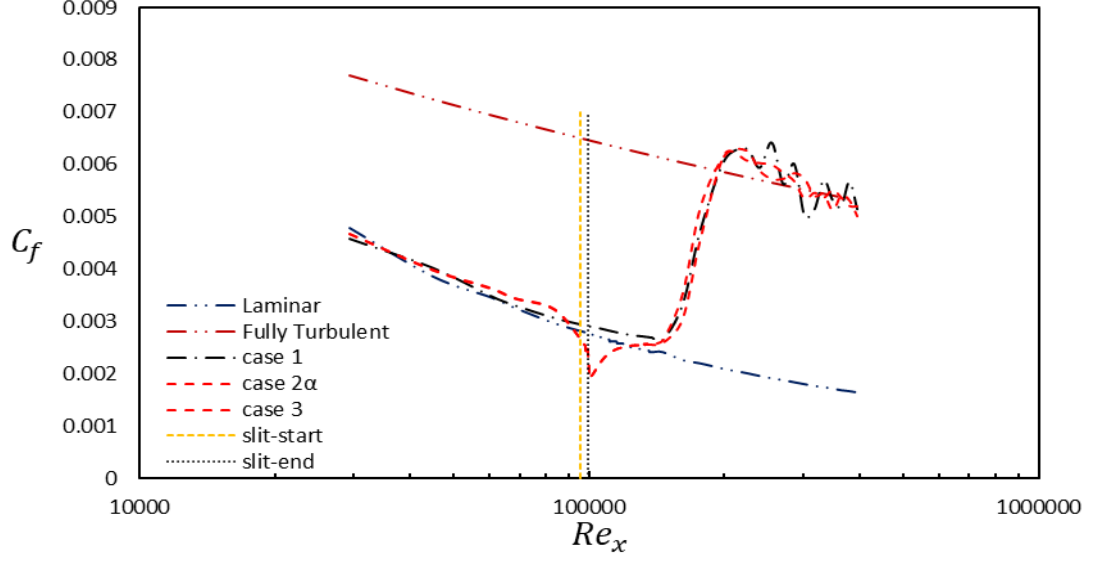


Figure (5.14) Skin friction coefficient dependence on wave amplitude.

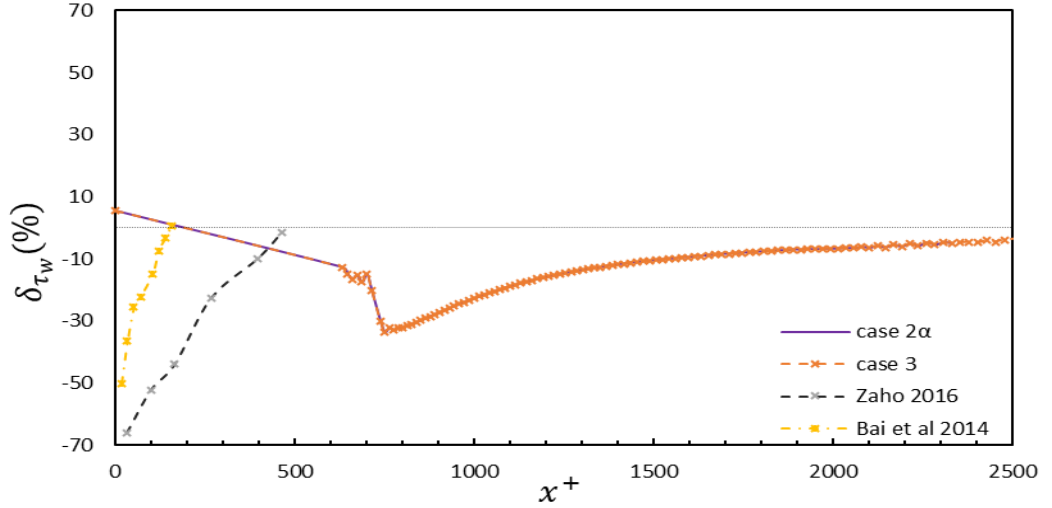


Figure (5.15) Streamwise location for the maximum drag reduction depending on wave amplitude.

5.4.3 Inclined spanwise travelling wave

Here in this section, the sinusoidal wave travelling in the spanwise direction is divided into two components one in the normal to the wall direction as in case 2α and 3 and the other one in the streamwise direction according to the inclination angle θ , illustrated in Figure (5.8). Many angles are examined (such as $\theta = 3, 10, 45, 90, 135, 160$). Figure (5.16) presents the skin friction coefficient C_f . Most of these angles produce similar behaviours but differ in the value of the maximum $\delta\tau_w$ and its location. Case 4 in Figure (5.16)-(a), $\theta = 3^\circ$, subjects to a

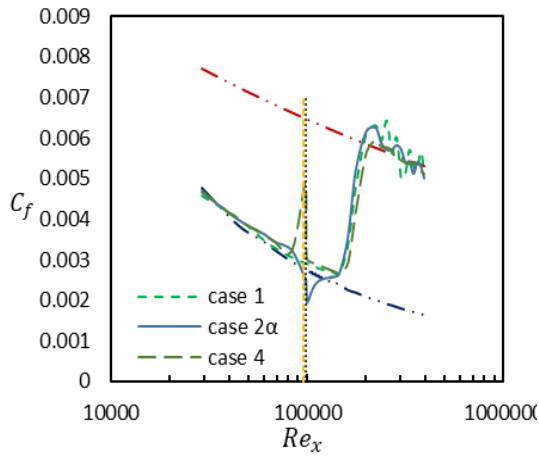
sudden increase in the drag before the slits and this is due to the injected wave leads to increase in the boundary layer thickness after the end of the slits and overflow above the boundary layer as the injection happens very close to the wall. This phenomenon results in increasing the mixing and the wall shear stress in that region before the slit. This mixing enhances itself and stabilizes the low-speed streaks by the end of the slits more than the original case, case 2α . This enhancement after the slits leads to delaying the bypass transition onset with about more than 4.5 times the length of the slits in the streamwise direction. While in case 5 in Figure (5.16)-(b), $\theta = 10^\circ$, as the inclination angle increases, the boundary layer thickness increases more, and the mixing region extends over the slits leading to an early transition to turbulent flow. By increasing the inclination angle, the flow starts to stabilize, and the skin friction coefficient comes back to the normal behaviour of case 2α as in case 6 in Figure (5.16)-(c), $\theta = 45^\circ$, where C_f goes smoothly in good agreement with that curve of case 2α till the region before the slits. At this point, it slightly increases due to the mixing before the slits but here its rise is low as with that angle the injected flow starts to have a weighted component in the normal to the wall direction which here decreases the vortices amplitude. By the end of the slits, it gives a smaller drag reduction than that one of case 2α due to stabilizing the streaks and reduce their instabilities until the transition occurs. Case 7 in Figure (5.16)-(d), $\theta = 135^\circ$, this angle gives the best performance for the drag reduction as it gives a sudden drop at the slits end and delays the bypass transition occurrence with a streamwise distance of more than 5 times and half of the length of the slits. This is because of the effect of blowing and suction of the sinusoidal wave which is able to relaminarize the flow after the slits by reducing the instabilities and enhancing the low-speed streaks when it is in the opposite direction to the streamwise vorticity. Although the total drag reduction is not so big, it was able to delay the bypass transition onset. Case 8 in Figure (5.16)-(e), $\theta = 160^\circ$, the skin friction coefficient drop starts to decrease again as the flow direction from the wave is nearly against the main flow direction and this may raise the rate of disturbances which leads to increasing the amplitude of the streaks instabilities.

Figure (5.17) presents all behaviours of C_f together in one curve for the comparison purpose. Also, the streamwise distance for each case to recover its original value is shown in Figure (5.18). Case 2α and 7 are the best cases without any drag increase through the flow and maximum streamwise distance to reach the initial

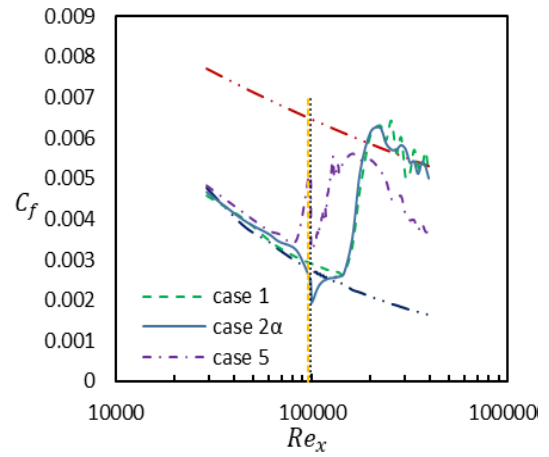
amplitude of the wall shear stress again before the transition onset. The maximum drag reduction percentages for all cases are presented in Table (5.4). Finally, an indication for the relation between the effect of the inclination angle of the injected sinusoidal wave and the maximum drag reduction occurs through the flow in the region before the transition onset is illustrated in Figure (5.19). δ_{τ_w} has no values in the small angles, θ , and start its appearance by increasing the angle till its maximum at $\theta = 90$ and then decreases again by increasing θ .

Table (5.4) Maximum drag reduction achieved by changing the inclination angle θ . (The values presented in this table are for indication only. For more information, see the Appendix)

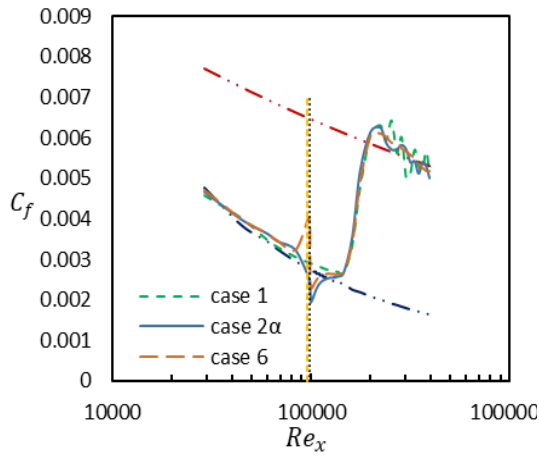
Angle θ	3	10	45	90	135	160
case	4	5	6	2α	7	8
δ_{τ_w} %	0	0	21.91	33.54	29.06	15.23



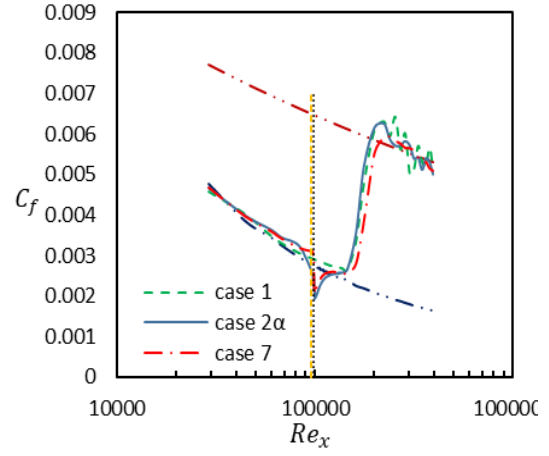
(a)



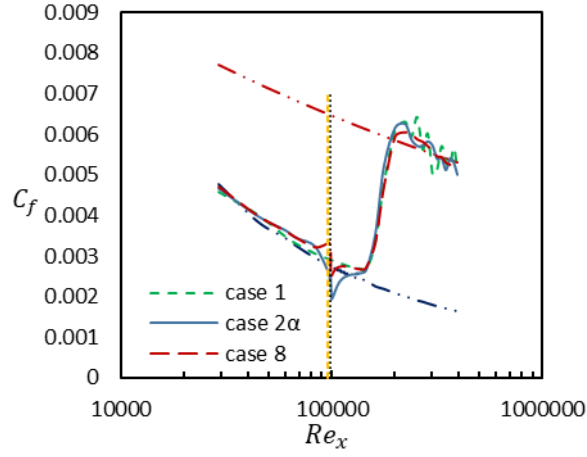
(b)



(c)



(d)



(e)

Figure (5.16) Skin friction coefficient dependence on inclination angles
(a) $\theta = 3^\circ$, (b) $\theta = 10^\circ$, (c) $\theta = 45^\circ$, (d) $\theta = 135^\circ$, (e) $\theta = 160^\circ$.

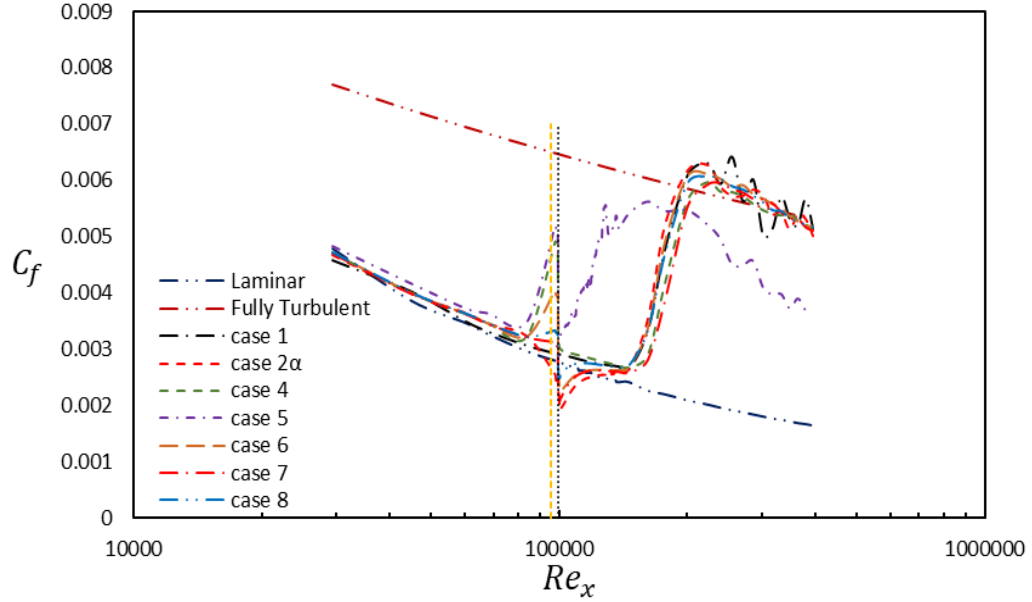


Figure (5.17) Skin friction coefficient dependence on the inclination angle.

The variation in the inclination angle of the wave from the slits leads to change in the skin friction drag reduction rate. To explain the angle effect, the streamwise vortices are investigated via its contours at different streamwise locations for case 2α , as in Figure (5.20), case 5, as in Figure (5.21), and case 7, as in Figure (5.22). These figures illustrate the vorticity behaviour and how it changes in the near-wall region, for example in case 2α , Figure (5.20)-(a, b, c, d) show how the vorticity radius decreases over the slits and turn the intermediate spaces between them to enhanced low-speed streaks. This process reduces the instabilities and leads to a drop in the skin

friction coefficient. While in case 5 with $\theta=10$ the number of vortices increases due to this inclination angle and this clear in Figure (5.21)-(b). As a result, the skin friction coefficient increases rapidly after the slits end leading to very early transition. On the other hand, case 7 with $\theta=135$, the vorticity distribution at the slit start was uniform with a large radius, Figure (5.22). By going downstream over the slit, the vorticity radius decreases and lead to a drop in the skin friction coefficient. In that time, vorticity distribution adjusted the behaviour of the low-speed streaks to get a delay in the bypass transition onset.

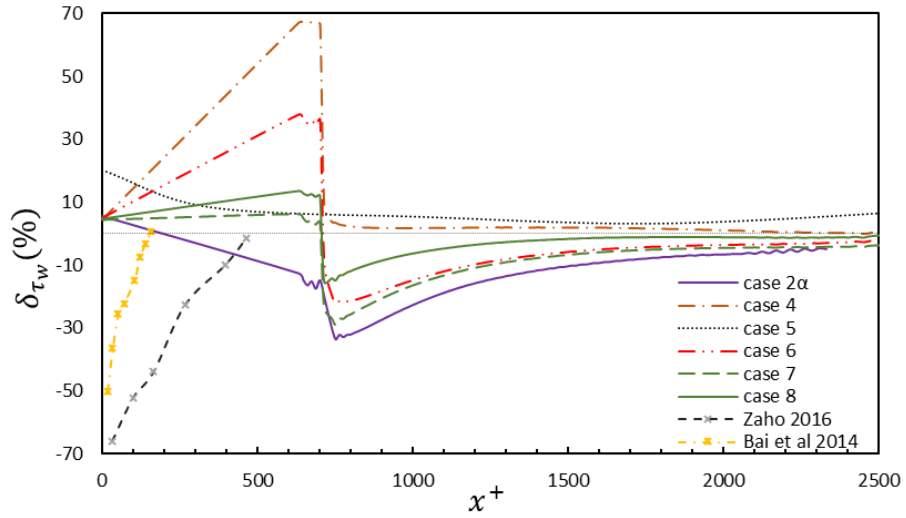


Figure (5.18) Streamwise location for the maximum drag reduction depending on the angle of inclination.

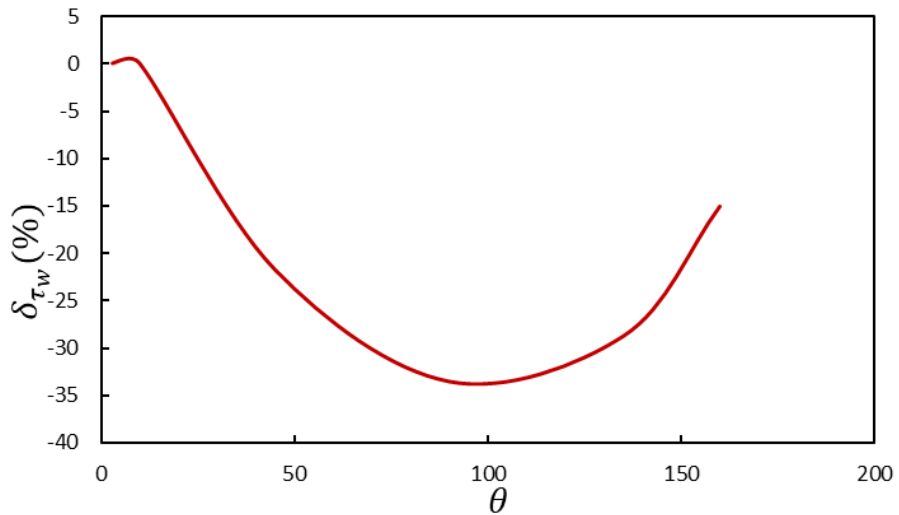
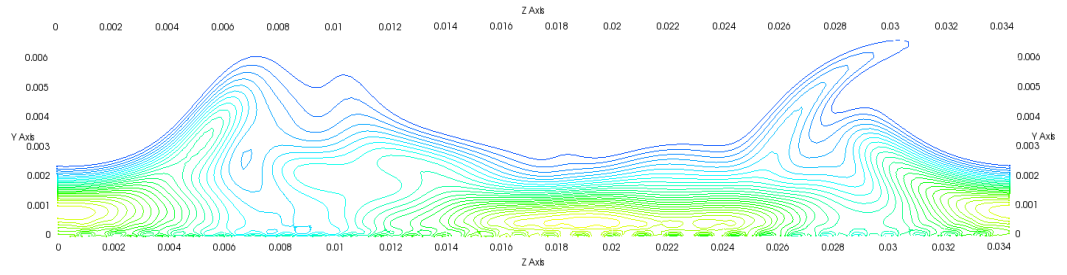
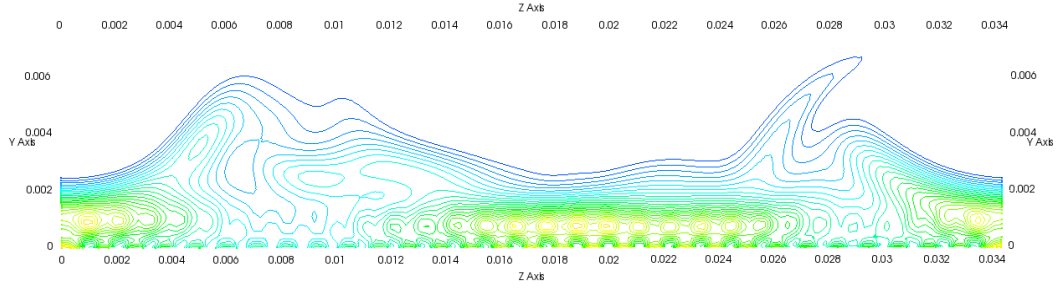


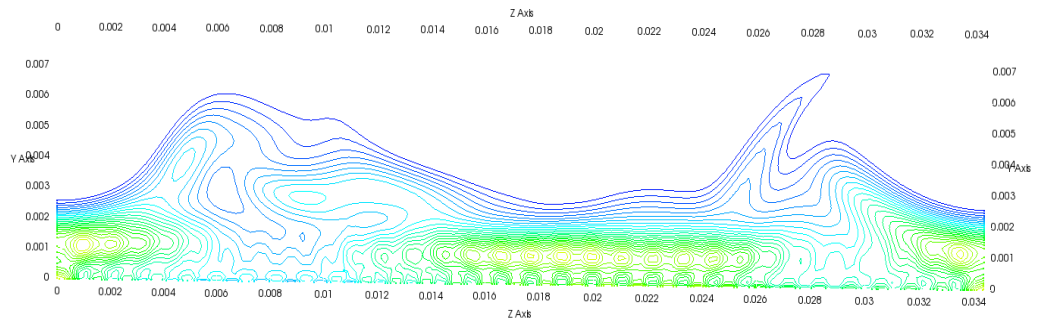
Figure (5.19) Maximum drag reduction, δ_{τ_w} vs the inclination angle θ .



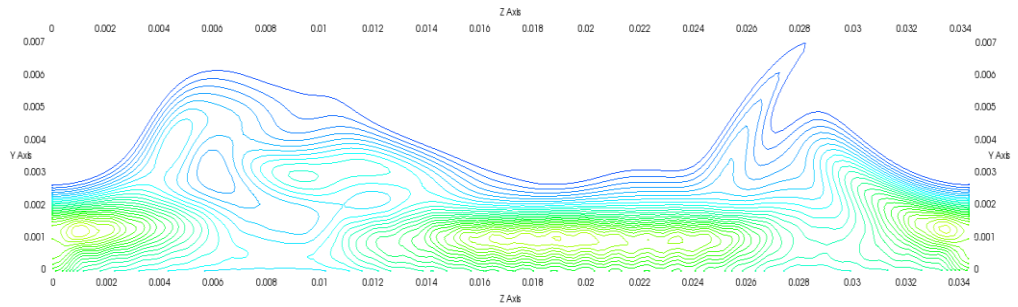
(a)



(b)



(c)



(d)

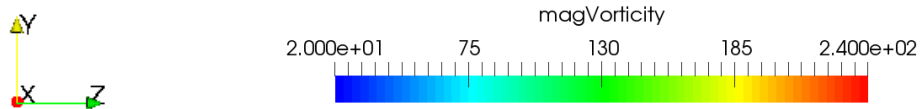


Figure (5.20) Effect of inclination angle on the streamwise vortices, case 2α , $\theta = 90^\circ$: (a) $\Delta x^+ = -82$, (b) $\Delta x^+ = 0$, (c) $\Delta x^+ = 82$, (d) $\Delta x^+ = 136$.

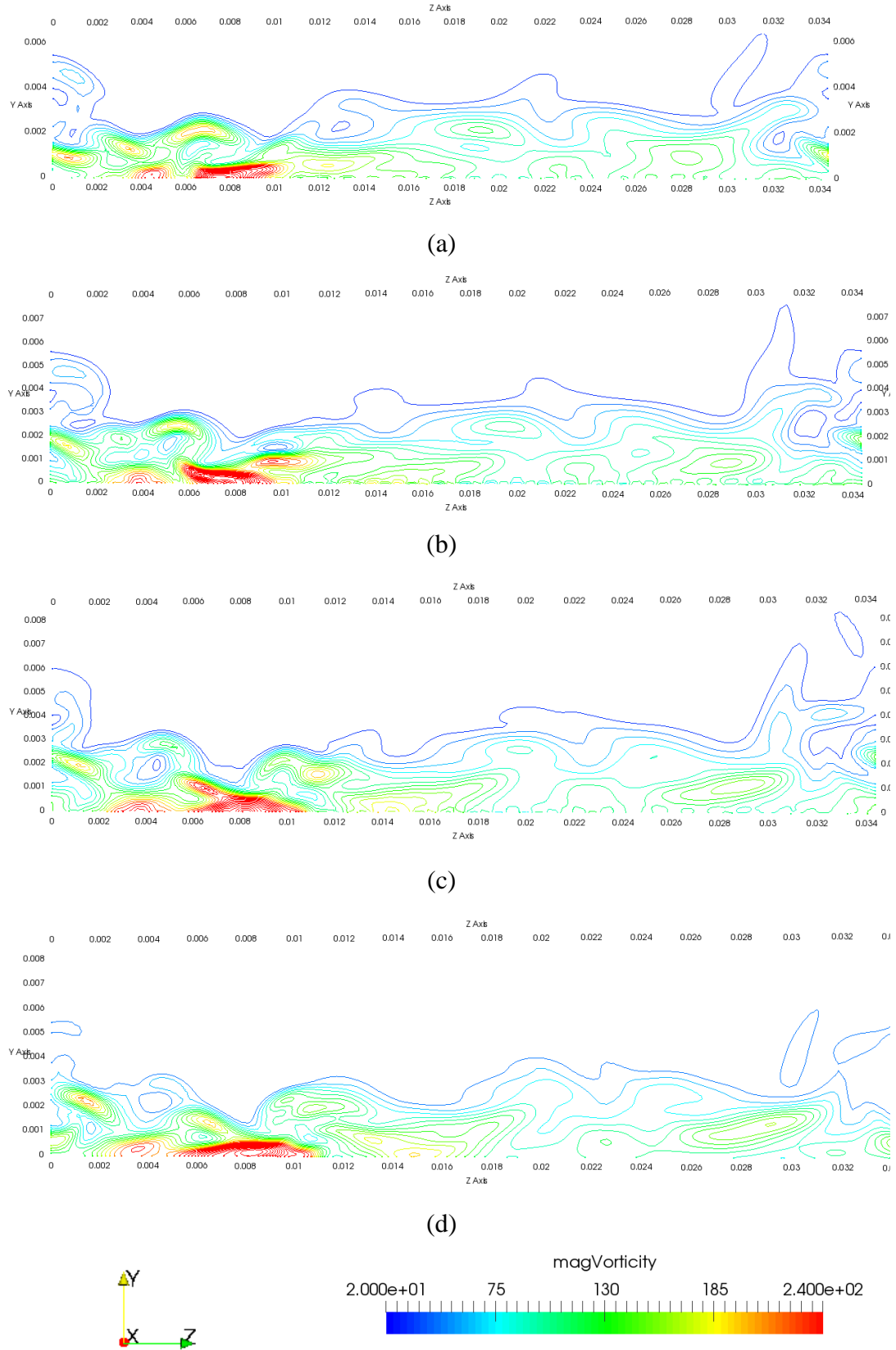


Figure (5.21) Effect of inclination angle on the streamwise vortices, case 5, $\theta = 10^\circ$: (a) $\Delta x^+ = -82$, (b) $\Delta x^+ = 0$, (c) $\Delta x^+ = 82$, (d) $\Delta x^+ = 136$.

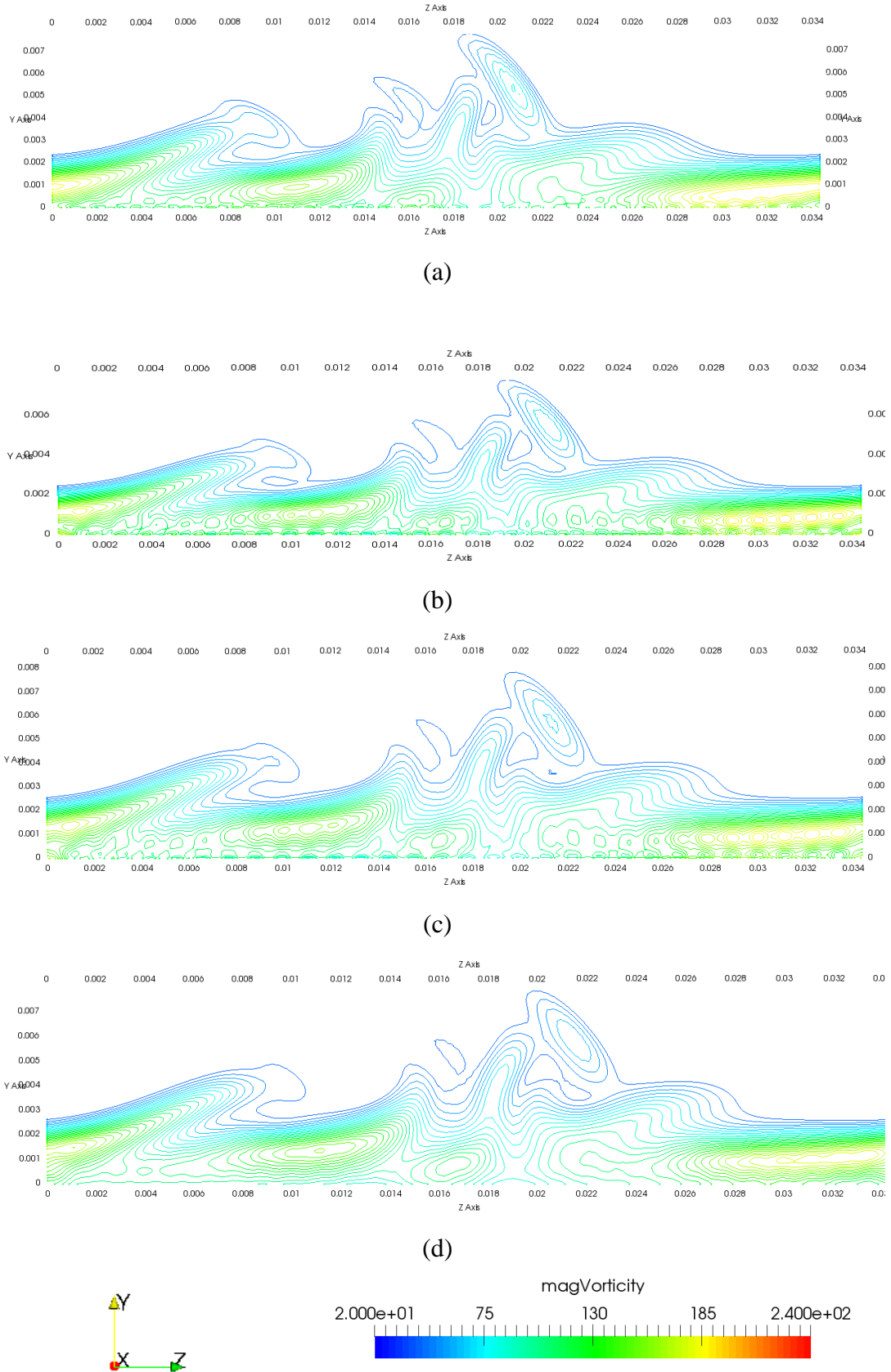


Figure (5.22) Effect of inclination angle on the streamwise vortices, case 7, $\theta = 135^\circ$: (a) $\Delta x^+ = -82$, (b) $\Delta x^+ = 0$, (c) $\Delta x^+ = 82$, (d) $\Delta x^+ = 136$

5.4.4 Effect of wave frequency

Changing the wave frequency has no big influence on the behaviour of the skin friction coefficient and even on the value of the maximum drag reduction value δ_{τ_w} . Different frequencies are used here in this study, as shown in Table (5.5). Figure (5.23) presents the skin friction coefficient, C_f , in which all curves for different frequencies have identical behaviour to that one without control in the laminar region. When the sinusoidal wave is applied, all of them followed the curve from case 2α with a slight difference in the drop value of C_f which recovers its original values at the transition onset. Figure (5.24) illustrates the drag reduction values across the channel and their maximum values δ_{τ_w} %. Although there is no big effect of the frequency, it can be seen that increasing the frequency gives higher drag reduction even with small amounts, this is confirmed with that results from Bai et al. (2014) that larger oscillation is needed to suppress the near-wall streaks which in-turn leads to larger drag reduction, shown in Figure (5.25).

Table (5.5) Applied frequencies and the resulted maximum drag reduction δ_{τ_w} . (The values presented in this table are for indication only. For more information, see the Appendix)

f^+	0.1	0.2	0.42	0.6
case	9	10	2α	11
δ_{τ_w} %	33.92	33.57	34.055	34.063

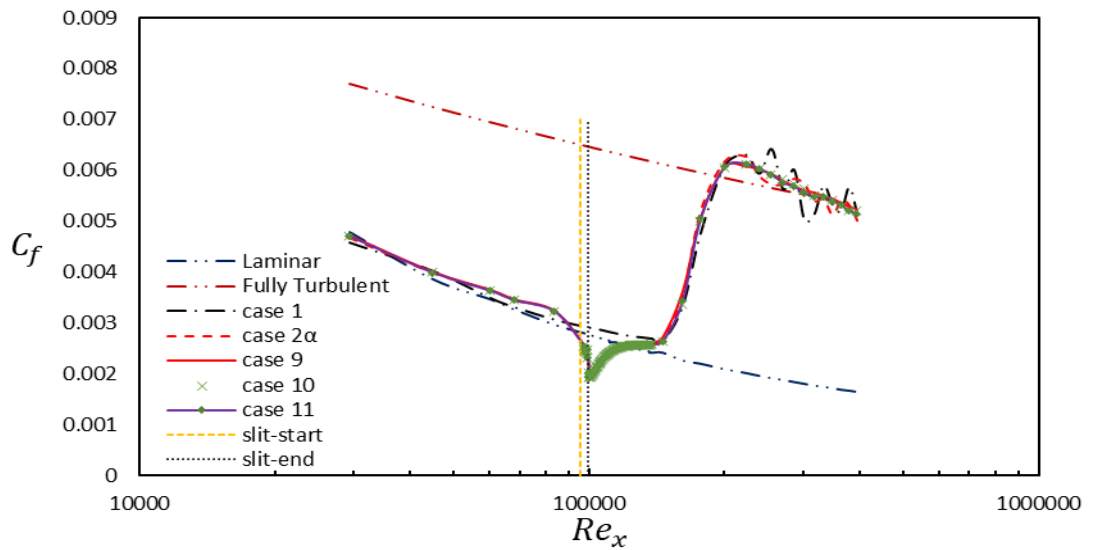


Figure (5.23) Skin friction coefficient dependence on wave frequency.

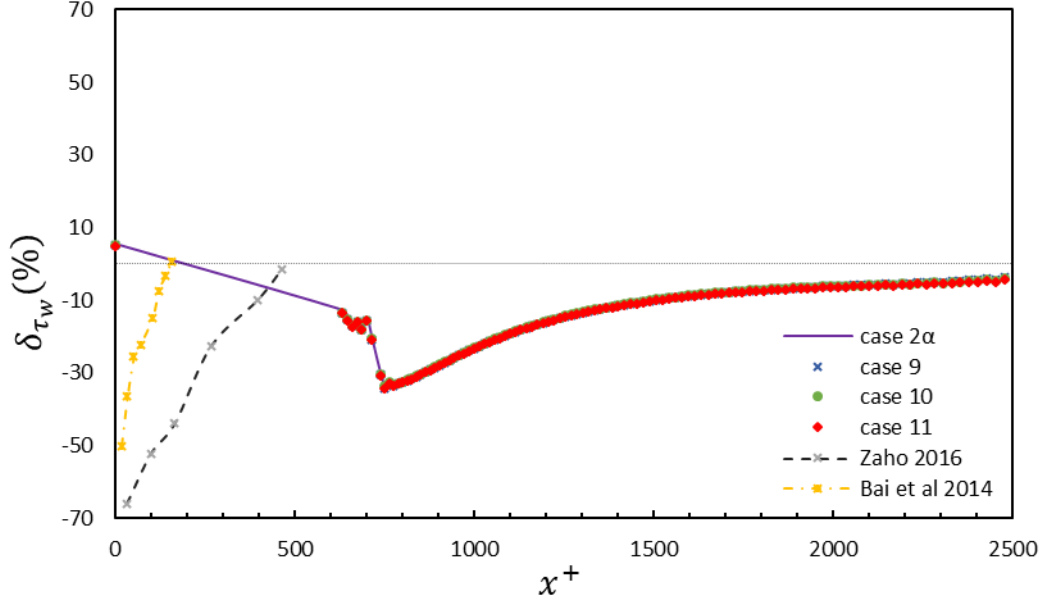


Figure (5.24) Streamwise location of maximum drag reduction achieved depending on different wave frequencies.

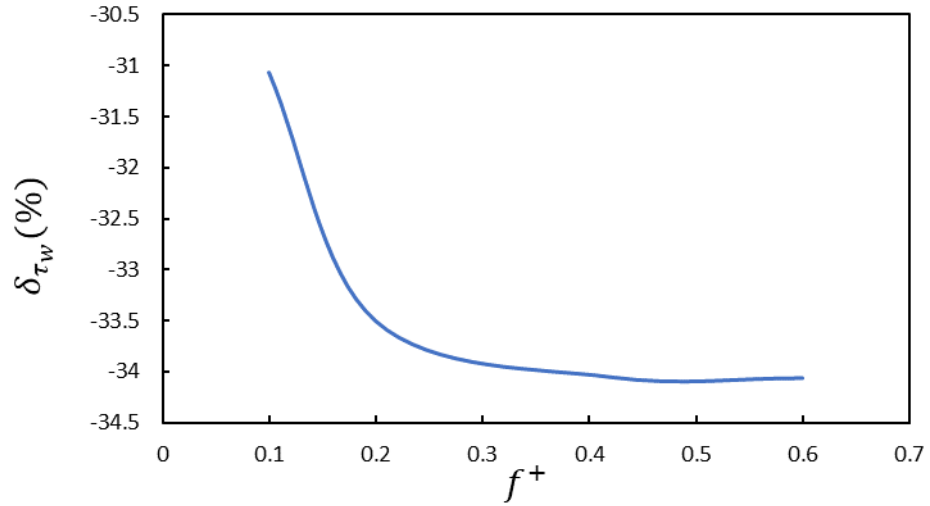


Figure (5.25) Relation between the wave frequency and the maximum drag reduction

5.4.5 Effect of wavelength λ_z^+ or $\varphi_{i,i+1}$

Variation of λ_z^+ is realized by controlling the phase shift between adjacent slits $\varphi_{i,i+1}$. Figure (5.26) explains the dependence of $\delta\tau_w$ on wavelength λ_z^+ , in wall units. It can be concluded that the inline oscillation for the sinusoidal wave is not effective with low values of wave numbers as there is no significant difference in the maximum drag reduction $\delta\tau_w$ appears between the used numbers of the wave as shown in Table (5.6). This may be due to that the spanwise distance between two adjacent peaks

of any of the used waves in cases 2α and 12 is large relative to the wavelength of the streamwise vortices, $\lambda_z^+ = 100$, then there is no effect on the sweep and ejection processes responsible for low and high-speed streaks and turbulence spots. While in case 13 and 14 it leads to enhancing the behaviour of the skin friction coefficient in the turbulent region, as it goes smoothly without any fluctuations relative to that behaviour in case 2α . Figure (5.27) presents the location of maximum drag reduction compared with case 2α .

Table (5.6) Maximum drag reduction according to λ_z^+ or $\varphi_{i,i+1}$.
(The values presented in this table are for indication only. For more information, see the Appendix)

N	1	3	4	5
Case	2α	12	13	14
φ	12.41°	37.24°	49.65°	62.06°
λ_z^+	406	135	101	81
$\delta_{\tau_w} \%$	33.54	34.15	34.13	34.12

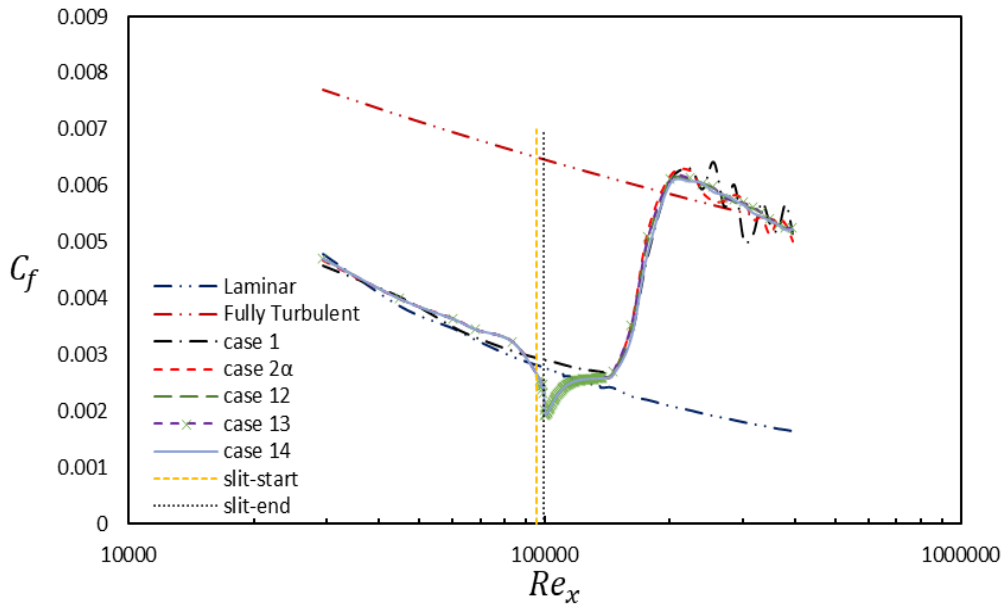


Figure (5.26) Skin friction coefficient dependence on λ_z^+ or $\varphi_{i,i+1}$: case 2α : $\varphi = 12.41^\circ$, case 12: $\varphi = 37.24^\circ$, case 13: $\varphi = 49.65^\circ$, case 14: $\varphi = 62.06^\circ$

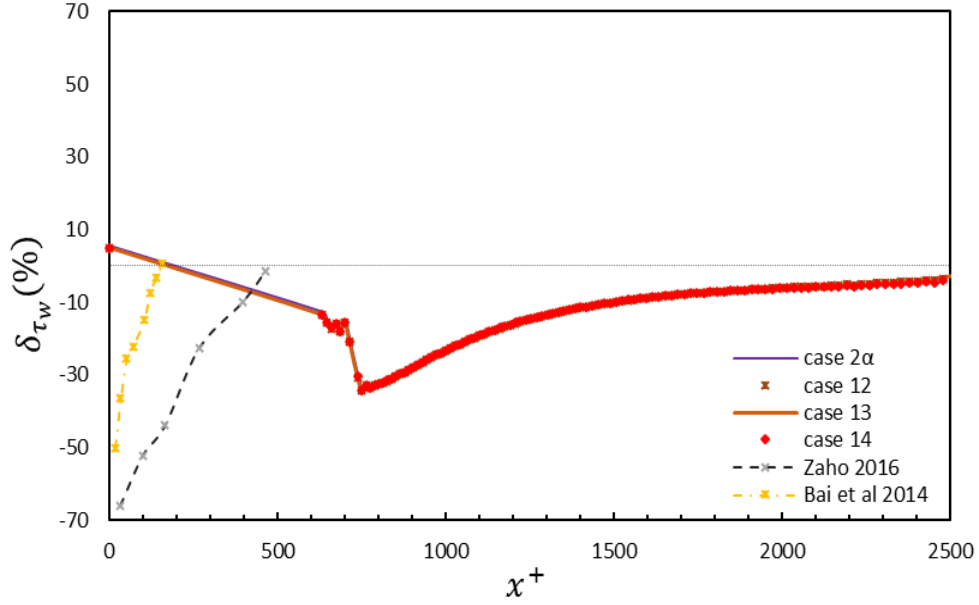


Figure (5.27) Streamwise location of maximum drag reduction achieved depending on different wavelengths.

5.4.6 Effect of mean velocity coming out from the slit $UMean_{slit}$

Value of mean velocity coming out from each slit, $UMean_{slit}$, has a significant effect in reshaping the performance of the turbulence structures after the slits, as it is the main parameter to determine the penetration depth inside the main flow in addition to the wave amplitude, studied before. Here in the current section, different $UMean_{slit}$ values are investigated as a percentage from the friction velocity of no-control, case 1, $u_{\tau, NoControl}$, and its values are selected according to the studies of Moarref and Jovanović (2010). Figure (5.28) shows the behaviour of the skin friction coefficient relative to each value of $UMean_{slit}$ and the streamwise location for its drop which refers to the value and location of maximum drag reduction obtained in each case. In case 15, $UMean_{slit} = 0.2 u_{\tau, NoControl}$, the curve of C_f starts smoothly in the laminar region with that one from case 2α and drops slightly before the slits start due to the laminarization effect of the sinusoidal wave. As the value of $UMean_{slit}$ here is small relative to the main flow velocity, so its penetration and effect on the streamwise vortices is very small, it achieves maximum drag reduction of smaller than half of that one achieved by case 2α at the centre of slits and recovered its original values again quickly after a long streamwise distance. With increasing $UMean_{slit}$, the drop-in skin friction coefficient increases and relative to it the drag reduction increases with a

slower rate to regain its normal behaviour before the transition onset. As illustrated from figure Figure (5.28), cases 16 and 17 achieve drag reduction rate more than the double of this one from case 2α . In case 17 and due to its high penetration depth in the main flow, the increase of C_f before the slits start indicates the disturbances happened by that high value of $UMean_{slit}$. These disturbances increase the amplitude of the low speed streaks instabilities but with enhanced behaviour which leads at the slits end to reduce the wall shear stress (WSS), achieving maximum drag reduction. The increased amplitude of the low-speed streaks causes an early transition to turbulent flow. The streamwise location for the maximum drag reduction and streamwise distance after the slits to recovers its normal values before the transition are presented in Figure (5.29). Finally, Figure (5.30) illustrates the relation between δ_{τ_w} and $UMean_{slit}$ without any regarding to the location of transition onset location.

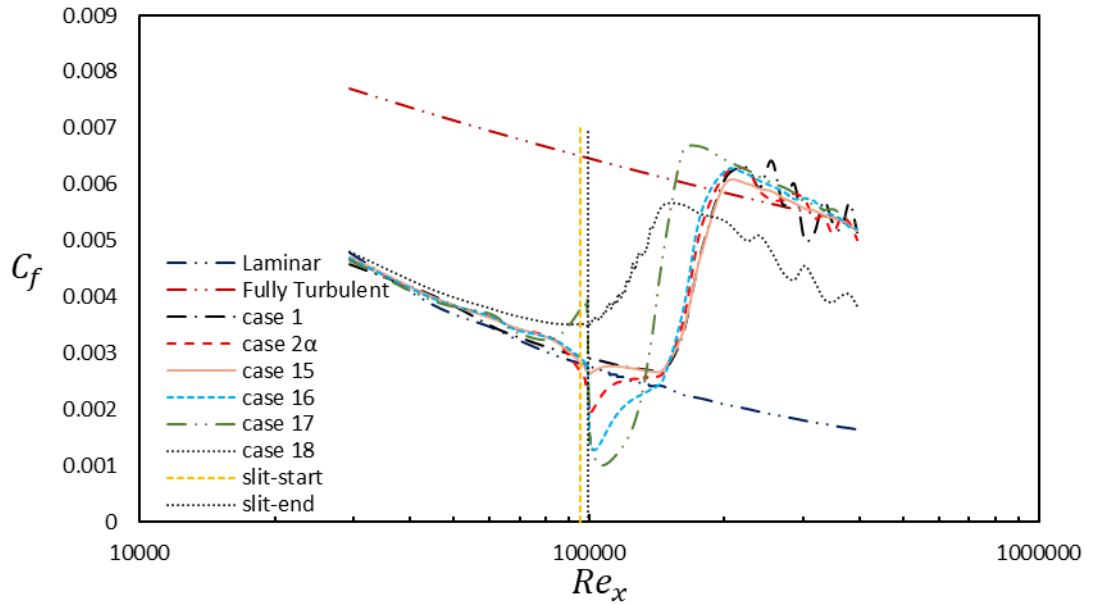


Figure (5.28) Skin friction coefficient dependence on different $UMean_{slit}$.

Figure (5.31) presents the vorticity distribution for case 15. Due to the low value of the mean velocity, the effect of the wave is very small relative to that one if compared with case 2α through all streamwise stations. Figure (5.32) shows how the high increase in the mean velocity of the flow comes out from the slits leads to increase in the vorticity magnitude in the near to the wall region over the slits leading to early transition.

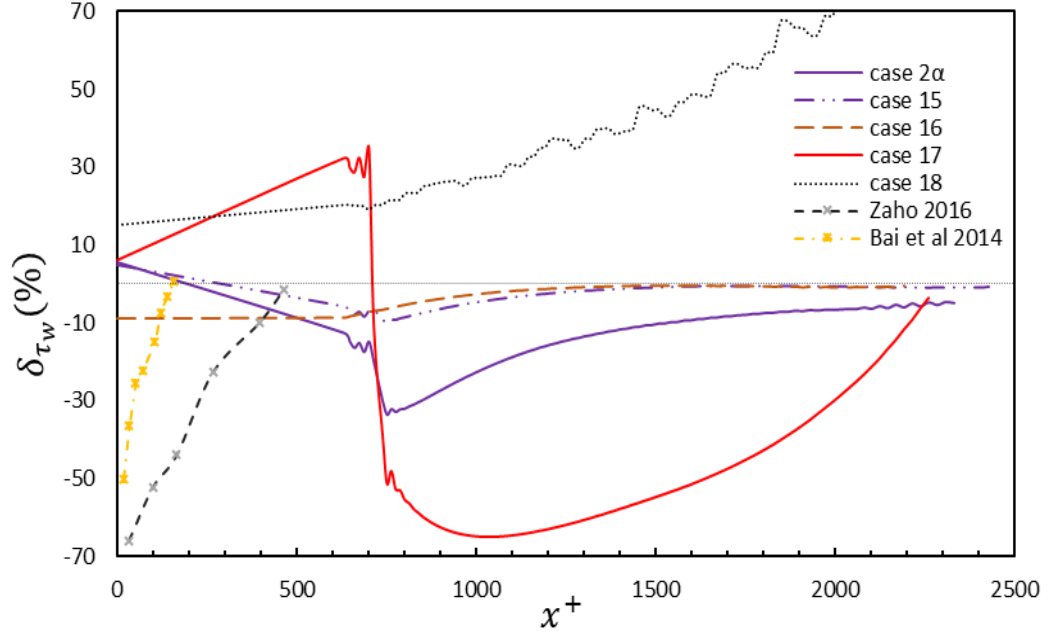


Figure (5.29) Streamwise location for the maximum drag reduction depending on $UMean_{slit}$.

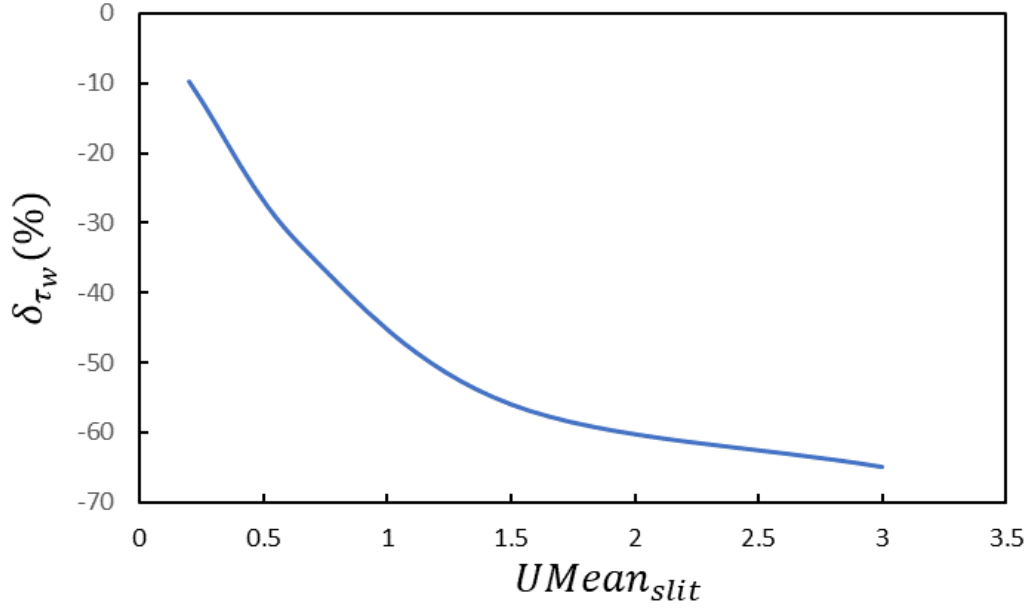


Figure (5.30) Relation between $\delta\tau_w$ and $UMean_{slit}$.

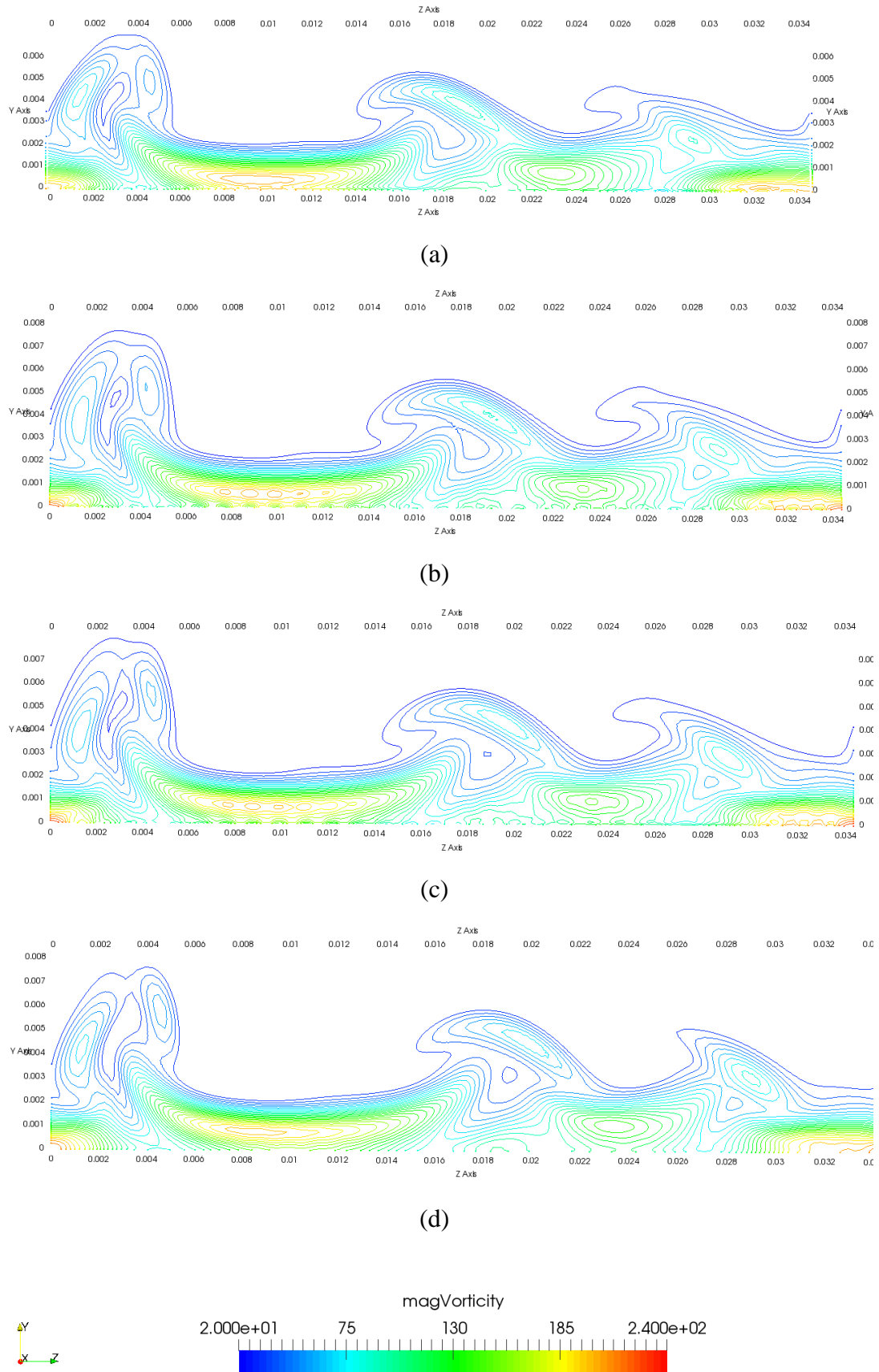


Figure (5.31) Effect of mean velocity out from the slit on the streamwise vortices, case 15: (a) $\Delta x^+ = -82$, (b) $\Delta x^+ = 0$, (c) $\Delta x^+ = 82$, (d) $\Delta x^+ = 136$.

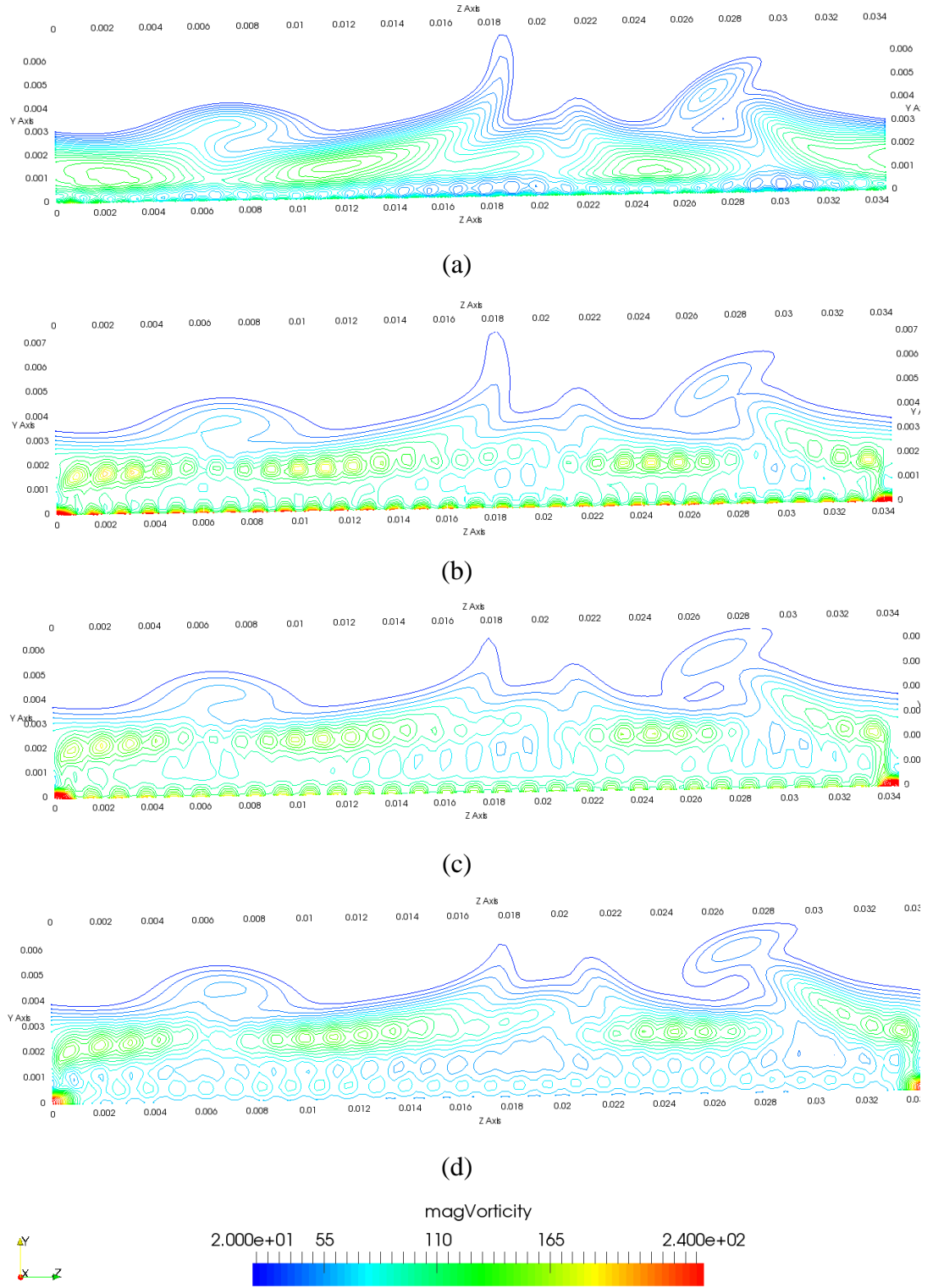


Figure (5.32) Effect of mean velocity out from the slit on the streamwise vortices, case 17: (a) $\Delta x^+ = -82$, (b) $\Delta x^+ = 0$, (c) $\Delta x^+ = 82$, (d) $\Delta x^+ = 136$.

5.4.7 Effect of streamwise location of slits on δ_{τ_w}

Streamwise location of the slits array is considered as the essential part of determining the region of transition to turbulent flow or the location of the maximum drag reduction due to the active control. In case 19, the slits array is moved upstream with a streamwise distance of $\Delta x^+ = 340$ in wall units and the same parameters values for case 2α are applied. The results in Figure (5.33) show that the bypass transition onset has moved slightly upstream with a streamwise distance which is almost equal to that distance moved by the slits. It achieves a reasonable drag reduction relative to that one achieved by case 2α . On the other hand, in case 20 the slits array is moved downstream in the streamwise direction and it was found that bypass transition onset was delayed with a distance in the same range of that distance moved by the slits array. This streamwise distance is not in the same order with the distance moved by the slits array. This may be due to that at this new location for the slits, the amplitude of the low-speed streak instabilities is high enough to resist the effect of the sinusoidal wave to reduce the amplitude of the streamwise vortices for longer distance. Although this case gives a larger drag reduction, it recovers its original values very quickly.

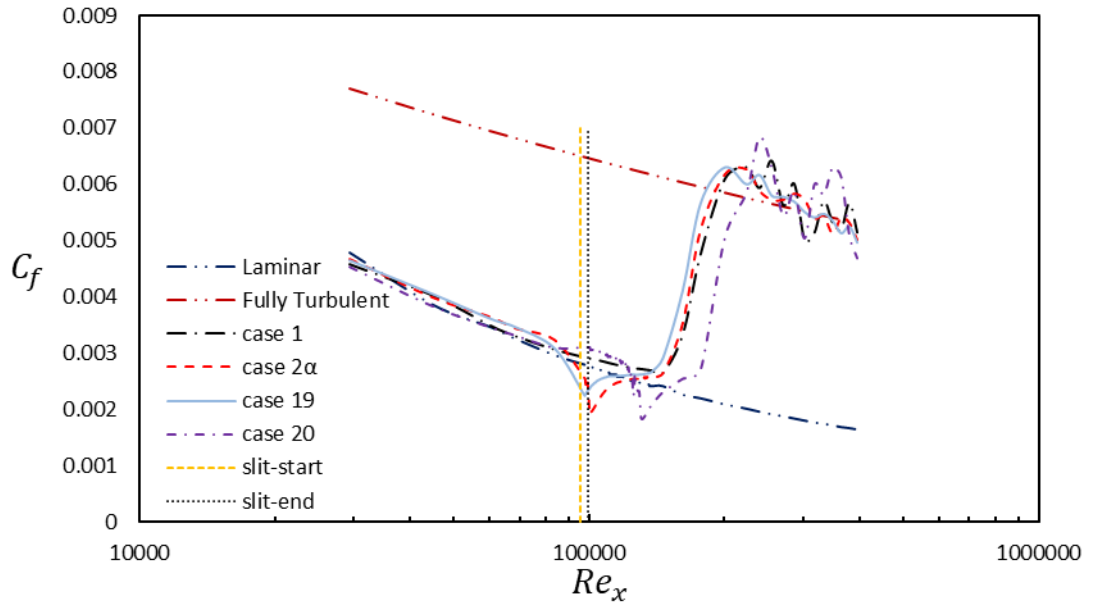


Figure (5.33) Maximum drag reduction dependence on the streamwise location of slits.

5.4.8 Effect of streamwise length of slits

The streamwise length of the slits is increased by a factor of 1.5 relative to the previous cases. Applying it in case 21, the maximum drag reduction is increased compared with this percentage of case 2α . Also, it gives a slower rate of the recovery to its normal values before the transition occurs, as suggested by Li and Zhou (2016) and shown in Figure (5.34). This may have happened due to an increase in the streamwise length of the slits which increases the affected length from the main flow. Figure (5.35) shows exactly how much distance is increased due to increasing the streamwise length of the slits and its slow recovery rate than that one of case 2α .

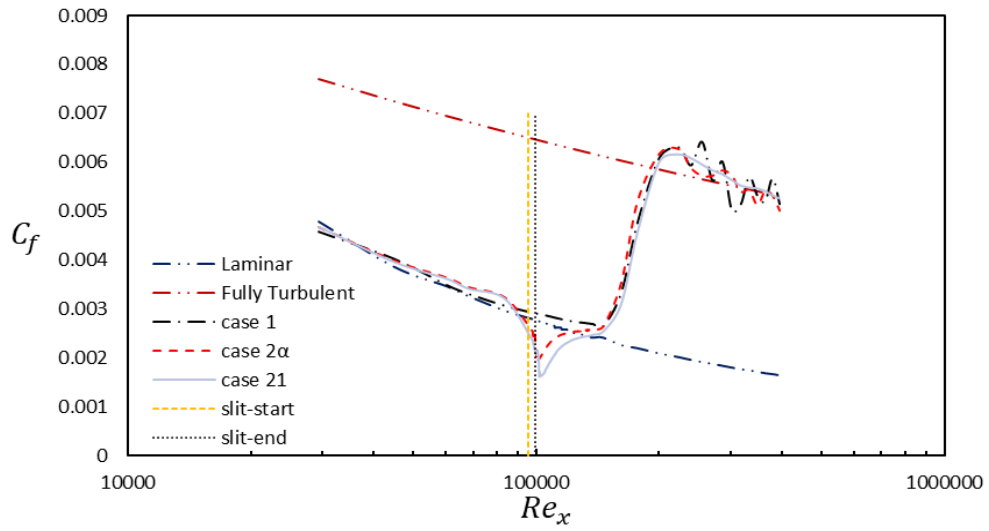


Figure (5.34) Skin friction coefficient for longer slits.

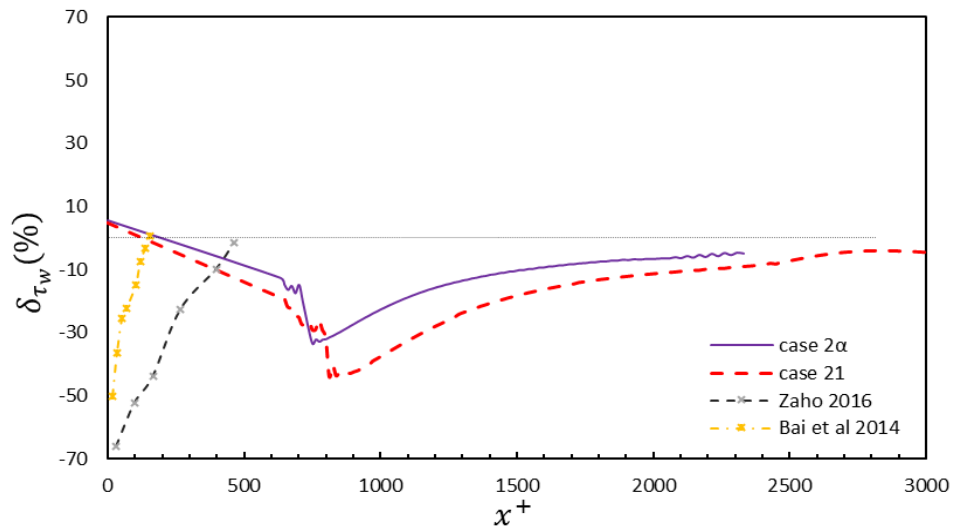


Figure (5.35) Streamwise location for the maximum drag reduction depending on longer slits.

5.5 Summery

A combination of the MILES solver and the isotropic homogeneous boundary condition, mentioned in Chapter (3)Chapter (4), is applied to generate the bypass transition in a channel flow. The solver reproduced the bypass transition, while the control of drag reduction in the transitional boundary layer is investigated. This combination gives good agreement with the previous DNS studies for turbulence intensities $Tu = 3, 7\%$.

This solver is able to save time and reduce the computation resources and costs for all the numerical simulations required in the current research with acceptable accuracy for the results relative to the previous DNS studies. For example, in the case of $Tu = 3\%$, a mesh resolution of (400x125x123) cells is used and decomposed over 224 processors running in parallel with a running time of 150 CPU hours per processor for the base case to generate the bypass transition. On the other hand, the DNS study used a mesh of (2048x180x192) cells using 128 processors with a CPU hours of 500 per processor (Jacobs and Durbin, 2001). This means that the solver is able to save around 47.5% of the running time and cost.

Numerical analysis of active control of the skin friction drag before the transition occurs over a flat plate is applied via applying a sinusoidal travelling wave in the spanwise direction using the current mesh which will be validated via a thorough grid independence study in the future work followed to this research. Different numerical experiments are studied to produce the effect of wave parameters variation on the skin friction drag and the bypass transition onset through the channel. It is concluded from the studied cases that the wave amplitude has a small effect on the maximum drag reduction and even the bypass transition onset. While, the wave inclination angle, θ , in the streamwise direction proves its ability to control the behaviour of the skin friction over the flat plate. As in case 4, there is an increase in the C_f reaching its maximum with $\theta = 10^\circ$ and starts to adjust itself again to get the maximum drag reduction percentage at $\theta = 90^\circ$, case 2α . By increasing the inclination angle till $\theta = 135^\circ$, in addition to the drop in the skin friction drag, it leads to delaying the bypass transition onset with a streamwise distance of 5 times and half of the slits length, more increasing produces more disturbances and reduces the C_f drop. Variation in wave frequency and using large wavelengths produce a small change in the skin

friction drag behaviour through the channel. While the mean velocity comes out from the slit is shown to be considered as a key parameter during this study. Increasing $UMean_{slit}$ leads to redistributing the flow in the near to the wall region and increasing the maximum drag reduction in case 16 and 17 but with early bypass transition. Also, the location of the slits is investigated, and it is found that late slits and before reaching the bypass transition onset of the uncontrolled case lead to transition-delay without any extra drop of C_f .

Chapter (6)

Conclusion and Future Work

This study was motivated by the growing interest of the engineering community in controlling the turbulence structures, how to reduce the skin friction drag over a flat plate, delaying the flow transition to turbulence, and finally, need to accurate and less costly methods to simulate those structures. A proposed method based on the generation of spanwise mean velocity gradients in a flat plate boundary layer by introducing a sinusoidal travelling wave in the spanwise direction before the transition to turbulence occurrence is used for the drag reduction. A numerical solver has been developed using the open-source CFD software OpenFOAM libraries. This solver consists of a combination of generation a synthetic isotropic homogeneous turbulence at the inlet plane of the channel and solving the Navier Stokes equations by using the Monotonically Integrated Large Eddy Simulation solver (MILES) method.

6.1 Conclusion Remarks

The main contribution and conclusion of the investigated studies in the current thesis are explained in the following paragraphs:

The development of the monotonically integrated large eddy simulation (MILES) solver for capturing the turbulence structures using the open-source CFD software OpenFOAM libraries has been successfully applied. An investigation for classifying the flux limiters has been run and it has been found that gamma and VanLeer limiters are identical in their behaviour and along with VanAlbada limiter can be considered as the less diffusive limiters. On the other hand, superBee limiter produces acceptable behaviour for simulating the turbulence structures in a fully developed flow through a channel. Also, it has been found that the mesh resolution has a big effect on the MILES performance especially for high friction Reynolds numbers, Re_τ . It has been concluded that using superBee limiter with moderate mesh resolution, relative to the resolution of the DNS studies, will give suitable accuracy for the results and make it as a good alternative to the DNS in those studies with high Re_τ .

Development of a systematic synthetic isotropic homogeneous turbulence inlet boundary condition based on the work of Davidson (2007) has been provided. In this boundary condition, most of the turbulence parameters at the inlet plane of the channel can be controlled. The integral length scale can be adjusted according to the mesh size at the inlet plane. It is easy to specify the required velocity profile at the inlet plane either laminar, laminar with a specific amount of disturbances, relative to the required turbulence intensity at the inlet plane, or fully developed flow with a pre-specified friction Reynolds number required through the channel. Also, the time scale can be assigned, and other parameters can be selected before the start of the numerical run. Optimization of these properties of the developed boundary condition leads to an improvement in the development of turbulence structures through the channel as it reaches to fully developed steady-state within a streamwise distance of 5 times the half channel height (δ) after the inlet plane. This distance is shorter than the other streamwise distances from similar boundary conditions. These improvement results in a considerable reduction in overall channel length and hence reducing the associated computation cost and time.

The combination of the MILES solver and the synthetic isotropic homogeneous turbulence inlet boundary condition has shown its ability to reproduce the bypass transition to turbulent in the channel flow. The resulted solver is able to save time and reduce the computation resources and costs for all the numerical simulations required in the current research with a satisfying accuracy for the results relative to the previous DNS studies. For example, in the case of $Tu = 3\%$, the DNS previous study used a mesh of (2048x180x192) cells through 128 processors with 500 CPU hours per processor (Jacobs and Durbin, 2001). While in the current study, a mesh resolution of (400x125x123) cells is used 224 processors running in parallel with a running time of 150 CPU hours per processor for the base case 2α to generate the bypass transition with an acceptable accuracy compared with the DNS previous study. This means that the solver is able to save around 47.5% of the running time.

Active control of the skin friction drag in the transitional boundary layer has been applied via generating a sinusoidal travelling wave in the spanwise direction. Different numerical experiments have been studied to show the effect of wave parameters variation on the skin friction drag and the bypass transition onset through the channel. The applied mesh density in those numerical experiments will be validated through a

mesh independence study in the future work followed to this thesis. It is been concluded that using small Tu at the channel inlet leads to increasing the streamwise distance required by the skin friction coefficient to regain to its original values after the drop. For example, in the reference case 2α , the decrease in the skin friction coefficient has achieved its maximum value and has started to regain its original values very slowly. The distance required for the skin friction coefficient to regain its original values is much larger than that one when applying the control in a turbulent boundary layer, $Tu \geq 10\%$, such as in (Bai et al., 2014) in which they got $\Delta x^+ = 160$ with maximum drag reduction of 50%, and that one from Li and Zhou (2016) of $\Delta x^+ = 460$ with a maximum drag reduction of 70%.

The numerical predictions have shown that the amplitude of the wave has a small effect on the skin friction drag. While the inclination angle, θ , of the wave in the streamwise direction produces a significant effect on the amount of the drag reduction and even on the bypass transition onset. Small values of θ result in a sudden rise in the drag at the region of the slits with an early transition, such as $\theta = 10^\circ$, then it improves its behaviour and reaches maximum drag reduction at $\theta = 90^\circ$. By increasing the inclination angle till $\theta = 135^\circ$, in addition to the drop in the skin friction drag, it leads to delay the bypass transition onset with a streamwise distance of 5 times and half the slits length, more increasing produces more disturbances and reduces the C_f drop. On the other hand, average velocity gets out from the slits, $U_{Mean_{slit}}$, has the main weight in the drag reduction and the bypass transition onset through the channel with maximum drag reduction achieved of more than 2 times that one of case 2α , as illustrated from Figure (5.28), but with early bypass transition. Finally, the slit's location affects only on the location of the bypass transition onset while increasing in the slit's length effects on the magnitude of the drag reduction and decreases its rate to regain to its original values.

6.2 Suggestions for Future Work

The following points can be considered as future work to the current research:

1. Upgrading the solver for cases converging-diverging duct flows including shock flows.

2. Applying different profiles of injection flows such as nonuniform, irregular wave pattern, and adding some eddies to the injected flow and investigating their effects on the performance of the active control and their interaction with the quasi-streamwise vortices.
3. Applying a thorough grid independence study to validate and approve the mesh used in controlling the drag over the flat plate.
4. Studying different friction pattern for the plate surface using different surface roughness sources in the transitional boundary layer and their effect on the skin friction drag control and the transition onset.
5. Studying the effect of the intermediate streamwise distance between the slits arrays in the case of using multi-arrays on the behaviour of the skin friction coefficient.

Bibliography

- Abe, H., Kawamura, H., & Matsuo, Y. (2001). Direct numerical simulation of a fully developed turbulent channel flow with respect to the Reynolds number dependence. *Journal of fluids Engineering*, 123(2), 382-393.
- Adedoyin, A. A., Walters, D. K., & Bhushan, S. (2015). Investigation of turbulence model and numerical scheme combinations for practical finite-volume large eddy simulations. *Engineering Applications of Computational Fluid Mechanics*, 9(1), 324-342.
- Alfredsson, P., & Matsubara, M. (2000). *Free-stream turbulence, streaky structures and transition in boundary layer flows*. Paper presented at the Fluids 2000 Conference and Exhibit.
- Bai, H., Zhou, Y., Zhang, W., Xu, S., Wang, Y., & Antonia, R. (2014). Active control of a turbulent boundary layer based on local surface perturbation. *Journal of fluid mechanics*, 750, 316-354.
- Bailly, C., & Juve, D. (1999). *A stochastic approach to compute subsonic noise using linearized Euler's equations*. Paper presented at the 5th AIAA/CEAS Aeroacoustics Conference and Exhibit.
- Batten, P., Goldberg, U., & Chakravarthy, S. (2004). Interfacing statistical turbulence closures with large-eddy simulation. *AIAA journal*, 42(3), 485-492.
- Bechert, D., Bruse, M., Hage, W. v., Van der Hoeven, J. T., & Hoppe, G. (1997). Experiments on drag-reducing surfaces and their optimization with an adjustable geometry. *Journal of fluid mechanics*, 338, 59-87.
- Berger, T. W., Kim, J., Lee, C., & Lim, J. (2000). Turbulent boundary layer control utilizing the Lorentz force. *Physics of fluids*, 12(3), 631-649.
- Bernard, P. S., Thomas, J. M., & Handler, R. A. (1993). Vortex dynamics and the production of Reynolds stress. *Journal of fluid mechanics*, 253, 385-419.
- Bewley, T. R. (2001). Flow control: new challenges for a new renaissance. *Progress in Aerospace sciences*, 37(1), 21-58.
- Bewley, T. R., & Aamo, O. M. (2004). A 'win-win' mechanism for low-drag transients in controlled two-dimensional channel flow and its implications for sustained drag reduction. *Journal of fluid mechanics*, 499, 183-196.
- Bewley, T. R., Moin, P., & Temam, R. (2001). DNS-based predictive control of turbulence: an optimal benchmark for feedback algorithms. *Journal of fluid mechanics*, 447, 179-225.
- Billson, M. (2004). *Computational techniques for turbulence generated noise*: Chalmers University of Technology.

- Billson, M., Eriksson, L.-E., & Davidson, L. (2003). *Jet noise prediction using stochastic turbulence modeling*. Paper presented at the 9th AIAA/CEAS Aeroacoustics Conference and Exhibit.
- Boris, J., Grinstein, F., Oran, E., & Kolbe, R. (1992). New insights into large eddy simulation. *Fluid dynamics research*, 10(4-6), 199-228.
- Borue, V., & Orszag, S. A. (1998). Local energy flux and subgrid-scale statistics in three-dimensional turbulence. *Journal of fluid mechanics*, 366, 1-31.
- Brandt, L., Schlatter, P., & Henningson, D. S. (2004). Transition in boundary layers subject to free-stream turbulence. *Journal of fluid mechanics*, 517, 167-198.
- Chang, Y., Collis, S. S., & Ramakrishnan, S. (2002). Viscous effects in control of near-wall turbulence. *Physics of fluids*, 14(11), 4069-4080.
- Choi, H., Moin, P., & Kim, J. (1993). Direct numerical simulation of turbulent flow over riblets. *Journal of fluid mechanics*, 255, 503-539.
- Choi, H., Moin, P., & Kim, J. (1994). Active turbulence control for drag reduction in wall-bounded flows. *Journal of fluid mechanics*, 262, 75-110.
- Choi, K.-S., DeBisschop, J.-R., & Clayton, B. R. (1998). Turbulent boundary-layer control by means of spanwise-wall oscillation. *AIAA journal*, 36(7), 1157-1163.
- Chong, P., Jin-Jun, W., & Guo-Sheng, H. (2012). Experimental investigation of wake-induced bypass transition control by surface roughness. *Chinese Physics Letters*, 29(10), 104704.
- Chung, Y. M., & Talha, T. (2011). Effectiveness of active flow control for turbulent skin friction drag reduction. *Physics of fluids*, 23(2), 025102.
- Colella, P., & Woodward, P. R. (1984). The piecewise parabolic method (PPM) for gas-dynamical simulations. *Journal of computational physics*, 54(1), 174-201.
- Commission, E. Climate change: commission proposes bringing air transport into EU emissions trading scheme. In.
- commission, E. C. (2013). <http://www.ec.europa.eu/analysis> by source sector, EU-28).
- Davidson, L. (2007). *Using isotropic synthetic fluctuations as inlet boundary conditions for unsteady simulations*. Paper presented at the Advances and Applications in Fluid Mechanics.
- Davidson, L., & Billson, M. (2006). Hybrid LES-RANS using synthesized turbulent fluctuations for forcing in the interface region. *International journal of heat and fluid flow*, 27(6), 1028-1042.

- Dean, B., & Bhushan, B. (2010). Shark-skin surfaces for fluid-drag reduction in turbulent flow: a review. *Philosophical Transactions of the Royal Society A: Mathematical, Physical and Engineering Sciences*, 368(1929), 4775-4806.
- Dean, R. (1978). Reynolds Number Dependence of Skin Friction and Other Bulk Flow Variables in Two-Dimensional Rectangular Duct Flow. *Journal of fluids Engineering*, 100(2), 215-223.
- Di Mare, L., Klein, M., Jones, W., & Janicka, J. (2006). Synthetic turbulence inflow conditions for large-eddy simulation. *Physics of fluids*, 18(2), 025107.
- Domaradzki, J. A., Xiao, Z., & Smolarkiewicz, P. K. (2003). Effective eddy viscosities in implicit large eddy simulations of turbulent flows. *Physics of fluids*, 15(12), 3890-3893.
- Driscoll, R. J., & Kennedy, L. A. (1983). A model for the turbulent energy spectrum. *The Physics of fluids*, 26(5), 1228-1233.
- Druault, P., Lardeau, S., Bonnet, J.-P., Coiffet, F., Delville, J., Lamballais, E., . . . Perret, L. (2004). Generation of three-dimensional turbulent inlet conditions for large-eddy simulation. *AIAA journal*, 42(3), 447-456.
- Du, Y., & Karniadakis, G. E. (2000). Suppressing wall turbulence by means of a transverse traveling wave. *Science*, 288(5469), 1230-1234.
- Du, Y., Symeonidis, V., & Karniadakis, G. (2002). Drag reduction in wall-bounded turbulence via a transverse travelling wave. *Journal of fluid mechanics*, 457, 1-34.
- Eitel-Amor, G., Örlü, R., & Schlatter, P. (2014). Simulation and validation of a spatially evolving turbulent boundary layer up to $Re_\theta = 8300$. *International journal of heat and fluid flow*, 47, 57-69.
- Endo, T., Kasagi, N., & Suzuki, Y. (2000). Feedback control of wall turbulence with wall deformation. *International journal of heat and fluid flow*, 21(5), 568-575.
- Eurostat. (2018). Change in CO2 emissions, 2017/2016
- Fransson, J. H., Brandt, L., Talamelli, A., & Cossu, C. (2005). Experimental study of the stabilization of Tollmien–Schlichting waves by finite amplitude streaks. *Physics of fluids*, 17(5), 054110.
- Fukagata, K., Iwamoto, K., & Kasagi, N. (2002). Contribution of Reynolds stress distribution to the skin friction in wall-bounded flows. *Physics of fluids*, 14(11), L73-L76.
- Fukagata, K., Kern, S., Chatelain, P., Koumoutsakos, P., & Kasagi, N. (2008). Evolutionary optimization of an anisotropic compliant surface for turbulent friction drag reduction. *Journal of Turbulence*(9), N35.

- Fureby, C., & Grinstein, F. F. (2002). Large eddy simulation of high-Reynolds-number free and wall-bounded flows. *Journal of Computational Physics*, 181(1), 68-97.
- Gad-el-Hak, M. (2001). Flow control: The future. *Journal of Aircraft*, 38(3), 402-418.
- García-Mayoral, R., & Jiménez, J. (2011). Drag reduction by riblets. *Philosophical Transactions of the Royal Society of London A: Mathematical, Physical and Engineering Sciences*, 369(1940), 1412-1427.
- Ge, X. (2015). A bypass transition model based on the intermittency function.
- Ge, X., Arolla, S., & Durbin, P. (2014). A bypass transition model based on the intermittency function. *Flow, turbulence and combustion*, 93(1), 37-61.
- Ghasemi, E., McEligot, D., Nolan, K., Crepeau, J., Tokuhiro, A., & Budwig, R. (2013). Entropy generation in a transitional boundary layer region under the influence of freestream turbulence using transitional RANS models and DNS. *International Communications in heat and Mass transfer*, 41, 10-16.
- Glaze, D. J., & Frankel, S. H. (2003). Stochastic inlet conditions for large-eddy simulation of a fully turbulent jet. *AIAA journal*, 41(6), 1064-1073.
- Goldstein, M. (1983). The evolution of Tollmien–Schlichting waves near a leading edge. *Journal of fluid mechanics*, 127, 59-81.
- Gottlieb, S., & Shu, C.-W. (1998). Total variation diminishing Runge-Kutta schemes. *Mathematics of computation of the American Mathematical Society*, 67(221), 73-85.
- Grinstein, F. F. (1995). Self-induced vortex ring dynamics in subsonic rectangular jets. *Physics of fluids*, 7(10), 2519-2521.
- Grinstein, F. F., & Fureby, C. (2005). On monotonically integrated large eddy simulation of turbulent flows based on FCT algorithms. In *Flux-Corrected Transport* (pp. 79-104): Springer.
- Grinstein, F. F., & Fureby, C. (2006). *Recent progress on flux-limiting based implicit Large Eddy Simulation*. Paper presented at the European Conference on Computational Fluid Dynamics, ECCOMAS CFD.
- Grosjean, C., Lee, G., Hong, W., Tai, Y., & Ho, C. (1998). *Micro balloon actuators for aerodynamic control*. Paper presented at the Micro Electro Mechanical Systems, 1998. MEMS 98. Proceedings., The Eleventh Annual International Workshop on.
- Grundmann, S., & Tropea, C. (2007). Experimental transition delay using glow-discharge plasma actuators. *Experiments in Fluids*, 42(4), 653-657.

- Hack, M. P., & Zaki, T. A. (2014). The influence of harmonic wall motion on transitional boundary layers. *Journal of fluid mechanics*, 760, 63-94.
- Hammond, E., Bewley, T., & Moin, P. (1998). Observed mechanisms for turbulence attenuation and enhancement in opposition-controlled wall-bounded flows. *Physics of fluids*, 10(9), 2421-2423.
- Harimi, I., & Pishavar, A. R. (2013). Evaluating the capability of the flux-limiter schemes in capturing strong shocks and discontinuities. *Shock and Vibration*, 20(2), 287-296.
- Herbert, T. (1988). Secondary instability of boundary layers. *Annual review of fluid mechanics*, 20(1), 487-526.
- Huang, L., Fan, B., & Dong, G. (2010). Turbulent drag reduction via a transverse wave traveling along streamwise direction induced by Lorentz force. *Physics of fluids*, 22(1), 015103.
- Hurst, E., Yang, Q., & Chung, Y. M. (2014). The effect of Reynolds number on turbulent drag reduction by streamwise travelling waves. *Journal of fluid mechanics*, 759, 28-55.
- Hussain, A., & Reynolds, W. (1975). Measurements in fully developed turbulent channel flow. *Journal of fluids Engineering*, 97(4), 568-578.
- Ioannou, P., & Farrell, B. (1999). Active control of turbulence in boundary layer flows. In *Fundamental Problematic Issues in Turbulence* (pp. 67-73): Springer.
- Itoh, M., Tamano, S., Yokota, K., & Taniguchi, S. (2006). Drag reduction in a turbulent boundary layer on a flexible sheet undergoing a spanwise traveling wave motion. *Journal of Turbulence*(7), N27.
- Iwamoto, K., Suzuki, Y., & Kasagi, N. (2002). Reynolds number effect on wall turbulence: toward effective feedback control. *International journal of heat and fluid flow*, 23(5), 678-689.
- Jacobs, R., & Durbin, P. (2001). Simulations of bypass transition. *Journal of fluid mechanics*, 428, 185-212.
- Jacobson, S. A., & Reynolds, W. C. (1998). Active control of streamwise vortices and streaks in boundary layers. *Journal of fluid mechanics*, 360, 179-211.
- Jarrin, N., Benhamadouche, S., & Laurence, D. R. (2005). *Inflow Conditions for Large-Eddy Simulation Using a New Vortex Method*. Paper presented at the TSFP DIGITAL LIBRARY ONLINE.
- Jarrin, N., Prosser, R., Uribe, J.-C., Benhamadouche, S., & Laurence, D. (2009). Reconstruction of turbulent fluctuations for hybrid RANS/LES simulations using a synthetic-eddy method. *International journal of heat and fluid flow*, 30(3), 435-442.

- Jiménez, J., Wray, A. A., Saffman, P. G., & Rogallo, R. S. (1993). The structure of intense vorticity in isotropic turbulence. *Journal of fluid mechanics*, 255, 65-90.
- Joslin, R. D. (1998). Aircraft laminar flow control. *Annual review of fluid mechanics*, 30(1), 1-29.
- Jung, S. Y., & Zaki, T. A. (2015). The effect of a low-viscosity near-wall film on bypass transition in boundary layers. *Journal of fluid mechanics*, 772, 330-360.
- Jung, W., Mangiavacchi, N., & Akhavan, R. (1992). Suppression of turbulence in wall-bounded flows by high-frequency spanwise oscillations. *Physics of Fluids A: Fluid Dynamics*, 4(8), 1605-1607.
- Kametani, Y., & Fukagata. (2011). Direct numerical simulation of spatially developing turbulent boundary layers with uniform blowing or suction. *Journal of fluid mechanics*, 681, 154-172.
- Kametani, Y., Fukagata, K., Örlü, R., & Schlatter, P. (2015). Effect of uniform blowing/suction in a turbulent boundary layer at moderate Reynolds number. *International journal of heat and fluid flow*, 55, 132-142.
- Kametani, Y., Fukagata, K., Örlü, R., & Schlatter, P. (2016). Drag reduction in spatially developing turbulent boundary layers by spatially intermittent blowing at constant mass-flux. *Journal of Turbulence*, 17(10), 913-929.
- Kametani, Y., Kotake, A., Fukagata, K., & Tokugawa, N. (2017). Drag reduction capability of uniform blowing in supersonic wall-bounded turbulent flows. *Physical Review Fluids*, 2(12), 123904.
- Kang, S., & Choi, H. (2000). Active wall motions for skin-friction drag reduction. *Physics of fluids*, 12(12), 3301-3304.
- Karniadakis, G., & Choi, K.-S. (2003). Mechanisms on transverse motions in turbulent wall flows. *Annual review of fluid mechanics*, 35(1), 45-62.
- Karweit, M., Blanc-Benon, P., Juvé, D., & Comte-Bellot, G. (1991). Simulation of the propagation of an acoustic wave through a turbulent velocity field: A study of phase variance. *The Journal of the Acoustical Society of America*, 89(1), 52-62.
- Kasagi, N., Suzuki, Y., & Fukagata, K. (2009). Microelectromechanical systems-based feedback control of turbulence for skin friction reduction. *Annual review of fluid mechanics*, 41, 231-251.
- Kim, J. (1983). On the structure of wall-bounded turbulent flows. *The Physics of fluids*, 26(8), 2088-2097.

- Kim, J. (2003). Control of turbulent boundary layers. *Physics of fluids*, 15(5), 1093-1105.
- Kim, J., & Bewley, T. R. (2007). A linear systems approach to flow control. *Annu. Rev. Fluid Mech.*, 39, 383-417.
- Kim, J., Moin, P., & Moser, R. (1987). Turbulence statistics in fully developed channel flow at low Reynolds number. *Journal of fluid mechanics*, 177, 133-166.
- Klebanoff, P. S., Tidstrom, K., & Sargent, L. (1962). The three-dimensional nature of boundary-layer instability. *Journal of fluid mechanics*, 12(1), 1-34.
- Klein, M., Sadiki, A., & Janicka, J. (2003). A digital filter based generation of inflow data for spatially developing direct numerical or large eddy simulations. *Journal of computational physics*, 186(2), 652-665.
- Kline, S. J., Reynolds, W., Schraub, F., & Runstadler, P. (1967). The structure of turbulent boundary layers. *Journal of fluid mechanics*, 30(4), 741-773.
- Kraichnan, R. H. (1970). Diffusion by a random velocity field. *The Physics of fluids*, 13(1), 22-31.
- Kravchenko, A. G., Choi, H., & Moin, P. (1993). On the relation of near-wall streamwise vortices to wall skin friction in turbulent boundary layers. *Physics of Fluids A: Fluid Dynamics*, 5(12), 3307-3309.
- Kubacki, S., & Dick, E. (2016). An algebraic model for bypass transition in turbomachinery boundary layer flows. *International journal of heat and fluid flow*, 58, 68-83.
- Lardeau, S., Leschziner, M., & Zaki, T. (2012). Large eddy simulation of transitional separated flow over a flat plate and a compressor blade. *Flow, turbulence and combustion*, 88(1-2), 19-44.
- Le, H., Moin, P., & Kim, J. (1997). Direct numerical simulation of turbulent flow over a backward-facing step. *Journal of fluid mechanics*, 330, 349-374.
- Lee, C., Min, T., & Kim, J. (2008). Stability of a channel flow subject to wall blowing and suction in the form of a traveling wave. *Physics of fluids*, 20(10), 101513.
- Lee, M., & Moser, R. D. (2015). Direct numerical simulation of turbulent channel flow up to $\text{Re}_\tau \approx 5200$. *Journal of fluid mechanics*, 774, 395-415.
- Lee, S., Lele, S. K., & Moin, P. (1992). Simulation of spatially evolving turbulence and the applicability of Taylor's hypothesis in compressible flow. *Physics of Fluids A: Fluid Dynamics*, 4(7), 1521-1530.
- LeVeque, R. J. (2002). *Finite volume methods for hyperbolic problems* (Vol. 31): Cambridge university press.

- Li, Y., & Zhou, Y. (2016). Skin Friction Drag Reduction Based on Unsteady Blowing Through One Array of Streamwise Slits. In *Fluid-Structure-Sound Interactions and Control* (pp. 157-161): Springer.
- Lieu, B. K., Moarref, R., & Jovanović, M. R. (2010). Controlling the onset of turbulence by streamwise travelling waves. Part 2. Direct numerical simulation. *Journal of Fluid Mechanics*, 663, 100-119.
- Lohse, J., Barth, H. P., & Nitsche, W. (2016). Active control of crossflow-induced transition by means of in-line pneumatic actuator orifices. *Experiments in Fluids*, 57(8), 124.
- Lu, S., & Willmarth, W. (1973). Measurements of the structure of the Reynolds stress in a turbulent boundary layer. *Journal of fluid mechanics*, 60(3), 481-511.
- Luchini, P. (2000). Reynolds-number-independent instability of the boundary layer over a flat surface: optimal perturbations. *Journal of fluid mechanics*, 404, 289-309.
- Luchini, P., Manzo, F., & Pozzi, A. (1991). Resistance of a grooved surface to parallel flow and cross-flow. *Journal of fluid mechanics*, 228, 87-109.
- Lund, T. S., Wu, X., & Squires, K. D. (1998). Generation of turbulent inflow data for spatially-developing boundary layer simulations. *Journal of computational physics*, 140(2), 233-258.
- Mamori, H., & Fukagata, K. (2011). *Drag reduction by streamwise traveling wave-like Lorenz Force in channel flow*. Paper presented at the Journal of Physics: Conference Series.
- Mamori, H., & Fukagata, K. (2014). Drag reduction effect by a wave-like wall-normal body force in a turbulent channel flow. *Physics of fluids*, 26(11), 115104.
- Mamori, H., Fukagata, K., & Hoepffner, J. (2010). Phase relationship in laminar channel flow controlled by traveling-wave-like blowing or suction. *Physical Review E*, 81(4), 046304.
- Mamori, H., Iwamoto, K., & Murata, A. (2014). Effect of the parameters of traveling waves created by blowing and suction on the relaminarization phenomena in fully developed turbulent channel flow. *Physics of fluids*, 26(1), 015101.
- Margolin, L., & Rider, W. (2005). The design and construction of implicit LES models. *International journal for numerical methods in fluids*, 47(10-11), 1173-1179.
- Margolin, L. G., & Rider, W. J. (2002). A rationale for implicit turbulence modelling. *International journal for numerical methods in fluids*, 39(9), 821-841.

- Min, T., Kang, S. M., Speyer, J. L., & Kim, J. (2006). Sustained sub-laminar drag in a fully developed channel flow. *Journal of fluid mechanics*, 558, 309-318.
- Mishra, M., & Skote, M. (2015). Drag reduction in turbulent boundary layers with half wave wall oscillations. *Mathematical Problems in Engineering*, 2015.
- Moarref, R., & Jovanović, M. R. (2010). Controlling the onset of turbulence by streamwise travelling waves. Part 1. Receptivity analysis. *Journal of fluid mechanics*, 663, 70-99.
- Mori, E., Quadrio, M., & Fukagata, K. (2017). Turbulent Drag Reduction by Uniform Blowing Over a Two-dimensional Roughness. *Flow, turbulence and combustion*, 99(3-4), 765-785.
- Murdock, J. W. (1980). The generation of a Tollmien-Schlichting wave by a sound wave. *Proc. R. Soc. Lond. A*, 372(1751), 517-534.
- Nakanishi, R., Mamori, H., & Fukagata, K. (2012). Relaminarization of turbulent channel flow using traveling wave-like wall deformation. *International journal of heat and fluid flow*, 35, 152-159.
- Noguchi, D., Fukagata, K., & Tokugawa, N. (2016). Friction drag reduction of a spatially developing boundary layer using a combined uniform suction and blowing. *Journal of Fluid Science and Technology*, 11(1), JFST0004-JFST0004.
- Nouar, C., Bottaro, A., & Brancher, J. (2007). Delaying transition to turbulence in channel flow: revisiting the stability of shear-thinning fluids. *Journal of fluid mechanics*, 592, 177-194.
- Orlandi, P., & Jiménez, J. (1994). On the generation of turbulent wall friction. *Physics of fluids*, 6(2), 634-641.
- Ovchinnikov, V. (2006). *Numerical simulation of boundary layer transition due to external disturbances*. University of Maryland, College Park,
- Ovchinnikov, V., Choudhari, M. M., & Piomelli, U. (2008). Numerical simulations of boundary-layer bypass transition due to high-amplitude free-stream turbulence. *Journal of fluid mechanics*, 613, 135-169.
- Pamiès, M., Garnier, E., Merlen, A., & Sagaut, P. (2007). Response of a spatially developing turbulent boundary layer to active control strategies in the framework of opposition control. *Physics of fluids*, 19(10), 108102.
- Pamiès, M., Weiss, P.-E., Garnier, E., Deck, S., & Sagaut, P. (2009). Generation of synthetic turbulent inflow data for large eddy simulation of spatially evolving wall-bounded flows. *Physics of fluids*, 21(4), 045103.
- Pang, J., & Choi, K.-S. (2004). Turbulent drag reduction by Lorentz force oscillation. *Physics of fluids*, 16(5), L35-L38.

- Peet, Y., & Sagaut, P. (2009). Theoretical prediction of turbulent skin friction on geometrically complex surfaces. *Physics of fluids*, 21(10), 105105.
- Poletto, R., Craft, T., & Revell, A. (2013). A new divergence free synthetic eddy method for the reproduction of inlet flow conditions for LES. *Flow, turbulence and combustion*, 91(3), 519-539.
- Quadrio, M., & Ricco, P. (2004). Critical assessment of turbulent drag reduction through spanwise wall oscillations. *Journal of fluid mechanics*, 521, 251-271.
- Quadrio, M., Ricco, P., & Viotti, C. (2009). Streamwise-travelling waves of spanwise wall velocity for turbulent drag reduction. *Journal of fluid mechanics*, 627, 161-178.
- Rao, V. N., Tucker, P., Jefferson-Loveday, R., & Coull, J. (2013). Large eddy simulations in low-pressure turbines: Effect of wakes at elevated free-stream turbulence. *International journal of heat and fluid flow*, 43, 85-95.
- Reed, H. L., Saric, W. S., & Arnal, D. (1996). Linear stability theory applied to boundary layers. *Annual review of fluid mechanics*, 28(1), 389-428.
- REN, Z.-t., Horus, Y., LEUNG, R. C., LI, S.-h., & Min, Z. (2018). Large Eddy Simulation of Planar Free Jet Flow Using the Space-Time Conservation Element/Solution Element Scheme. *DEStech Transactions on Computer Science and Engineering*(pcmm).
- Reshotko, E. (1976). Boundary-layer stability and transition. *Annual review of fluid mechanics*, 8(1), 311-349.
- Reynolds, O. (1883). An Experimental Investigation of the Circumstances Which Determine Whether the Motion of Water Shall Be Direct or Sinuous, and of the Law of Resistance in Parallel Channels. *Philosophical Transactions of the Royal Society of London A: Mathematical, Physical and Engineering Sciences*, vol. 174, pp. 935–982.
- Roach, P., & Brierlay, D. (1989). The influence of a turbulent freestream on zero pressure gradient transitional boundary layer development including the condition test cases T3A and T3B. *Numerical Simulation of Unsteady Flows and Transition to Turbulence*, 319-347.
- Roe, P. L. (1986). Characteristic-based schemes for the Euler equations. *Annual review of fluid mechanics*, 18(1), 337-365.
- Rothstein, J. P. (2010). Slip on superhydrophobic surfaces. *Annual review of fluid mechanics*, 42, 89-109.
- Sagaut, P. (2006). *Large eddy simulation for incompressible flows: an introduction*: Springer Science & Business Media.

- Saric, W. S., Helen, L., & Sadiki, A. (2002). Boundary-layer receptivity to freestream disturbances. *Annual review of fluid mechanics*, 34(1), 291-319.
- Sattarzadeh, S. S., & Fransson, J. H. (2017). Spanwise boundary layer modulations using finite discrete suction for transition delay. *Experiments in Fluids*, 58(3), 14.
- Schlatter, P., & Örlü, R. (2010). Assessment of direct numerical simulation data of turbulent boundary layers. *Journal of fluid mechanics*, 659, 116-126.
- Schlatter, P., Örlü, R., Li, Q., Brethouwer, G., Fransson, J. H., Johansson, A. V., . . . Henningson, D. S. (2009). Turbulent boundary layers up to $Re_\theta = 2500$ studied through simulation and experiment. *Physics of fluids*, 21(5), 051702.
- Schoppa, W., & Hussain, F. (1998). A large-scale control strategy for drag reduction in turbulent boundary layers. *Physics of fluids*, 10(5), 1049-1051.
- Schoppa, W., & Hussain, F. (2002). Coherent structure generation in near-wall turbulence. *Journal of fluid mechanics*, 453, 57-108.
- Segawa, T., Kawaguchi, Y., Kikushima, Y., & Yoshida, H. (2002). Active control of streak structures in wall turbulence using an actuator array producing inclined wavy disturbances. *J. Turbul*, 3(1), 1-14.
- Sergent, E. (2002). *Vers une methodologie de couplage entre la Simulation des Grandes Echelles et les modeles statistiques*. Ecully, Ecole centrale de Lyon,
- Shao, L., Sarkar, S., & Pantano, C. (1999). On the relationship between the mean flow and subgrid stresses in large eddy simulation of turbulent shear flows. *Physics of fluids*, 11(5), 1229-1248.
- Smirnov, A., Shi, S., & Celik, I. (2001). Random flow generation technique for large eddy simulations and particle-dynamics modeling. *Journal of fluids Engineering*, 123(2), 359-371.
- Spalart, P. R. (1988). Direct simulation of a turbulent boundary layer up to $Re_\theta = 1410$. *Journal of fluid mechanics*, 187, 61-98.
- Stroh, A., Frohnäpfel, B., Schlatter, P., & Hasegawa, Y. (2015). A comparison of opposition control in turbulent boundary layer and turbulent channel flow. *Physics of fluids*, 27(7), 075101.
- Sweby, P. K. (2007). High resolution schemes using flux limiters.
- Tabor, G. R., & Baba-Ahmadi, M. (2010). Inlet conditions for large eddy simulation: a review. *Computers & Fluids*, 39(4), 553-567.
- Tardu, F. S., Nacereddine, R., & Doche, O. (2008). An interactive bypass transition mechanism in wall-bounded flows. *Journal of fluid mechanics*, 615, 345-369.

- Tennekes, H., Lumley, J. L., & Lumley, J. (1972). *A first course in turbulence*: MIT press.
- Tomiyama, N., & Fukagata, K. (2013). Direct numerical simulation of drag reduction in a turbulent channel flow using spanwise traveling wave-like wall deformation. *Physics of fluids*, 25(10), 105115.
- Touber, E., & Leschziner, M. A. (2012). Near-wall streak modification by spanwise oscillatory wall motion and drag-reduction mechanisms. *Journal of fluid mechanics*, 693, 150-200.
- Van Leer, B. (1974). Towards the ultimate conservative difference scheme. II. Monotonicity and conservation combined in a second-order scheme. *Journal of Computational Physics*, 14(4), 361-370.
- Wallace, J. M., Eckelmann, H., & Brodkey, R. S. (1972). The wall region in turbulent shear flow. *Journal of fluid mechanics*, 54(1), 39-48.
- Walsh, M. J. (1983). Riblets as a viscous drag reduction technique. *AIAA journal*, 21(4), 485-486.
- Wei, T., & Willmarth, W. (1989). Reynolds-number effects on the structure of a turbulent channel flow. *Journal of fluid mechanics*, 204, 57-95.
- Wilkinson, S., & Balasubramanian, R. (1985). *Turbulent burst control through phase-locked traveling surface depressions*. Paper presented at the Shear Flow Control Conference.
- Wood, R. M. (2004). *Impact of advanced aerodynamic technology on transportation energy consumption* (0148-7191). Retrieved from
- Xia, Q.-J., Huang, W.-X., Xu, C.-X., & Cui, G.-X. (2015). Direct numerical simulation of spatially developing turbulent boundary layers with opposition control. *Fluid Dynamics Research*, 47(2), 025503.
- Xiao, D., & Papadakis, G. (2017). Nonlinear optimal control of bypass transition in a boundary layer flow. *Physics of fluids*, 29(5), 054103.
- Yan, H., Knight, D., & Zheltovodov, A. (2002). Large-eddy simulation of supersonic flat-plate boundary layers using the monotonically integrated large-eddy simulation (MILES) technique. *Journal of fluids Engineering*, 124(4), 868-875.
- Zeng, X. (2016). A general approach to enhance slope limiters in MUSCL schemes on nonuniform rectilinear grids. *SIAM Journal on Scientific Computing*, 38(2), A789-A813.
- Zhang, W.-Y., Huang, W.-X., Xu, C.-X., & Cui, G.-X. (2016). Suboptimal control of wall turbulence with arrayed dimple actuators for drag reduction. *Journal of Turbulence*, 17(4), 379-399.

Zhu, Z., Bai, P., & Shang, Q. (2018). *Large Eddy Simulation of Laminar Separation Flow Past the SD7003 Airfoil*. Paper presented at the Asia-Pacific International Symposium on Aerospace Technology.

Appendix

Mesh resolution study for a single slit

As already mentioned in Chapter 5, the numerical simulations presented in Chapter 5 need a dense mesh, so the accuracy of the current simulations should be validated via a thorough grid independence study which will be considered as a future work for the current study. Below is a preliminary grid test towards that effort.

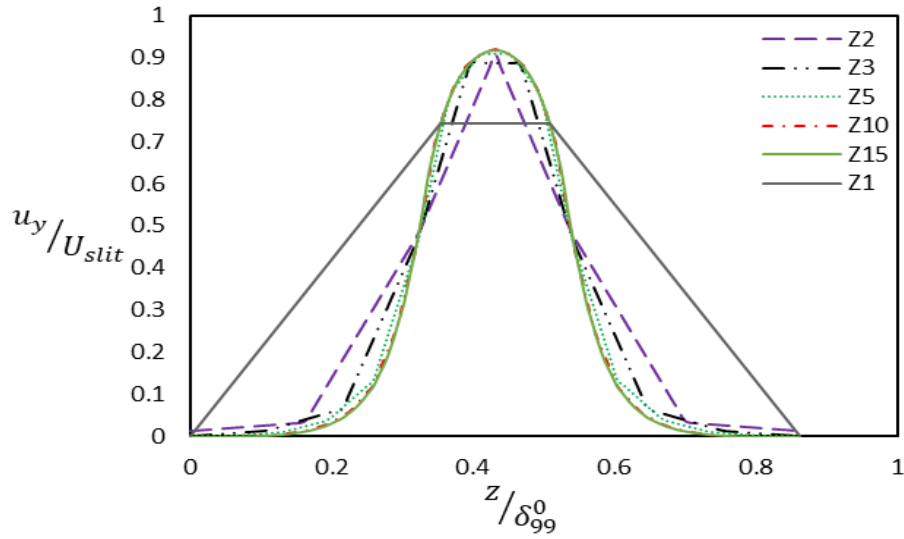
Ruiz et al. (2015) and Di Venuta et al. (2018) studied the behaviour of a jet flow by using the velocity profile of the jet inside the main flow or by the flow concentration when the injected fluid differs from the mainstream fluid. Both the velocity profile and the concentration have the Gaussian shape in the effected zone above the jet. In this study, the jet flow and the mainstream flow both are water, hence the velocity profile of the jet is been used to investigate the grid dependence on results. The geometry of the computational domain is made of a rectangular box with the dimensions of $(L_x, L_y, L_z) = (12\pi \delta \times 2 \delta \times 3Z_{slit})$, where Z_{slit} is the slit width in spanwise direction and δ is the half channel height. Six different meshes distributions have been used for the computational domain with one slit during this study as shown in Table (A). The meshes distribution is uniformly spaced in the spanwise direction, while in wall-normal direction, an expanding mesh towards the channel centre is used.

Table (A) Single jet meshes

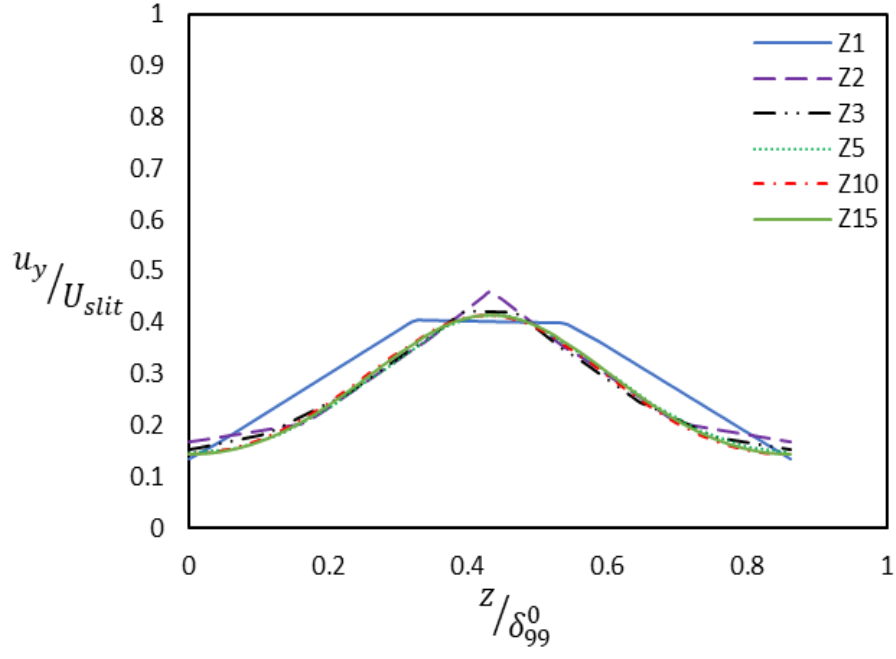
Case	$N_x \times N_y \times N_z$
Z1 (single grid point /slit)	400 x 125 x 3
Z2 (2 grid points /slit)	400 x 125 x 6
Z3 (3 grid points /slit)	400 x 125 x 9
Z5 (5 grid points /slit)	400 x 125 x 15
Z10 (10 grid points /slit)	400 x 125 x 30
Z15 (15 grid points /slit)	400 x 125 x 45

The mean velocity profiles of the jets inside the channel for the above cases are plotted in Figure (I) at different values of $y_{slit}^+ = (u_{\tau-slit} * y) / \gamma = \mathbf{1.5, 10, 15}$, as

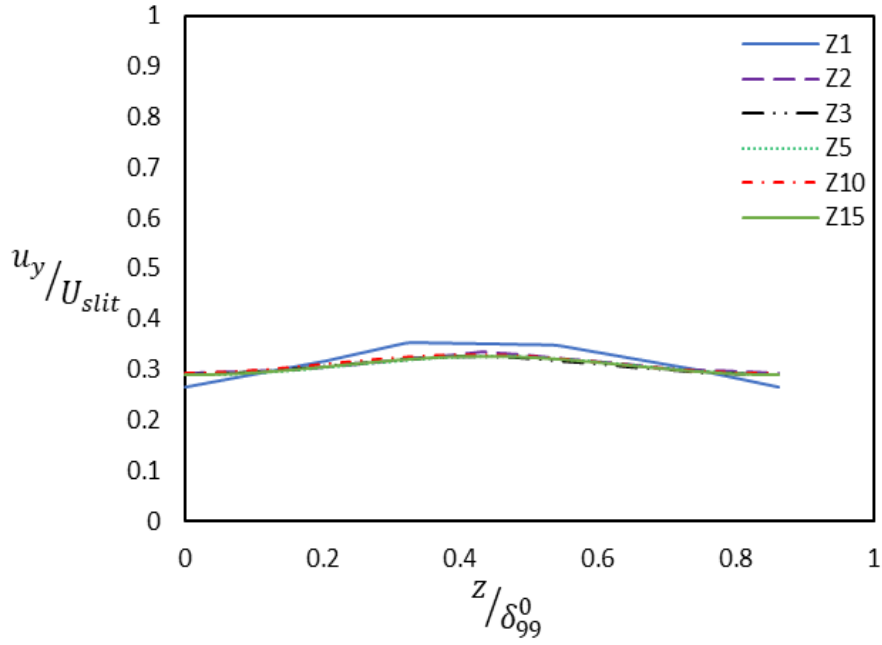
shown in Figure (I)-(a)-(b) and (c) respectively. The velocity contours are produced in Figure (II) for the flow above the slit which also shows how the velocity distribution follows the Gaussian shape above the slit. The relative errors in the results are analysed in Table (B). From Figure (I)-(a), case Z1 doesn't produce the Gaussian profile and has an error percentage of 19.1% relative to the case of Z15 at the peak point of the curve. While, cases Z3, Z5, Z10, Z15 reproduced the velocity profile with a relatively very small percentage of error, according to Table (B). In Figure (I)-(b) and (c), case Z3 and Z5 start to produce the same behaviour as the other cases especially at $y_{slit}^+ \geq 10$ which is considered as the main region of the wave effect on the turbulence structures of the flow as illustrated in Chapter 2 of the thesis. All the results are produced after 10 RTPT (Required Time Per One Trip). Figure (II) and Figure (III) show the velocity contour profiles above the slit. Figure (II)–(b) shows the weak effect of the mesh resolution on the jet behaviour and how the velocity profile is produced with sharp edges of the velocity contours at the centre of the jet. But case Z3 still produces good results with small error percentage as shown in Table (B) in the region of wave effect on the turbulence structures. It's clear from both figures how the Gaussian shape is produced for cases Z3, Z5, Z10, Z15.



(a)



(b)



(c)

Figure (I) Jet velocity profile in the spanwise direction at different normal to the wall locations; (a) $y_{slit}^+ = 1.5$, (b) $y_{slit}^+ = 10$, (c) $y_{slit}^+ = 15$

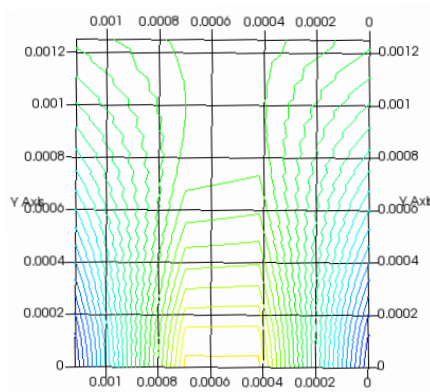
Table (B) Results analysis of the mesh independence study for the Jet flow

No. of grid points per slit	1	2	3	5	10	15
Error % @ $y^+ = 1.5$	19.1	1.09	3.48	1.14	0.1	-
Error % @ $y^+ = 10$	3.03	6.01	1.54	0.04	0.0107	-
Error % @ $y^+ = 15$	5.22	2.58	0.26	0.35	0.34	-
No. of processors used	6	9	10	32	52	112
Total wall hours	31	33	120	40	55	96
Total CPU hours	186	297	1200	1280	2860	10752
Time ratio %	1.72	2.76	11.16	11.9	26.59	-

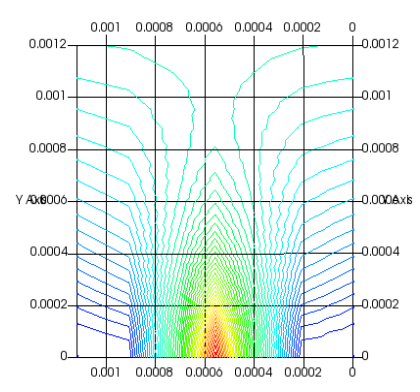
The penetration depth of the jet inside the mainstream flow is produced in Figure (II) and Figure (III) and measured relative to the boundary layer thickness at the inlet plane of the channel in Table (C):

Table (C) Jet flow penetration length

No. of grid points per slit	1	2	3	5	10	15
L_y / δ_{99}^0	0.5986	0.6172	0.6943	0.6558	0.6837	0.6789



(a)



(b)

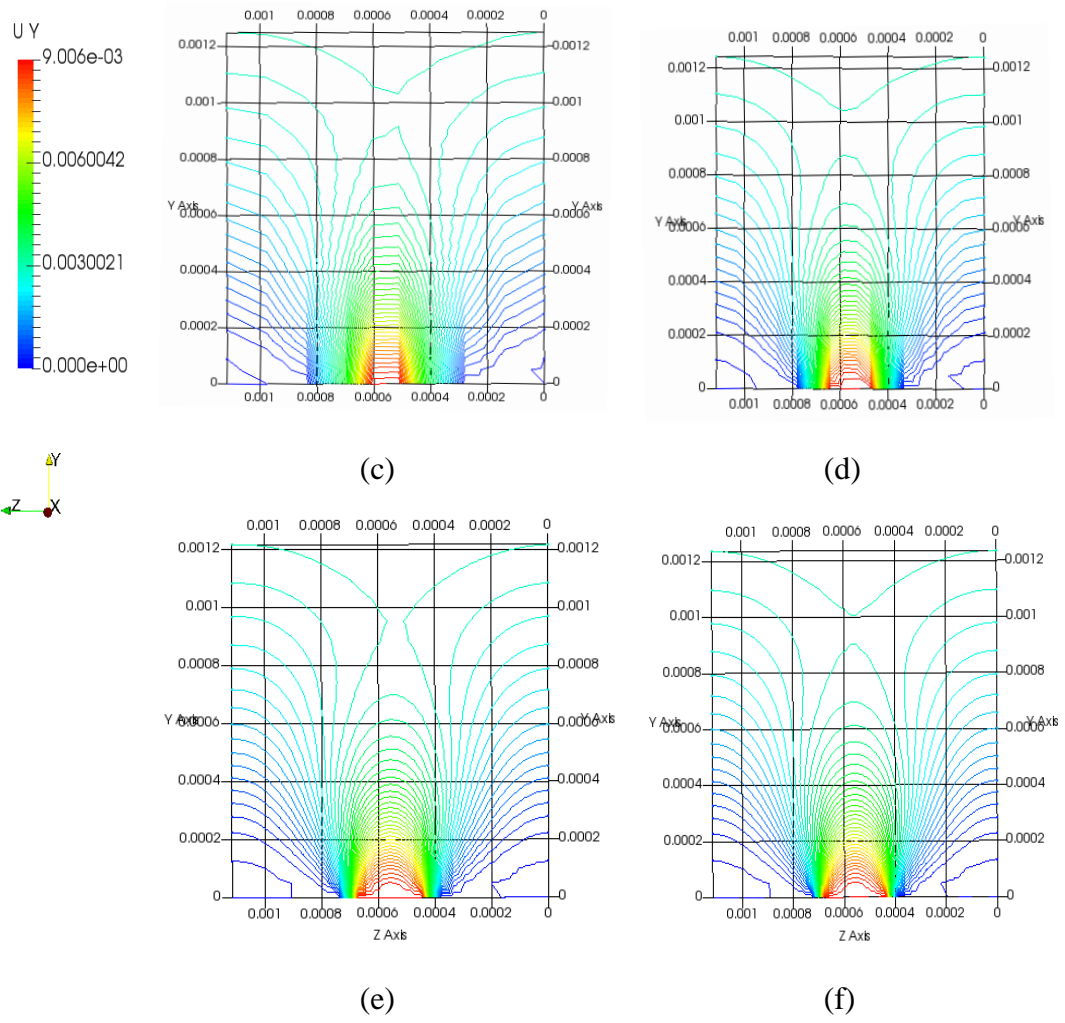
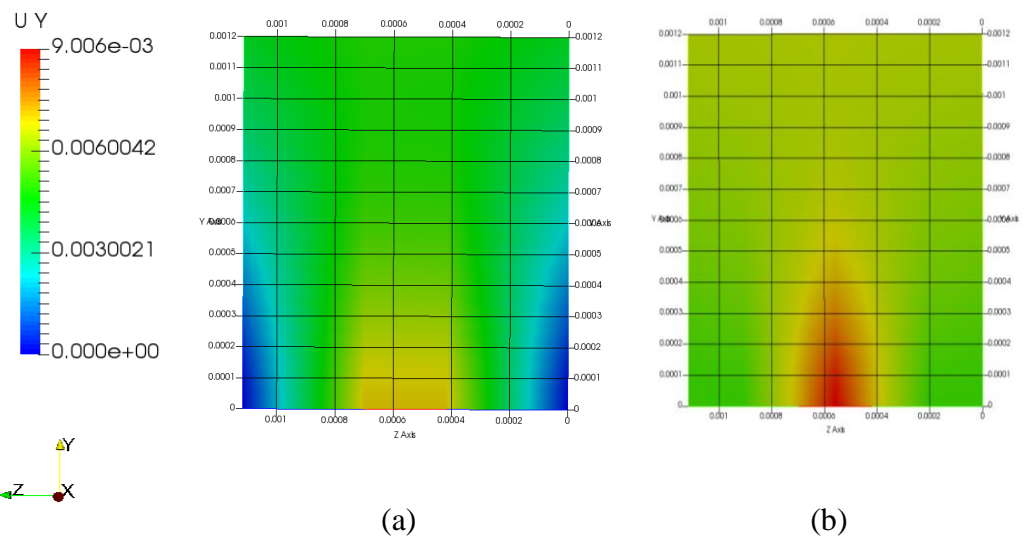
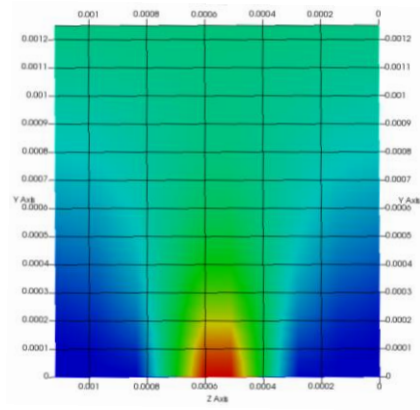
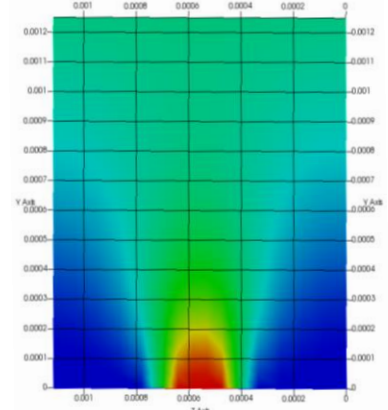


Figure (II) Jet velocity contours at streamwise mid-section of the slit
(a) Z1; (b) Z2; (c) Z3; (d) Z5; (e) Z10; (f) Z15

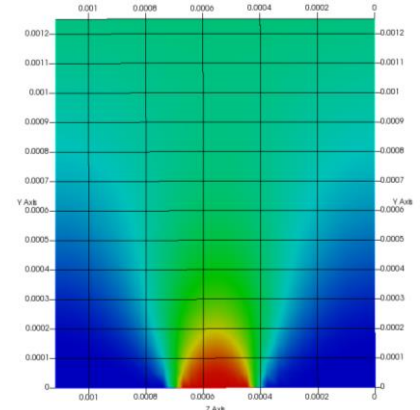




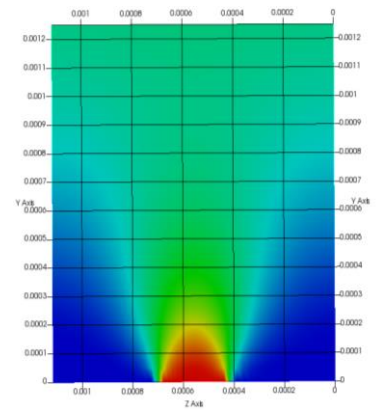
(c)



(d)



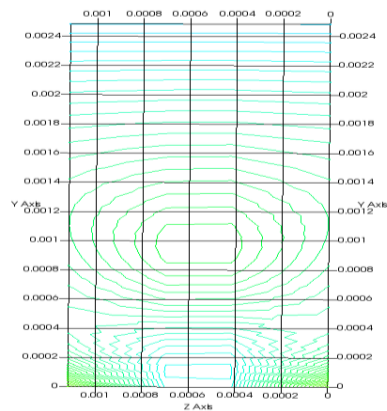
(e)



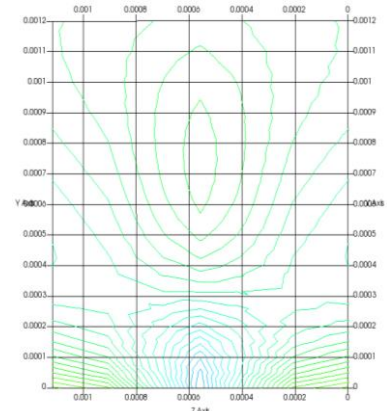
(f)

Figure (III) Jet velocity distribution at streamwise mid-section of the slit.
(a) Z1; (b) Z2; (c) Z3; (d) Z5; (e) Z10; (f) Z15

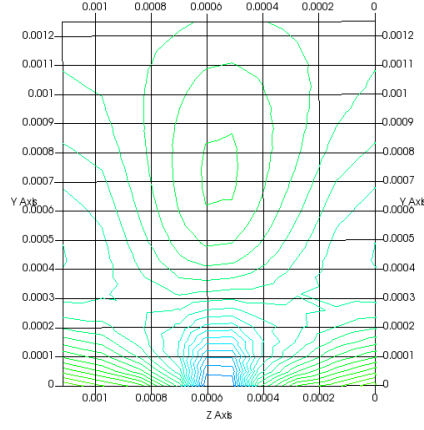
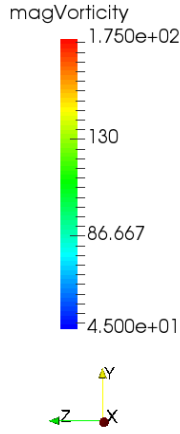
Figure (IV) shows the flow vorticity at the mid-section of the slit and ensures that cases Z3 and Z5 reproduce suitable results in comparison to the increase mesh resolution per each slit cases Z10 and Z15.



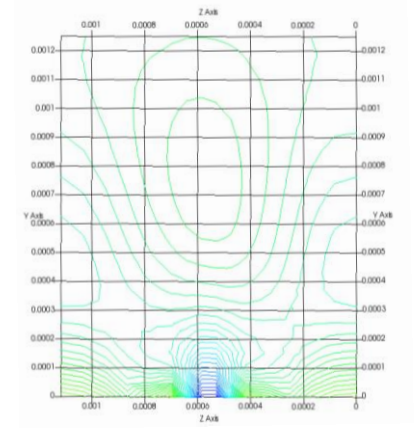
(a)



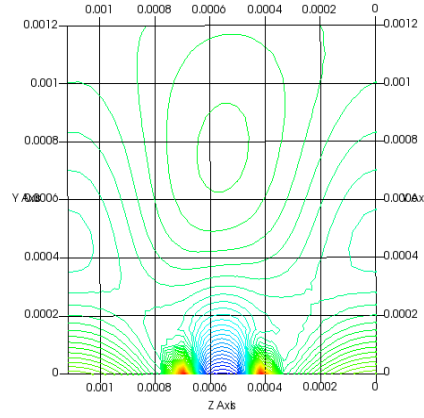
(b)



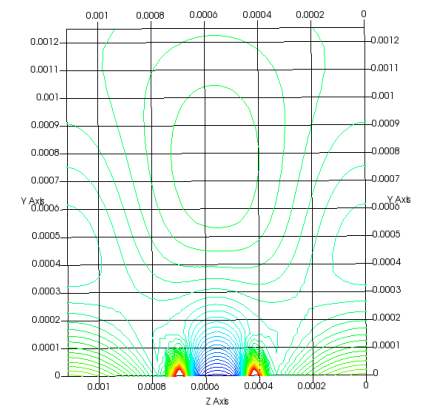
(c)



(d)



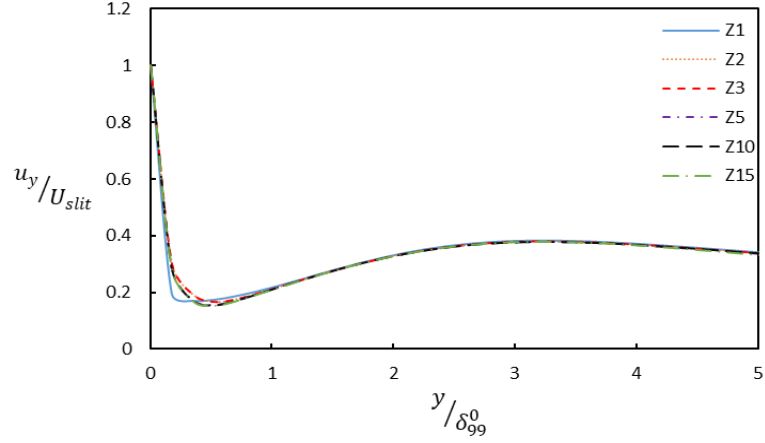
(e)



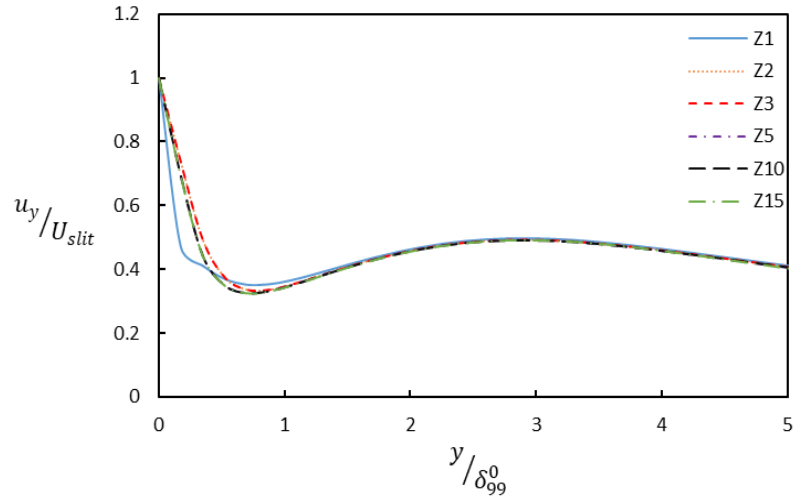
(f)

Figure (IV) Vorticity of the flow
(a) Z1; (b) Z2; (c) Z3; (d) Z5; (e) Z10; (f) Z15

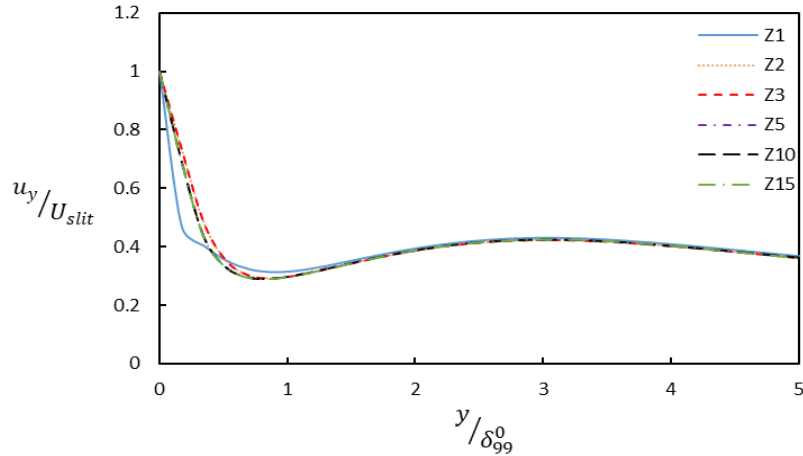
Figure (V) produces the normal to the wall mean velocity profile of the jet penetration inside the channel at different streamwise stations of the slit. As shown, Figure (V)-(a) shows the jet penetration depth at the start of the slit in the streamwise direction, in which the jet penetrates the mainstream flow until $y/\delta_{99}^0 = 0.52$ with velocity decreasing till $u_y/U_{slit} = 0.153$ then it starts to increase with increasing the penetration depth inside the channel. For case Z2, Z3, Z5, Z10, Z15, they appear to give the same behaviour for the jet penetration inside the mainstream. While case Z1 shows some deviation near to the wall before the deflection point of the curve with a steeper velocity decreasing rate. Figure (V)-(b) shows the jet penetration at the mid-section of the slit in the streamwise direction. The jet penetration with decreasing the velocity lasts till $u_y/U_{slit} = 0.326$ at $y/\delta_{99}^0 = 0.694$ with same behaviour of case Z1. Finally, Figure (V)-(c) shows the same behaviour in Figure (V)-(b) with deflection point of $u_y/U_{slit} = 0.293$ at $y/\delta_{99}^0 = 0.694$.



(a) $X=0.3$ (m) start of the slit in the streamwise direction



(b) $X=0.306$ (m) mid of the slit in the streamwise direction

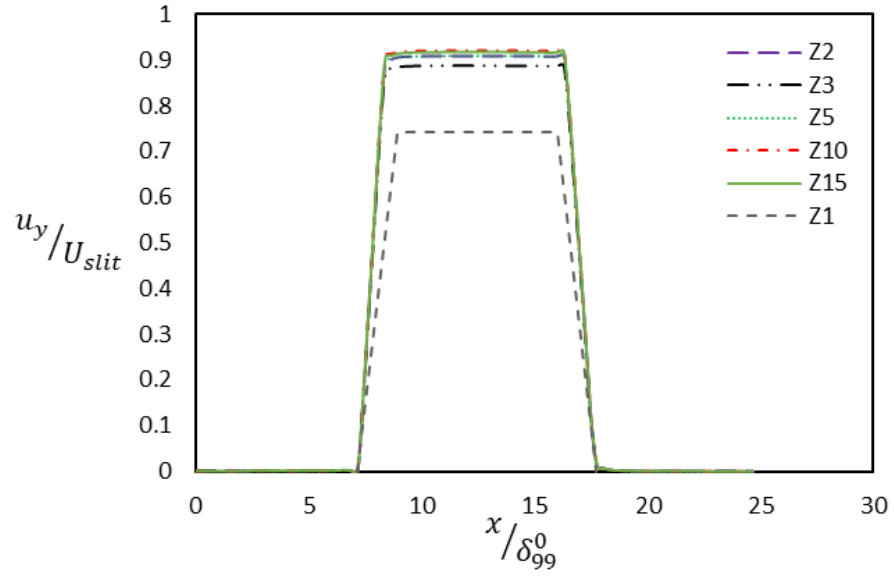


(c) $X=0.31$ (m) end of the slit in the streamwise direction

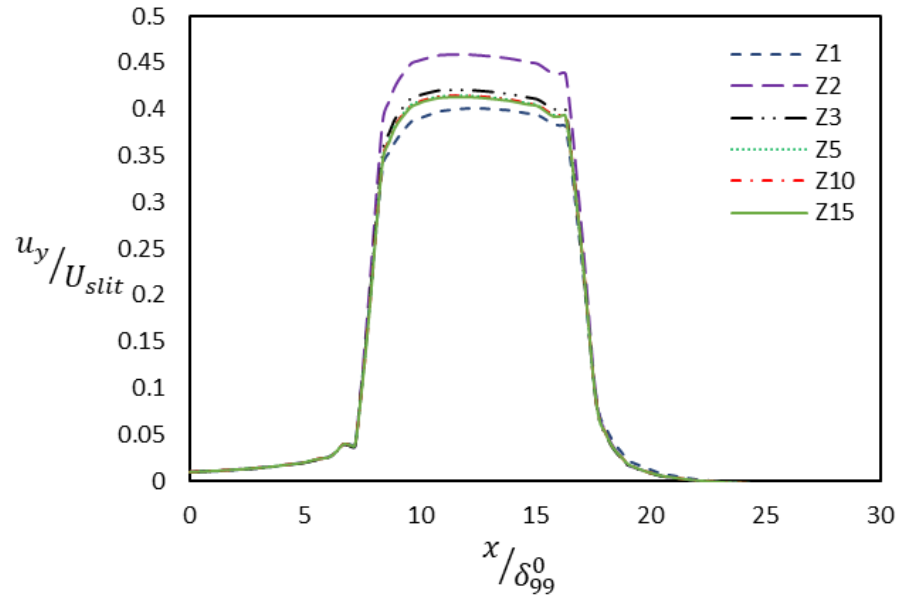
Figure (V) Normal to the wall mean velocity variation of the jet penetration normalised by the inlet boundary layer thickness and the mean velocity of the jet

Also, the mean velocity profile is drawn in the streamwise direction over the slit at different normal to the wall distances $y_{slit}^+ = (u_{\tau-slit} * y)/\gamma = 1.5, 10, 15$, as

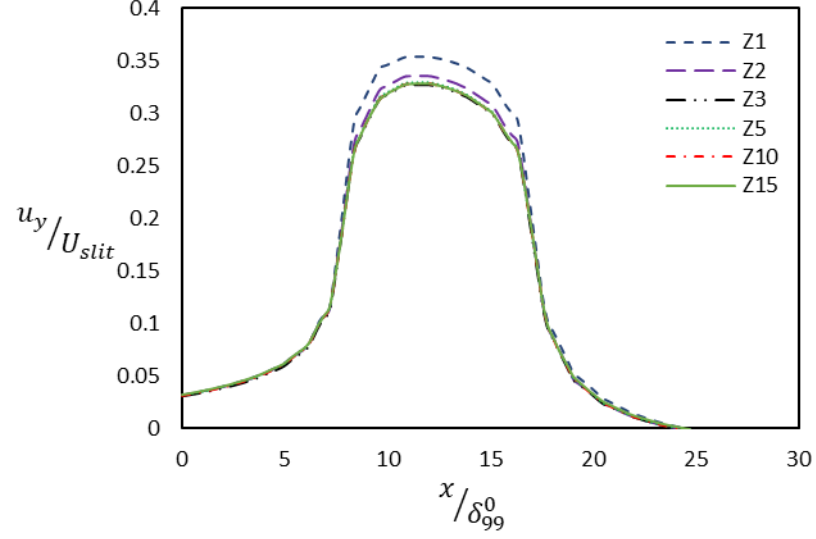
shown in Figure (VI). Figure (VI)-(a) ensures the less accuracy of case Z1 to produce the jet behaviour near to the wall. While Figure (VI)-(b and c) shows that cases Z3, Z5, Z10, Z15 are able to produce the jet behaviour along the slit in the streamwise direction. The same as mentioned before in Figure (I).



(a)



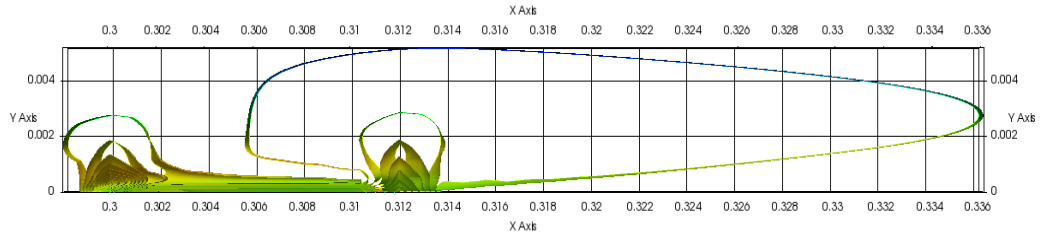
(b)



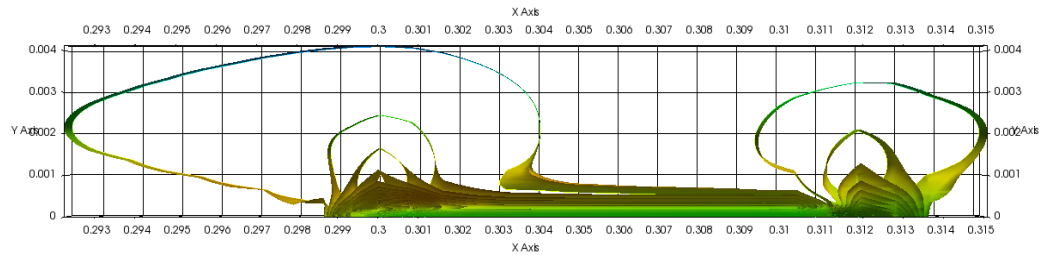
(c)

Figure (VI) Jet velocity profile in the streamwise direction at different normal to the wall distances; (a) $y_{slit}^+ = 1.5$, (b) $y_{slit}^+ = 10$, (c) $y_{slit}^+ = 15$

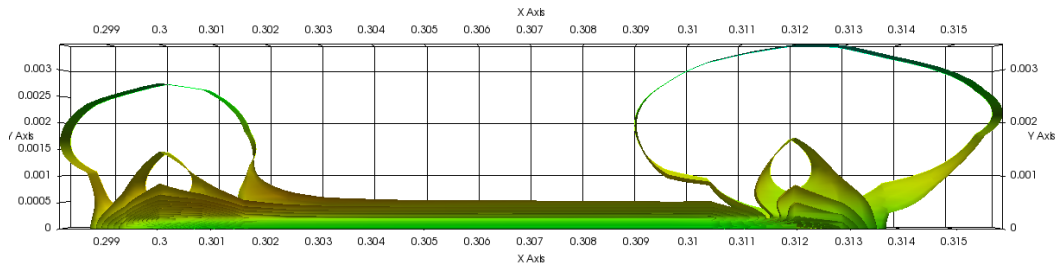
The three-dimensional positive Q isosurfaces are shown in Figure (VII), coloured with vorticity magnitude, in the streamwise section between $x/\delta_{99}^0 = 224$ and $x/\delta_{99}^0 = 270$ while the slit starts at $x/\delta_{99}^0 = 230$ and ends at $x/\delta_{99}^0 = 240$ from the inlet plane of the channel. As shown in the figures, the variation of Q at the start and the end of the slit differs with increasing the mesh resolution in the spanwise direction. Cases Z3 and Z5 produce good approximation for the behaviour of Q relative to that one of case Z15.



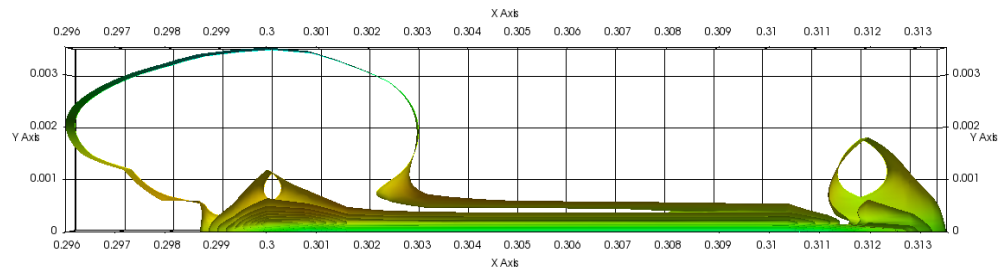
(a)



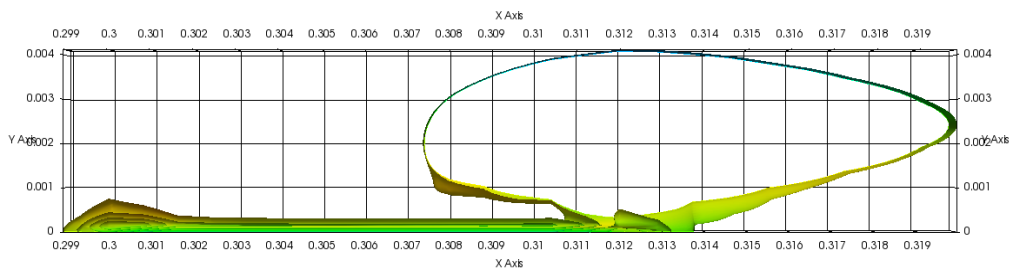
(b)



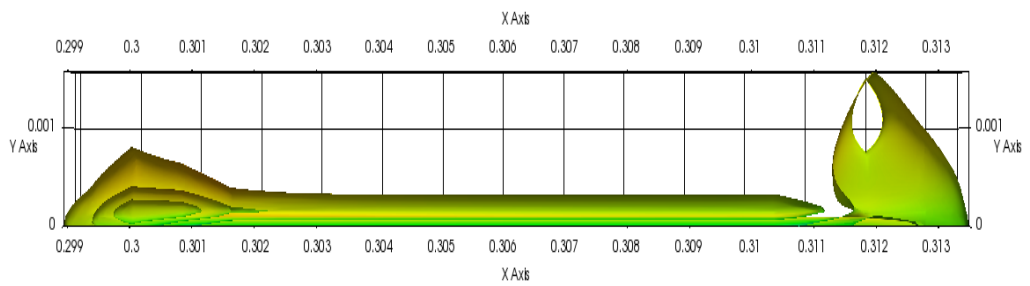
(c)



(d)



(e)



(f)

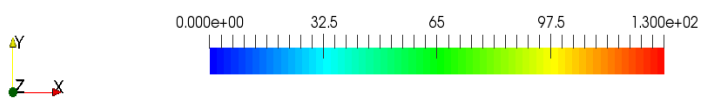


Figure (VII) Isosurfaces of Q coloured with the magnitude of the vorticity
(a) $Z1$; (b) $Z2$; (c) $Z3$; (d) $Z5$; (e) $Z10$; (f) $Z15$

From the previous results, it can be concluded that cases Z3 and Z5 produce the effect of jet flow inside the channel with a good agreement relative to the cases of Z10 and Z15. While, cases Z1 and Z2 produce this agreement at a normal to the wall distance of $y_{slit}^+ \geq 10$ with a maximum percentage error of 5.22%.

The main scope of the current study is applying a complete sinusoidal travelling wave in the spanwise direction, using multi-slits, to study its effect on the drag reduction and the transition onset. So, a complete 3 different cases, with 30 slits in each, using a mesh resolution of a single grid point, 2 grid points, and 3 grid points per each slit are investigated to show the wave performance through each mesh. The computation domain dimensions for these 3 cases is the same as that one used in Section 5.2.4 in this thesis. These 3 cases are mentioned as $N_z = 123$, $N_z = 246$ (2 points case per slit) and $N_z = 369$ (3 points case per slit). Figure (VIII) shows the skin friction coefficient through the channel and the wave effect on it. It can be seen that increasing the resolution of the mesh in the spanwise direction produces further streamwise location for the bypass transition onset with almost the same position as the maximum drag drop. In the cases of $N_z = 246$ and $N_z = 369$, a maximum drag reduction of 35% is achieved compared to 33.9% in the case of $N_z = 123$, while the start of the bypass transition is shifted in downstream.

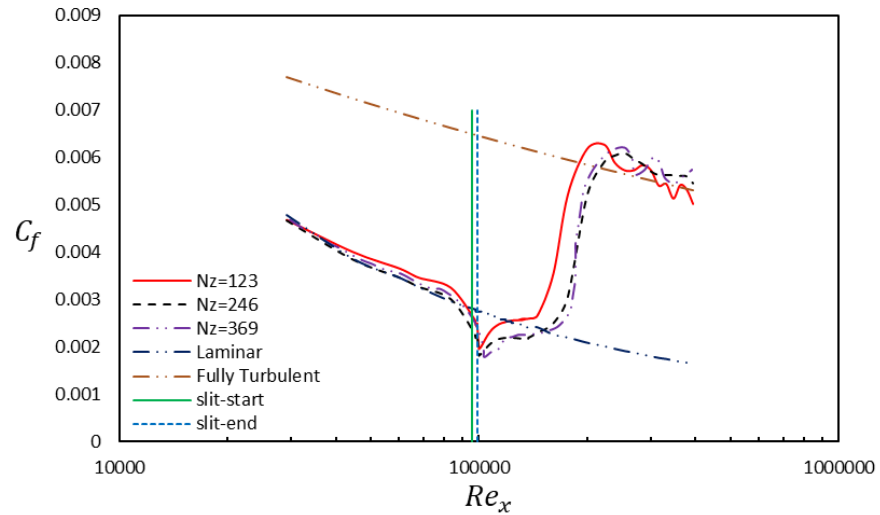


Figure (VIII) Maximum drag reduction and bypass transition onset at different spanwise mesh resolution

References

- Di Venuta, I., Petracci, I., Angelino, M., Boghi, A., & Gori, F. (2018). Numerical simulation of mass transfer and fluid flow evolution of a rectangular free jet of air. *International Journal of Heat and Mass Transfer*, 117, 235-251.
- Ruiz, A., Lacaze, G., & Oefelein, J. (2015). Flow topologies and turbulence scales in a jet-in-cross-flow. *Physics of fluids*, 27(4), 045101.